Development of the Pixel Detector for the Belle II experiment and top quark mass measurement in radiative events at the future electron-positron linear collider

VNIVERSITAT DE VALÈNCIA

Pablo Gomis López

Bajo la supervisión de *Juan Fuster Verdú*
Carlos Mariñas Pardo

Facultad de Física
Departamento de Física Atómica, Molecular y Nuclear

Doctorado en Física

València, Septiembre 2019

Declaración

Prof. Juan A. Fuster Verdú
Profesor de investigación del CSIC, y
Dr. Carlos Mariñas Pardo
Investigador distinguido (GenT) del CSIC

CERTIFICAN:

Que la presente memoria que tiene por título "Development of the Pixel Detector for the Belle II experiment and top quark mass measurement in radiative events at the future electron-positron linear collider" ha sido realizada bajo su dirección, en el Instituto de Física Corpuscular (centro Mixto Universidad de Valencia y CSIC) por Pablo Gomis López y que constituye su trabajo de tesis doctoral en el Departamento de Física Atómica, Molecular y Nuclear para optar al grado de Doctor en Física por la Universidad de Valencia. Y para que conste, firman el presente certificado.

Prof. Juan A. Fuster Verdú **Dr. Carlos Mariñas Pardo**

Visto bueno del tutor,
Prof. Armando Pérez Cañellas

València, Septiembre 2019

El presente trabajo ha sido realizado en el grupo de Futuros Aceleradores del Instituto de Física Corpuscular (IFIC) en Paterna (València), España.

Dentro del marco del Programa de Ayudas para la Contratación de Personal Investigador en Formación de carácter predoctoral (ACIF16/2016/099) de la Consellería de Educación, Investigación, Cultura y Deporte de la Comunitat Valenciana.

El IFIC es un centro mixto del Consejo Superior de Investigaciones Científicas (CSIC) y de la Universitat de València (UV). En Julio de 2015 recibió la acreditación Severo Ochoa (SEV-2014-0398) que le distingue como Centro de Excelencia. Dicha acreditación reconoce la excelencia y las contribuciones científicas que realizan los centros y unidades a nivel nacional e internacional, su impacto empresarial y social y su capacidad para atraer talento.

Agradecimientos

La redacción de esta tesis marca el final de un capítulo de mi vida. Durante estos últimos años he tenido que enfrentarme a multitud de retos y situaciones que me han hecho superarme y progresar. Y a mi lado, durante todo este tiempo siempre ha habido gente acompañándome y guiándome en esta aventura. Esta sección va por todos ellos.

En primer lugar, agradecer a Armando Pérez el introducirme en el mundo de la investigación científica y proporcionarme la primera oportunidad de convertirme en investigador. A Juan Fuster y Carlos Mariñas por apostar por mi y guiarme durante todos estos años, estando siempre ahí cuando les he necesitado, y a la vez dándome la autonomía necesaria para poder crecer personal y profesionalmente. Sin vosotros no sería el científico que hoy soy. También a Marcel Vos, Esteban Fullana y el resto de compañeros del IFIC por sus consejos, su apoyo y toda la ayuda que me han brindado a lo largo de este camino.

A Marçà, Nacho, Miguel Ángel, Martín, Deltoro, Guillem y el resto de compañeros del IFIC, por esos momentos que hemos disfrutado juntos en congresos, estancias, el laboratorio, los debates de los almuerzos de las 11, y... cómo no, en las calçotadas a can Miguel. No sólo me llevo esos momentos, si no también grandes amigos. Agradecer especialmente a Marçà por ser mi mentor y allanarme el camino, enseñándome a utilizar las herramientas adecuadas y transfiriéndome sus conocimientos. Nunca olvidaré todos esos momentos en Múnich durante aquella montaña rusa que fue probar el primer módulo final.

Special thanks to my host in Munich, Hans-Günther Moser, for welcoming me into his group and taking care of me during my long stay, it is much appreciated. Also, thanks to the MPP and HLL crews, specially to Phillipp, Felix, Christian, Laci, Eddie, Mitja and Stefan for making me feel one more of the group, and, being there as friends for me over all those months. It has been an amazing experience. Last, I also wanted to thank the SiLab Bonn guys, specially Botho, Bruno and Patrick. It was a lot of fun sharing those weeks in Bonn and Tsukuba with you guys.

Quisiera agradecer a mis amigos de Valencia por acompañarme durante toda esta etapa de mi vida. Estos diez años han sido alucinantes y dejan grandes recuerdos que nunca olvidaré: esas laaargas jornadas de estudio en la Eduard Boscà, las quedadas por Burja, los interrailes, las pachangas, las paellas, los carnavales, los viajes... podría estar todo el día. Entre todos -y muy especialmente, mis compañeros del *BurjaPiso*- habéis convertido Valencia en mi hogar. Gracias a todos vosotros por estar ahí.

Por último, agradecer también a mi familia y amigos de Elche y Santa Pola. Pese a la distancia, habéis estado ahí siempre que lo he necesitado. De hecho, habéis estado ahí siempre, toda la vida, acompañándome paso a paso y compartiendo cada suceso de importancia, cada instante determinante. Gracias de corazón.

Y no podría terminar esta sección sin dedicarle la tesis a mi familia más cercana. A mi padre, mi madre y mi hermana. Estos últimos años han sido muy intensos, con momentos muy buenos, buenos y momentos no tan buenos, y ahí habéis estado siempre, al pie del cañón. Sois y siempre seréis el pilar maestro de mi vida. Nada de esto hubiera sido posible sin vosotros.

Abstract

The last hundred years of discoveries at particle colliders and theoretical breakthroughs have allowed particle physicists to elaborate the Standard Model, the most successful theoretical model to date. In spite of its huge success, the Standard Model cannot describe all the observed phenomenology in the different experiments. New colliders are needed to provide the much-needed new physics that will allow us to elaborate models that resolve these unexplained phenomena.

To face this challenge, the particle physics community unites forming large collaborations, with the purpose of building the colliders of the future. The works in this thesis join these efforts, making a small contribution to the progress of the field.

This thesis is divided into two parts, divided in six Chapters. The first part is dedicated to the development of the Pixel Detector (PXD), the innermost detector of the Belle II experiment in the SuperKEKB collider. The second part is focused on the proposal of a new observable to measure the mass of the top quark in the future electron-positron linear collider.

The first two Chapters give the necessary context to understand the works carried out as part of the thesis. In particular, Chapter 1 provides an introduction to the particle physics field from the phenomenologist point of view, peeking at the Standard Model, its accomplishments, its shortcomings, and its most plausible successors. Chapter 2 introduces the new generation of lepton colliders: the SuperKEKB collider, the International Linear Collider (ILC) and the Compact Linear Collider (CLIC).

Chapters 3 and 4 describe the DEPFET-based Pixel Detector and its production, respectively, including the quality control of the PXD production carried out at the clean room of the MPG Halbleiterlabor in Munich as the IFIC contribution to the PXD collaboration. Chapter 5 summarizes the characterization of a PXD module, including the measurement of the sensor internal gain g_q.

Finally, Chapter 6 introduces a new observable, analyzing the potential of ILC and CLIC to produce precise measurements of the top quark mass in radiative events in a theoretically sound renormalization scheme.

Contents

Nomenclature

1S	1S renormalization scheme
AC	Alternating Current
ACMC	Analog Common Mode Correction
ADC	Analog to Digital Converter
ADU	Analog to Digital Unit
AGS	Alternating Gradient Synchrotron
AMS	Austria Mikro Systeme
ASIC	Application Specific Integrated Circuit
ATLAS	A Toroidal LHC Apparatus
BCB	Benzocyclobutene
BDS	Beam Delivery System
BEAST II	Beam Exorcism for A Stable experiment II
BNL	Brookhaven National Laboratory
BSM	Beyond Standard Model
c	Speed of light in vacuum

CDC	Central Drift Chamber
CDF	Collider Detector at Fermilab
CDR	Conceptual Design Report
CERN	European Organization for Nuclear Research
CKM	Cabbibo-Kobayashi-Maskawa matrix
CLIC	Compact Linear Collider
CLICdet	CLIC detector concept
CLICdp	CLIC detector and physics collaboration
CML	Current Mode Logic
CMS	Compact Muon Solenoid
CP	Charge inversion and Parity combined symmetry
CPT	Charge inversion, Parity and Time reversal combined symmetry
CSS	Control System Studio
DAC	Digital to Analog Converter
DAQ	Data Acquisition system
DBA	Drive Beam Accelerator
DCD	Drain Current Digitizer
DEPFET	Depleted Field Effect Transistor
DESY	Deutsches Elektronen-Synchrotron
DHC	Data Handling Concentrator
DHE	Data Handling Engine

DHH	Data Handling Hub
DHI	Data Handling Interface
DHP	Data Handling Processor
DONUT	Direct Observation of the Nu Tau
ECAL	Electromagnetic Calorimeter
EMCM	Electrically active Multi-Chip Module
EM	Electromagnetism
EOS	End Of Stave
EPICS	Experimental Physics and Industrial Control System
EW	Electroweak theory
E-XFEL	European X-Ray Free-Electron Laser Facility
FSR	Final State Radiation
FTD	Forward Tracking Disks
FTSW	Frontend Timing Switch
GND	Ground power net
GR	General Relativity
GUI	Graphical User Interface
GUT	Grand Unified Theory
HCAL	Hadronic Calorimeter
HEP	High Energy Physics
HER	High Energy Ring

HL-LHC	High Luminosity LHC
HLL	MPG Halbleiterlabor
HV	High Voltage
IB	Inner Backward
IFIC	Instituto de Física Corpuscular
IF	Inner Forward
ILC	International Linear Collider
ILD	International Large Detector
IOC	Input-Output Controller
ISR	Initial State Radiation
JTAG	Joint Test Action Group
KEK	High Energy Accelerator Research Organization
KLM	K_L and Muon detector
λ_I	Interaction length
ΛCDM	Lambda Cold Dark Matter model
LBNL	Lawrence Berkeley National Laboratory
LCFI	Linear Collider Flavour Identifier
LER	Low Energy Ring
LHC	Large Hadron Collider
Linac	Linear accelerator
LMU PS	Ludwig-Maximilians-Universität Power Supply

LO	Leading Order
LVDS	Low Voltage Differential Signaling
MOSFET	Metal-Oxide-Semiconductor Field Effect Transistor
MPGD	Micropattern Gaseous Detector
MPG	Max-Planck Society
$\overline{\text{MS}}$	Modified Minimal Substraction renormalization scheme
MSR	MSR renormalization scheme
NLO	Next to Leading Order
NNLL	Next to Next to Leading Log
NNLO	Next to Next to Leading Order
NRQCD	Non-Relativistic QCD
OB	Outer Backward
OF	Outer Forward
ONSEN	Online Selection Node
PCB	Printed Circuit Board
PETRA	Positron Electron Tandem Ring Accelerator
PFA	Particle Flow Analysis
PID	Particle ID
PTSL	Probe Test Solutions Ltd.
PXD	Belle II Pixel Detector
QCD	Quantum Chromodynamics

QCS	Final-focus quadrupole magnet
QED	Quantum Electrodynamics
QFT	Quantum Field Theory
RF	Radiofrequency
RICH	Ring-Imaging Cherenkov detector
ROI	Region Of Interest
RPC	Resistive Plate Chamber
RTML	Ring To Main Linac
$\sqrt{s}$	center-of-mass energy
SCB	Support and Cooling Block
SCRF	Superconducting Radiofrequency
SC	Superconductor
SiD	Silicon Detector
SiLab	Silicon Laboratory at Bonn University
SiPM	Silicon Photomultiplier
SLAC	Stanford Linear Accelerator Center
SLC	SLAC Linear Collider
SMD	Surface Mount Device
SM	Standard Model of particle physics
SNR	Signal-to-Noise Ratio
SO(N)	Special Orthogonal group of degree N

SPEAR	Stanford Positron Electron Asymmetric Rings
Sp$\bar{p}$S	Super Proton-Antiproton Synchrotron
SSM	Supersymmetric Model
SU(N)	Special Unitary group of degree N
SVD	Silicon Vertex Detector
SW	Switcher
TDR	Technical Desing Report
TOE	Theory Of Everything
TOP	Time Of Propagation
TPC	Time Projection Chamber
TSMC	Taiwan Semiconductor Manufacturing Company
UBM	Under Bump Metallization
UDP	User Datagram Protocol
UMC	United Microelectronics Corporation
U(N)	Unitary group of degree N
VLC	Valencia jet reconstruction algorithm
VXD	Vertex Detector
X_0	Radiation length

Chapter 1

Particle physics

> "Ever since the dawn of civilization, people have not been content to see events as unconnected and inexplicable. They have craved an understanding of the underlying order in the world. Today we still yearn to know why we are here and where we came from. Humanity's deepest desire for knowledge is justification enough for our continuing quest. And our goal is nothing less than a complete description of the universe we live in."
>
> Stephen Hawking in *A Brief History of Time* [1]

That's precisely the goal of particle physics, to address the fundamental questions *What is matter made of?* and *How does matter interact?*. Particle physicists all around the world join their efforts in the investigation of the smallest building blocks, called *elementary particles*, and the interactions between them, the *fundamental forces* or *fundamental interactions*.

In this Chapter, our current knowledge about the elementary particles and the interactions between them is introduced, following the textbook [2]. First, the observed non-composite particles (namely quarks, leptons and bosons) and their

properties (spin, charge, etc.) are reviewed. Then, a summary of the fundamental interactions between these particles, and their phenomenology depending on the particle's properties is presented.

After the introduction of the phenomenology, a light description of the best theoretical model to date, the Standard Model of particle physics, based on the formulation in [3] and [4] will be made from the experimentalist perspective. Emphasizing on how the model is built and what are the implications and consequences of the current formulation.

To finalize, new theories that address open questions left unanswered by the Standard Model are introduced, taking a look to the way forward in the path to improve our understanding of nature.

1.1 Elementary particles and fundamental forces

The elementary particles are the point-like particles with no observed sub-structure that build up our world. Depending on their spin value, they may behave as fermions or as bosons. As seen in Figure 1.1, the elementary fermions are the constituents of matter, and can be classified as quarks, charged leptons and neutral leptons depending on their color and electric charges. On the other hand, the elementary bosons mediate in the fundamental interactions.

Fermionic particles possess half integer spin values and follow the Fermi-Dirac statistics, therefore obeying the Pauli exclusion principle, meaning that only one particle can occupy a given quantum state[1] (i.e. spin projection, spatial probability distribution, momentum probability distribution, etc.).

Bosonic particles on the other hand have integer spin and follow the Bose-Einstein statistics. Contrary to the fermions, bosons do not obey the Pauli exclusion principle, allowing for the population of quantum states with multiple particles, as it happens for example in Bose-Einstein condensates.

[1] For example, due to the exclusion principle only two electrons (the two possible projections of their spin) can be accommodated in a given atomic orbital.

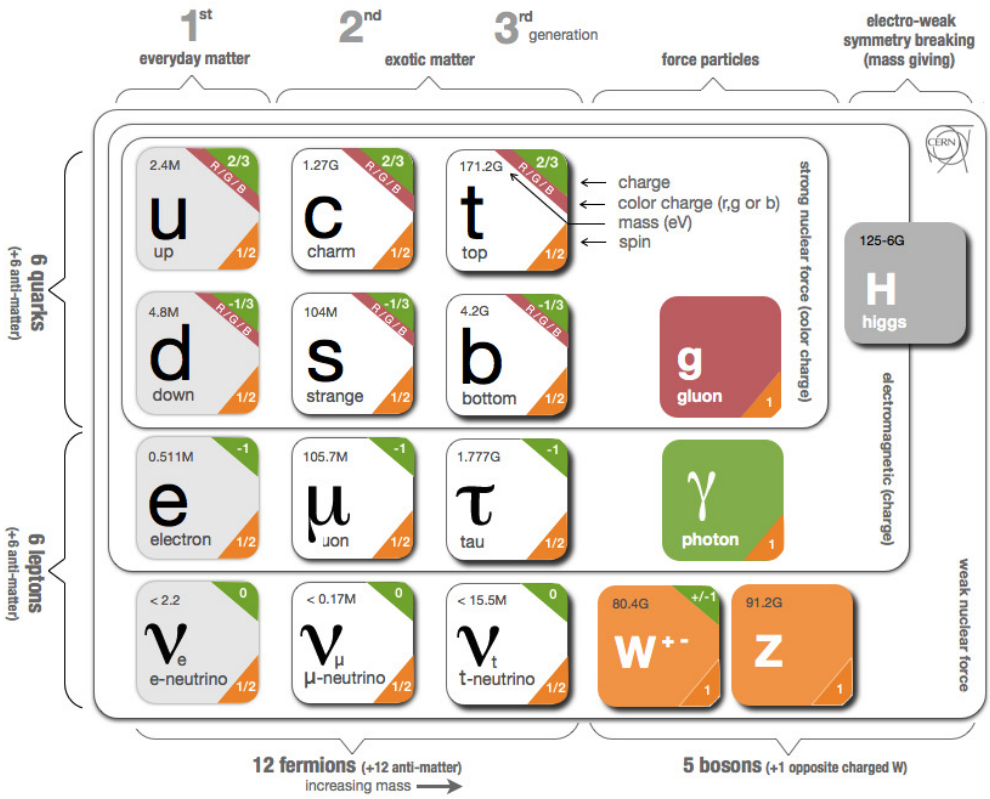

Fig. 1.1 Observed elementary particles to date [5].

In the fermionic sector, six flavours (i.e. varieties) of elementary particles called quarks (u, d, c, s, t and b) possess both electric charge q and color charge $r/g/b$. These cannot be observed freely, and can only be spotted inside hadrons, due to the so called *color confinement*. This confinement causes free quarks to instantly rearrange *hadronize* into *colorless* systems (i.e. physical systems with neutral color charge). Depending on their quark composition, hadrons can be classified as mesons (such as pions), formed as a quark-antiquark pair with opposite color charge; or baryons (such as protons or neutrons), formed as a trio of quarks with the three possible colors.

The remaining fermions do not carry color charge and can be divided into three flavours of electrically charged leptons (e^-, μ^- and τ^-), and another three flavours of its complementary neutral leptons or neutrinos (ν_e, ν_μ and ν_τ). The charged leptons are related with the neutral leptons by their quantum lepton number. With every flavour having its own leptonic number, i.e. both the e^- and the ν_e share the L_e quantum number, and so do μ^- and the ν_μ with L_μ, and τ^- and the ν_τ with L_τ. Unlike quarks, leptons can be observed freely, as the electrons that conform a thunder, or the electronic clouds of atoms.

These fermionic particles can be divided into three families or generations, where successive generations are heavier copies of the previous family, with identical charges and behavior. Being the state of lowest energy, the lightest family (u, d, e^- and ν_e) is the one that makes up the everydays matter, while heavier fermions decay into particles of the 1st generation.

For each of the fermions introduced, a copy with the same mass and oposed charges and quantum numbers called *antiparticle* exists, yielding a total of 24 $(12 + 12)$ elementary fermions. The antiparticles of quarks are denoted $\bar{u}$, $\bar{d}$, $\bar{c}$, $\bar{s}$, $\bar{t}$ and $\bar{b}$; in the case of the charged leptons the notation is e^+, μ^+ and τ^+; and for the neutral leptons is $\bar{\nu}_e$, $\bar{\nu}_\mu$ and $\bar{\nu}_\tau$. When these antiparticles encounter their respective particles they annihilate, releasing their energy and producing new particles[2].

On the other hand, the elementary bosons can be divided between the force carriers and the Higgs boson. The four spin-1 elementary bosons γ, g, Z and $W^\pm$ propagate the electromagnetic, strong nuclear force and weak nuclear force respectively. The fundamental interactions between the fermions above can be pictured as the exchange of the spin-1 bosons. As for the spin-0 Higgs boson, it is believed that its existence provides masses to the rest of particles[3]. The W^+ and W^- are each other's antiparticle, while the rest of the bosons are their own antiparticles.

[2]For example, at low energies, if a positron collides with an electron, they annihilate producing two photons.

[3]More on this in the spontaneous symmetry breaking description in the following section.

As for the interactions, four fundamental forces exist: gravitation, electromagnetism, weak force and strong force. The rest of perceived forces (i.e. mechanical tensions, friction, viscosity, etc.) can be derived from these.

Gravitation acts on the particles mass and energy. Its small interaction strength makes it really difficult to observe it on elementary particles, and therefore it is not described yet in most particle physics models. Although gravitation has a relatively tiny strength, its infinite interaction range and the fact it is a purely attractive force result in large effects at the macroscopic scale, such as the movement of the planets around the sun. The best description of the gravitational so far is General Relativity (GR), and it models the influence of massive objects on the space-time fabric around them.

Electromagnetism is mediated by the γ and acts on the particles electric charge. Its macroscopic behavior is described by the Maxwell's equations, while its microscopic behavior is modeled by the Quantum Electrodynamics (QED) theory. Its strength (10^{40} times that of gravity) and its infinite range produces visible effects in the macroscopic world such as the formation of bound states in matter (atoms, molecules), the tensions between different bodies (such as a leaf floating on water) and more.

The strong force is mediated by g and acts on the particles color charge. Although its interaction range is rather short (10^{-15} m), its large interaction strength (10^{42} respect to gravitation) produce the color confinement and the impossibility of observing free-quarks. As a result, quarks are confined together forming the protons and neutrons that compose everyday matter. This force is also the responsible of the formation of atoms' nuclei, overcoming the electromagnetic repulsion between protons, thus, allowing for multi-proton nucleus.

The weak force is mediated by the $W^{\pm}$ and Z bosons and acts on the weak isospin carried by left-handed fermions[4]. The weak force is the only one capable of changing the flavour of the particles, thus, allowing the quarks and leptons to change their type, and, being the responsible for the desintegration of unstable

[4]Left-handed particles have opposite spin projection and momenta.

particles. The interactions can be either charged-current interactions (mediated by the $W^{\pm}$, carrying a weak isospin of $T_3 = \pm 1$), or neutral (mediated by the Z, carrying 0 weak isospin). Its small strength (10^{29} times that of gravity, or 10^{-11} that of electromagnetism) combined with its limited range (10^{-15} m) make it considerably weaker than the other forces. One of the best examples of the weak force at work is the radioactive beta decay, in which an isotope radiates an electron at the same time that one of its neutrons is converted into a proton. This phenomenon can be explained as the change of flavour of one of the d quarks inside the neutron into a u quark through the mediation of a W^-, as seen below

$$
\begin{aligned}
{}^{90}_{38}\mathrm{Sr} &\longrightarrow {}^{90}_{39}\mathrm{Y} + e^- + \bar{\nu}_e, && (1.1)\\
n\ (u\ d\ d) &\longrightarrow p\ (u\ u\ d) + e^- + \bar{\nu}_e, && (1.2)\\
d &\longrightarrow u + W^- \longrightarrow u + e^- + \bar{\nu}_e. && (1.3)
\end{aligned}
$$

The short-lived W^- boson quickly decays into an e^- and its antineutrino $\bar{\nu}_e$, resulting in the perceived beta decay phenomenology.

As seen in Table 1.1, only the left-handed fermions possess weak isospin. As a result, the weak force does not interact with right-handed fermions[5], becoming the only interaction that is not symmetric under parity (i.e. it does not remain the same under mirrored reflection). The interaction also violates the compound charge conjugation-parity (CP) symmetry, which means that antiparticles in a mirrored space do not behave like particles in *straight* space, under certain circumstances [6]. It does preserve CPT though, meaning that antiparticles in a mirrored space and mirrored time do behave like particles in *straight* space-time.

Interactions between the different particles are allowed except if they explicitly violate the conservation laws. To date, these include 4-momenta, angular momenta, electric charge q, color charge $r/g/b$, weak isospin T_3, the barion number[6] and the three leptonic quantum numbers.

[5]Right-handed particles have aligned spin projection and momenta.

[6]The baryon number is proportional to the number of quarks minus the number of antiquarks in a given system. Its conservation ensures that for any quark produced an antiquark is also produced, although, they do not have to be of the same flavour.

Table 1.1 Weak isospin value for the elementary left-handed fermions. The right-handed fermions possess 0 weak isospin. In the case of the antiparticles, the right-handed antiparticles do have weak isospin, while left-handed do not.

1st generation	2nd generation	3rd generation	Weak isospin (T_3)
u_L	c_L	t_L	$1/2$
d_L	s_L	b_L	$-1/2$
e_L	μ_L	τ_L	$-1/2$
ν_{e_L}	ν_{μ_L}	ν_{τ_L}	$1/2$

Summarizing, the first generation of fermions compose everydays matter. Quarks organize into baryons, forming the protons and neutrons that are glued by the strong nuclear force into the atoms nuclei. On the other hand, the charged leptons are bound to the nucleus due to electromagnetic forces, conforming the atoms that build our world. The interactions between these are mediated by the fundamental bosons, that act as force carriers, propagating the interactions.

1.2 Standard Model overview

The Standard Model (SM) is a self-consistent theoretical model describing the electromagnetic, weak and strong interactions between the elementary particles. It was formulated in the mid 1970s, predicting the existence of all the particles in Figure 1.1, some of which were later discovered at particle colliders.

The model builds upon the Quantum Field Theory (QFT) framework, where each particle (and its antiparticle) is mathematically described as the excitation of a related quantum field that fills the entire space-time. The heart of the model lies in its Lagrangian $\mathcal{L}_{SM}$, that describes the kinematics of the particle fields, and the possible interactions between them. It can be separated in the following terms:

$$\mathcal{L}_{SM} = \mathcal{L}_{kin} + \mathcal{L}_{int}, \tag{1.4}$$

$$\mathcal{L}_{int} = \mathcal{L}_{QCD} + \mathcal{L}_{EW} + \mathcal{L}_{H} + \mathcal{L}_{\text{Yukawa}}, \tag{1.5}$$

where $\mathcal{L}_{kin}$ describes the kinematics of the elementary particles, $\mathcal{L}_{QCD}$ implements the strong interactions between the colored particles, $\mathcal{L}_{EW}$ specifies the electromagnetic and weak interactions, and the $\mathcal{L}_H$ and $\mathcal{L}_{\text{Yukawa}}$ terms describe the Higgs boson field and its coupling to quarks and charged leptons that concedes them their masses.

The theory is constructed by postulating a series of symmetries of the interactions, and writing down the most general renormalizable QFT Lagrangian. These symmetries include both the gauge and reference-frame invariance, and are implemented as:

- The global Poincaré group symmetry, represented as a 10-dimensional non-abelian Lie group that includes the following symmetries:
  - Translations in the space-time.
  - Three dimensional rotations in space.
  - Changes of inertial reference frames in the spacial relativity framework.
- The local $\text{SU}(3)_C \otimes \text{SU}(2)_L \otimes \text{U}(1)_Y$ gauge symmetries, that define the strong, weak and electromagnetic interactions.

As per Noether's theorem[7], all these symmetries result in conserved quantities such as the 4-momenta and angular momenta for the Poincaré symmetry group; and the electric charge q, the weak isospin T_3 and the color charges $r/g/b$ for the $\text{SU}(3)_C \otimes \text{SU}(2)_L \otimes \text{U}(1)_Y$ gauge symmetries.

The interactions of the SM (Figure 1.2) are described by the Quantum Chromodynamics (QCD) and the Electroweak (EW) Yang-Mills theories[8]. Quantum Chromodynamics is based on the $\text{SU}(3)_C$ local symmetry group, and describes the strong interactions. The Electroweak theory on the other hand is based on the $\text{SU}(2)_L \otimes \text{U}(1)_Y$ groups, and describes the weak and electromagnetic interactions

[7] Noether's theorem states that for every continuous symmetry in the Lagrangian of a physical system, a corresponding conserved quantity arises, resulting in a conservation law.

[8] Which are gauge theories based on non-abelian Lie groups, such as SU(3). In these, the field operators do not commute, and the order of the fields affects the outcome of the operations.

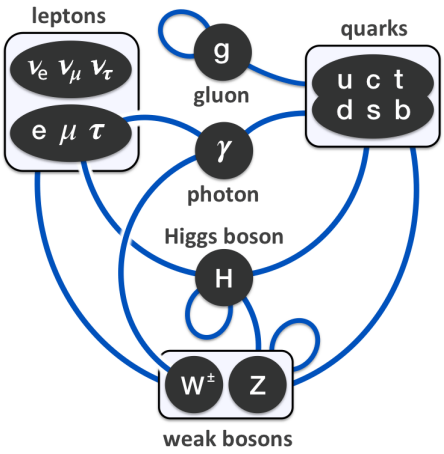

Fig. 1.2 Interactions between the elementary particles allowed by the Standard Model [7].

and the spontaneous symmetry breaking mechanism that provides the elementary particles with masses.

The Quantum Chromodynamics theory describes the interactions between the particles that carry color charge, i.e. quarks and gluons[9]. It allows for three basic interactions: emission or absorption of gluons by quarks, emission or absorption of gluons by other gluons, and direct interaction between gluons (such as glueballs[10]). Its two main phenomenological features are color confinement, that implies that *colored* states cannot be isolated, and therefore any free quark quickly hadronizes into *colorless* states; and, asymptotic freedom, that reduces the intensity of the strong interactions in higher energy scales, thus weakening the interaction at infinitesimal distances.

The Electroweak theory on the other hand describes both the weak and electromagnetic interactions between left-handed fermions and charged particles respectively. The theory models both interactions as two manifestations of the

[9]The fact that the mediator carries color charge allows for the self-interaction of the gluon, producing effects such as the color confinment.

[10]Theory-predicted bound state -i.e. particle- composed only by gluons.

same force. At high energy scales, the EW interactions are mediated by the W_1, W_2, W_3 and B massless gauge bosons, acting on particles with weak isospin and weak hypercharge. But, at energies lower than the Higgs field vacuum expectation value, the Higgs mechanism spontaneously breaks [8] the $\mathrm{SU}(2)_L \otimes \mathrm{U}(1)_Y$ symmetry into the $\mathrm{SU}(2)_L$ and the $\mathrm{U}(1)_{EM}$ groups, that describe the weak and electromagnetic interactions, respectively.

As a result, the W_1, W_2 gauge bosons are combined into the $W^{\pm}$ bosons that mediate the charged currents weak interactions, while the W_3 and B bosons are coalesced into the Z and γ bosons that mediate the neutral current weak interactions and the electromagnetic interactions, respectively. As a consequence of the gauge boson mixing in the Higgs mechanism, the Z and W bosons acquire masses, while the γ remains massless. In the aftermath of the symmetry breaking, the terms of the Yukawa interactions between the charged fermions and the Higgs fields take the form of mass terms, thus providing masses to quarks and charged leptons.

In total, the model requires 18 measurable parameters, including the nine masses of the elemental fermions (quarks and charged leptons), or equivalently their Yukawa couplings; the four parameters that define the Cabbibo-Kobayashi-Maskawa matrix, that measures the probability of flavour changing weak interactions between the different quarks; the three gauge couplings of the $\mathrm{SU}(3)_C \otimes \mathrm{SU}(2)_L \otimes \mathrm{U}(1)_Y$ groups, that determine the strength of the fundamental interactions; and, the Higgs boson mass and its vacuum expectation value, that fine tune the spontaneous symmetry breaking mechanism.

As a consequence of the SM formulation, four accidental U(1) global symmetries arise. And, as per Noether's theorem, these cause four additional conservation laws: baryon and the three leptonic numbers (i.e. electron, muon and tau numbers).

In practice, observables $\mathcal{O}$ cannot be computed exactly from the $\mathcal{L}_{SM}$ Lagrangian. To cast predictions, perturbations around the exact solutions of $\mathcal{L}_{kin}$ (which is solvable) are calculated in the QFT mathematical framework[11]. These

[11] These define the particles in the asymtoptically free states, i.e. in abscence of interactions.

approximations consist in performing series expansions around the free particle exact solutions. These take the form

$$\mathcal{O} = \mathcal{O}_0 + \alpha\ \mathcal{O}_1 + \alpha^2\ \mathcal{O}_2 + \alpha^3\ \mathcal{O}_3 + \dots \tag{1.6}$$

where $\mathcal{O}_0$ is the exact solution of the free particle, α is the coupling constant, and $\alpha^n\ \mathcal{O}_n$ the n-th term in the expansion of the interactions in the lagrangian $\mathcal{L}_{int}$ around the $\mathcal{O}_0$ solution. In the particle physics jargon, we say that a calculation is performed at *tree level* (or leading order) when only the first term of the expansion ($\alpha\ \mathcal{O}_1$) is included. If the next order ($\alpha^2\ \mathcal{O}_2$) is included, then we say that they are next-to-leading order (NLO) calculations. For higher orders $\alpha^{n+1}\ \mathcal{O}_{n+1}$ they are called N^{n}LO calculations.

When performing these perturbative calculations infinites may arise if the theory is not ultraviolet complete. To deal with these infinites and obtain finite solutions renormalization techniques are employed. These are based in the fact that divergences are local and therefore can be absorbed into Lagrangian parameters.

Depending on the calculation at hand, different local divergencies may arise, resulting in different renormalization strategies (or *schemes*). As the result of performing calculations in a given scheme, the measured physical quantities do not correspond directly to the SM Lagrangian parameters, but to renormalized quantities in that scheme.

In most schemes, the contributions absorbed depend on the renormalization scale[12] in the process that it is being calculated. As a result, the renormalized quantities change their value depending on the energy scale. This is known as the *running* of constants with the energy scale.

[12] Which in practice is chosen similar to the energy of the process.

1.3 Beyond the Standard Model

Despite the huge successes of the Standard Model, the theory is not perfect. It has some serious shortcomings, as it leaves some observed phenomena unexplained, and it makes some predictions that have not been observed yet. In particular, these are the most candent problems to address:

Neutrino masses and oscillation. The different neutrino flavours are massless in the SM. Yet, we know from many experiments both in cosmology and particle physics that they do possess mass. Extensions of the SM to accommodate mass terms for the neutrinos exist, but they rely in the seesaw mechanism and break the renormalizability of the Lagrangian. On the other hand, the neutrino flavour has also been observed to oscillate, meaning that a neutrino observed in a given family (e.g. an electron neutrino) can be later measured as a neutrino of different flavour (e.g. a muon neutrino). These flavour oscillations explicitly violate the lepton number conservation, and thus are incompatible with the SM.

CP violation in the strong sector. In the current formulation of the QCD theory, the CP symmetry is not explicitly conserved, and therefore CP violating phenomena should occur in the strong sector [9]. Yet, to date, no CP violation has been observed in the strong sector.

Gravity interaction. The SM does not provide a description of the gravitational interaction.

Dark energy, dark matter and baryon asymmetry. Assuming the validity of the ΛCDM model (also called the Standard Model of cosmology), the universe is composed approximately in a 69% of dark energy (that causes the accelerated expansion of the universe), a 26% of dark matter (that explains the angular speed in the rotation of galaxies), and, a 5% of SM matter (only in the particle sector, with no significant parts of antimatter) [10]. The SM does not provide any candidate that might explain dark matter and dark energy observations in the cosmology field. Moreover, the SM does not

predict the huge observed difference between *regular* matter and antimatter in the universe. Consequently, the SM of particle physics is not compatible with the SM of cosmology.

Many theories have been postulated as either extensions of the SM or new models that try to address these problems while replicating the current description of the phenomena in the SM. These are often referred as Beyond Standard Model (BSM) theories, and include between many others:

Grand unified theories (GUTs). Grand unified theories [11] try to replicate the milestone of the electromagnetic and weak unification, with QCD and EW, merging the three forces into a unique force at a higher energy scale. These model the interactions in a big Lie group, typically SU(5) or SO(10), reducing the number of gauge couplings from three to one.

Supersymmetric models (SSM). The supersymmetric models [12] extend the SM by introducing new symmetries and particle fields into the Lagrangian. These theories postulate that every particle in the SM has an associated partner, called its superpartner, which differs by half-integer spin, and has equal quantum numbers and mass. In this sense, every fermion in the SM would have a supersymmetric boson partner, and vice versa. Typically, SSM theories provide a symmetry breaking mechanism that explains why the superpartners are not observable at this energy scale.

Theories of everything (TOEs). Theories of everything [13] try to merge QFT with the GR framework in order to obtain a theory that describe all the fundamental interactions. The two major theories under this category are loop quantum gravity, that proposes the quantization of time and space; and, the string theories, that describes the current elementary particles as composite, proposing one-dimensional structures called strings as the fundamental building blocks of matter.

In order to progress in our understanding of the fundamental interactions and the building blocks of nature, new physics experiments are needed that helps us

build robust theoretical models that fully explain our observations. To do so, two main approaches can be followed:

- Searches for new phenomena such as new particles or new interactions between already observed particles. These new observations could deny or point towards given BSM theories.
- Performance of precision measurements that allow us to spot significant deviations from theory predictions or inconsistencies within the theory. In the particle physics field, observations are considered discoveries when they reach 5σ of statistical significance[13]. Thus, in order spot these significant deviations or inconsistencies, ultra-precise measurements and state-of-the-art calculations are needed.

[13]These 5σ, as in standard deviations, refer to the confidence interval of normally distruted data. 5σ is roughly equivalent to a 99.99994% probability.

Chapter 2

Electron positron colliders

As seen in Chapter 1, the Standard Model has been a very successful theory in the particle physics field, predicting many elementary particles that were later observed. Yet, it is not able to describe all the observed phenomena. To fill the gaps, a number of alternative theories have arisen, that either extend the SM or propose a new theoretical approach.

In order to confirm or deny the BSM theories, searches for new physics are carried out by experimental particle physicists. In these explorations, experimentalists either confirm or prove wrong the predictions from a given theory, advancing our understanding of the field. Depending on the approach, these searches can be categorized as explorations in the energy, intensity or cosmic frontiers (Figure 2.1) [14].

In the energy frontier, experiments are performed where particles interact at unprecedented energy scales, opening a window to new *high energy physics* processes. The exploration of the intensity frontier requires experiments with high luminosities (i.e. really large datasets) and ultra-sensitive detectors look for rare events and tiny deviations from our current theory predictions. Whereas the cosmic frontier experiments use the universe as a laboratory, detecting naturally occurring phenomena in our atmosphere and in the outer space.

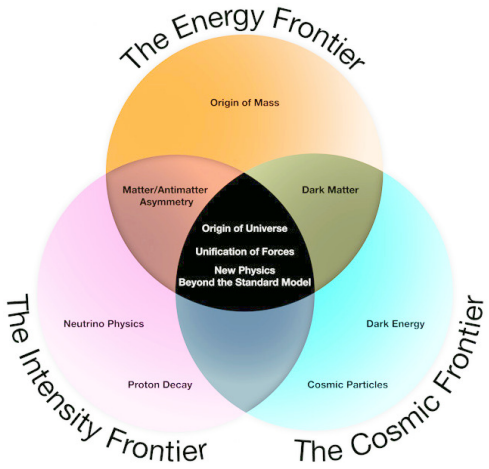

Fig. 2.1 Venn diagram of the three discovery frontiers in particle physics and their related topics [14].

In the recent past, high energy colliders have proven to be the most effective way to search for new physics, discovering all the predicted elementary particles by the SM, as seen in Table 2.1. It is reasonable then, to advocate for the construction of new high energy colliders that help us deepen our understanding of the particle physics phenomenology.

Table 2.1 Elementary particle discoveries by particle colliders since 1970 [15].

Year	Particle	Institution	Collider (experiment)	Beams
1974	c	SLAC / BNL	SPEAR / AGS	e^+e^- / p
1975	τ	SLAC & LBNL	SPEAR	e^+e^-
1977	b	Fermilab	Proton Area (E288)	p
1979	g	DESY	PETRA (TASSO)	e^+e^-
1983	W and Z	CERN	Sp$\bar{\text{p}}$S (UA1 & UA2)	$p\bar{p}$
1995	t	Fermilab	Tevatron (CDF & DØ)	$p\bar{p}$
2000	ν_τ	Fermilab	Tevatron (DONUT)	p
2012	h	CERN	LHC (CMS & ATLAS)	pp

Although hadron colliders are able to reach higher energies than those achievable by lepton colliders, these provide a series of advantages that can outweigh the energy gap. The most important difference between both collider strategies is the knowledge of the initial state, which results crucial in the study of some processes. Given the compositeness of hadrons, the initial state on hadron colliders cannot be known, as the actual collision is between individual quarks (or gluons) that carry a fraction of the hadrons momenta. On the other hand, leptons are elementary particles, resulting in point-like interactions and known initial states in the lepton colliders. Furthermore, the environment at lepton colliders is much cleaner, reducing the experimental complexity of the measurements and allowing for the design of more precise detectors.

All in all, due to their simplicity and cleaner environments, lepton colliders can provide unprecedented precision measurements that allow for the search of new physics. Table 2.2 summarizes the reach of their physics programs for different energy scales.

In this Chapter three next generation lepton colliders are introduced: the SuperKEKB collider, the International Linear Collider (ILC), and the Compact Linear Collider (CLIC). The SuperKEKB collider in Japan is an intensity frontier B-factory[1] experiment, producing over 5×10^{35} b, c and τ pairs, which allow for precise CP symmetry violation measurements. The ILC and CLIC projects are TeV-scale linear collider proposals that would provide unparalleled measurements of the Higgs boson, the t quark, possible undiscovered particles, and the interactions between them. These two proposals lie in between the energy frontier and the intensity frontier experiments with their direct searches of new physics and precise measurements of the current phenomena.

[1] B factories are experiments centered in the $B^0\bar{B}^0$ production resonance. The B^0 is a meson formed by the $d\bar{b}$ quark-antiquark pair.

Table 2.2 Major Standard Model (and Beyond Standard Model) physics processes accessible in e^+e^- colliders at different energy scales [16].

Energy	Process	Physics case
10.6 GeV	$e^+e^- \to \Upsilon(4s) \to B^0\bar{B}^0$	precision flavour physics
91 GeV	$e^+e^- \to Z$	precision electroweak parameters
160 GeV	$e^+e^- \to WW$	precision W mass
250 GeV	$e^+e^- \to Zh$	precision Higgs couplings
350 - 400 GeV	$e^+e^- \to t\bar{t}$	top quark mass and couplings
	$e^+e^- \to WW$	precision W couplings
	$e^+e^- \to \nu\bar{\nu}h$	precision Higgs couplings
500 GeV	$e^+e^- \to f\bar{f}$	precise search for Z'
	$e^+e^- \to t\bar{t}h$	Higgs-top quark coupling
	$e^+e^- \to Zhh$	Higgs self-coupling
	$e^+e^- \to \tilde{\chi}\tilde{\chi}$	search for supersymmetry
	$e^+e^- \to AH, H^+H^-$	search for extended Higgs states
700 - 1000 GeV	$e^+e^- \to \nu\bar{\nu}hh$	Higgs self-coupling
	$e^+e^- \to \nu\bar{\nu}VV$	search for composite Higgs
	$e^+e^- \to \nu\bar{\nu}t\bar{t}$	search for composite top quark
	$e^+e^- \to \tilde{t}\tilde{t}^*$	search for supersymmetry

2.1 SuperKEKB

The SuperKEKB [17] is an asymmetric energy electron positron collider built by upgrading the previous KEKB collider [18]. It runs at the $\Upsilon(4s) \to B^0\bar{B}^0$ resonance, converting the collider in a factory of B mesons. The design luminosity is $8 \times 10^{35}\text{cm}^{-2}\ \text{s}^{-1}$, 40 times the highest value achieved at KEKB. As seen in Figure 2.2, over the running time of the experiment an integrated luminosity of 50 ab^{-1} will be produced, a factor 50 over the KEKB dataset.

The asymmetric beams provide a boost to the $B^0\bar{B}^0$ of $\beta\gamma = 0.28$, allowing for time dependent CP symmetry violation measurements. To provide the asymmetric beams two storage rings are used: the high energy ring, which stores the 7 GeV

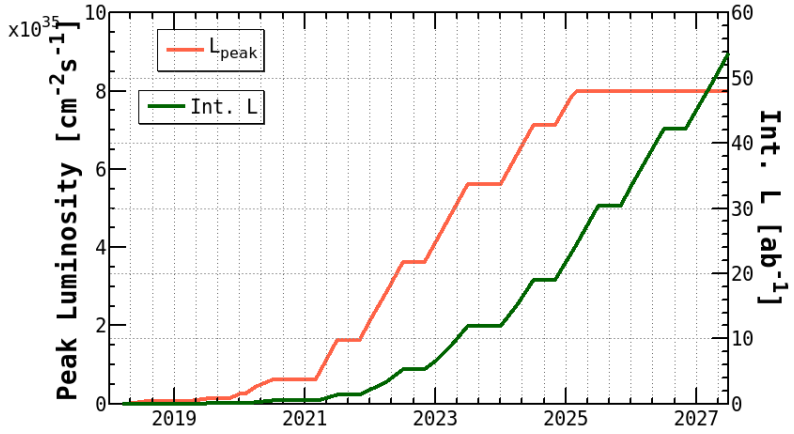

Fig. 2.2 Integrated and instantaneous luminosity of SuperKEKB during its operating time [19].

electrons and the low energy ring, which stores the 4 GeV positrons. The main parameters of both beams are summarized in Table 2.3.

Its intensity frontier physics program relies in precision measurements to spot significant deviations from the SM predictions. Scales of up to 100 TeV can be probed, depending on the strength of the flavour violating couplings in BSM theories. In particular, SuperKEKB can address the following flavour physics topics: the search for new CP violating phenomena in the strong sector, that might explain the observed baryonic asymmetry in the universe [20]; the search for extended Higgs states (such as charged Higgs bosons, doublets, ...); the measurement of flavour changing neutral currents beyond the SM; and, the measurement of lepton flavour violation. Apart from the flavour physics program, and, given the known initial state and the optimal $B^0\bar{B}^0$ reconstruction by the detector, the experiment is also well suited for searches of elusive low mass dark matter candidates that may be spotted via missing energy decays.

The SuperKEKB factory complex (Figure 2.3) at the KEK campus consists of the HER, the LER, and the injector linear accelerator with a 1.1 GeV positron damping ring. The different components of the complex are described below.

Table 2.3 Main parameters of the SuperKEKB accelerator [17].

Parameter	Symbol (Unit)	LER (e^+)	HER (e^-)
Beam energy	E_B (GeV)	4.0	7.007
Crossing angle	θ_x (mrad)	83	
Repetition frequency	f_{rep} (Hz)	50	
Beam current	I (A)	3.6	2.6
Number of bunches	n_b	2500	
Bunch population	N ($\times 10^{10}$)	9.04	6.53
Bunch length	σ_z (mm)	6.0	5.0
Horizontal beam size	σ_x^* (µm)	10.1	10.7
Vertical beam size	σ_y^* (nm)	48	62
Energy loss per turn	U_0 (MeV)	1.76	2.43
Luminosity	$\mathcal{L}$ (cm^{-2} s^{-1})	8×10^{35}	
Integrated luminosity	$\mathcal{L}_{\text{int}}$ (ab^{-1})	50	
Beam power	P_b (MW)	8.3	7.5
Circumference	C (m)	3016.315	

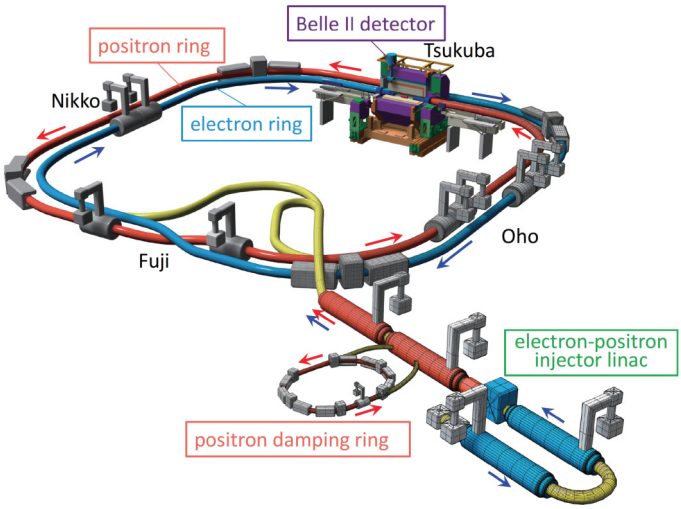

Fig. 2.3 Scheme of the SuperKEKB accelerator complex at the KEK campus in Tsukuba, Japan [17].

Electron source. Due cost and space considerations a damping ring cannot be employed to reduce the electron emittance, and given the nano-beam requirements of SuperKEKB, a low-emittance electron source is needed. To provide them a photo-cathode high-current RF gun is used. The gun consists on a Nd:YAG laser that excites the electrons in the Ir_5Ce cathode, that are accelerated by a quasitraveling-wave side-couple cavity, providing electron beams of 4.4 nC with an emittance of 10 mm mrad.

Positron source. To produce the positron beams, a high-current 10 nC electron beam is generated by a thermionic gun. The primary electrons is directed towards a 14-mm tungsten target to produce the positrons. These are captured using a flux concentrator and large-aperture accelerating structures. The emittance of the 4 nC positron beam is later reduced in the 1.1 GeV damping ring in the injector linac.

Injector linac. The electron and positron beams are accelerated in the 600 m injector linac, equipped with 60 high-power radiofrequency accelerating units operating at 50 Hz. The linac acts as two virtual independent accelerators, changing the parameters in a pulse-by-pulse basis at 50 Hz. It the positrons into the LER at 4 GeV, and the electrons into the HER at 7 GeV.

Low energy ring (LER). The 4.0 GeV positron beam is stored in the low energy ring, where the linac continuously injects charge to keep the beam current at 3.6 A. The ring maintains the 4.0 GeV energy of the positrons by accelerating them 1.76 MeVs per turn.

High energy ring (HER). The 7.0007 GeV electron beam is stored in the high energy ring, where the linac continously injects charge to keep the beam current at 2.6 A. The ring maintains the 7.0 GeV energy of the electrons by accelerating them 2.43 MeVs per turn.

Final-focus superconducting magnet system (QCS). Near the interaction point, in the Tsukuba hall, eight main quadrupole magnets, 43 corrector magnets and four compensation solenoid coils focus the electron and positron

beams into the interaction point, producing the collisions at a 83 mrad crossing angle.

The SuperKEKB colliders hosts one detector at the interaction point, the Belle II experiment, which has been specifically designed to accurately reconstruct the boosted $B^0\bar{B}^0$ pairs.

2.1.1 Belle II

The Belle II detector [21] has been optimized for the $B^0\bar{B}^0$ identification and reconstruction. Compared to the previous Belle detector, it has to operate in the higher background environment that comes associated with the higher luminosities. To cope with the higher backgrounds, the detector has been designed to withstand high event rates while retaining an excellent performance. The cornerstone point of the detector is its vertexing and tracking capabilities that allow for the discrimination of the B^0 from the $\bar{B}^0$. The main attributes of the Belle II detectors and subdetectors are summarized in Table 2.4 and described in detail below.

Vertex detector (VXD). The VXD consists on 6 layers (Figure 2.4) of silicon detectors, providing an excellent vertex resolution of 50 µm. The first two layers comprise the pixel detector (PXD), and are based on the DEPFET pixel technology. The latter four comprise the silicon vertex detector (SVD), and are based on double sided silicon strips. An in-depth description is available in Chapter's 3 introduction.

Central drift chamber (CDC). The tracking is provided by the CDC, a large volume He-C_2H_6 50:50 drift chamber with small drift cells. The chamber contains 14336 wires arranged in 56 axial (aligned with the magnetic field) or stereo (slanted respect the axial wires) layers. A full 3D helix track can be obtained using the information from the axial and stereo wires, in a maximum time of about 350 ns. The tracker provides excellent reconstruction efficiencies, good momentum resolutions and deposited energy capabilities

(dE/dx) for charged particles with momenta ranging from 50 MeV/c to 8 GeV/c.

Particle ID system (PID). Charged particle identification to separate pions, kaons, protons, electrons and muons is performed by the ring-imaging Cherenkov detectors situated around the CDC (TOP) and in the forward endcap (ARICH). These are optimized for the separation of π from K mesons in the 0.4 GeV/c to 4 GeV/c range.

Electromagnetic calorimeter (ECL). A highly segmented array of 8736 Tl-doped cesium iodide crystals coupled with photo-sensors equipped with wafe-form-sampling readout electronics in projective geometry conform the ECL. Its mission is to measure the energy deposited by the traversing particles with energy resolutions in the order of $\sigma_E/E = 4\%$ at 100 MeV (1.6% for 8 GeV), with a an angular resolution of 13 (3) mrad. It provides 0.8 λ_I.

K_L **and muon detector (KLM).** The KLM is formed by alternating 4.7 cm iron plates and scintillators with SiPM detectors surrounding the solenoid. The iron plates provide the magnetic flux return for the solenoid. The detector also provides 3.9 interaction lengths of material, containing most of the particles escaping the calorimeter, such as the K_L^0 hadronic showers.

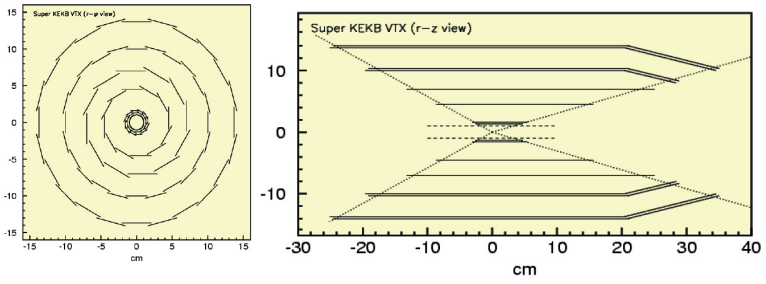

Fig. 2.4 Schematic axial (in the left) and lateral (in the right) view of the VXD [22].

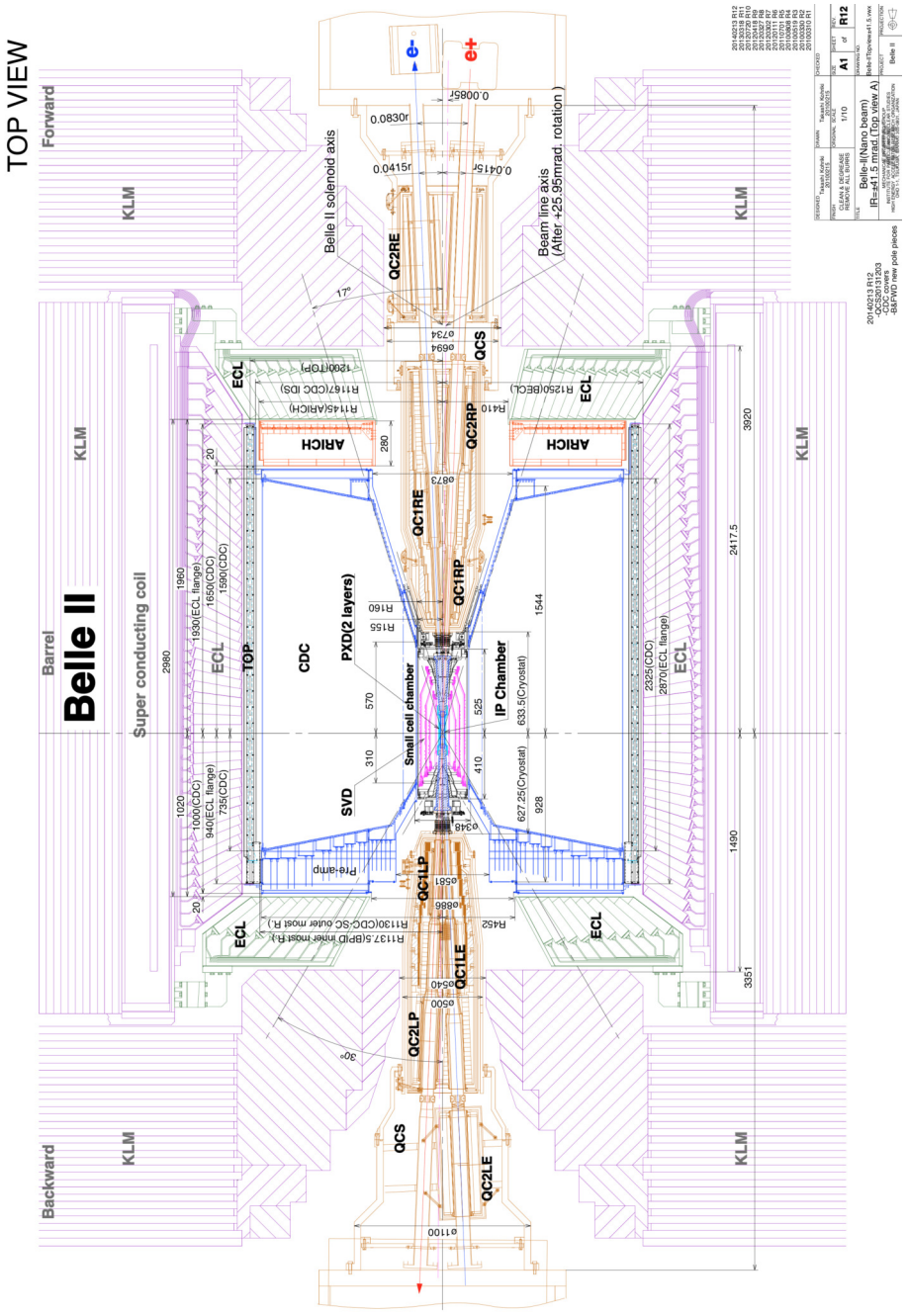

Fig. 2.5 Schematic top view of the Belle II experiment [22].

Table 2.4 Main parameters of the Belle II experiment [22].

Purpose	Detector	Configuration	Geometry
Beampipe	Beryllium	10 µm Au, 0.6 mm Be, 1 mm paraffin, 0.4 mm Be layers	$r = 10$ mm
Tracking	PXD	Two layers of DEPFET silicon pixels	$17° < \theta < 155°$, $r = 14, 22$ mm
	SVD	Four layers of double sided silicon strips	$17° < \theta < 155°$, $r = 38, 80, 115, 140$ mm
	CDC	He-C_2H_6 drift chamber with 14336 wires	$17° < \theta < 155°$, $160 < r < 1130$ mm
Particle ID	TOP	Ring imaging Cherenkov detector with quartz radiator	$31° < \theta < 128°$, $r \sim 1200$ mm
	ARICH	Ring imaging Cherenkov detector with aerogel radiator	$14° < \theta < 30°$, $125 < r < 162$ cm
Calorimetry	ECL	CsI(Tl) calorimeter barrel	$32.2° < \theta < 128.7°$, $125 < r < 162$ cm
		CsI(Tl) calorimeter endcap	$12.4° < \theta < 31.4°$, $130.7° < \theta < 155.1°$, $-102 < z < 196$ cm
Muon ID	KLM	2 layers of scintillator strips and 12 layers of RPCs in the barrel	$40° < \theta < 129°$
		12 layers of scintillator strips in the endcap	$25° < \theta < 40°$, $129° < \theta < 155°$

2.2 International Linear Collider

The International Linear Collider (ILC) [23] is a 250 GeV (upgradable up to 1 TeV) linear electron positron collider under consideration for the next global project in particle physics. The accelerator design is based in the mature 1.3 GHz superconducting radiofrequency (SCRF) technology that can provide up to 35

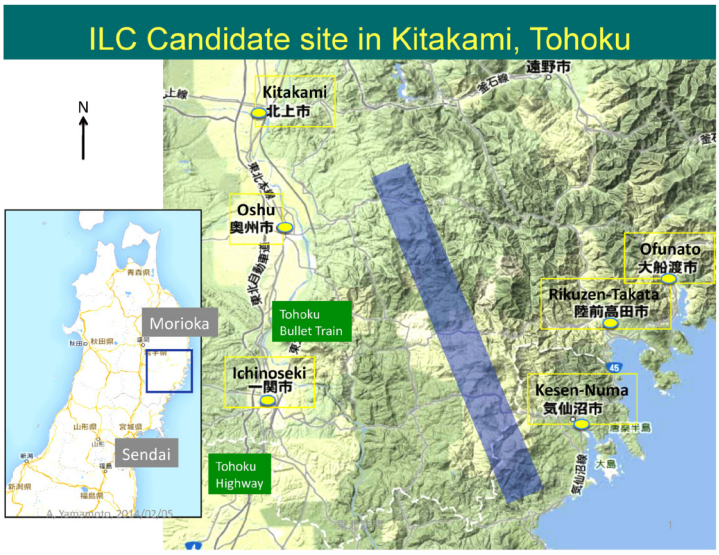

Fig. 2.6 Candidate construction site for the ILC at the Kitakami mountains in Tohoku, Japan [23].

MV/m. Detailed studies on the accelerator and detector technologies, as well as the physics potential have been produced and published in the technical design report (TDR) in 2013 [16].

The ILC Strategy Council announced in 2014 that the best possible ILC site is Japan. Japanese experts from academia and the industry as well an international committee considered the Kitakami mountains (see Figure 2.6) as the best technical and socio-environmental building site. Recently, the ILC Advisory Panel of the Japanese Government reviewed the ILC project, estimating the building and running costs. As of today, the Japanese Government is in negotiations with the US Government and the European Union to fund the project and proceed to construction.

Initially, the ILC would be built as a 250 GeV collider, with possible upgrades to 500 GeV and 1000 GeV. As seen in Figure 2.7, the nominal 22 year program *H20 scenario* considers three energy stages of 250 GeV, 350 GeV and 500 GeV, accumulating integrated luminosities of 2, 0.2 and 4 ab^{-1} respectively.

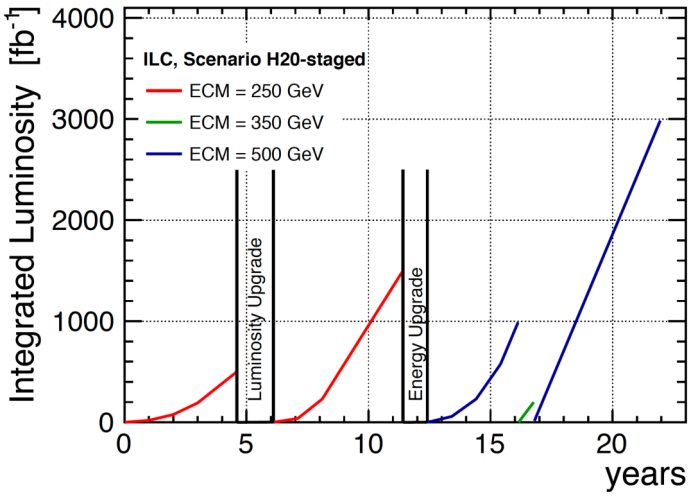

Fig. 2.7 Integrated luminosity of the ILC in the *H20 scenario* for its 22 year program [23].

The collider parameters for the different stages are summarized in Table 2.5. The initial stage collects data near the Higgstrahlung process threshold[2], allowing for a high precision characterization of the Higgs boson. The 500 GeV upgrade would grant access to a top physics program through the $t\bar{t}$ and $t\bar{t}H$ channels. A fraction of the running time would be employed in a top quark pair production scan around the 350 GeV center of mass region.

The ILC accelerator provides the high-energy electron and positron beams. The main focus of the accelerator is the energy-efficiency, being capable of providing the 250 center of energy collisions at a 129 MW power consumption. This is accomplished using the SCRF technology that has already been proven in experiments like the European X-Ray Free-Electron Laser Facility (E-XFEL) [24]. The description of the acceleration complex shown in Figure 2.8 for the initial stage is summarized below.

[2]The production of the Higgs is heavily suppressed in the s-channel. Making the radiation of Higgs bosons by heavy particles the best channel to study its properties.

Table 2.5 Main parameters of the ILC accelerator for its different stages [23].

Parameter	Symbol (Unit)	Initial	Upgrade I	Upgrade II
Collision energy	$\sqrt{s}$ (GeV)	250	500	1000
e^- polarization	P_{e^-}	80%	80%	80%
e^+ polarization	P_{e^+}	30%	30%	20%
Repetition frequency	f_{rep} (Hz)	5	5	4
Bunches per train	n_b	1312 (2625)	1312 (2625)	2450
Bunch interval	Δt_b (ns)	554 (366)	554(366)	366
Bunch population	N ($\times 10^{10}$)	2	2	1.74
Current in pulse	I (mA)	5.8	5.8	7.6
Pulse duration	t_{pulse} (µs)	727 (961)	727 (961)	897
Horizontal beam size	σ_x^* (nm)	516	474	335
Vertical beam size	σ_y^* (nm)	7.7	5.9	2.7
Luminosity	$\mathcal{L}$ ($\times 10^{34}$ cm^{-2} s^{-1})	1.35 (2.7)	1.8 (3.6)	4.9
Luminosity in top 1%	$\mathcal{L}_{0.01}/\mathcal{L}$	73%	58.3%	44.5%
Beam power	P_b (MW)	5.3 (10.5)	10.5 (21)	27.2
Site AC power	P_{AC} (MW)	129	163	300
Site length	L (km)	20.5	31	40

Electron source. The source design is based on the SLC polarized electron source. The gun consists on a Ti:sapphire laser that excites the electrons in a GaAs/GaAsP photocathode, producing electron bunches with polarizations up to an 85%.

Positron source. To produce the positron beams, electrons from the main linac are used to generate polarized hard photons in a helical undulator. Then, the polarized photons impact with a rotating target, producing positrons with a 30% of longitudinal polarization.

Damping rings. The generated electrons and positrons are accelerated to 5 GeV and injected into two oval damping rings of 3.2 km. These accept the large emittance leptons, damp the incoming beam jitter and provide a reduction of the emittance up to six orders of magnitude.

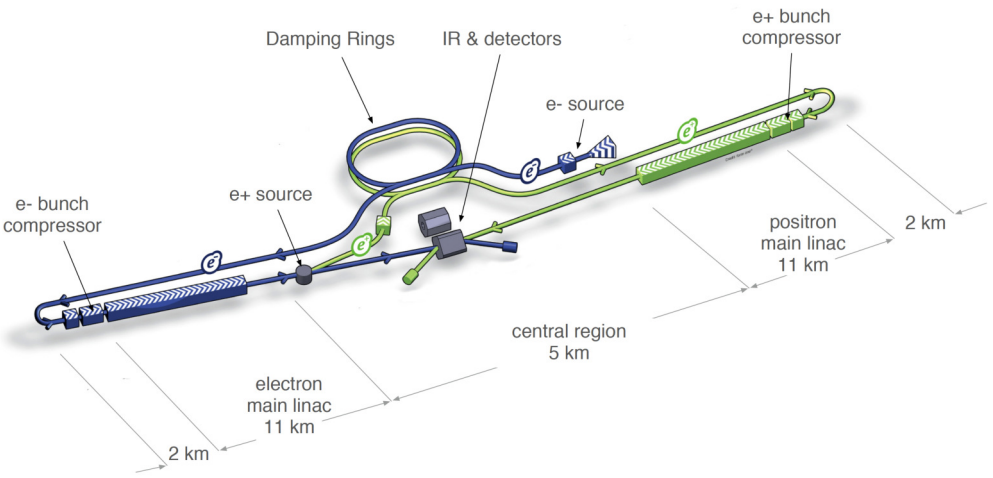

Fig. 2.8 Scheme of the ILC accelerator complex for the 500 GeV stage [16].

Ring to main linac (RTML). The beams are transported from the damping rings to the main linacs by the RTML system. The system transports the leptons at a stable 5 GeV energy, with a minimal emittance increase, collimating the beam halos and rotating the spin polarization to their final angle at the interaction point.

Main linac. Final acceleration of the electrons and positrons is provided by the two main linacs. The first stage in the linac consist in the bunch compressor system, that reduces the bunch length from 6 to 0.3 mm, while accelerating the beams from 5 GeV to 15 GeV. The second stage consists in the 6 km cryomodules section that accelerate the beams to the 125 GeV target. These cryomodules consists on a series of RF cavities powered by klystrons that provide acceleration gradients of 31.5 MV/m, and a set of a superconducting quadrupole with corrector magnets that keep the beam focused.

Beam delivery system (BDS). The BDS is the responsible of transporting the beams from the end of the linacs to the interaction point where the collisions occur. In particular, the BDS takes care of the diagnostic and collimation of the beams, the feedback-aware final focus system, the machine

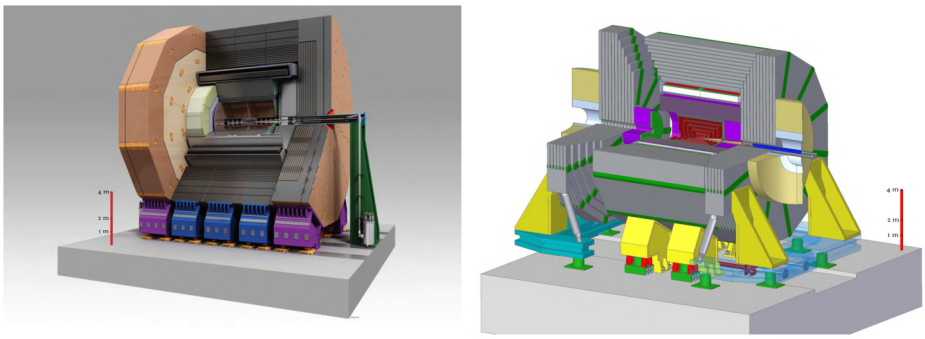

(a) ILD concept. **(b)** SiD concept.

Fig. 2.9 Renders of the International Large Detector (in the left) and Silicon Detector (in the right) concepts [23].

detector interface, the measurement of the beam parameters, and the dump of the beams after traversing the interaction point.

The ILC is planned with one interaction region and two experiments: the International Large Detector (Figure 2.9a), and the Silicon Detector (Figure 2.9b). These two are swapped in and out the interaction point following the *push-pull* scheme depicted in Figure 2.10. The *push-pull* allows for quick exchange (within a day) of the experiments.

Both experiments are equipped with detectors designed from the beginning to enable particle reconstruction using the particle flow analysis (PFA). The PFA algorithms use all the available information from tracks, calorimeter clusters and hits in the muon detectors to fully reconstruct individual particles and their four-momenta.

2.2.1 Silicon Detector

The SiD is a general-purpose detector, designed to satisfy the demanding performance needed to successfully implement the PFA algorithms. The SiD is a compact detector mostly based in silicon detectors. The sub-detectors geometry

and technology of choice are summarized in Table 2.6. Its main sub-systems are described below.

Vertex detector. Heavy flavour tagging plays a critical role in the selection and reconstruction of events for many physics processes. The main tool for flavour identification is a high-resolution lightweight vertex detector that minimizes multiple Coulomb scattering. The SiD vertex detector accomplishes it with five layers of 20×20 μm^2 in the barrel region, and three silicon pixel disks in the endcaps.

Tracker. To realize the full potential of the PFA excellent tracking, efficiency and particle separation are needed, with momentum resolutions in the order of $\delta(1/p_T) \approx 5 \times 10^{-5}$ GeV/c. The main tracker consists of five nested cylinders of single-sided silicon strip detectors in the barrel and four conical disks in the endcaps. The combination of the vertex detector and the main tracker under the 5 T magnetic field can fulfill these requirements.

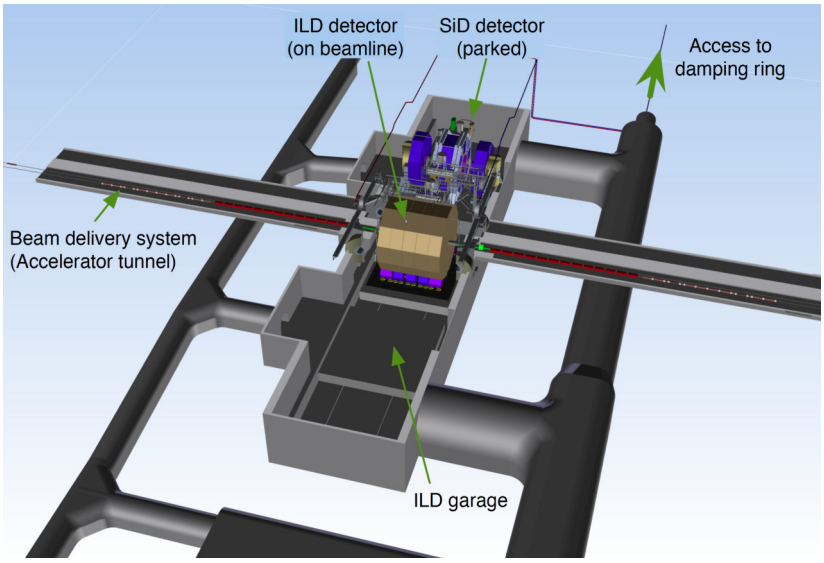

Fig. 2.10 Scheme of the dual detector "push-pull" configuration [16].

Main calorimeters. The electromagnetic calorimeter (ECAL) consist on up to 30 layers of silicon pixels (1.25 mm readout gap) with tungsten absorbers (2.50 mm thick for the first 20 layers, 5 mm the rest), providing an excellent energy resolution of $\sigma/E = 0.17/\sqrt{E} \oplus 0.009$ % and a total depth of 26 X_0. After the ECAL, the segmented hadronic calorimeter (HCAL) of 4.5 λ_I, formed by layers of scintillator tiles followed by SiPMs with steel absorbers.

Forward calorimeters. For the very forward angles, two high precision radiation hard calorimeters are considered: the LumiCal for precise measurements of the luminosity, and the BeamCal to assist in the estimation of the collision parameters and the identification of forward-scattered beam particles.

Magnet coil and muon system. The superconducting coil is based on the CMS implementation, providing the necessary modifications to yield a 5 T central field. An iron yoke around the coil acts both as the magnetic flux return, and the muon detector. The yoke will be equipped with either scintillators followed by SiPMs or RPCs.

2.2.2 International Large Detector

The ILD is a multi-purpose detector, designed to deliver excellent physics performance for center of mass collisions between 90 and 1000 GeV. The main difference with the SiD is the micropattern gas detector (MPGD) time projection chamber (TPC) used to track the charged particles. The sub-detectors geometry and technology of choice are summarized in Table 2.5. Its main sub-systems are described below.

Vertexing and tracking. Vertexing is realized with 6 layers of pixel detectors grouped in pairs, forming three cylindrical super-layers enclosing the beampipe. The technology to implement the vertex detector (VTX) is not decided yet, but the main priority is to obtain point resolution within minimal material thickness. The vertex detector is surrounded by two layers of silicon strip detectors (SIT) that close the gap between the VTX and the

Table 2.6 Main properties of the Silicon Detector [23].

Barrel	Technology	r_{in} (cm)	r_{out} (cm)	z (cm)
Vertex detector	Silicon pixels	1.4	6.0	±6.25
Tracker	Silicon strips	21.7	122.1	±152.2
ECAL	Silicon pixels - W	126.5	140.9	±176.5
HCAL	Scintillator - Steel	141.7	249.3	±301.8
Solenoid	5 Tesla SC	259.1	339.2	±298.3
Flux return	Scintillator - Steel	340.2	604.2	±303.3
Endcaps	**Technology**	z_{in} (cm)	z_{out} (cm)	r (cm)
Vertex detector	Silicon pixels	±7.3	±83.4	16.6
Tracker	Silicon strips	±77.0	±164.3	125.5
ECAL	Silicon pixels - W	±165.7	±180.0	125.0
HCAL	Scintillator - Steel	±180.5	±302.8	140.2
Flux return	Scintillator - Steel	±303.3	±567.3	604.2
LumiCal	Silicon - W	±155.7	±170.0	20.0
BeamCal	Semiconductor - W	±277.5	±300.7	13.5

time projection chamber (TPC). To cover the forward region, two silicon pixel disks and five silicon strip disks (FTD) provide low angle tracking. The TPC is the main tracker of the experiment, providing up to 224 tracking points, and allowing for 3D point reconstruction, as well as for particle identification through dE/dx measurement. The gap between the TPC and the electromagnetic calorimeter will be filled with a silicon strip detector (SET), providing additional redundancy in the regions between the tracker volume and the calorimeters.

Calorimetry. The electromagnetic calorimeter (ECAL) consist on up to 30 layers of silicon diodes (or scintillator strips) with tungsten absorbers, providing up to 30 sampling points in depth with a great transverse granularity due to the small cell sizes. After the ECAL, the segmented hadronic calorimeter (HCAL) is formed by 48 layers of scintillator tiles (or gas-based readout) with steel absorbers. For the very forward angles, high precision radiation hard

Table 2.7 Main properties of the International Large Detector [25].

Barrel	Technology	r_{in} (cm)	r_{out} (cm)	z (cm)
Vertex detector	Silicon pixels	1.6	6.0,	±12.5
SIT	Silicon strips	15.3	30.0,	±64.4
SET	Silicon strips	181.1	181.1	±230.0
TPC	MPGD	33.0	180.8,	±235.0
ECAL	Si pixels / Scint. - W	184.3	202.8,	±235.0
HCAL	Gas RPC / Scint. - Fe	205.8	341.0,	±235.0
Coil	3.5 Tesla	334.0	440.0,	±395.0
Muon detector	Scintillator / RPC	445.0	775.5,	±280.0
Endcaps	**Technology**	z_{in} (cm)	z_{out} (cm)	r (cm)
FTD	Si pixels / strips	±22.0	±37.1	-
ETD	Silicon strips	±242.0	±244.5	41.9 - 182.2
ECAL	Si pixels / Scint. - W	±245.0	±263.5	-
HCAL	Gas RPC / Scint. - Fe	±265.0	±393.7	33.5 - 319.0
BeamCal	GaAs - W	±359.5	±371.5	2.0 - 15.0
LumiCal	Silicon - W - W	±250.0	±263.4	7.6 - 28.0
LHCAL	W absorber	±268.0	±320.5	9.3 - 33.1
Muon detector	Scintillator / RPC	±256.0	-	30.0 - 775.5

calorimeters (BeamCal, LumiCal and LHCAL) are considered, extending the coverage to almost 4π.

Coil and yoke. A high volume superconducting coil surrounds the HCAL, creating an axial magnetic field of 3.5 T. An iron yoke around the coil acts both as the magnetic flux return, and the muon detector. The yoke will be equipped with either scintillator strips or RPCs.

2.3 Compact Linear Collider

The Compact Linear Collider (CLIC) [26] is a high-luminosity linear electron positron collider capable of reaching up to 3 TeV of center of mass energies under

development by the CLIC accelerator collaboration. The accelerator design is based in a novel two-beam acceleration technique with normal RF accelerating structures that can provide up to 100 MV/m. Detailed studies on the detector technologies, design of the detector and physics potential of CLIC are carried out by the CLIC detector and physics collaboration (CLICdp). A conceptual design report (CDR) was published in 2012 [27], proving the feasibility of the CLIC accelerator at high energies (3 TeV) and the collider's physics potential under realistic conditions.

The project is foreseen to be built in the Swiss-French border, near CERN premises (see Figure 2.11). The accelerator would be constructed in three stages, with center of mass energies of 380 GeV, 1500 GeV and 3000 GeV. As seen in Figure 2.12, these three stages are expected to run for 8, 7 and 7 years, accumulating integrated luminosities of 1, 3 and 5 ab^{-1} respectively.

The collider parameters for the different stages are summarized in Table 2.8. The first stage provides collisions at 380 GeV, giving access to an extensive Higgs

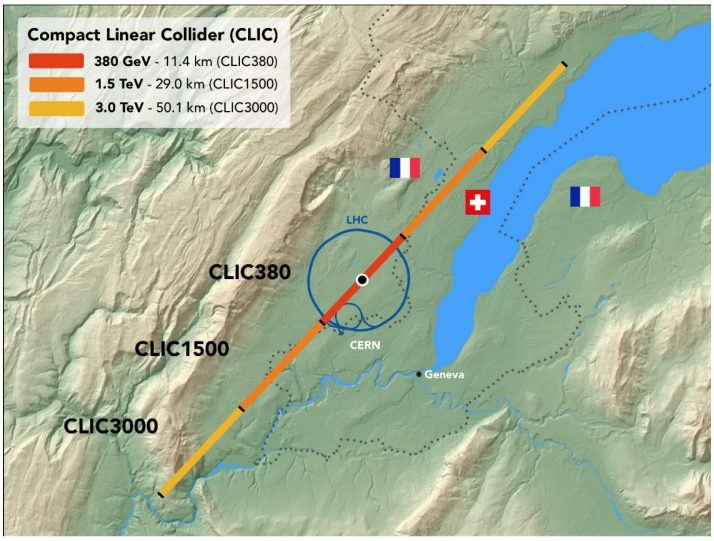

Fig. 2.11 Candidate construction site for the CLIC in the Swiss-French border near CERN [26].

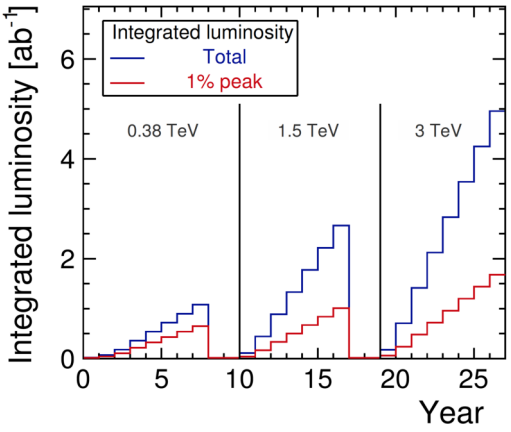

Fig. 2.12 Integrated luminosity of the CLIC during its operating time for the different energy stages [26].

program through the Higgstrahlung and WW-fusion processes. A fraction of the running time will be employed in a top quark pair production scan around the 350 GeV center of mass region.

The second and third stages at the TeV scale open the energy frontier, providing unprecedented access to new physics phenomena. In particular, the second stage provides a window to the double Higgstrahlung process $e^+e^- \rightarrow Zhh$, making possible the measurement of the Higgs self-coupling, the Higgs-top quark coupling and rare Higgs branching ratios. The third stage widens the physics potential, allowing for searches of new particles such as dark matter candidates, supersymmetric particles and more. Moreover, indirect searches for new physics at CLIC are sensible to scales up to 40 TeV.

The CLIC accelerator provides high-energy high-luminosity sources in a very compact size. The total site length ranges from the 11.4 to the 50.1 km from the 380 GeV stage to the 3000 GeV stage, respectively. The acceleration technology is based on accelerating a low-current high-voltage main beam by tranferring the energy from high-current low-voltage drive beams using the decelerators. The description of the acceleration complex shown in Figure 2.13 for the first stage is summarized below.

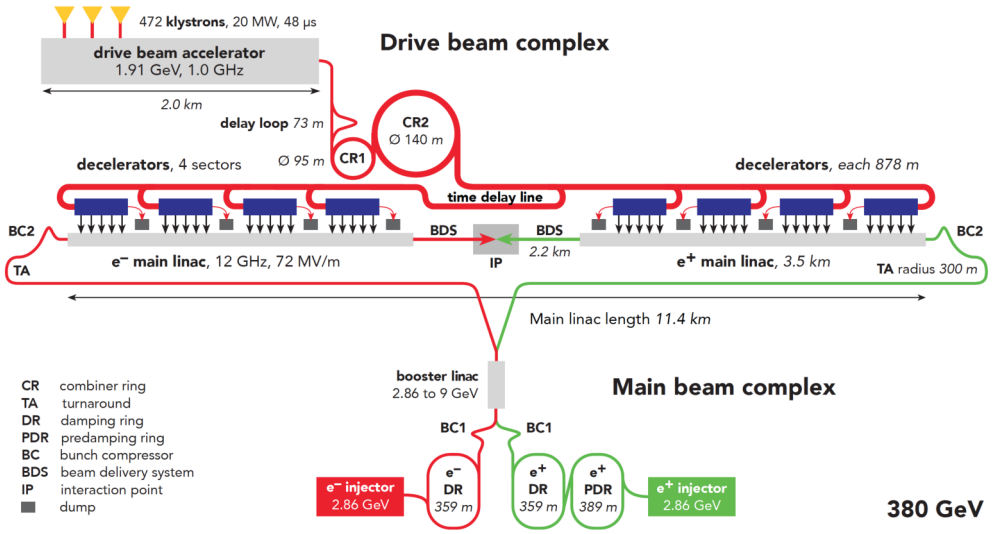

Fig. 2.13 Scheme of the CLIC accelerator complex for the initial 380 GeV stage [26].

Table 2.8 Main parameters of the CLIC accelerator for its different stages [26].

Parameter	Symbol (Unit)	Stage I	Stage II	Stage III
Collision energy	$\sqrt{s}$ (GeV)	380	1500	3000
Crossing angle	θ_x (mrad)	16.5	20	20
e^- polarization	P_{e^-}	80%	80%	80%
e^+ polarization	P_{e^+}	0%	0%	0%
Repetition frequency	f_{rep} (Hz)	50	50	50
Bunches per train	n_b	352	312	312
Bunch interval	Δt_b (ns)	0.5	0.5	0.5
Bunch population	N ($\times 10^9$)	5.2	3.7	3.7
Bunch length	σ_z (µm)	70	44	44
Horizontal beam size	σ_x^* (nm)	149	60	40
Vertical beam size	σ_y^* (nm)	2.9	1.5	1
Luminosity	$\mathcal{L}$ ($\times 10^{34}$ cm^{-2} s^{-1})	1.5	3.7	5.9
Luminosity in top 1%	$\mathcal{L}_{0.01}/\mathcal{L}$	60%	38%	34%
Site AC power	P_{AC} (MW)	168	364	589
Site length	L (km)	11.4	29.0	50.1

Electron source. The electron beam is produced in a conventional RF source, a spin-rotator polarizes the electrons up to an 80%.

Positron source. A 5 GeV electron beam is sent into a crystal, producing energetic photons that hit a second target producing electron-positron pairs. The positron are captured, conforming the positron beam.

Damping rings. The generated leptons are accelerated to 2.86 GeV and injected into a 359 m damping ring in the case of the electrons; and a 389 m pre-damping ring in the case of the positrons. After an initial emittance reduction, the positrons are transferred from the pre-damping ring to a 359 m damping ring. These damping rings accept the large emittance leptons, damp the incoming beam jitter and provide low-emittance beams.

Ring to main linac (RTML). The beams are transported from the damping rings to the main linacs by the RTML system. The first stage of the RTML consists in the booster linac, that accelerates the beams to 9 GeVs. Then, the bunch compressors reduce the bunch length of the beams. Finally, the beams are injected into the main linac.

Drive beam accelerator (DBA). The DBA is a central complex that generates 1.91 GeV beams at a frequency of 1.0 GHz. The beams are fed to two combiner rings of 95 and 140 m of diameter, where they are combined into a higher current beam.

Main linac. Final acceleration of the electrons and positrons is provided by the two 3.5 km main linacs. These are powered by the power extraction and transfer structures (PETS), that transfer the power from the DBA high-current beams into the low-current beam in the main linac. The main linac operates at 12 GHz, providing a gradient of 72 MV/m and accelerating the beams from 9 GeV to 190 GeV.

Beam delivery system (BDS). The BDS removes the transverse tails of the beams with collimators, compresses the beam to the required size, and

focuses the beam to collide in the interaction point. The BDS also guides the beams through post-collision lanes to beam dumps.

The Compact Linear Collider consists in one experiment, where the CLIC detector is the sole responsible of reconstructing the collisions. The detector concept is described in detail in the following subsection.

2.3.1 CLIC detector

The CLIC detector concept [28] shown in Figure 2.14 is the experiment of the CLIC, providing the measurements to realize the physics studies. Its main design consideration is to optimize the PFA performance. To do so, the CLIC detector concept aims for:

- Excellent momentum resolution for the high momentum tracks in the barrel, in the order of $\sigma_{p_T}/p_T^2 \leq 2 \times 10^{-5}$ GeV^{-1}.
- Precise impact parameter resolution to accurately flavour tag the quark jets, in the order of $\sigma_{d_0}^2 \leq (5\mu\text{m})^2 + (15 \text{ m GeV})^2/(p^2\sin^3\theta)$.
- Fine jet-energy resolution for light quark jets in the order of $\sigma_E/E \leq 3.5-5\%$ for jet energies in the 100 GeV to 1 TeV range.
- Great detector acceptance (in the order of 10 mrad) for electrons and photons, to assist with the background rejection.

To reach these targets the CLIC detector concept is conformed by many segmented subdetectors. The main sub-systems are the following:

Vertexing and tracking. The vertex detector consists in 6 layers of pixel detectors (with a material budget of 0.2% X_0 per layer) grouped in pairs, forming three cylindrical super-layers enclosing the beampipe from $r = 31$ to $r = 60$ mm and a series of discs in the endcaps. The vertex detector is surrounded enclosed inside the main tracker, consisting in 6 silicon layers

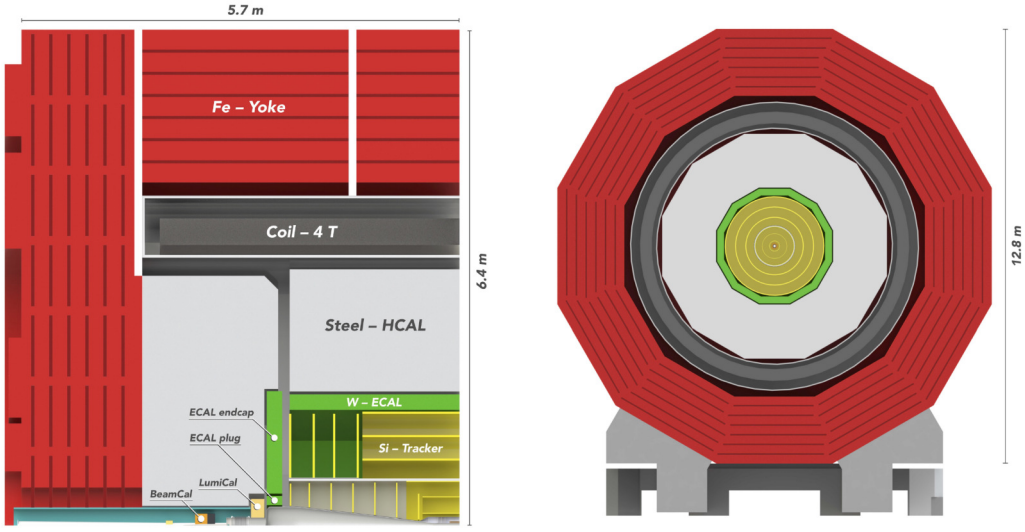

Fig. 2.14 Lateral section view (in the left) and axial viex (in the right) renders of the CLIC detector concept [28].

(with a material budget of 1-2% X_0 per layer) from $r = 127$ to $r = 1486$ mm. To cover the forward region, seven silicon pixel inner disks and four silicon pixel outer disks provide low angle tracking. Both the vertex and tracker detectors will be implemented as 25 µm × 25 µm pixel detectors, allowing for an excellent transverse momentum resolution of $\sigma_{p_T}/p_T^2 \leq 2 \times 10^{-5}$ GeV^{-1} and a single point resolution of 3 µm in the vicinity of the interaction point.

Calorimetry. The physics program requires a high energy resolution for light quark jets, in the order of $\sigma_E/E \leq 3.5\%$. To accomplish it the calorimeters design is optimized for PFA reconstruction, prioritizing for high granularity and particle separation capabilities. The 22 X_0 electromagnetic calorimeter (ECAL) consist on 40 layers of 5×5 mm^2 silicon detector cells with 1.9 mm thick tungsten absorbers, providing a great reduction of the electromagnetic showers, thus reducing the overlapping of neighboring showers. After the ECAL, the segmented 7.5 λ_I hadronic calorimeter (HCAL) is formed by 60 layers of 5×30 mm^{3}0 scintillator tiles with 19 mm thick steel absorbers.

For the very forward angles, high precision radiation hard calorimeters (BeamCal and LumiCal) with up to 40 sandwich layers are considered.

Coil and yoke. A high volume superconducting coil surrounds the entire detector, creating an axial magnetic field of 4 T. An iron yoke interleaved with detectors around the coil acts both as the magnetic flux return, and the muon detector.

Chapter 3

Belle II Pixel Detector

The Vertex Detector (VXD) of the Belle II experiment is the innermost sub-system, and it should be able to accurately measure the tracks from the B meson decays in order to reconstruct and flavour tag the vertices of the interactions.

Due to the 40-fold increase in the instantaneous luminosity of SuperKEKB with respect to the KEKB accelerator, the VXD has to operate in a high track density environment and has to be designed to withstand the high radiation doses. Given the softness of the tracks at Belle II (reaching 50 MeV/c), the VXD should also introduce as little scattering material as possible in the acceptance region. And, to compensate the smaller boost at SuperKEKB (from $\beta\gamma = 0.42$ at KEKB, compared to $\beta\gamma = 0.28$ in the new machine) the VXD should also have an excellent position resolution, improving the impact parameter by a factor of 2 when compared to Belle [22]. To fulfill these requirements, the VXD is comprised of six layers of active silicon forming a cylinder around the beam pipe (see Figure 3.1), covering all the acceptance region of the experiment [21].

Considering the large track density in the surroundings of the interaction point, the silicon strip detectors used in Belle are no longer suitable for the innermost layers of the VXD. The large occupancies that these detectors would experience lead to a high pileup, thus rendering the previous VXD unable to perform. The

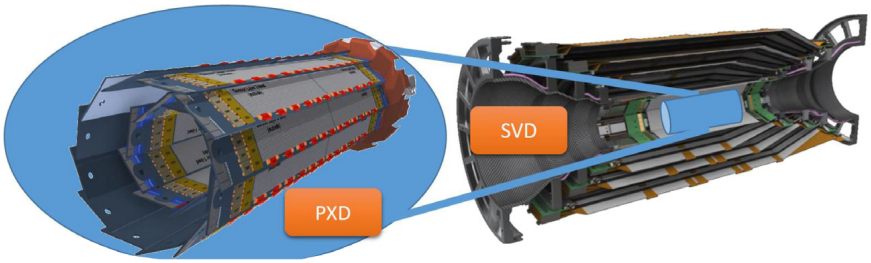

Fig. 3.1 Belle II Vertex Detector concept. In the picture, a magnified PXD (in the left) is surrounded by the SVD (in the right) [29].

solution is to use pixel detectors, which are more granulated and therefore have lower occupancies, for the two innermost layers. The details for the different VXD layers are collected in Table 3.1.

Table 3.1 Main parameters of the Belle II VXD [29].

Subdetector	PXD		SVD [30]			
Technology	DEPFET pixels		Double sided silicon strips			
Layer	1	2	3	4	5	6
Radii[1](mm)	14	22	38	80	115	140
Ladders	8	12	8	10	14	17
Readout channels (thousands)	3072	4608	24.576	38.4	71.68	108.8
Coberture	$17° < \theta < 155°$					

Given how close the two first layers are from the interaction point, the pixel technology chosen for the pixel detector had to be granular, fast, lightweight, and able to withstand the high radiation environment. To fulfill all these requirements (for details, see Table 3.2), thinned DEPFET sensors with a geometrical layout that keeps the readout electronics and its active cooling outside the acceptance region were chosen.

The PXD [31] is designed as two layers of active silicon forming 14 mm and 22 mm radii cylinders around the beampipe. These are built by combining 8 and

[1]The beampipe sits at a 10 mm radii from the interaction point.

Table 3.2 Technical requirements for the PXD [21].

Occupancy	0.4 hits/µm^2/s (<3%)
Radiation dose	2 Mrad/year
Frame time	20 µs
Material budget	0.2% X_0/layer
Resolution	15 µm (50 × 70 µm^2)

12 planar ladders into a slightly overlapping octagon and dodecagon respectively. In order to reduce readout times and to improve the manufacturing yield, the ladders are split into two modules[2] (see Figure 3.4), which are the smallest fully functional building blocks of the PXD. Each of the modules host a DEPFET pixel matrix with 250 columns along the z direction (parallel to the beam) and 768 rows along the φ direction (perpendicular to the beam); and the most power hungry electronics next to the sensor, outside of the detector acceptance. To build the ladders, two mirrored modules along the z direction are glued together head to head, such that the electronics of both sensors are located in the ends of the ladder.

3.1 DEPFET active pixel sensor

The Depleted Field Effect Transistor (DEPFET) is an advanced semiconductor detector technology that allows for combined particles detection and amplification in the same device. The original concept was proposed by Josef Kemmer and Gerhard Lutz in 1987 [32], and the first working prototype was built by 1990 [33]. Different DEPFET based detectors have been proposed and constructed in the recent years, including x-ray spectroscopy sensors and HEP vertex detectors.

The DEPFET pixels implemented in the Belle II PXD consist in a p-channel MOSFET (Figure 3.2a) integrated onto a fully depleted n-type high-resistivity silicon detector substrate [21]. A potential minimum is created by sidewards

[2]By halving the size of the sensors, smaller silicon wafers can be processed, increasing dramatically the manufacturing yield.

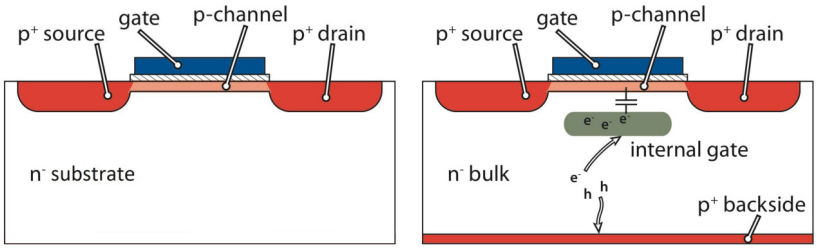

(a) P-channel MOSFET. **(b)** DEPFET pixel.

Fig. 3.2 Schematic depiction of p-channel MOSFET (left), and a MOSFET derived DEPFET (right) [34].

depletion[3] in the plane around a micron below the MOSFET gate. This potential minimum attracts the excited electrons[4], while the holes drift into the p^+ back contact.

As seen in Figure 3.2b, an additional deep n-doping region, called the internal gate, is created right underneath the MOSFET gate. The electrons are collected in the internal gate, generating mirror charges in the MOSFET channel and thus increasing its conductance. When the external gate is activated, the capacitive coupled internal gate modulates the p-channel current (I) from the source to the drain depending on the amount of stored charge (q) in the internal gate. This modulation is given by

$$g_q = \frac{dI}{dq} \propto \sqrt{\frac{I_d \mu}{L^3 W C_{ox}}}, \tag{3.1}$$

[3]In this depletion scheme two p^+ implants surround the n-type silicon bulk forming two diodes. Reverse biasing the two diodes, a depletion region is formed around the implants, leaving an undepleted region in between them. When the voltage applied is sufficient, the depletion regions meet in the bulk, generating a plane of minimum potential. By applying different voltages to the p^+ implants, the minimum potential plane can be shifted vertically. For the DEPFET pixel the front side p^+ implants are the source and drain structures of the MOSFET.

[4]Either generated by the ionizing particles traversing the depleted silicon bulk, or by thermal excitation.

where g_q is the internal amplification[5] of the DEPFET pixel. I_d is the transistor's drain current, μ is the carrier mobility[6], L and W are the length and width of the gate, and C_{ox} is the capacitance of the gate oxide [35].

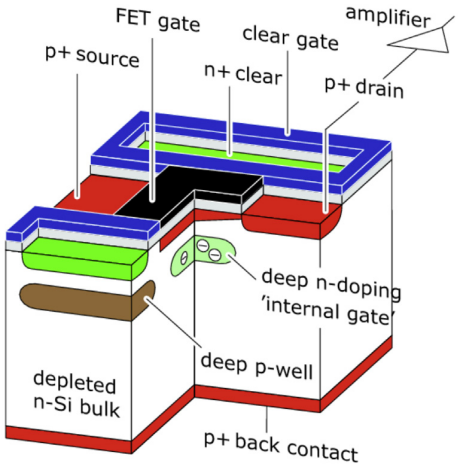

Fig. 3.3 Section of a DEPFET pixel with a n^+ clear implantation [35]. By activating the clear signal, the charge collected in the internal gate can be removed.

As the electrons stored in the internal gate are not removed after readout, and given that the capacity of the gate to host electrons is finite[7], a charge removal method is implemented. A n^+ contact -the clear contact- is implanted in the neighborhood of the internal gate (see Figure 3.3). When a positive voltage is pulsed[8] at the clear contact, the implant becomes the most attractive region in the pixel, making the stored electrons flow from the internal gate to the clear implant.

[5]The DEPFET design for the Belle II PXD yields an expected $g_q \sim 750$ pA/e$^-$.

[6]Hole mobility in the case of the p-channel MOSFET.

[7]The internal gate is designed to store up to 40000 electrons ($\sim$ 6 mips for 75 µm of silicon) before having an impact on the response's linearity. Furthermore, the saturation of the internal gate does not occur till around 60000 electrons for the PXD design. In the absence of a clear pulse, the internal gate quickly ($\sim$ 100 ms, at room temperature) fills up with thermal electrons, shielding the internal gate against new electrons.

[8]With a clear voltage pulse around 15 V, the internal gate can be completely emptied in $\sim$ 10 ns.

An additional deep p^+ implantation -the deep p well- is created around the clear contact to prevent the electrons from drifting to the clear contact during the charge collection phase. To help in the clearing process the cleargate polysilicon structure is implemented, forming an n-channel between the internal gate and the clear implant. This channel is capacitively coupled to the clear contact, thus lowering the potential barrier from the internal gate to the clear implant when the last one is activated.

The DEPFET pixel design comes with a series of intrinsic advantages: very low noise, even at room temperature, due to the small capacitance of the internal gate; in-situ signal amplification, avoiding charge loss between collection and amplification, and yielding a signal that can be directly read[9]; and, the ability to perform non-destructive readings of the stored charge, allowing for different readout schemes. Any of these schemes boil down to a sequence of the following procedures:

Collection. With the bulk of the silicon depleted and with the help of static voltages, the electrons are guided below the internal gate, where they gather. The external gate remains powered off. Since the transistor remains off in this phase, the pixel is consuming almost no energy.

Sampling. The DEPFET pixel is activated by applying a voltage to the external gate. The current starts flowing from the source into the drain contact. This current consists on the MOSFET intrinsic current (also called pedestal) and the increase due to the internal gate modulation (i.e. the signal). By subtracting the pedestal to the total current, the signal can be obtained.

Clearing. By applying a voltage to the clear contact[10], a punch-through channel is created between the contact and the internal gate. The charge is attracted to the contact and the internal gate is emptied.

[9] A minium ionizing particle traversing 75 µm of fully depleted silicon creates around 6000 electron-hole pairs. Resulting in around 4.5 µA of current increase in a DEPFET pixel assuming $g_q \sim 750$ pA/e$^-$.

[10] During the clearing process the external gate is kept active to enlarge the potential gap between the internal gate and the clear implant, thus speeding up the clearing process.

3.2 Module

As pointed in the introduction, the smallest fully functional building blocks of the PXD are the modules. The module [35], illustrated in Figure 3.4, is a self-sustaining monolithic silicon structure hosting a matrix of DEPFET pixels, its steering electronics and the contact pads to address the module.

The sensor is manufactured on a 75 µm thin detector grade silicon bonded onto a 450 µm silicon handling wafer that provides mechanical support and stiffness. On the top of the module there is a three-layer metal system with two 1 µm aluminum layers and one 5 µm copper layer, with BCB layers acting as insulators between them. The handling wafer is thinned by means of anisotropic etching, leaving the sensitive area completely exposed and surrounded by a 525 µm frame. The top and left sides of the frame depicted in Figure 3.4 are 0.6 mm and 0.4 mm wide respectively, while the right and bottom sides amount to 2.4 mm and 23.2 mm.

The right side -called the balcony- houses the Switchers, which are the six ASICs steering the input voltages of the DEPFETs allowing for readout and clearing processes. As the balcony is inside the acceptance region, small openings are carved underneath the frame to reduce its impact in the material budget. By doing so, a material reduction around 30% is accomplished while retaining the mechanical stiffness. The left side (opposite to the balcony) is also carved in order to reduce the material budget as much as possible.

The bottom side of the frame -called the End Of Stave (EOS)- remains outside of the PXD acceptance, and houses the bump-bonded[11] readout ASICs and the contact pads of the flexible Kapton[12] cable connecting the module with the services[13]. Next to the matrix are the four Drain Current Digitizers (DCDs) that digitize the drain current from the DEPFET pixels. Behind each of the DCDs a

[11] A dedicated under-bump copper layer is present on the module to allow for ASIC and SMD bump bonding.

[12] Kapton is the commercial name a polyimide film developed by DuPont de Nemours, Inc..

[13] Allocating the readout ASICs outside of the detector acceptance greatly reduces the impact on the material budget of the module.

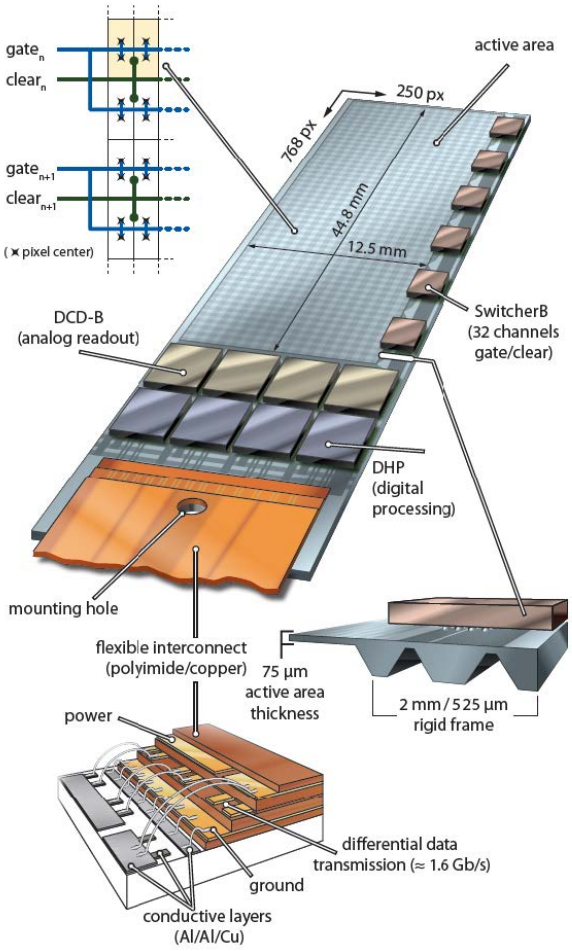

Fig. 3.4 Depiction of an inner layer PXD module showcasing the DEPFET pixel matrix, the three ASIC types needed for operation and the Kapton cable used to interconnect the module with the power supply, the control electronics and the DAQ [34].

Data Handling Processor (DHP) controls the module operation and processes the incoming data and transmits it to the outside through the Kapton cable.

The Kapton cable carries all the electrical signals needed to power, control and retrieve the data from the module. The cable is around 50 cm long and connects the module with a patch panel that breaks out into the power cable, control cable and data cable. On the extreme that connects with the module:

the back side is soldered directly onto four big copper pads at the bottom of the module, providing the mechanical and electrical connections to the analog ground, digital ground and the power for the analog part of the DCDs; the remaining electrical connections are realized through wire bonding between the 73 aluminum pads on the module and pads on the upper side of the Kapton cable. The other extreme is terminated with a tiny 100 pin connector[14].

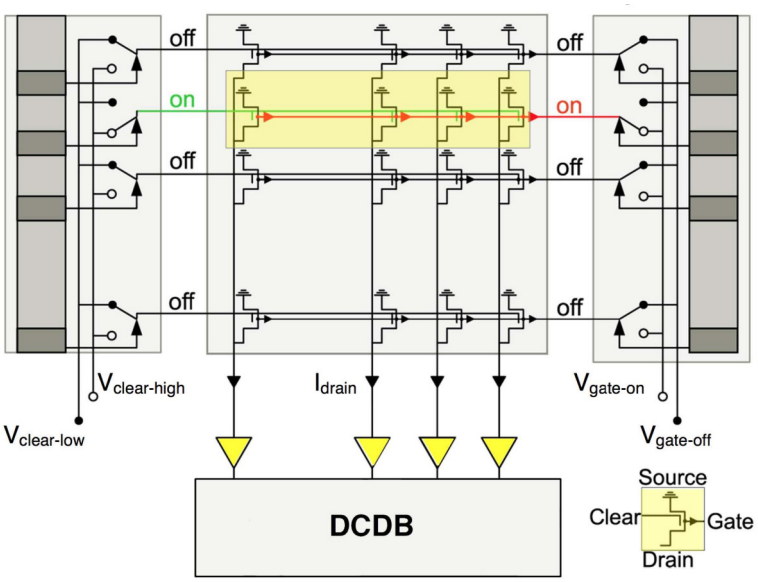

Fig. 3.5 Scheme of the reading of a DEPFET pixel matrix [36]. The gate and clear voltages that allow for sampling and clearing of the pixels are controlled row-wise by the Switchers. The output drain current of the pixels are digitized by the DCDs. The full matrix is looped sampling, clearing and repeating for the next row .

The sensor itself consist in a matrix of 250 columns × 768 rows DEPFET pixels. The geometrical rows of the matrix share the same electrical lines for the external gates and the clear implantations (i.e. the pixels in the same row have their implantations connected in series). Likewise, the geometrical columns share the electrical lines for the source and drain implantations.

[14] A Samtec SS4-50 connector.

Activating one row at a time, only one DEPFET pixel per column is contributing to the current in the drain line, allowing for independent pixel measurements by the DCDs. As seen in Figure 3.5, the full matrix is digitized by iterating the sampling and clearing procedures row by row in the so-called rolling shutter mode [34].

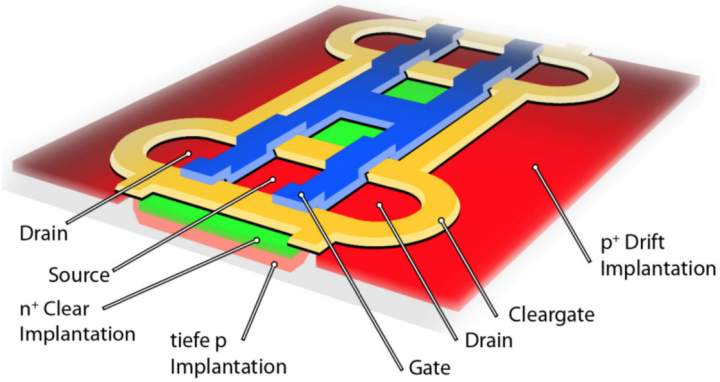

Fig. 3.6 Layout of the DEPFET pixel structure in the sensor [34]. The pixels are arranged in two double cells, which consist on two mirrored DEPFET pixels. The fourfold share the gate (in blue), cleargate (in orange) and clear (in green) structures. The double cells share the source implants, and each individual pixel has its own drain implant. The whole structure is filled with drift implantations (in red).

In order to optimize the electrical routing of the module while speeding up the reading process a fourfold pixel layout is implemented. In the layout shown in Figure 3.6, two mirrored pixels sharing a common source stablish a double cell, and two cells are grouped together in the fourfold. The space between the gates is filled by drift implants, that define a surface potential in the areas farther from the gates, scaling the pixel size. The fourfold shares the electrical lines for the gate and clear lines. The source implant is shared between the pixels in the cell, while each of the pixels has a dedicated drain line. By doing so, the 4 pixels can be activated simultaneously and sampled concurrently by the DCDs[15]. At the matrix level this means that 4 rows (one gate) are read concurrently over the 250 columns using 1000 drain lines.

[15] At the expense of having to quadruple the number of ADCs.

The pixel size for the inner layer is 50 × 55 µm^2 ($\varphi \times z$) for the 256 pixel rows closest to the interaction point, and 50 × 60 µm^2 for the remaining 512 rows. For the outer layer, the pixel size is 50 × 70 µm^2 and 50 × 85 µm^2 respectively. The rationale after the different pixel pitch design is to compensate for the inclination of the impinging particles. Tracks crossing through the central region intersect at normal incidence with the sensor, while tracks crossing in the farther regions traverse multiple pixels due to the inclination. With the variable pixel pitch, the module is optimized to produce 2-cluster hits along all the sensor, yielding a higher spatial resolution when applying a center of gravity algorithm [37].

Table 3.3 Geometrical properties of the PXD [35].

	Inner layer	Outer layer
Modules	16	24
Ladder size (mm^2)	136 × 15.4	170 × 15.4
Module size (mm^2)	67.975 × 15.4	84.975 × 15.4
Sensor size (mm^2)	44.8 × 12.5	61.44 × 12.5
Sensor thickness (µm)	75	
Pixels	250 columns × 768 rows	
Pixel size (µm^2)	50 × 55 (rows 1 to 256) 50 × 60 (rows 257 to 768)	50 × 70 (rows 1 to 256) 50 × 85 (rows 257 to 768)

3.2.1 Switcher

The Switcher [38] is a HV-CMOS ASIC designed for the addressing of the matrix rows. It steers the fast high voltage pulses supplied to its 32 gate and clear channels that allow for the reading and clearing mechanisms of 128 rows of the DEPFET matrix. The chip is manufactured using the AMS 180 nm HV process, has a designed size of 1470 × 3600 µm^2 with a thickness of 300 µm, and its interface with the module consists of 96 bumps realized through flip chip [39].

Each of the output channels consist on two high voltage switches that generate the clear and gate signals. The output switches between upper and lower voltages, with voltage swings up to 30 V. The channels are activated one after the other by a shift register that goes along the channels. These are activated by fast differential control signals provided by the controller DHP[16]. The six Switchers can be daisy chained connecting the serial output of the Switcher to the serial input of the next one. The configuration of the Switcher registers is addressed via the daisy-chained JTAG protocol.

3.2.2 Drain Current Digitizer

The DCD [40] is an ASIC designed to be the analog front-end and ADC chip used to digitize the DEPFET drain currents. It is formed by 256 analog channels that digitize the incoming currents. The chip is manufactured using the UMC 0.18 µm process, has a size of 3240 × 5100 µm^2 with a thickness of 350 µm, and its interface with the module consists of 431 bumps realized through flip chip [39].

250 analog channels are bump bonded to 250 DEPFET channels in the module, leaving 6 channels disconnected. The 256 channels are organized in 8 columns with 32 channels each, the digitized output of the column is multiplexed into an 8-bit wide parallel bus that sends the digital data to the DHP at a rate of 320 Mb/s. Each of the columns have a 2-bit wide bus input used to offset correct the input currents by the so-called 2-bit DAC. Each of the channels consist in a current receiver, and a transimpedance amplifier, followed by an 8-bit pipeline ADC based on current memory cells. These have a sampling time of 100 ns and a dynamic range in the order of 20 to 40 µA depending on the receiver gain.

As discussed in the previous section, the input current is the sum of the pedestal (the current flowing through the DEPFET when there is no external stimulus) and the signal (the extra current flowing due to charges accumulated in the internal gate). The total current is in the order of 100 µA, while the signal is

[16]The DHP closest physically to the Switchers is the one in charge of providing the sequence of control signals.

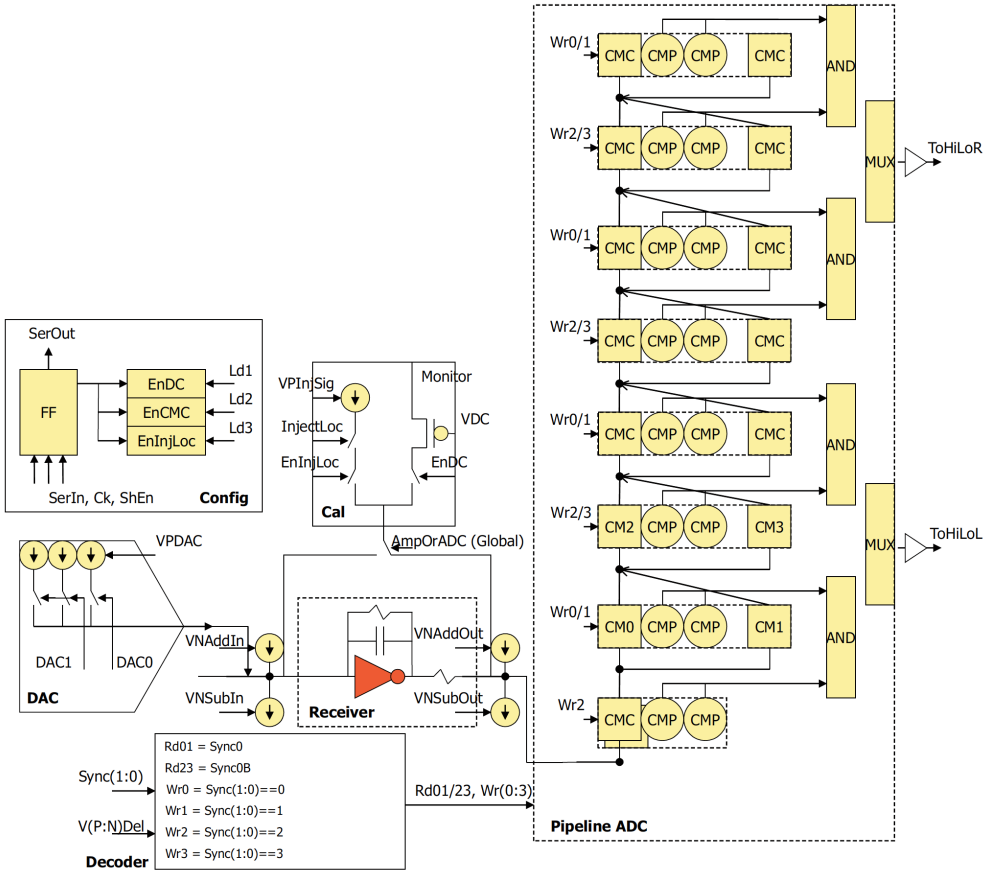

Fig. 3.7 Basic scheme of the analog circuit of the DCD [40].

in the order of 10 µA. Given the finite dynamic range of the ADCs, a series of offsets have to be leveraged so that the pedestals can be compressed in the low end of the dynamic range, leaving the rest to accommodate the signal.

As seen in Figure 3.7 the incoming currents are first offset via the global current adder and subtractor *VNAddIn* and *VNSubIn* respectively[17]. An additional current adder, the 2-bit DAC, sums 3, 2, 1 or 0 times the reference current *IPDAC* on a per channel basis. The reference current is set globally for all the channels in the DCD, while the 2-bit multiplier -called the offset- is sent over the 2-bit input

[17]These are set globally for all the channels in the DCD.

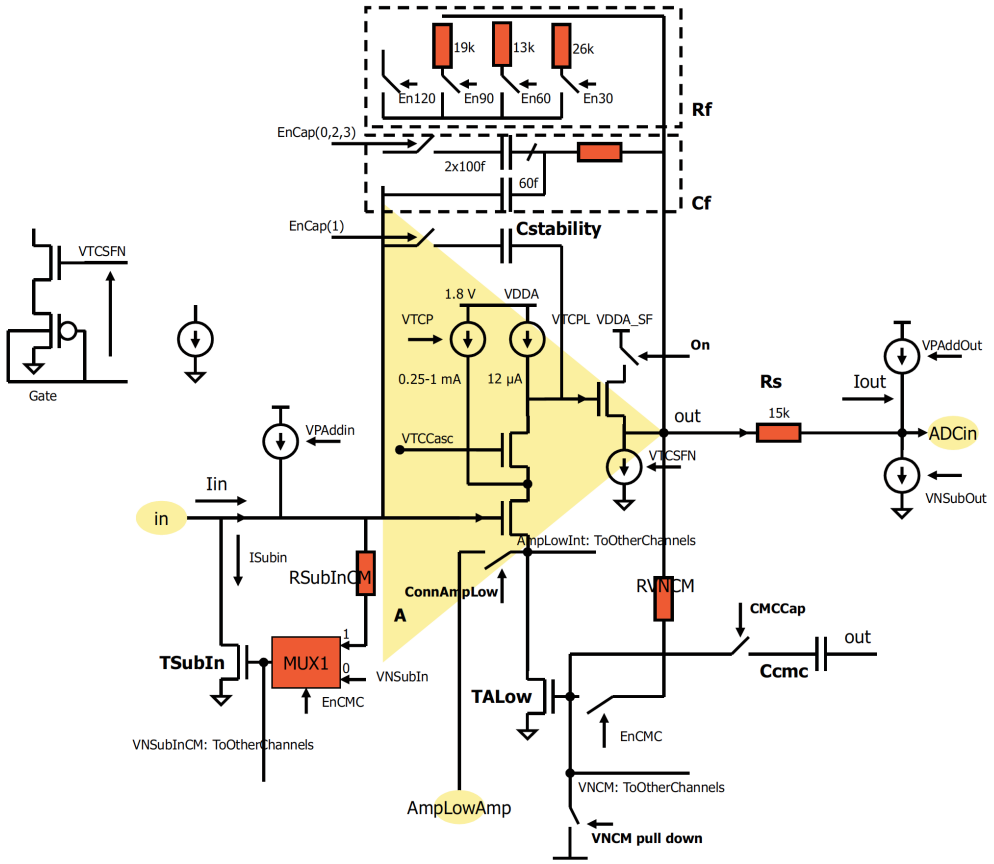

Fig. 3.8 ADC current receiver circuit [40].

bus from the DHP. Synchronizing the offsets with the rolling shutter reading, individual values can be set for each of the DEPFET pixels, thus reducing the pedestal spread of the matrix to one fourth.

The corrected current I_{in} is then amplified in the resistive current receiver depicted in Figure 3.8. The receiver is based on a transimpedance amplifier with an output resistor. The transimpedance amplifier converts the input current and converts it into the output voltage

$$V_{out} = V_{in} - I_{in} \times R_f. \tag{3.2}$$

Since the input voltage V_{in} is held by the ADC at a constant potential, the current by the output resistor R_s results into

$$I_{out} = \frac{R_f}{R_s} \times I_{in} - I_{offset}, \tag{3.3}$$

where $I_{offset} = (V_{in} - V_{ADCin})/R_s$ is fixed and can be compensated by the current offsets or the 2-bit DAC; and $G = R_f/R_s$ is the gain of the receiver. The output resistor R_s is fixed to 15 kΩ, while the feedback resistor R_f may take 7 different values depending on the state of the switches $En90$, $En60$ and $En30$. The value of the R_f resistor is the sum in parallel of the resistors activated.[18]

The amplifier has an analog common mode correction ($ACMC$) circuit that corrects the common noise[19] by calculating the mean of the input currents and subtracting it to every channel.

After the amplification stage, there is another global current adder and subtractor *VNAddOut* and *VNSubOut* respectively. The resulting current goes into the pipeline current-mode ADC.

The pipeline ADC consists in 8 blocks of double memory cells with two comparators. By performing comparisons of the stored currents with referenced currents and performing additions and subtractions the incoming currents are digitized into 8-bit signed integer numbers.

Apart from the current receiver and the pipeline ADC, each channel has a calibration circuit to inject current in front of the receiver; a pixel shift register with the configuration of the analog channel; and the decoder, that generates the signals to control the ADCs and indicate the sampling timing.

Besides the 256 channels, a large digital logic block is in charge of generating the control signals for the ADCs, converting the digitized values coming from

[18] The DCD can be configured to operate in 7 different gain values. This can help mitigate the loss of the DEPFET gain once the modules are irradiated. The modules start with a low gain configuration, and move to higher gains with irradiation.

[19] The common mode noise is produced by small instabilities in the power supply and the electronics. Due to the rolling shutter mode, this noise affects by the same amount to all the pixels in the rows that are being read concurrently.

the ADCs in redundant binary representation to standard binary format, and the serialization of the data and transmission to the DHP. To ensure the data transmission from DCD to DHP, a known test pattern is hard coded in the digital block. A JTAG compliant interface is available to set internal registers of the ASIC.

3.2.3 Data Handling Processor

The main tasks of the DHPs [41] are to control the DCDs and Switchers, and the processing of the data. The chip is manufactured using the TSMC 65 nm process, has a size of 3280×4200 µm^2 with a thickness of 350 µm, and its interface with the module consists of 296 bumps realized through flip chip [39].

The module is controlled through the correct configuration of the shift registers in the three types of ASIC. These registers can be written and read via the JTAG protocol. The JTAG commands are sent in series, i.e. the slow control signals go from ASIC to ASIC and then back to the controller. This is called the JTAG chain, and has the following geometry: the first DHP is configured, then its DCD is configured, second DHP and DCD are configured, and so on. The Switchers are included in the chain after the DCD closest physically to them. The DHPs have internal switches to shorten the JTAG chain if needed, so that individual DCDs can be excluded from the chain[20].

The DHP closest to the Switchers is in charge of providing them with the Switcher sequence, thus, controlling the matrix readout. Each of the DHPs feed their DCD with the offsets for the 2-bit DAC at the correct moment, so that the offset applied matches the activated gate by the Switcher. These offsets are written into the DHP memory and sent to the DCD via the eight 2-bit wide input buses.

The digitized currents transmitted from the DCD are received by the DHP's deserializer (see Figure 3.9) and are stored into the raw data memory. Then, the

[20] If the DCD closest to the Switchers is excluded from the JTAG chain, all the Switchers are also excluded.

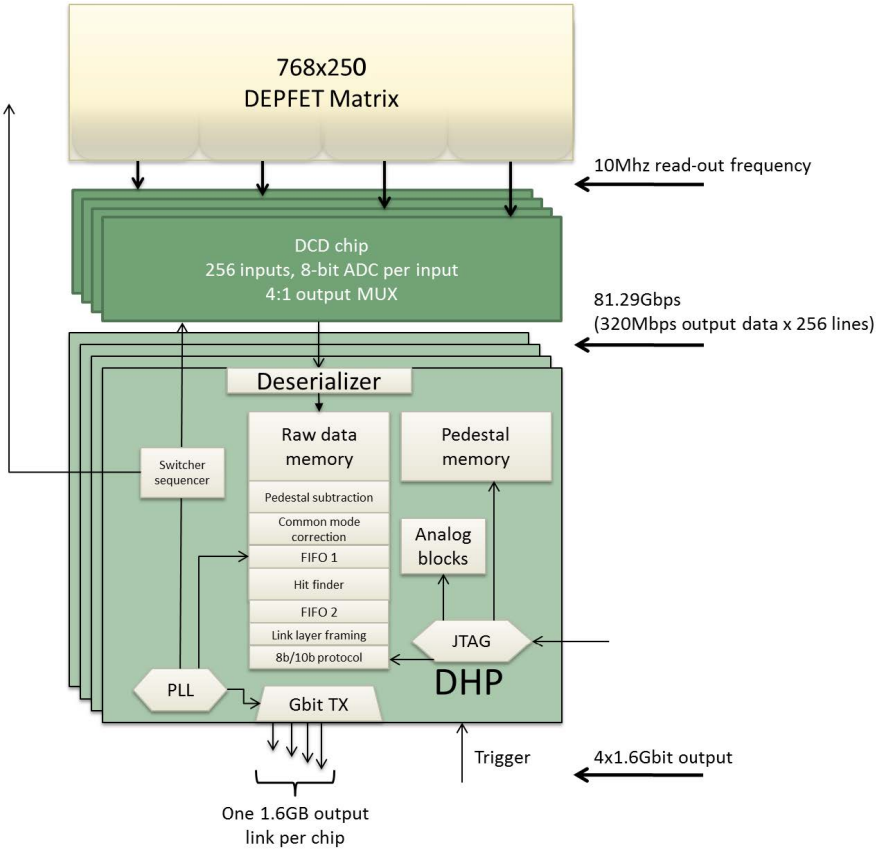

Fig. 3.9 Block diagram of the DHP [41]. The diagram can be divided in three parts: the data processing part, the Switcher sequencing and the DCD control.

pedestal subtraction is done by deducing a pedestal map previously uploaded to the DHP. After the pedestal subtraction, they can be common mode corrected digitally in a similar fashion of what was done with the ACMC.

Given that a full frame of 8-bit values would have a size of 192 kB, and that the required frame time is of 20 µs, a module would transmit around 9.6 GB/s (384 GB/s for the full PXD). To reduce the data size a zero suppression cut is implemented. The cut is applied by removing all the data below a fixed threshold -called the zero suppressed threshold-. The resulting data frame is encoded in the

Aurora 8b/10b protocol and sent over four 1.6 Gb/s High Speed Links (one per DHP) to the DAQ system.

Intercommunications

The DCD data is transferred to the DHP behind it through the eight 8-bit wide buses, consisting on 64 LVDS transfer lines. Due to space constraints in the silicon, only the positive ends of the LVDS lines are routed. The DHP decoder receives the signals at its end. The decoder has to sample at the precise time to successfully decode the signals. To find the correct sampling point, a series of registers to enable a global delay for the sampling of all lines, and local delays for each of the 64 transfer lanes are present [41]. By requiring the DCD to send the hardcoded test pattern and iterating over the delays error-free communication for the DCD data can be ensured.

Likewise, the 2-bit DAC offsets are transmitted over the eight 2-bit wide buses, consisting on 16 LVDS lines connected on their positive end. These lines have their own delay settings, and can be optimized by iterating over the delays and testing that the correct offsets show up in the targeted pixels.

Then, the data is sent from the DHPs to the DHE through the High Speed Links, going from the DHP to the DAQ system through: the metallization layer in the silicon, the wire bonds that connect it to Kapton cable, the Patch Panel and an InfiniBand cable. All these cables and tracks act as a low pass filter, distorting the signal received by the DAQ. To ensure the correct transmission, a Current Mode Logic (CML) driver is implemented. The CML performs a pre-emphasis of the signal (see Figure 3.10), enhancing the higher frequencies so that after the attenuation the signal is still recognizable by the DAQ [42]. The output of the CML can be adjusted by three parameters:

bias. Sets the amplitude of the signal.

biasd. Sets the amplitude of the enhancement of the higher frequencies (or equivalently, around the edges).

dly. Sets frequency threshold from which the enhancement is applied (or equivalently, the time that the enhancement is applied around the edges).

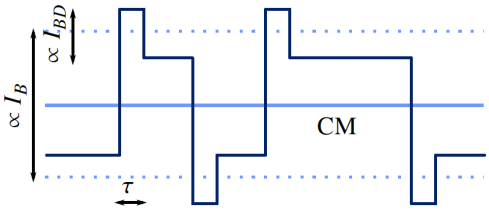

Fig. 3.10 Scheme of the CML parameters and their impact on the signal morphology in the time domain. The I_B *bias* parameter sets the amplitude of the signal, the I_{BD} *biasd* parameter sets the height of the enhancement around the edges (high frequencies), and the τ *dly* parameter sets the lenght of the enhancement application [42].

3.3 Services

The PXD uses many electrical service lines for power, control and data transmission [21]. These lines are designed having a compromise between performance and space requirements[21]. The layout scheme of the services and connections is depicted in Figure 3.11.

The connector at the end of the Kapton cable is attached to a Patch Panel that splits the signals into three 2 meter cables: an ethernet, an InfiniBand and a Glenair cable[22]. The three cables connect to a dock box PCB located outside of the CDC outer wall, where the power cable is split into two low resistivity power cables[23] that go to the Power Supply (LMU PS), and the ethernet and InfiniBand signals are split into a camera link cable and an optical fiber[24] that go to the Data Handling Hub (DHH).

[21] Given that the PXD is the innermost detector, the service cables have to share space with other subdetectors.

[22] The Glenair cable corresponds to the M83513-03-G 14 C part, with 51 lanes.

[23] The cables are custom made, using a mixed layout DSub 36W4, with 32 regular contacts and 4 special contacts.

[24] Initially, the idea was to transmit the signals over 20 m copper cables, but the instability in the signal due to cable imperfections lead to signal loss. To avoid it, optical fibers are deployed

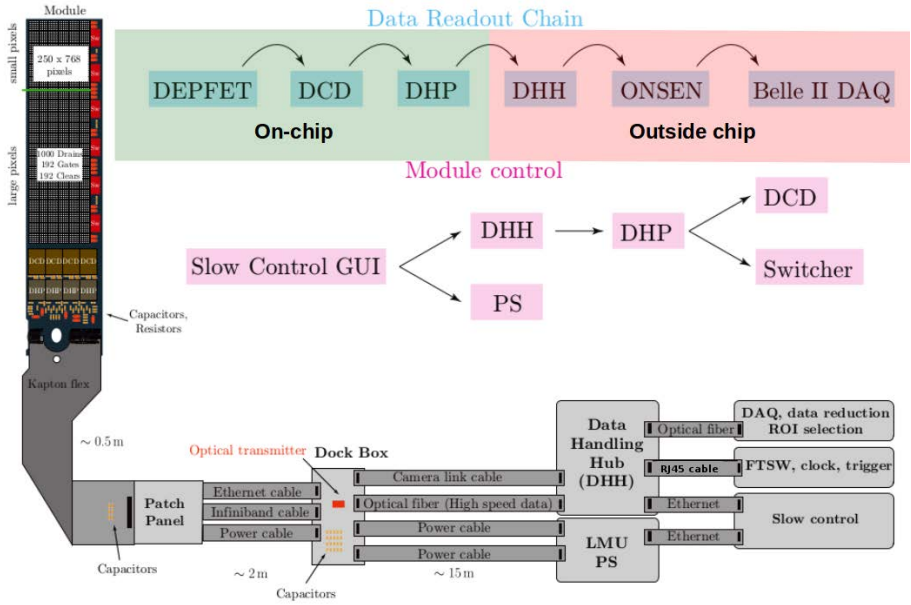

Fig. 3.11 Services and connections needed to operate a PXD module [43].

The DHH handles the readout and the configuration of the PXD. It receives the clocks and triggers from the Frontend Timing Switch (FTSW) that distributes the timing from the global Belle II DAQ system through an ethernet cable. The PXD data is sent forward through an optical fiber using the Aurora 8/10b encoding to the Online Selection Node (ONSEN) that reduces the data using a Region of Interest (ROI) strategy and transmits the remaining data to the Belle II DAQ. The DHH also generates the JTAG commands that configure the ASICs in the modules.

Both the DHH and the LMU PS are controlled through the slow control system [44], which consists on a series of IOC servers that can be addressed through

to carry the High Speed Link signals, and a camera link cable transmit the global clock and the JTAG signals.

EPICS[25] [45] broadcasted variables. These IOC servers controls the hardware via the UDP-based IPbus protocol developed at CERN. A PC in the local network running Control System Studio implements a GUI to set and read the EPICS variables, allowing the operator to control the module.

3.3.1 Power supply

The modules are powered by the LMU PS that provide the 23 power nets and 2 ground nets necessary to operate the modules [21]. The powering scheme with the nominal biasing voltages can be visualized in Figure 3.12. The power lanes can be classified by their usage:

Grounding. The modules have an analog ground *AGND* and a digital ground *DGND* net. These two are actually shorted later on in the Kapton cable, when connected to the Belle II common ground.

Switcher. Three voltages are supplied to the digital circuit of the Switcher: *sw-dvdd*, *sw-refin* and *sw-sub*.

DCD. One net is required to power the digital part of the DCDs, the *dcd-dvdd*; while three nets are required to power the analog block: *dcd-avdd*, *dcd-refin* and *dcd-amplow*.

DHP. Two voltages are required to power the digital blocks: *dhp-io*, and *dhp-core*.

DEPFET Switcher voltages. Four analog voltages are supplied to the Switchers: *gate-on1*, *gate-on2* or *gate-on3*; *gate-off*, *clear-on* and *clear-off*. In the case of the *gate-on* voltages, they are split into three different nets. The first one services the first two Switchers, the second, the third and fourth Switchers, and the last one the last two Switchers.[26]

[25] Experimental Physics and Industrial Control System, a distributed control system used broadly in HEP experiments.

[26] The *gate-on* threshold for the DEPFET transistor shifts with the radiation dose that the pixel receives. Therefore, the gate-on voltages are split in order to have some granularity when compensating the damage with lower voltages.

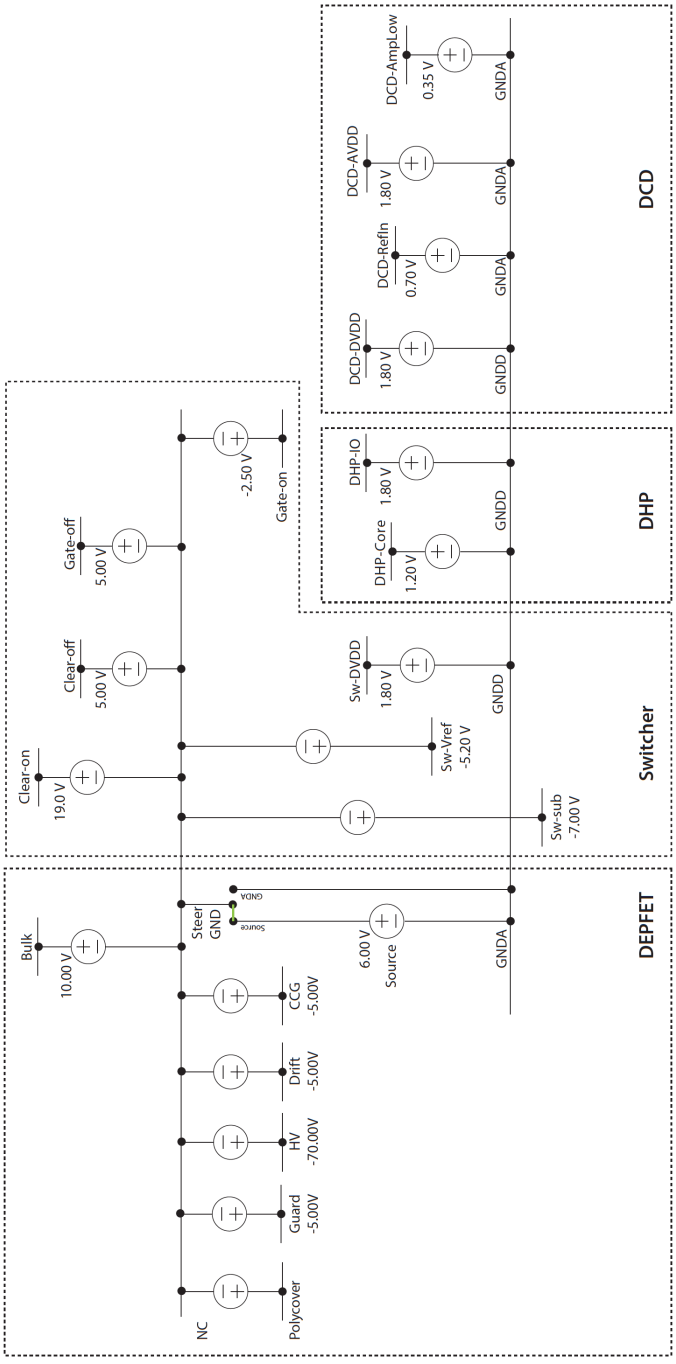

Fig. 3.12 Biasing scheme of a PXD module [46].

DEPFET static voltages. A total of nine analog voltages are supplied to the matrix: the capacitively coupled clear-gate voltages *ccg1*, *ccg2* and *ccg3*; *bulk*[27], *source*, *drift*, the sidewards depletion voltage *HV* and *guard*[28]. The *ccg* voltages are split in the same way that the *gate-on* nets.

The LMU PS is equipped with sense lines[29] that provide feedback to the power driver, so that the power supply can compensate voltage drops in the power lines, ensuring that the required voltages are applied at destination.

An emergency shutdown sequence is implemented in the power supplies to ensure proper shutdown of the modules in the case of connection loss with the slow control, or the triggering of any of the interlocks. An over voltage protection condition can also trigger the emergency shutdown in the case of over-voltage or over-current events.

3.4 Data Handling Hub

The Data Handling Hub (DHH) [47] consists on eight Data Handling Concentrators (DHC) that controls five Data Handling Engines (DHE) and one Data Handing Interface (DHI) [48]. Figure 3.13 shows the basic scheme of the DHH system.

The DHCs are responsible from distributing the global clock from the Belle II DAQ system [49] and the triggers provided by the FTSW modules to the DHI. The DHI trigger the PXD modules, and the corresponding DHE receives the zero suppressed frame. The DHI also handles the configuration of the PXD modules through the JTAG interface. The whole system is configured and controlled through the IOCs in the Data Quality Monitor PC.

[27] The bulk contact is set to a higher voltage than source to prevent forward biasing of the pn-junction.

[28] The guard ring is a structure surrounding the sensor that prevents outside electrons from drifting into the pixels.

[29] Most of the sense lines go all the way down to the module, some of them are sensed in the PS output or the dock box. The ASIC power nets are sensed in the module, as well as the DEPFET Switcher voltages, with the exception of *sw-sub*. DEPFET static voltages are sensed in the PS or dock box, with the exception of *source*.

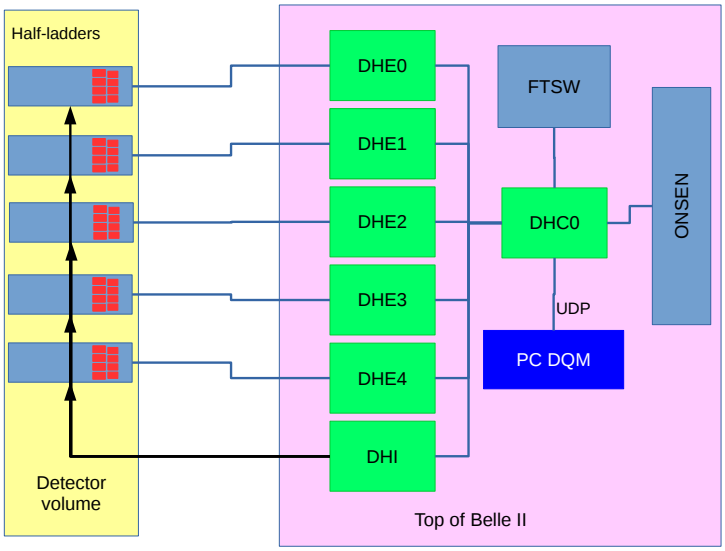

Fig. 3.13 Data readout scheme from the PXD modules to the Belle II DAQ system [48].

Each DHE is directly connected to a PXD module, receiving the incoming data from the DHPs. The hit information from the DHE is sent upwards to the DHC through a 6.5 Gbps Aurora link, where a sub-event is built and a trigger number is assigned. These sub-events are then sent to the Online Selection Node (ONSEN) [50] via four 6.5 Gbps Aurora links.

The ONSEN system is able to buffer the entire PXD zero suppressed data for 5 seconds. During that time, the DAQ uses the tracks detected by the surrounding detectors (mainly the CDC and SVD) to extrapolate regions of interest (ROIs) in the PXD. To reduce the produced data and avoid fake hits, all the data outside of the ROIs is discarded, resulting in a data reduction factor around one order of magnitude. The resulting events are sent downstream to the Belle II DAQ.

3.5 Mechanical support and cooling

The power consumption of the sensor is quite low, due to the fact that only the gated pixels contribute to the power consumption. The power dissipated by the whole sensor is in the order of

$$P = I_{drain} \times V_{source} \times N_{gated\ pixels} = 100\ \mu\text{A} \times 6\ \text{V} \times 1000 = 0.6\ \text{W} \qquad (3.4)$$

where I_{drain} is the average pixel drain current, V_{source} is the *source* voltage, and $N_{gated\ pixels}$ is the number of active pixels at the same time (four rows, given the fourfold structure). The ASICs in the other hand consume around 0.2 W in the case of the Switchers, 6.5 W the DCDs and 1.5 W the DHPs. In total, a single PXD module dissipates 0.8 W in the sensor region (~ 155 mW/cm^2 for the smaller modules) and 8 W in the EOS (~ 2.25 W/cm^2) [35].

To ensure the correct functioning of the PXD active cooling is required. The sensors and the Switchers are cooled by carbon pipes that run along the ladders balconies, blowing nitrogen directly onto the modules. The EOS, on the other

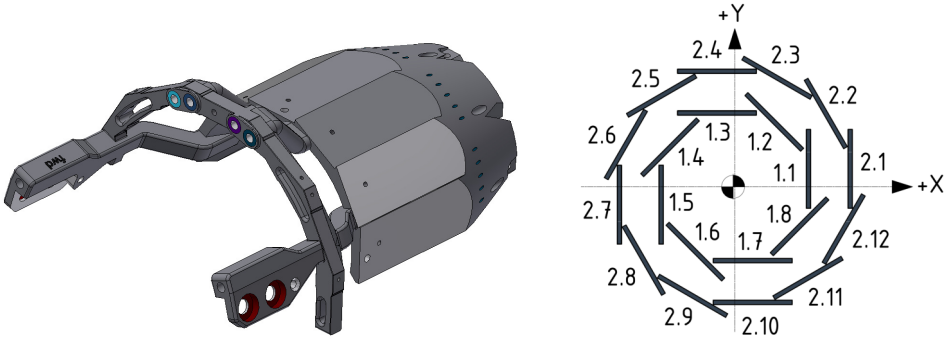

(a) Support and cooling block [51]. **(b)** PXD ladders arranging [52].

Fig. 3.14 Arrangement of the PXD in the support and cooling blocks. The ladders are mounted into four SCBs. Bi-phase CO_2 flows inside the blocks, cooling the whole structure to -30°C. DEPFET matrices and Switchers are cooled down by a gentle N_2 blow from the SCB.

hand, is cooled down by conduction, being in direct contact with the support and cooling block (SCB, Figure 3.14a) [53].

The SCB is a 3D printed stainless steel structure that allow for the mounting of the EOS regions of the PXD ladders, providing the mechanical support and cooling of the PXD. In order to reduce the material budget of the PXD, these massive structures are kept outside of the acceptance region.

As seen in Figure 3.15, the SCBs are placed head to head, supporting the EOS at both extremes of the DEPFET ladder. The outer layer is screwed in the exterior of the cylinder formed by the SCBs, while the inner layer is screwed to the interior of the cylinder, inside the SCBs. The SCB is designed so that the mounted ladders overlap their balconies with the sensitive areas of the adjacent ladder (see Figure 3.14b), ensuring that hits can be detected in the full acceptance

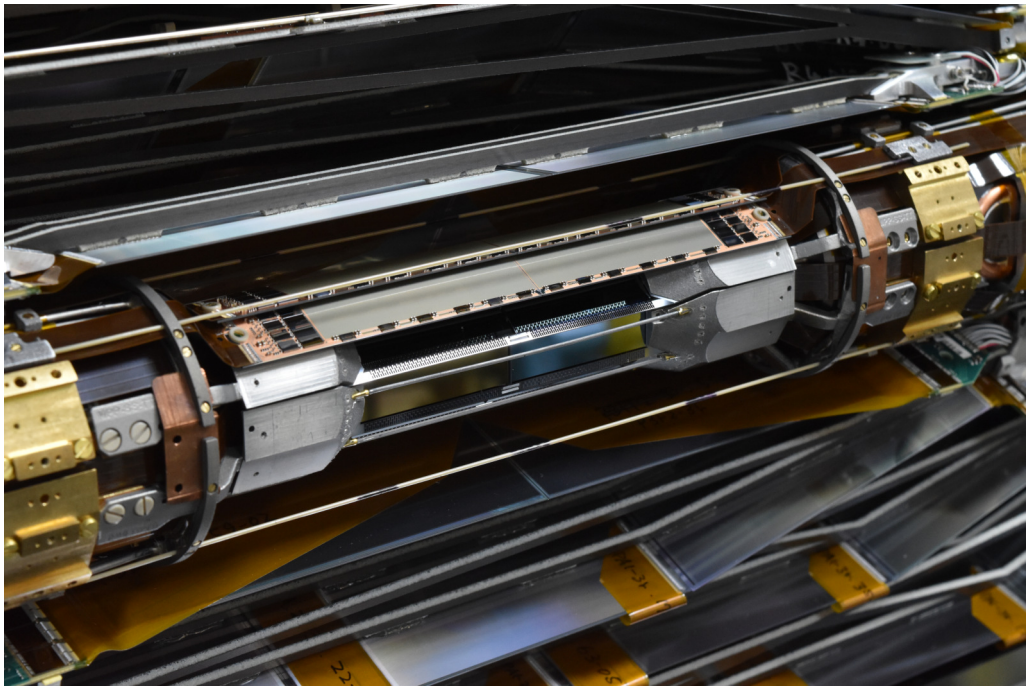

Fig. 3.15 Photograph of the de-scoped PXD installed in September 2018 for the Phase 3 of the Belle II experiment [54].

region. Given that the PXD ladders have a small insensitive area in the joint between the two modules, the inner and outer layers are displaced by 5 mm along the beampipe direction, so that at least one of the layers is able to register a track that travels through a glue joint.

Bi-phase CO_2 is circulated inside the SCBs through a series of pipes, keeping them at $-20 \sim 25°C$, and converting the SCBs into thermal reservoirs that evacuate most of the generated heat. Given the low surface temperatures in the SCBs surface, to avoid condensation, the whole VXD is enclosed in a carbon fiber cylinder that isolates the system from the CDC, creating a cold dry volume.

Chapter 4

Quality control in the PXD production

The PXD production is a complex process, involving several stages. In this Chapter the steps to produce the DEPFET modules will be summarized, emphasizing on the quality control tests performed prior to the final assembly.

These quality control tests are part of the IFIC team contribution to the DEPFET Collaboration in the building of the Belle II PXD. The contribution started with the design and production of the probe card (and its setup), and the outline of the testing protocol by the previous PhD student, Marçà Boronat [55]; and it concludes with the comissioning of the final testing protocol and the implementation of the protocol in the PXD mass production performed as part of this thesis.

First, the experimental setup and the testing protocol will be introduced. Then, the results of the testing campaigns will be examined, highlighting the yield improvement in the production due to early detection of hardware failures. To conclude the Chapter, a summary of the results with the lessons learned over the PXD production will be discussed.

4.1 PXD production

The assembly of the PXD modules [35] starts with the processing of the DEPFET structures in a silicon wafer. A summarized scheme of the wafer production is depicted in Figure 4.1.

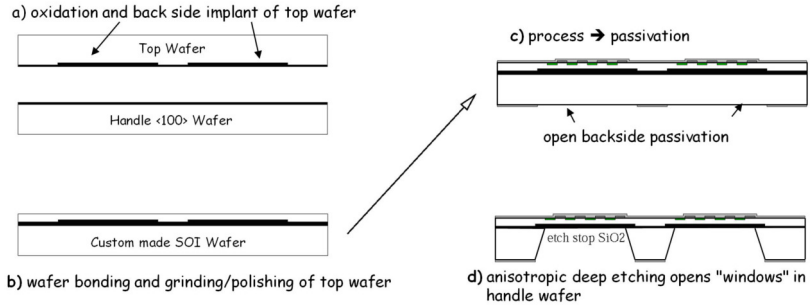

Fig. 4.1 Basic steps involved in the thinning of DEPFET sensors at the wafer level [35].

The first step consists on the implantation of the p^+ contacts on the backside of a detector grade silicon wafer called the *top wafer*. After that, the wafer is bonded to a second silicon wafer, the *handle wafer*. Once both wafers are bonded, the top wafer is polished and thinned down to the required 75 µm. Then, the DEPFET structures and different metal layers are processed on the top wafer. A summary of the steps involved in the processing of these structures include:

- Thermal oxidation of the gate and cleargate oxides.
- Implantation of the n-type structures of the buried channel.
- Processing of the poly[1] layer 1 for the cleargate.
- Oxidation to insulate the polylayer 1.
- Implantations for the internal gate (n-type), clear contact (n-type) and clear shield (p-type).

[1]Polycristalline silicon. Due to its increased conductivity, can act as the metal in the gate of a MOSFET.

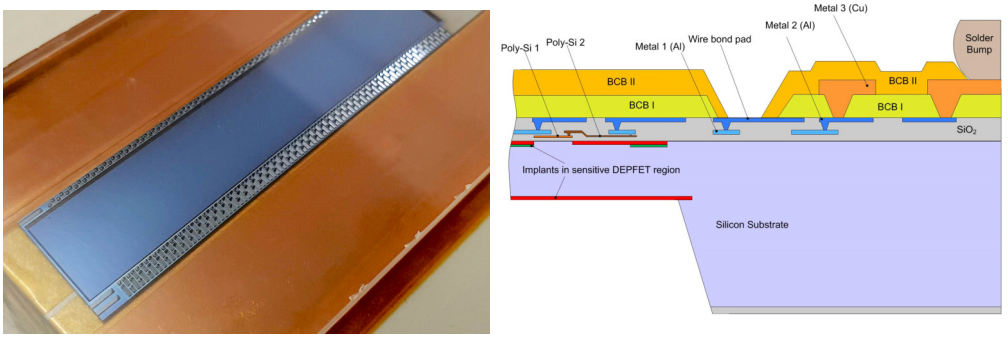

(a) Backside of a thinned module. **(b)** Scheme of the metal system [35].

Fig. 4.2 Photograph of the backside of a PXD module (in the left), and depiction of the metal and passivation layers in a module (in the right).

- Processing of the poly layer 2 for the DEPFET external gate.
- Implantations for the source and drain contacts (p-type).
- Oxidation to insulate the gates from the metal layer 1.
- Processing of the metal layer 1 (Al) to route the control lines for clear, gate and source.
- Oxidation to insulate the metal layer 1 from the metal layer 2.
- Processing of the metal layer 2 (Al) to route the drain lines and the source stitch.
- Testing of the pixel yields at the wafer level with the ATG[2] flying probe.
- Dielectric BCB[3] passivation to insulate metal layer 2 from metal layer 3.

Subsequently, the backside is thinned down by means of deep anisotropic etching of the handle wafer, leaving the sensor area completely exposed, supported by a semi-hollowed out thick frame (see Figure 4.2a). Then, the metal layer 3

[2]ATG Luther & Maelzer GmbH is the manufacturer of the flying probe test system.
[3]The benzocyclobutene is a dielectric polymer commonly used for passivation in microelectronics.

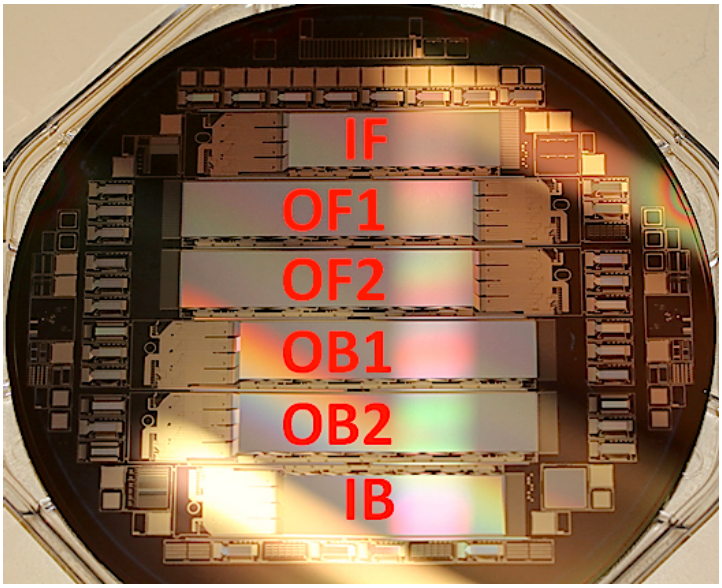

Fig. 4.3 PXD silicon wafer hosting six modules alongside a series of test structures [56].

(Cu) is processed in order to provide the under-bump metallization (UBM) for the ASICs and surface mounted devices (SMDs), and the solder pad for the Kapton cable. Last, the second dielectric BCB passivation is deposited, to protect the module and act as a solder stop, concluding the wafer production. A detailed view of the metal and passivation layers can be seen in Figure 4.2b.

As seen in Figure 4.3, each of the wafers hosts six PXD modules and some test structures. By cutting the wafer, a total of six modules in four different geometrical configurations[4] are retrieved: one inner forward (IF), one inner backward (IB), two outer forward (OF) and two outer backward (OB). These are named by the number and its position, i.e. the module W09_IB in Figure 4.5 is the IB module from the ninth production wafer.

To finalize the module assembly, the ASICs and SMDs are bump bonded onto the module. To do so, solder bumps are placed in the metal pads of the ASICs,

[4]As the ladders are split in two modules glued face to face, the backward module must be a mirrored version of the forward module. Given that the length of the ladders is different for the inner and outer layer, a total of four geometrical types of modules have to be manufactured.

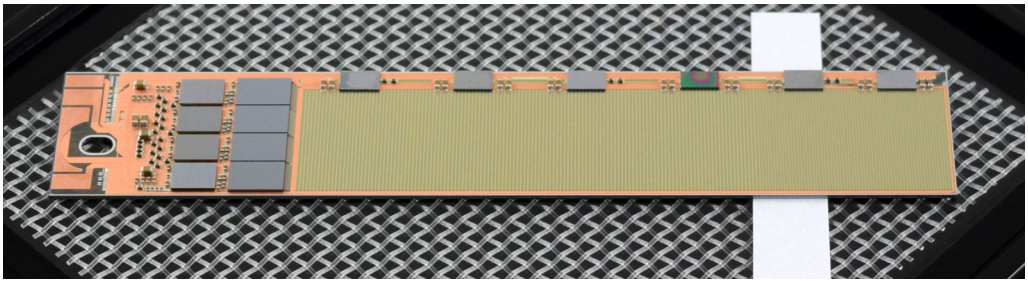

Fig. 4.4 PXD outer forward module after ASIC flip chip and SMD bump bonding.

then, these are flipped and placed on top of their under-bump metallization pads in the module, where a reflow melts the solder bump, effectively bump bonding the ASIC to the module. Once the ASICs are assembled, around 100 SMDs are placed in the module by means of depositing the solder paste on the UBM, placing the SMD and doing a reflow. At this point, the modules are completely assembled (see Figure 4.4) and ready to be operated.

Before continuing with the assembly of the module a test of its basic functionality is performed. A probe card is used to substitute the Kapton cable as the interface between the module and the services. If the module does not pass the test, an attempt to recover the module is performed by reworking the faulty part.

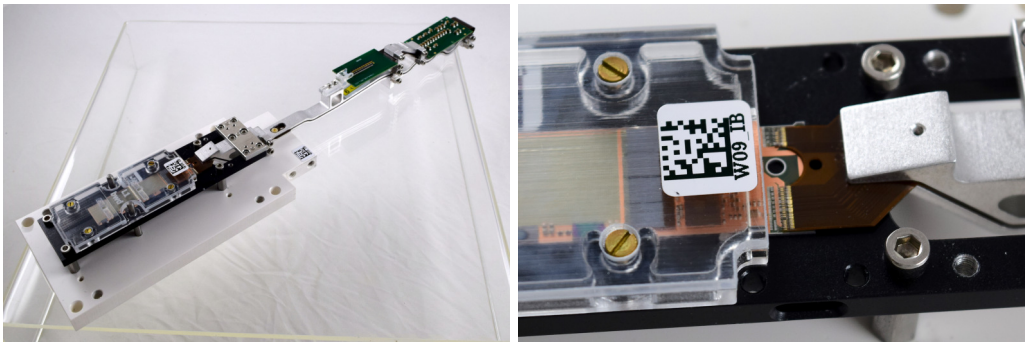

(a) PXD module with the Kapton attached. **(b)** Kapton cable attachment closeup.

Fig. 4.5 W09_IB module with the Kapton cable attached, ready to be characterized and assembled into a PXD ladder.

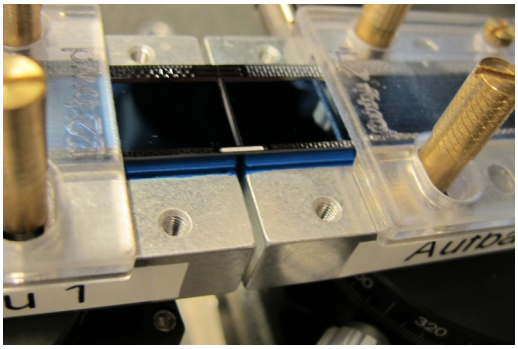

Fig. 4.6 Two PXD modules, a forward and a backward module, are glued together into a ladder [35]. Ceramic inserts in the backside ensure the alignment and reinforce the joint.

If the module does pass the test, then the Kapton cable is attached to it. First, the back of the cable is soldered onto the big copper pads that carry the highest currents. Then, the contacts from the top of the Kapton cable and the contact pads in the module are bridged via wire bonding. A finalized module with the Kapton attached and a closeup of the wire bonding can be seen in Figure 4.5.

Once finalized, the module is sent to one of the institutes participating in the mass testing campaign, where the module is characterized and optimized for operation. This procedure includes an optimization of all the ASICS and its interconnections, a calibration of the ADCs, an optimization of the pedestal map, and a radioactive source scan to optimize the DEPFET matrix voltages. After the mass testing, similar performing modules are glued together forming a ladder of a given quality. The process is depicted in Figure 4.6.

Finally, six outer layer and four inner layer ladders are mounted into the SCBs (see Figure 3.14a) forming half of the detector (known as the *half shell*). To complete the PXD, two half shells are assembled and mounted onto the beampipe as seen in Figure 3.15.

4.2 Probe card testing

As it was discussed in the previous section, one of the crucial steps on the module production is the bump bonding of the SMDs and flip chip of the ASICs in the module. Around 600 bumps are used to bond the Switchers, 1700 to bond the DCDs, 1200 for the DHPs and around 200 for the SMDs in each module. Totaling to around 3700 bumps in the module, entailing a high number of possible points of failure.

To check for these, the most straightforward way is to characterize and optimize the module, ensuring that its performs adequately. If a faulty chip is spotted, the module might be reworked by removing the failing component and repeating the bonding process.

In order to perform the rework, the Kapton cable has to be detached from the module, as it greatly compromises the handling of the module, making impossible the removal and re-attachment of the offending component. Removing the Kapton cable might be problematic though, as it endures a high risk of ripping apart the contact pads when the wire bonds are removed, rendering the module unusable.

These risks can be avoided by operating the module before the Kapton cable is attached. The solution is to test the module using a *probe card*, interfacing the module with its services. Thus, after SMD attachment, all the modules endure the probe card test [55] consisting on

- Sanity checks of the power consumption for all the power nets in the module.
- Configuration of the ASICs through the JTAG interface. Checks of the JTAG chain integrity by reading registers with a known value (such as the IDCODE of the ASICs).
- Testing of the logic blocks of the different ASICs through a boundary scan test [57]. To perform this tests, small circuits are implemented around the digital connections (called the *boundary scan register cells*) in the ASICs designs. These cells are transparent to the regular operation of the chip,

but can be addressed through the JTAG interface. During the test, the cells can check the interconnections between the logic in the ASICs, by means of feeding a given state from one cell and retrieving the expected response in the following cell.

- Basic operation of the module such as the successful transmission of data through the High Speed Links and obtaining the sensor's pedestals.

4.2.1 Probe station setup

The probe card testing was performed in a permanent setup at the clean room of the Halbleiterlabor (HLL) of the Max Planck Society at the Siemens campus in Neuperlach, Munich. The setup is shown in Figure 4.7.

The central piece of the setup is the probe card, which is anchored to the probe station with the help of custom designed rails. Under the probe card, the chuck hosts the cooling block, where the modules can be positioned and secured by toggling the vacuum switch[5]. Cool water circulates inside the cooling block, converting it in a thermal reservoir that removes the heat of the module once in operation.

Three micrometric screws allow for the correct positioning of the module respect to the needle spider. The X and Y screws translates the chuck respect the probe card, while the third screw rotates the chuck in the XY plane. A fourth screw, adjusts the elevation of the probe card respect to the station.

The probe card (Figure 4.8a) provides connectors for the Glenair, RJ-45 and InfiniBand cables; used to power and control the module, and to transmit the data to the DAQ, respectively. The Glenair cable leads to a power breakout board where the power lanes are split into two low resistivity cables connected to the LMU PS. The InfiniBand and RJ-45 cables are connected to the JTAG breakout

[5]The modules are previously placed on a Parylene coated aluminum jig -the *base jig*- that can be screwed into the cooling block. Both the base jig and the cooling block are machined so that the vacuum coming from the chuck can make its way through to the balcony and the EOS in the module, keeping the module fixed in place.

board, where a XJLink2 controller is able to perform a boundary scan of the module's logic via the JTAG protocol. From the board, a second set of InfiniBand and RJ-45 cables carry the signals up to a DHE card with the laboratory firmware. With this firmware, the DHE replaces the entire DHH system: it addresses the system through the slow control, triggers the module and receives the incoming data from the DHPs.

To interface the power supply and the DHE, a Scientific Linux 7 laboratory PC -the *pxdtest6*- is employed. The PC hosts the IOC servers that control with the different services; it also acts as the DAQ, processing and storing the incoming data from the DHE; and, it provides the graphical interface to control the IOCs through the Control System Studio program. Another PC, a Windows laptop,

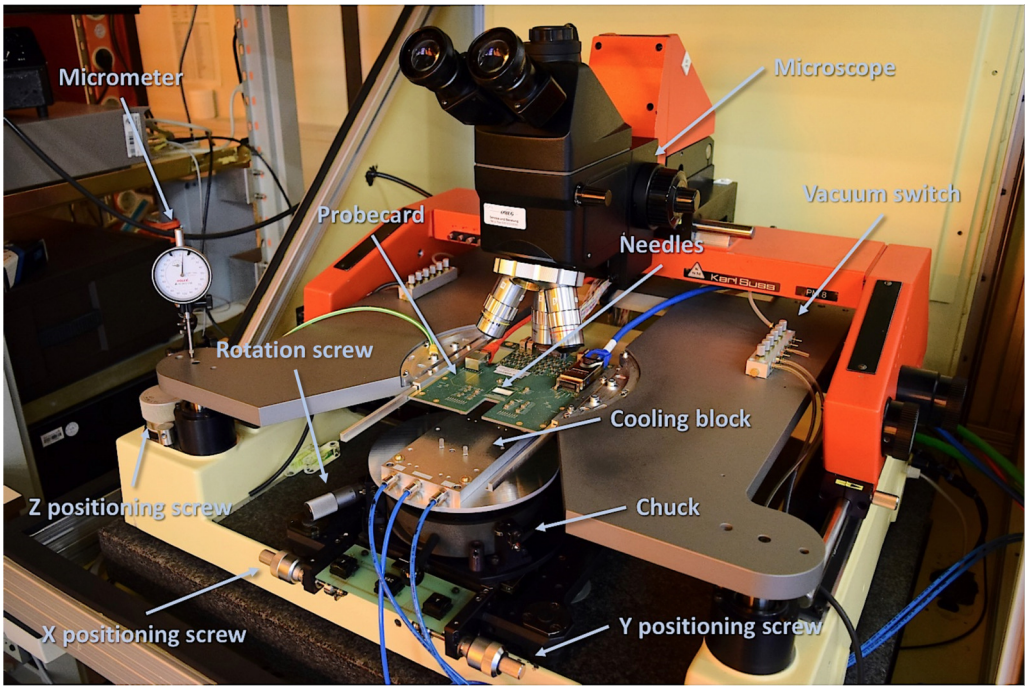

Fig. 4.7 Probe station at the clean room of the HLL. To perform the tests, the module is positioned in the cooling block and secured with vacuum. With the help of the microscope, the pads in the module are aligned with the needles in the probe card by moving the chuck in XY plane. Then, using the micrometer, a 50 µm touchdown is performed.

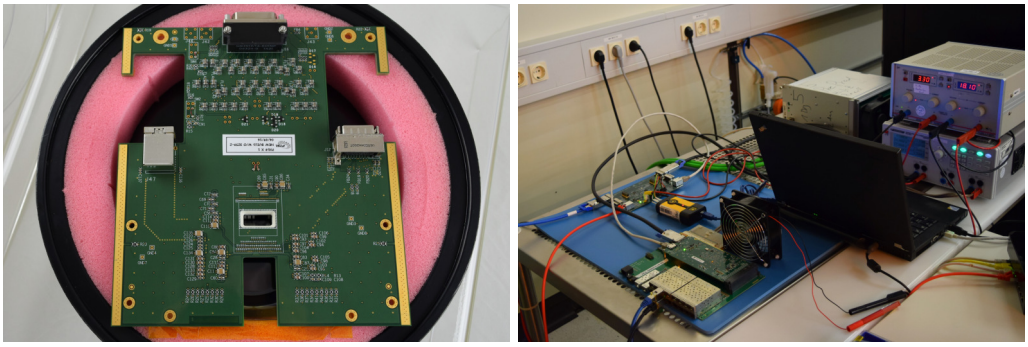

(a) Probe card. **(b)** Services.

Fig. 4.8 Probe card with the RJ45, Glenair and InfiniBand connectors in that order (in the left picture) used to interface the module to the services (in the right picture).

is also employed to address the XJLink 2 controller through the XJDeveloper program, used to perform the boundary scan in the module.

The probe card consists on a passive PCB hosting a needle spider under its vision hole, and the Glenair, RJ-45 and InfiniBand connectors. The basic functionality of the PCB is to route the traces from the connectors to the correct needles in the spider, in order to successfully address the module.

Two major considerations were taken into account in the PCB design: to sense the voltages before the needles instead of the module, preventing possible overvoltage surges due to a bad contact of the sense lines; and the minimization of the High Speed Links traces, keeping at a minimum the distortion of the signals[6]. Also, the PCB provides the grounding for the module, shorting the analog and digital ground nets in the module and providing a contact point to attach a ground cable.

In the middle bottom of the PCB is the Cantilever probe, consisting on a epoxy ring hosting the needle spider (see Figure 4.9a). The spider is formed by 110 L-shaped needles (see Figure 4.9b), each of which is able to carry a maximum current of 150 µA, and can be vertically bent up to 100 µm. In order to ensure

[6]The 1.6 Gbps link requires a high level of signal integrity. Too much distortion would prevent the DHE from establishing the link with the module.

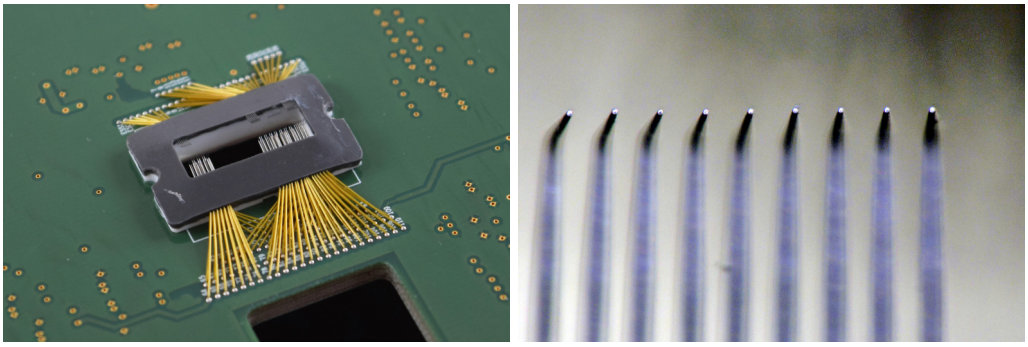

(a) Cantilever needle spider. **(b)** Needles closeup.

Fig. 4.9 The needle spider (in the left picture) is situated in the back of the probe card. The spider is formed by the L-shaped needles in the right picture.

a proper contact along the pads in the module, the needle spider is designed to have a planarity in the order of the 10 µm.

Given the current limitation, multiple needles are used to contact with the grounding and power pads. In total, 73 needles are used to contact the 59 aluminum pads in the module and 36 are used to contact the 4 high current copper pads.

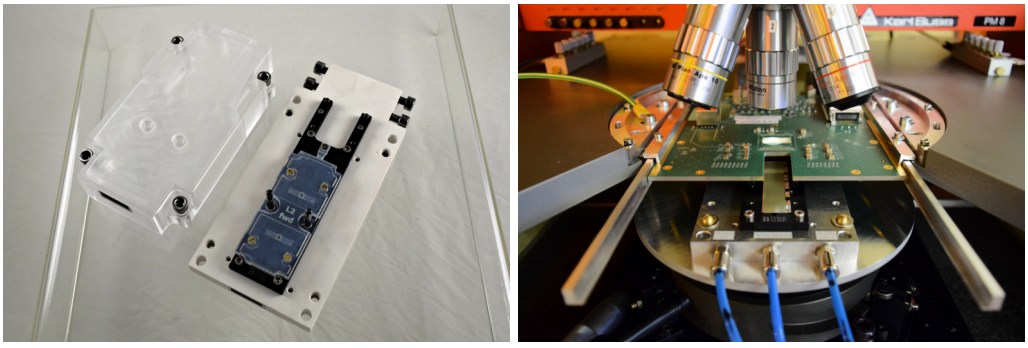

(a) Transport (white) and base (black) jigs. **(b)** Module at the probe station.

Fig. 4.10 In the left picture, the base jig (in black) used to host the modules during laboratory operation, and the transport jig (in white) used to storage the modules safely. In the right picture, a module secured into the probe station, ready to be tested.

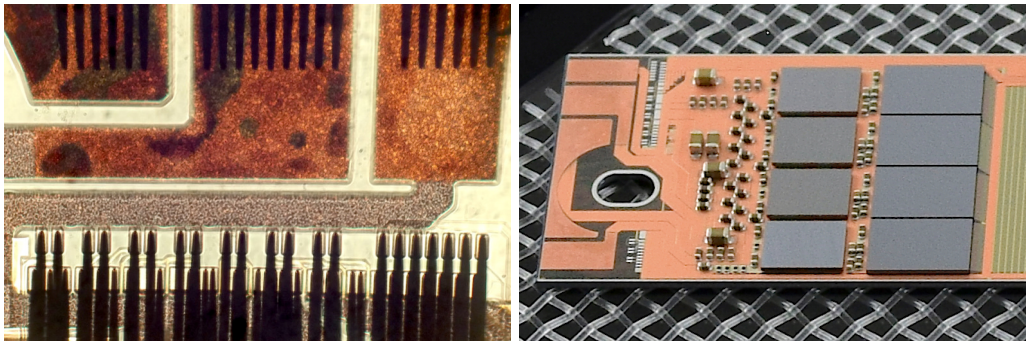

(a) Touchdown from tester's perspective. **(b)** End of stave closeup.

Fig. 4.11 Needle spider ready to perform the touchdown (in the left picture) contacting the pads in the EOS (in the right picture).

The four different types of the modules share the pad geometry by pairs, i.e. the IF and OB types share the pad layout, and so do the IB and OF types. To be able to perform the test on the four types of modules, two different probe cards -the model A for the IF/OB, and the model B for the IB/OF- were designed. Both the models and their needle spiders were designed in-house at IFIC by Daniel Esperante and Marçà Boronat. More details on the probe card design and schemes of the spider can be consulted at [55].

To perform the test, first, the module is retrieved from the Gel-Pak box (as the one in Figure 4.4) and placed into the Parylene coated aluminum base jig[7] (see Figure 4.10a). Then, the jig is screwed to the cooling block and the vacuum is switched on, fixing the module to the base jig. At this point, the module is completely secured at the probe station (see Figure 4.10b) and the touchdown may be performed.

In order to perform the touchdown, first the probe card and the module have to be aligned. With the help of the microscope, the projection of the needle spider into the module can be seen. Using the positioning screws in the chuck, the module is aligned with the probe card by superimposing the needles to the

[7]The base jig is machined in aluminum to ensure a great heat exchange capacity with the module. The Parylene coating provides electrical insulation between the jig and the module.

landing pads, as seen in Figure 4.11a. Then, using the Z positioning screw, the probe card slowly approaches the module until the tester observes the first needle bending, indicating the contact with the pad. That point, where the first needle touches the module, is taken as the touchdown reference.

The tester then continues approaching the module to make contact with the rest of the needles, applying a small safety margin to ensure the correct contact of all the needles. The final distance between the module and the probe card minus the touchdown reference is referred as the *overtravel*. The application of a small overtravel can cause stability problems, as some needles might be in loose contact with the module. Likewise, applying a huge overtravel might overbent the needles and damage the pads in the modules. Given that the maximum bent for the needles is in the order of 100 µm, and that the planarity of the spider is in the order of 10 µm, it was decided to target a 50 µm overtravel.

One of the biggest hitches encountered when performing the touchdown is having a tilt between the spider and the module. If the tilt is big enough, it could happen that the first needle is already applying a 50 µm overtravel while the needles in the opposite side of the spider are not yet touching the module. When this happens, the touchdown must be stopped and the probe card tilt must be corrected to ensure that all the needles can make contact. The marks left by a successful touchdown, touching all the pads with a 50 µm overtravel can be seen in Figure 4.12.

4.2.2 Testing protocol

Each one of the produced modules undergoes the probe card test right after the SMD assembly to qualify them for the Kapton cable attachment. The protocol consists in a series of sequential steps increasingly testing the different parts of the module. If at any point one of the steps results in a show stopper, then the faulty component is noted down and the module is sent for rework. The complete test is comprised of the following steps:

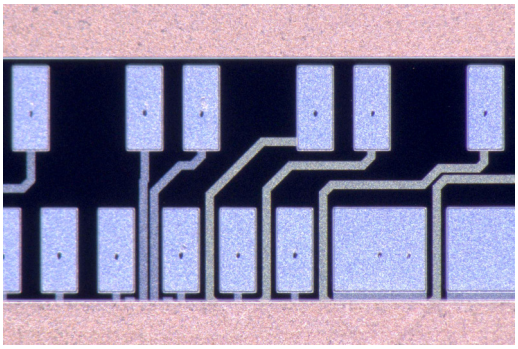

Fig. 4.12 Microscope image of the landing pads after a 50 µm overtravel touchdown. The marks in the middle of the pads are the result of the contact with the needle spider. These pads have a typical dimensions of 100 × 300 µm^2.

Module preparation The module is retrieved from the Gel-Pak boxes and inspected for possible flaws in the pads area. Then, the modules are placed in the base jig and installed into the cooling block at the probe station.

Touchdown Once the module is fixed and secured the touchdown is performed, aiming for 50 µm of overtravel. This is the most crucial step of the procedure, if the contact between the needles is not good enough, the rest of the protocol won't be possible to realize.

Digital power After the touchdown, the digital parts of the ASICs are powered up one by one, observing the power consumption through the control panel of the LMU PS (as in Figure 4.13). In the event of a power net having values out of range, the module is stopped and the involved ASIC is marked as faulty.

JTAG interface Once the ASICs are powered, these are configured through the JTAG interface. Configurating these lead to small changes in the power consumptions that are monitored by the tester. Furthermore, the JTAG chain's integrity is tested by writing and reading back some registers in the different ASICs, like their hardcoded IDCODEs. Then, the Switchers sequence is uploaded to the DHP memory closest to the balcony. And, finally the 192 registers that conform the sequence are read back to ensure

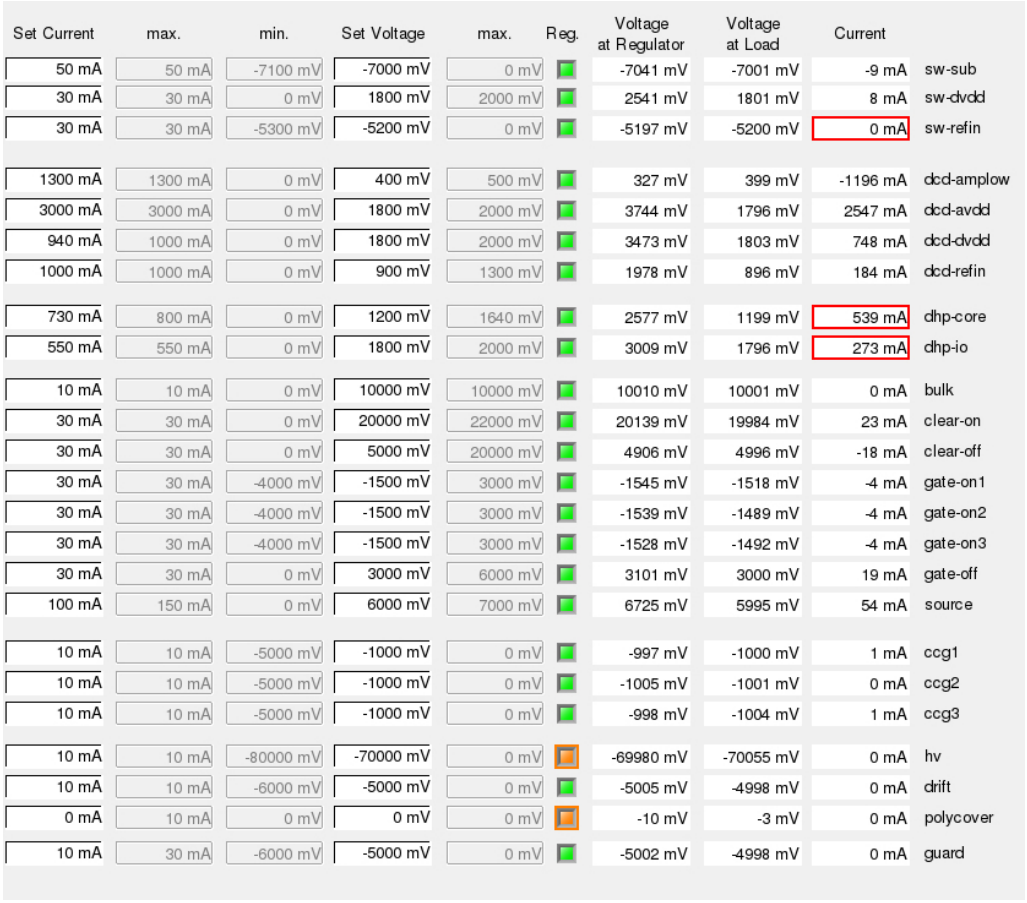

Set Current	max.	min.	Set Voltage	max.	Reg.	Voltage at Regulator	Voltage at Load	Current	
50 mA	50 mA	-7100 mV	-7000 mV	0 mV		-7041 mV	-7001 mV	-9 mA	sw-sub
30 mA	30 mA	0 mV	1800 mV	2000 mV		2541 mV	1801 mV	8 mA	sw-dvdd
30 mA	30 mA	-5300 mV	-5200 mV	0 mV		-5197 mV	-5200 mV	0 mA	sw-refin
1300 mA	1300 mA	0 mV	400 mV	500 mV		327 mV	399 mV	-1196 mA	dcd-amplow
3000 mA	3000 mA	0 mV	1800 mV	2000 mV		3744 mV	1796 mV	2547 mA	dcd-avdd
940 mA	1000 mA	0 mV	1800 mV	2000 mV		3473 mV	1803 mV	748 mA	dcd-dvdd
1000 mA	1000 mA	0 mV	900 mV	1300 mV		1978 mV	896 mV	184 mA	dcd-refin
730 mA	800 mA	0 mV	1200 mV	1640 mV		2577 mV	1199 mV	539 mA	dhp-core
550 mA	550 mA	0 mV	1800 mV	2000 mV		3009 mV	1796 mV	273 mA	dhp-io
10 mA	10 mA	0 mV	10000 mV	10000 mV		10010 mV	10001 mV	0 mA	bulk
30 mA	30 mA	0 mV	20000 mV	22000 mV		20139 mV	19984 mV	23 mA	clear-on
30 mA	30 mA	0 mV	5000 mV	20000 mV		4906 mV	4996 mV	-18 mA	clear-off
30 mA	30 mA	-4000 mV	-1500 mV	3000 mV		-1545 mV	-1518 mV	-4 mA	gate-on1
30 mA	30 mA	-4000 mV	-1500 mV	3000 mV		-1539 mV	-1489 mV	-4 mA	gate-on2
30 mA	30 mA	-4000 mV	-1500 mV	3000 mV		-1528 mV	-1492 mV	-4 mA	gate-on3
30 mA	30 mA	0 mV	3000 mV	6000 mV		3101 mV	3000 mV	19 mA	gate-off
100 mA	150 mA	0 mV	6000 mV	7000 mV		6725 mV	5995 mV	54 mA	source
10 mA	10 mA	-5000 mV	-1000 mV	0 mV		-997 mV	-1000 mV	1 mA	ccg1
10 mA	10 mA	-5000 mV	-1000 mV	0 mV		-1005 mV	-1001 mV	0 mA	ccg2
10 mA	10 mA	-5000 mV	-1000 mV	0 mV		-998 mV	-1004 mV	1 mA	ccg3
10 mA	10 mA	-80000 mV	-70000 mV	0 mV		-69980 mV	-70055 mV	0 mA	hv
10 mA	10 mA	-6000 mV	-5000 mV	0 mV		-5005 mV	-4998 mV	0 mA	drift
0 mA	10 mA	0 mV	0 mV	0 mV		-10 mV	-3 mV	0 mA	polycover
10 mA	30 mA	-6000 mV	-5000 mV	0 mV		-5002 mV	-4998 mV	0 mA	guard

Fig. 4.13 Screenshot of the LMU PS control panel in the Control System Studio while successfully operating a module. The control panel is used to monitor the power consumption of the nets in the Digital power, Analog power and Sensor power tests.

that JTAG write and read commands are working properly. In the case that the JTAG chain is in some way not behaving as expected, the test is repeated shorting the chain to try to spot the offending ASIC.

Boundary scan If the JTAG interface works correctly, then the boundary scan can be performed. Using the XJLink2 controller the logic blocks of all the

ASICs are tested. In the case of a boundary cell failing, the test will point out the failing component [57].

High Speed Links Establishing the HSL is the most time consuming part of the test. These links require great signal integrity and are really sensible to the touchdown condition. To increase our chance of success, the CML drivers are operated at half their nominal rate and at their minimum clock speed. In these conditions the links can be obtained often by tinkering with the *bias*, *biasd* and *dly_sel* parameters. If the links cannot be established with these means, the touchdown may be repeated to try to get a better contact with the needles. Once the links are working reliably, the DCD test pattern is retrieved to ensure the correct data transmission. An example of the test pattern is available at Figure 4.14a.

Analog power First, the Switcher analog power nets are correctly biased, enabling the analog outputs of the Switchers. Then, the current limit of the

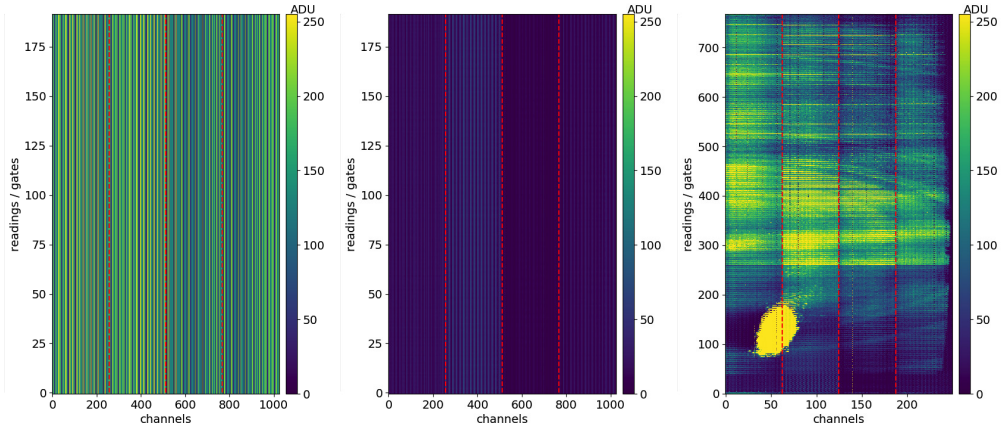

(a) DCD test pattern. **(b)** DCD pedestals. **(c)** Sensor pedestals.

Fig. 4.14 Pedestal maps of a module obtained during testing. In the left, the test pattern used to calibrate the DCD-DHP delays as part of the High Speed Links test; in the center, the pedestals with the sensor turned off as part of the Analog power test; and in the right, the pedestals of the module with the sensor turned on using a laser pointer to excite the DEPFET pixels, as part of the Pedestals test.

DCD analog block is increased in order to power up the ADCs. While switching on the ADCs, the power consumption of the *dcd-avdd* net is controlled through the control panel of the LMU PS. If the increase in the current consumption is within the designed range, a pedestal map of the module is taken, as in Figure 4.14b. A healthy DCD pedestal will show no signal at all, as the DEPFETs are off.

Sensor power If the system is stable enough, then the sensor voltages are sequentially biased, carefully observing the current consumption; with the exception of the *gate-on* voltages. If all the other voltages are within range, then the *gate-on* voltage is biased smoothly, while controlling the current increase in the *source* net[8]. For *gate-on* voltages in the order of -1.5 V, the expected *source* currents are in the order of 60 mA; in the case of -2.5 V, *source* goes up to 100-110 mA.

Pedestals Finally, a pedestal map of the module with the sensor on is taken. To ensure that pixels react to stimuli, successive pedestal maps are taken exciting different parts of the sensor with a laser pointer, producing a pedestal map as the one seen in Figure 4.14c. Obtaining these pedestals is the final objective of the test protocol, demonstrating that the module is fully working.

Module storage After the tests are over, the needle spider is separated from the module carefully, the vacuum is switched off, and the base jig is retrieved from the probe station, and secured into the transport jig. If the tests are successful, then the module is sent for Kapton attachment; if they are not, then it is sent to be reworked.

Report Once the module is stored away, a report is written and uploaded into the laboratory's ELOG[9]. The report includes the history of the different touchdowns performed, and a summary of the best results in the tests. An example is available in the Appendix A.

[8] Once the transistors are gated, the current from the source starts flowing to the drains.

[9] The ELOG is a web application used as a logbook for the different procedures at the laboratory.

Given the difficulty in achieving a stable HSL, the test is separated in two parts. The first part, the *basic tests*, checks the digital domain of the module through the Digital power, JTAG interface and Boundary scan tests. The second part, called the *extended tests*, may only be performed if a reliable and stable HSL connection is achieved. In that case, the data transfer, the analog part of the ASICs and the sensor response can be probed via the High Speed Links, Analog power, Sensor power and Pedestals tests. As not all the tests may be performed for all the modules, an **Overall** score is assigned to each module based on the results of the tests that could be performed.

4.2.3 Results

The testing protocol was applied to the different batches of PXD modules produced: the preproduction batch, used to qualify the production procedure; the phase 2 batch, used to build a detector demonstrator for the SuperKEKB accelerator commissioning; and the phase 3 batch, conceived to construct the full PXD.

The test results of each batch are summarized in Tables 4.1, 4.2, 4.3 and 4.4. In these, each of the subtests in the protocol are evaluated, and an overall score is assigned for each module. The possible outcomes for the subtests are:

✓ The test passed.

✗ The test failed. This failure prevents the system from being operated successfully. The module should not be sent for Kapton attachment. Instead, the failure must be investigated in order to repair the module.

● The result of the test was inconclusive. Either multiple measurements yield different results, pointing to contact instabilities; or it is not possible to distinguish in between a failing component or a bad touchdown. In these cases, the touchdown is repeated to try to get a conclusive result.

As seen in Appendix A, in a typical testing session, the full protocol can not be directly performed; and a mix of increasing the overtravel and repeating the

touchdown has to be used to finish the protocol. In some cases, when too many days have been spent, or too many touchdowns have been performed on a module, the module is stored away and the stuck test is marked as inconclusive. In order to assess this cases, a policy to set the overall outcome is conceived:

- If the *basic* or *extended tests* fail: the module is marked as defective, and set to be investigated and repaired.
- If the *basic tests* are inconclusive: the overall result is inconclusive, and the Kapton cable is attached, as no show stopper was spotted.
- If the *basic tests* pass and the *extended tests* are inconclusive, or, all the tests pass: the module is marked as working and sent for Kapton cable attachment.

Preproduction

The preproduction batch consisted in a series of modules manufactured to qualify the production process. At the time, only the first design of the probe card was available -the probe card A-, so only the IF and OB modules could be tested. The summary of the results obtained are gathered in Table 4.1.

Table 4.1 Test results of the preproduction batch and the reworked modules.

Module	PD	JTAG	BS	HSL	PA	PS	S	Overall
W31_IF	✓	✓	✓	✓	✓	✓	✗	✗
W36_IF	✓	✓	✓	✓	✓	✓	✓	✓
W31_IB (r/ak)	✗	✓	✓	✓				✗
W31_OB1	✓	✗						✗
W31_OB1 (r/ak)	✓	✓	✓	✓	✓	✗	✗	✗
W31_OB2	✓	✗						✗

(r/ak) reworked module after Kapton attachment
PD, PA, PS digital, analog and sensor power tests
S sensor pedestals and signal response
✓, ✗, ● passed, failed and inconclusive test
JTAG JTAG interface test
BS boundary scan
HSL High Speed Links test

Using the W36_IF module the probe card testing and the protocol was commissioned. Fortunately, the module was well behaved and could be fully operated in most touchdowns, allowing to qualify the viability of the probe card testing.

Nevertheless, the other three IF or OB modules produced did not pass the test. Both the W31_OB1 and W31_OB2 showed problems with the Switchers. As soon as these were included in the JTAG chain, the JTAG interface would not work. As for the W31_IF, the module could be operated to the point of obtaining sensor pedestals, but these showed three dead Switchers, rendering half of the pixels inoperable. Out of the four modules in the preproduction batch that were tested, three of them were faulty due to Switcher related problems.

At that point, it was clear that there was some problem in either the Switcher production, or the bump bonding to the module. To further investigate the problem a more stable platform than the probe card was needed, reason why the modules were Kapton attached. Except the W36_IF, that was kept as a guinea pig module, used as reference to re-qualify the probe card if needed.

The behavior observed in the test stands after the Kapton attachment was identical to what was observed in the probe card testing. As the operation of the modules did not yield information about the problem, it was decided to rip apart the Switchers of the W31_OB2 module. As seen in Figure 4.15, the Switcher bumps in the central part of the balcony did not get to wet the pads explaining the observed behavior. It seems that the reflow temperature was not reached in the middle of the balcony due to a bad contact with the heat plate, caused by a mix of the bowing of the module and a reduced contact area due to the perforations in the balcony.

To fix the problem it was proposed to increase the reflow temperature in the flip chip step. The solution was tested with the W31_OB2, repeating the flip chip procedure and removing the Switchers afterwards. In this second flip chip, the bumps wetted all the pads, and the Switchers were correctly bonded, solving

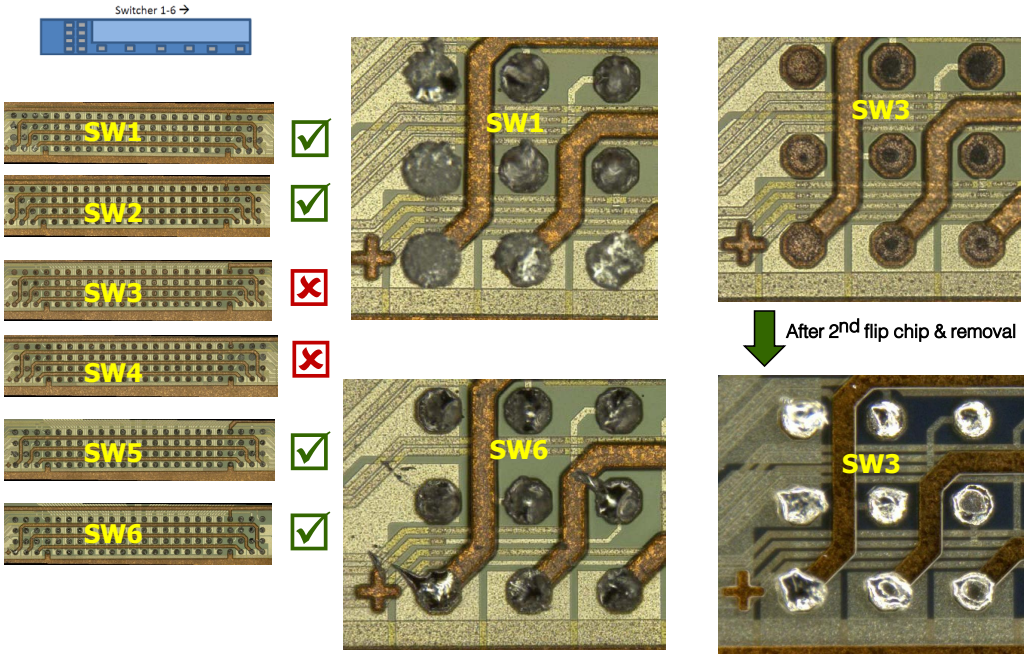

Fig. 4.15 To inspect the quality of the Switcher bonding, these were removed from the W31_OB2 module. It was observed that the Switchers in the central part of the module were not correctly bump bonded. A second flip chip was performed with an increased reflow temperature, successfully bonding all the Switchers to the module [58].

the problem. It was then decided to permanently increase the reflow temperature for all the modules produced.

After the preproduction, the second design of the probe card -the probe card B- was finalized and produced. To qualify this new probe card and obtain more hands-on experience with the setup, a batch of 12 EMCMs[10] was produced.

[10]Electrically active Multi-Chip Module. These are electrical prototypes of the PXD modules without a sensor. The EMCMs are populated with the same ASICs used in a real module, and can be operated as such.

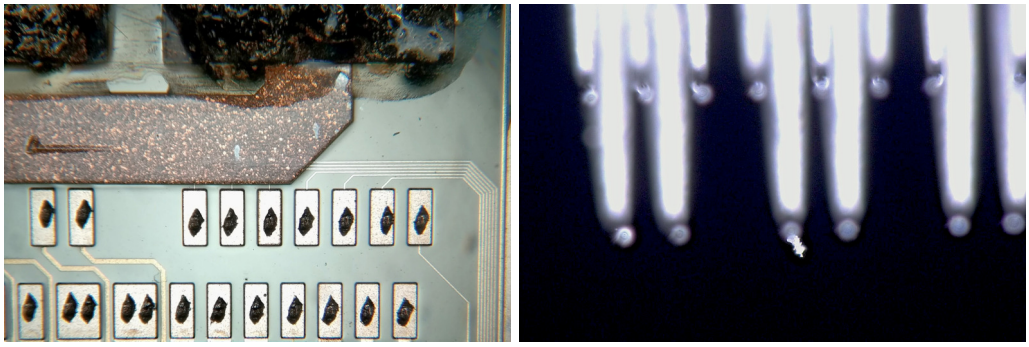

(a) Pad damage after Kapton removal. **(b)** Eroded needle tips.

Fig. 4.16 State of the probe card needles (in the right picture), after contacting the damaged pads from the Kapton detached modules (in the left picture).

The batch consisted on three modules of each type, six modules to operate with the probe card A, and the other six to qualify the probe card B. All of the 12 EMCMs were successfully operated, up to the High Speed Links test[11], correctly retrieving the test pattern for all of them. At this point, both probe cards and the testing protocol had been qualified and the setup was ready to receive the main PXD production.

While the new batches of modules were being produced, the W31_IB and the W31_OB1 preproduction modules had been reworked. Unfortunately, these modules had been Kapton attached to study the faulty Switchers behavior. The Kapton cable was disassembled from the modules by ripping the wire bonds, and detaching the cable from the copper pads. Then, the Switchers were removed and a second flip chip with an increased temperature was performed.

As seen in Figure 4.16a, the pad surface on these modules had been greatly damaged by the Kapton removal procedure. Nevertheless, the probe card testing was performed, trying to perform the touchdowns in the healthiest part of the pads. The results of the tests showed that the W31_IB had a short in the *dcd-dvdd* power net, rendering the DCDs unusable; while the W31_OB1 could be fully

[11] As there is no sensor in these prototypes, there was no reason to proceed further with the testing protocol.

operated, showing a high ohmic short between the *clear-on* and *clear-off* nets, and a dead Switcher, reducing the sensor pixel yield by a sixth.

As a consequence of performing the touchdown on these damaged pads the needles of both probe cards suffered a permanent deformation. As seen in Figure 4.16b, the needles planarity was affected, the tips were unsharpened, and some of the needles picked dirt from the pads.

An effort was made to try to recover the shape of the needles by using resharpening contact pads from different manufacturers. This helped to remove part of the dirt in the needles, and mildly sharpen the needles. Nevertheless, this method did not fix the deformation of the needle spider.

Phase 2 modules

The phase 2 batch consisted in four complete ladders, two modules of each type for the construction of the BEAST II detector. BEAST II stands for Beam Exorcism for A STable experiment II, a background detector for the commissioning of the Belle II experiment. Its purpose is understanding the beam backgrounds in detail to determine whether it is safe to install the VXD [59].

Out of the eight produced modules, two were unfortunately destroyed in transport when coming back from flip chip. The remaining six modules were tested, and the results are shown in Table 4.2.

In the case of the W37_IF module, no HSL was ever achieved in any of the touchdowns. W37_OF1 had even more unstable touchdowns, making impossible to even pass the boundary scan. As no show stopper was detected in any of these, both were sent forward for Kapton attachment. As for the faulty modules:

- W38_IB: showed a high power consumption for the *sw-dvdd* net, and the JTAG interface would not work if the Switchers were included in the chain. A detailed observation of the Switchers under the x-ray machine showed that one of the Switchers was rotated by 180 degrees. By removing the Switcher and bumping correctly a new one the module was repaired. The test was

Table 4.2 Test results of the phase 2 batch and the reworked module.

Module	PD	JTAG	BS	HSL	PA	PS	S	Overall
W37_IF	✓	✓	✓	●				✓
W40_IF	✓	✓	✓	✓	✓	✓	✓	✓
W38_IB	✗	✗						✗
W38_IB (r)	✓	✓	●	●				●
W37_OF1	✓	✓	●	●				●
W37_OB1	✓	✓	✓	✓	✓	✓	✓	✓
W38_OB1	✗	✗						✗

(r) reworked module
PD, PA, PS digital, analog and sensor power tests
S sensor pedestals and signal response
✓, ✗, ● passed, failed and inconclusive test
JTAG JTAG interface test
BS boundary scan
HSL High Speed Links test

repeated after the rework, but the same behavior as with the W37_OF1 module was observed. As no show stopper was spotted, the module was sent for Kapton attachment.

- W38_OB1: this module showed a short in between the *dhp-core* and *dhp-io* nets. It has not been possible to spot the faulty DHP, and it is yet to be reworked.

Due to the state of the needles after the tests on the Kapton removed modules from the preproduction batch it was really tricky to operate the modules from this batch. Achieving the High Speed Links was possible in only four of the six modules. Right after the testing campaign the probe cards were sent to PTSL[12] for a complete reshape of the needle spider, in order to recover the performance observed in the preproduction modules and EMCMs.

Phase 3 modules

The phase 3 batch consisted in the main production of the PXD. A total of thirty complete ladders, fifteen modules of each type were manufactured, enough to

[12]Probe Test Solutions Ltd., the manufacturer of the probe card.

build a PXD with a 50% contingency allowance. The results for the thirty forward and backward modules are shown in Tables 4.3 and 4.4 respectively.

As observed in the tables below, out of the 60 produced modules: 42 modules could be fully operated, obtaining the sensor pedestals and checking the matrix response; 12 of them passed the *basic test*, although the complete protocol could not be implemented due to instabilities in the touchdown; and 6 of them did not pass the test and were marked as faulty.

On the 12 modules with inconclusive results in the *extended tests*, the setup instabilities affected the measurements in different ways:

- W11_OF2: the consumption of the analog block of the DCD was out of range (in the low end). This could be explained by a high ohmic contact between the related pad and needle.
- W09_IB, and W32_OF2: the sensor power consumption values were out of range (in the low end). This could be explained by a high ohmic contact between the related pad and needle.
- W43_IB: even though the HSL between the DHP and the DHE could be established, no data could be retrieved from the module.
- W01_IB, W02_IB, W03_IB, W44_IB, W45_IB and W47_IB, W46_OF1 and W46_OF2: the HSL test passed, but the connection was latter lost in the successive tests, making impossible to complete the testing protocol for these.

As none of these modules showed any show stopper, they were marked as working and sent for Kapton cable attachment. As for the six faulty modules:

- W09_OB1, W43_OF1, W44_OF1 and W44_OF2: the *sw-dvdd* power net showed a high current consumption, and the JTAG interface would not function if the Switchers were included in the chain. Using a thermal camera, the faulty Switchers could be identified, as seen in Figure 4.17.

Table 4.3 Test results of the forward modules of the phase 3 batch.

Module	PD	JTAG	BS	HSL	PA	PS	Pedestals	Overall
W02_IF	✓	✓	✓	✓	✓	✓	✓	✓
W03_IF	✓	✓	✓	✓	✓	✓	✓	✓
W05_IF	✓	✓	✓	✓	✓	✓	✓	✓
W08_IF	✓	✓	✓	✓	✓	✓	✓	✓
W32_IF	✓	✓	✓	✓	✓	✓	✓	✓
W41_IF	✓	✓	✓	✓	✓	✓	✓	✓
W42_IF	✓	✓	✓	✓	✓	✓	✓	✓
W43_IF	✓	✓	✓	✓	✓	✓	✓	✓
W44_IF	✓	✓	✓	✓	✓	✓	✓	✓
W45_IF	✓	✓	✓	✓	✓	✓	✓	✓
W46_IF	✓	✓	✓	✓	✓	✓	✓	✓
W47_IF	✓	✓	✓	✓	✓	✓	✓	✓
W08_OF2	✓	✓	✓	✓	✓	✓	✓	✓
W09_OF1	✓	✓	✓	✓	✓	✓	✓	✓
W09_OF2	✓	✓	✗					✗
W11_OF1	✓	✓	✓	✓	✓	✓	✓	✓
W11_OF2	✓	✓	✓	✓	●			✓
W12_OF1	✓	✓	✓	✓	✓	✓	✓	✓
W32_OF1	✓	✓	✓	✓	✓	✓	✓	✓
W32_OF2	✓	✓	✓	✓	✓	●		✓
W33_OF1	✓	✓	✓	✓	✓	✓	✓	✓
W33_OF2	✓	✓	✓	✓	✓	✓	✓	✓
W41_OF1	✓	✓	✓	✓	✓	✓	✓	✓
W43_OF1	✗	✗	✗					✗
W44_OF1	✗	✗	✗					✗
W44_OF2	✗	✗	✗					✗
W45_OF1	✓	✓	✓	✓	✓	✓	✓	✓
W45_OF2	✗	✗	✗					✗
W46_OF1	✓	✓	✓	✓	✓	●		✓
W46_OF2	✓	✓	✓	✓	✓	●		✓

PD, PA, PS digital, analog and sensor power tests
BS boundary scan
S sensor pedestals and signal response
HSL High Speed Links test
✓, ✗, ● passed, failed and inconclusive test
JTAG JTAG interface test

Table 4.4 Test results of the backward modules of the phase 3 batch.

Module	PD	JTAG	BS	HSL	PA	PS	Pedestals	Overall
W01_IB	✓	✓	✓	✓				✓
W02_IB	✓	✓	✓	✓				✓
W03_IB	✓	✓	✓	✓				✓
W09_IB	✓	✓	✓	✓	✓	●		✓
W32_IB	✓	✓	✓	✓	✓	✓	✓	✓
W41_IB	✓	✓	✓	✓	✓	✓	✓	✓
W42_IB	✓	✓	✓	✓	✓	✓	✓	✓
W43_IB	✓	✓	✓	●				✓
W44_IB	✓	✓	✓	✓				✓
W45_IB	✓	✓	✓	✓				✓
W46_IB	✓	✓	✓	✓	✓	✓	✓	✓
W47_IB	✓	✓	✓	✓				✓
W03_OB1	✓	✓	✓	✓	✓	✓	✓	✓
W05_OB1	✓	✓	✓	✓	✓	✓	✓	✓
W06_OB1	✓	✓	✓	✓	✓	✓	✓	✓
W08_OB1	✓	✓	✓	✓	✓	✓	✓	✓
W08_OB2	✓	✓	✓	✓	✓	✓	✓	✓
W09_OB1	✗	✗	✗					✗
W09_OB2	✓	✓	✓	✓	✓	✓	✓	✓
W12_OB1	✓	✓	✓	✓	✓	✓	✓	✓
W12_OB2	✓	✓	✓	✓	✓	✓	✓	✓
W32_OB2	✓	✓	✓	✓	✓	✓	✓	✓
W33_OB1	✓	✓	✓	✓	✓	✓	✓	✓
W42_OB1	✓	✓	✓	✓	✓	✓	✓	✓
W42_OB2	✓	✓	✓	✓	✓	✓	✓	✓
W44_OB1	✓	✓	✓	✓	✓	✓	✓	✓
W44_OB2	✓	✓	✓	✓	✓	✓	✓	✓
W45_OB2	✓	✓	✓	✓	✓	✓	✓	✓
W46_OB1	✓	✓	✓	✓	✓	✓	✓	✓
W46_OB2	✓	✓	✓	✓	✓	✓	✓	✓

PD, PA, PS digital, analog and sensor power tests
S sensor pedestals and signal response
✓, ✗, ● passed, failed and inconclusive test
BS boundary scan
HSL High Speed Links test
JTAG JTAG interface test

  - W09_OB1: The second Switcher was identified as faulty. After exchanging it the module was Kapton attached and worked fine.
  - W43_OF1: The fourth Switcher was identified as faulty. After exchanging it the module was Kapton attached and worked fine.
  - W44_OF1: The module was broken in handling after performing the probe card test. There was no opportunity to repair it.
  - W44_OF2: The third Switcher was identified as faulty. After exchanging it the module was Kapton attached and a short was observed in the sixth Switcher, most probably due to the second reflow.

- W09_OF2: the boundary scan failed if the Switchers were included in the JTAG chain. The fifth Switcher was identified as faulty with the help of the thermal camera. After exchanging it the module was Kapton attached and worked fine.

- W45_OF2: the *dhp-core* power net power net showed a high current consumption. The third DHP was identified as faulty with the help of the thermal camera. After exchanging it the module was Kapton attached and worked fine.

Out of the six faulty modules, four could be successfully recovered, one was broken during handling, and one could not be recovered; resulting in a 96.7% production yield.

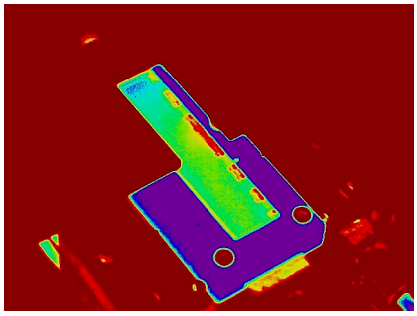

Fig. 4.17 Thermal picture of the W43_OF1 module in operation used to spot the faulty Switcher.

4.3 Conclusions and lessons learned

In this Chapter the quality assurance tests of the DEPFET-based Belle II Pixel Detector modules was introduced. As part of this thesis, the probe card testing was qualified for service with four preproduction modules and twelve electrical test modules. During the production commissioning, the probe card detected the Switcher related problems in the preproduction batch, proving a reliable tool for the quality control of the PXD module mass production.

As part of the mass production, the testing protocol was applied to a total of 66 final modules (6 for Belle II phase 2, and 60 for Belle II phase 3), of which 58 passed the test and 8 were marked as defective, resulting in an initial production yield of 88%. Thanks to the probe card, the faulty component in these modules could be identified: 6 of them had a faulty Switcher, and 2 had a faulty DHP. By removing the faulty component and repeating the flip chip process, 5 of these modules could be successfully repaired before the Kapton cable attachment, increasing the production yield to 96%.

The mass production of the PXD modules was a clear success. Bearing in mind that it included a 50% contingency allowance, and given the high production yield, enough modules were produced to populate the PXD while keeping a healthy stock of spares, as seen in Figure 4.18.

Over the 18 months that took probe card testing the knowledge over the system kept growing, learning some valuable lessons that helped improve the touchdown effectiveness. In particular, two aspects proved fundamental:

- The planarity of the needle spider respect to the module is key. Typically the tilt between both had to be corrected for each measurement, even though the spider planarity should not have changed, and the module topography was quite regular. There was though a pretty loose tolerance on the base jig dimensions, and every module was hosted by its own base jig. After the phase 2 testing campaign it was decided to use dedicated base jigs for the

measurements, avoiding the tilt realignment for each measurement, greatly improving the touchdown consistency.

  – Still one jig for each type of module was employed. A one size-fits-all kind of jig could help improve further the consistency of the touchdowns, avoiding the necessity of correcting the tilt.

- The needle spider deteriorates quickly with the touchdowns performed. Having a good maintenance of the needles helps improve the touchdown effectiveness. To keep the probe cards as good as new:

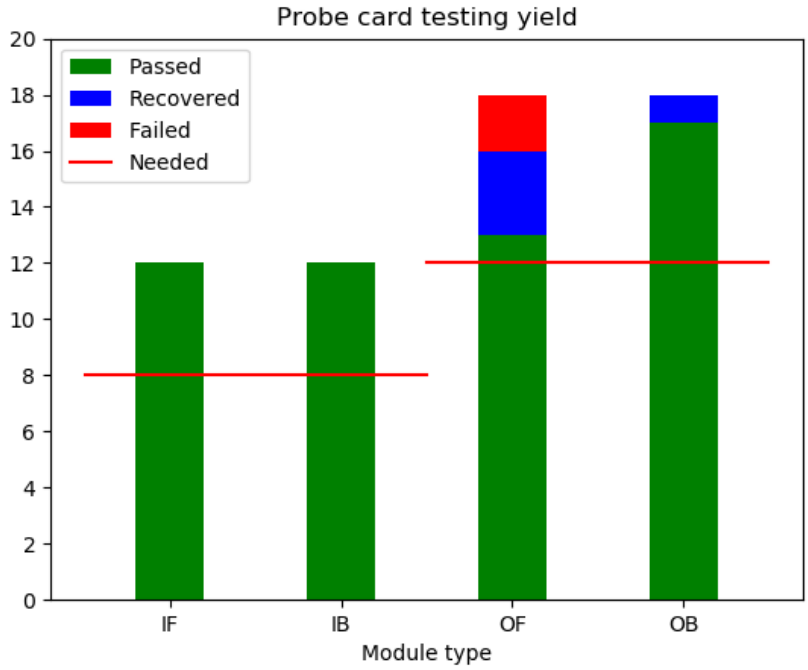

Fig. 4.18 Probe card testing yield in the mass production of the PXD (phase 3 only). Out of the 60 modules produced, 54 passed and 6 failed the test. From the 6 defective modules, 4 could be recovered.

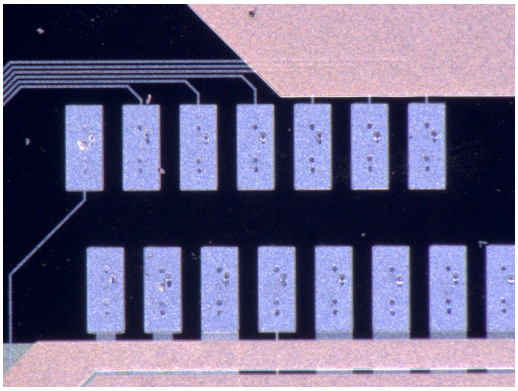

Fig. 4.19 Contact pads after five touchdowns. The high amounts of touchdowns deteriorates the surface on the contact pads.

- It is recommended to use the resharpening contact pads after a few touchdowns to keep the needle tips clean and sharp.
- After finalizing a batch, send the probe cards to PTSL for reshaping, ensuring their best possible performance for the next batch.

Even after considering the previous advice, some modules could still be complicated to operate. As seen in Figure 4.19, trying to achieve a stable High Speed Link connection can lead to performing many touchdowns in the module, deteriorating the pad surface and taking a great amount of man-hours, without guaranteeing a success. Actually, out of the 66 tested modules, in 13 of them the testing protocol could not be finished due to instability problems.

Moreover, all of the faulty modules were spotted during the *basic tests*, leaving the *extensive tests* as a really poor cost-effective solution. Even in the rare event of a module having a fault that could only be detected at the *extensive test*, the reworks of the W31_IB and W31_OB1 modules prove the feasibility of repairing a module after Kapton cable attachment, giving still a chance to recover the module.

Taking all this information into account, it is my recommendation to shorten the testing protocol for future productions, avoiding altogether the *extensive test*.

Doing so would greatly optimize the man-hours spent performing the quality control and preserve the contact pads integrity while still being a useful procedure to detect most (if not all) of the faulty modules.

Chapter 5

PXD module characterization

In this Chapter the detailed characterization of the PXD layer 2 module W46_OF1 (Figure 5.1a) will be discussed. Including a standard module characterization, an in-depth analysis of the sensor performance, an evaluation of the changes due to the variation of the zero suppressed threshold, and the extraction of the internal gain (g_q) of the DEPFET pixels.

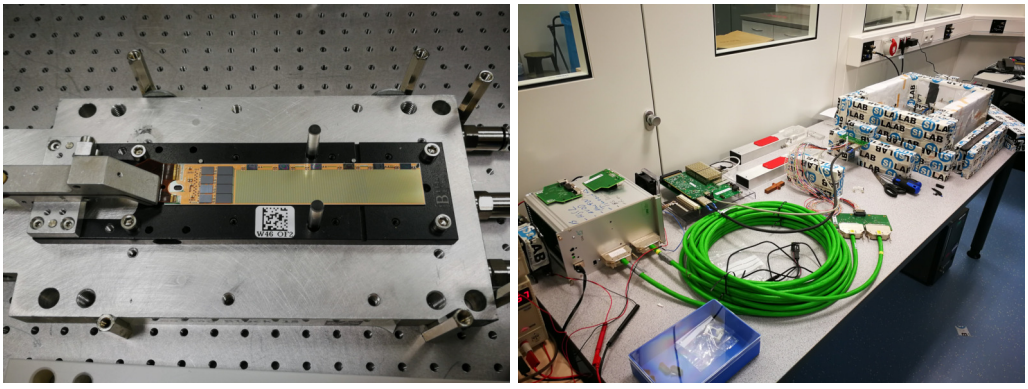

(a) Module at the test stand. **(b)** Services to operate the module.

Fig. 5.1 Testing setup in the clean room.

The measurements were performed in the clean room[1] at the Silicon Laboratory (*SiLab*) in the Physikalisches Institut of the Universität Bonn (Figure 5.1b). The SiLab setup does not differ much from the one described in Chapter 4 for the probe card testing. In this setup, the module rather than being in a probe station is inside a light-tight lead box; and instead of using the needle card to interface the module, the combination of the Kapton cable and the patch panel is used, similarly to the final experiment configuration.

5.1 Standard characterization

After their production, the modules are operated in a qualified test stand[2] where they are characterized. The characterization is performed following the procedures detailed in The PXD Mass Testing Handbook[3], to ensure that all the modules behave similarly.

First, a series of sanity checks on the module are performed: the electrical performance is checked (ie. the power consumption of the different the nets), and module steering through the JTAG interface is tested, writing and reading the registers of the different ASICs, checking if they can be addressed correctly.

Then, a thorough characterization is realized: first, a stable connection with the DHPTs through the High Speed Links is ensured; second, the interchip communication is fine-tuned; third, the pedestals are optimized; and last, the DEPFET matrix performance is studied.

[1] Operating the modules in a clean environment is therefore vital to ensure their safety.

[2] A guinea pig module is used to qualify the setups at different institutes before fresh modules are sent for testing.

[3] The Handbook defines the protocol to determine if a module fulfills the requirements to be installed, as well as the steps to obtain its optimal operation parameters.

5.1.1 Interchip communication

High Speed Links

To test the data transfer over the High Speed Links (HSL) a scan is performed over the *bias* and *biasd* pre-emphasis parameters[4] of each DHP recording the eye diagram amplitude perceived by the DHE receiver one second after initializing the connection.

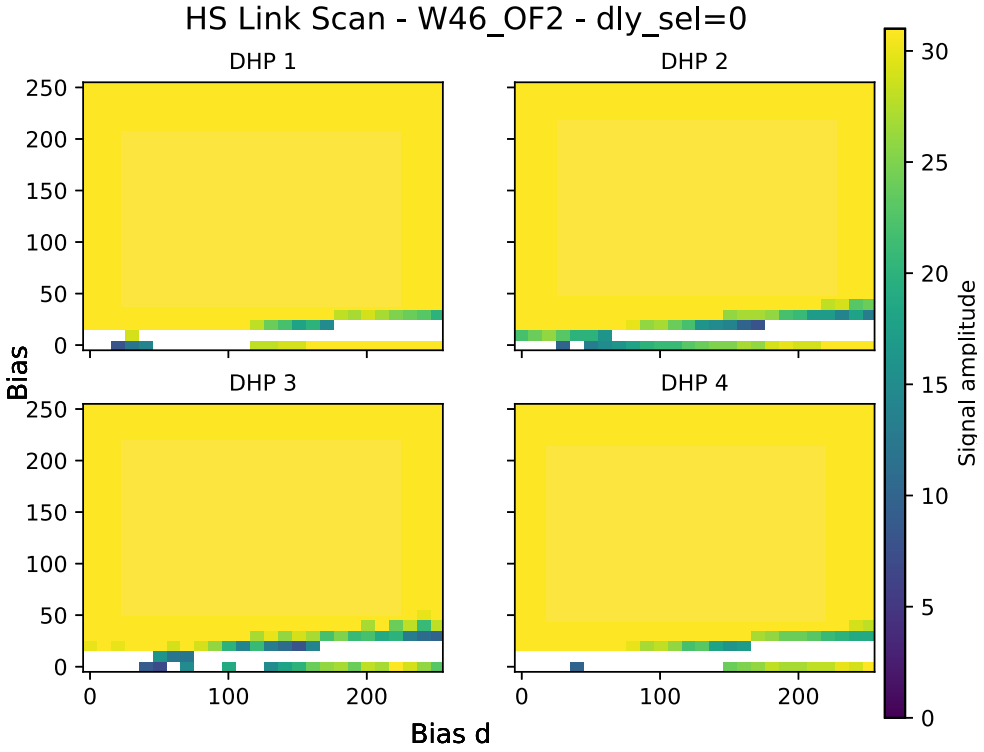

Fig. 5.2 Scan of the HSL *bias* and *biasd* parameters in the 0-250 range in steps of 10 units for each of the DHPs in the module. The color plot indicates the measured eye diagram amplitude by the DHE one second after establishing the HSL. The DHE can measure amplitudes in the 0 to 31 a.u. range.

[4]The *delay* parameter is set to 0.

A sweep is performed over the 0-250 values in steps of 10 for both parameters. For each measurement, the HSL are initialized and, after one second, if the links are still up, the amplitude measured by the DHE is noted down. The results are shown in Figure 5.2.

The huge yellow areas indicate a great electrical connection between the CML drivers and the DHEs, as the links could be established with the maximal measurable amplitude for most pre-emphasis configurations. The empty areas represent the points where either the link could not be established, or, the link is lost quickly (less than one second) after initialization.

As the DHE receiver does not have enough granularity to resolve the inner structure of the yellow areas, and the measurement does not probe the long-term stability of the links, the optimal pre-emphasis parameters are chosen instead relying in the extended measurements performed by the DHP specialist, Leo Germic [42]. The parameters are set to $bias = 225$, $biasd = 125$ for all DHP.

DCD delays

The digitized data from the ADCs are transmitted from the DCD to the DHP through 64 LVDS lanes. A proper selection of the sampling point in the DHP receiver is fundamental to ensure an error free transmission. To move the sampling point a *global delay* (which shifts the clock signal, affecting to all the sampling points at once) and *local delays* (which affect individually each lane) can be set.

To find the optimal sampling point the DCD test pattern (shown in Figure 4.14a) is sent to the DHP continuously while performing a sweep in the *global delay* and the *local delays*. By comparing the pattern with the received data, errors in the data transmission can be spotted.

The results in Figure 5.3 show a wide blue stripe in which the data is transmitted error-free for each one of the transfer lanes. These stripes overlap significantly, allowing for the successful data transfer from the DCD to the DHP.

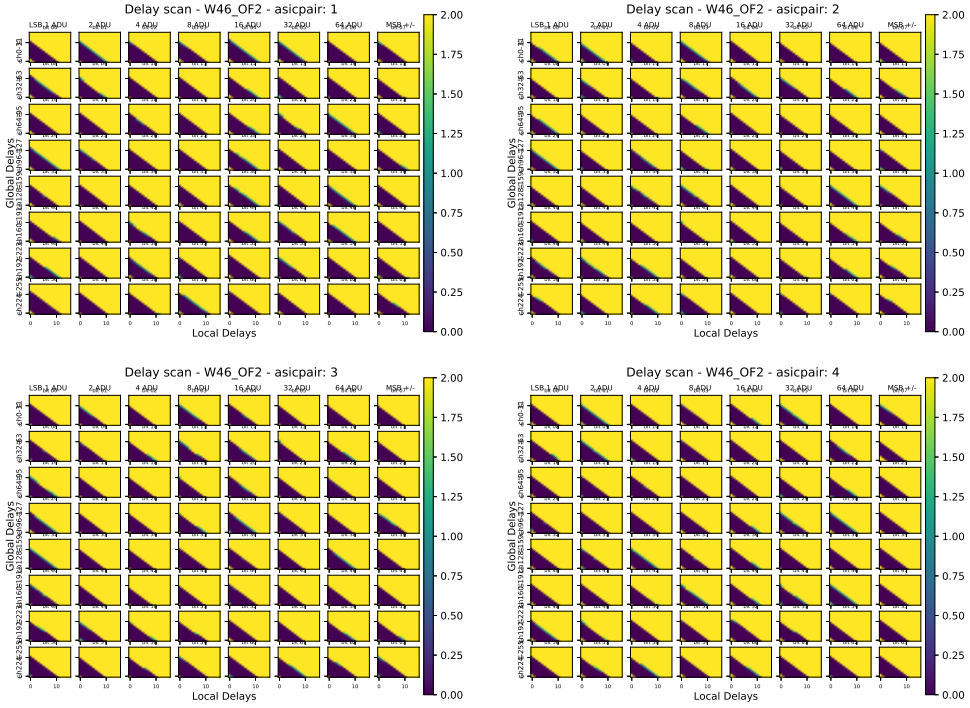

Fig. 5.3 Sweep of the DCD *local delays* and *global delay* to optimize the DCD to DHP communication. The color plots show the recorded number of communication errors for a given lane as a function of the applied delays. The diagonal blue stripes indicate the error-free communication parameter space.

The optimal point is chosen to be the center of the blue stripe overlap for each DCD. Having such a broad working parameter space helps avoid choosing metastable parameters that could eventually result in communication errors.

5.1.2 Sensor pedestals

After ensuring proper data transmission, a first look at the pedestals is taken to verify the healthiness of the sensor.

The *raw* (uncorrected) pedestal map of this module is shown in Figure 5.4. From the map it can be concluded that this module suffers from three different

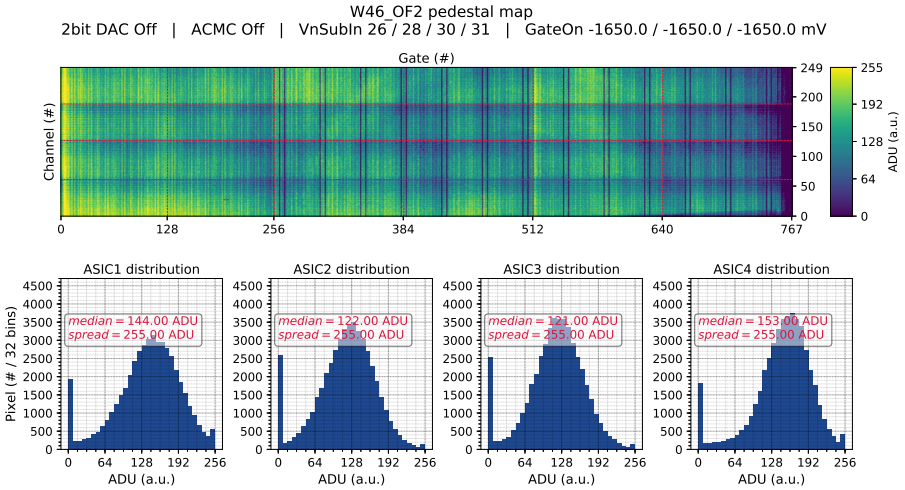

Fig. 5.4 Raw pedestal map of the W46_OF2 module. The mapping is chosen so the ASICs are in the right side, while the Switchers are in the bottom of the pedestal map. The dashed red lines in the pedestal map indicate the border between neighboring Switchers and ASICS. The 0 to 127 gates correspond to the first Switcher, 128 to 255 to second Switcher, and so on. Likewise, channels 0 to 62 correspond to the first ASIC pair, channels 62 to 124 to second ASIC pair, and so on. In the bottom of the figure, the four histograms are filled with the pedestal values for each ASIC pair, the median and the spread of the pedestal distribution is calculated for each histogram.

problems: four pixels are dead in the region of ASIC 1 with Switcher 2; a geometrical pattern in which some gates seem to be dead in the regions of Switchers 3 to 6; and some areas near the EOS and close to Switchers 5 and 6 also seem to be dead.

In order to distinguish between dead pixels and pixels out of dynamic range, different pedestal maps are taken varying the *VnSubIn* parameter[5]. By doing so it was observed that the four pixels were effectively dead, while the geometrical pattern and the EOS area were generated by pixels out of the ADCs dynamic range.

[5]This parameter subtracts current out of the drain line before the current is digitized by the ADCs.

These low gain areas near the EOS and Switchers 5 and 6 are produced by radiation damage during the module assembly. As a part of the PXD production the modules are x-ray inspected, checking ASICs and SMDs after the assembly for possible problems in the bump bonding. When performing these measurements, a shield is placed on top of the sensor to avoid its irradiation. The misplacement of this shield leads to the irradiation of the exposed area, thus reducing the gain in the damaged pixels.

As for the geometrical pattern, it can be explained by a mechanical resonance in the machinery used to produce the sensor. The pattern is only present from Switchers 3 to 6 area, where the pixel pitch is $85 \times 50\ \mu m$. In Switchers 1 and 2 areas the pixel pitch is smaller, thus breaking this mechanical resonance. The affected pixels suffer from lower gain, appearing as dead gates in the raw pedestal map.

Both effects can be mitigated using the 2-bit DAC to enhance the current in these pixels, bringing them back into the ADC dynamic range. Overall, this module possesses a pretty healthy sensor with just four dead pixels (out of 192000).

ADC scan

To ensure proper sensor response a closer look to the DCD performance has to be taken. To do so the ADC transfer curves are studied. These curves represent the digitization of the incoming current in the drain lanes to an 8-bit value, measured in analog to digital units (or ADU), which constitutes the measurement.

First, a sweep over the DCD voltages (*amplow*, *refin*, and the ADC parameters *ipsource*, *ipsource2* and *ifbpbias*) is performed, acquiring transfer curves for all the ADCs in the different configurations[6]. Then, the linearity, range of the signal and noise of the recorded transfer curves is studied. A quality criteria is established

[6]The rest of the parameters are kept at their default values. Out of the 7 possible gains, the DCDs are configured to only have the *En60* resistor activated, yielding a relative gain of the ADC receiver of $G = R_f/R_s = 13k\Omega/15k\Omega \approx 0.86$.

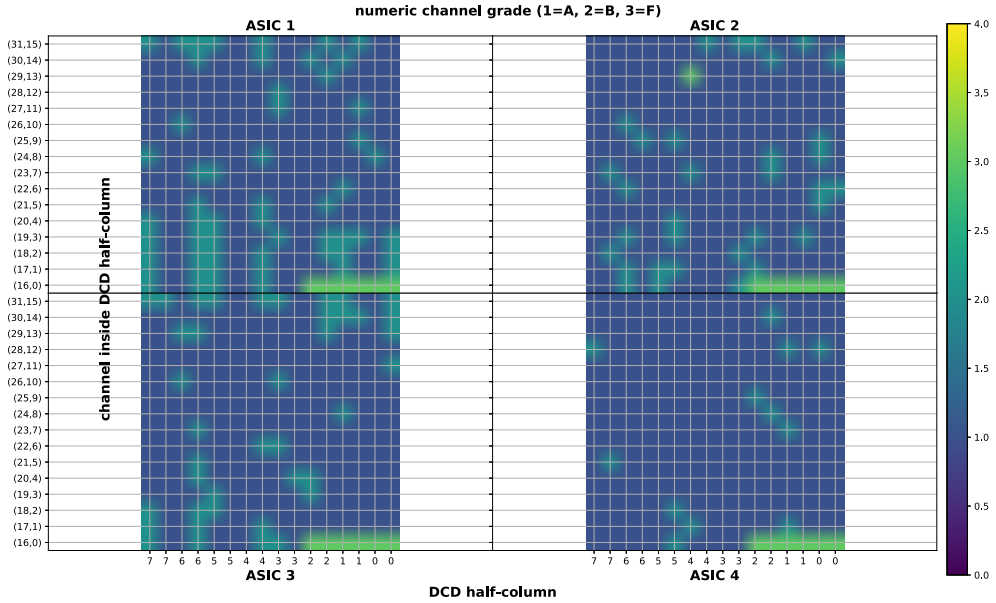

Fig. 5.5 Quality grades of the ADCs in their optimal configuration. The grading system is defined as: 1 - perfectly working ADC, 2 - minor issues in the ADC, 3 - major issues or disconnected ADC. The last 6 channels of each DCD are disconnected from the sensor.

taking into account all of these properties. By maximizing the value of this criteria, the optimal point is chosen.

To obtain the transfer curves three different inputs are available: the DCD internal current generator, the external current injector from the DHE, or, the DEPFET pixels used as a current generator varying the gate-on voltages. Due to the high volume of transfer curves to be recorded, the DEPFET pixel method -which is by orders of magnitude the fastest method- is employed.

The measurement sweeps are discussed in detail in the Appendix B. A summary of the results is available in Figure 5.5, where the different channels are graded in the optimal configuration. The results show great DCD performances, yielding a total of 999 prime grade and 1 defective channels.

ADC calibration

Once the ADCs are optimized, a calibration of the DCD absolute gain is performed. To do so, transfer curves for all ADCs are measured using the DHE current injector as the source. An example of such transfer curves is shown in Figure 5.6a. The gain (in ADU/DAC) of a particular ADC can be computed by performing a linear fit of its transfer curve. Averaging over all the ADCs, an overall gain can be computed for each DCD.

By performing a calibration of the DHE current source [60], the absolute gain of the DCDs can be computed. As seen in Figure 5.6b, using the $f = 3814.33 \pm 0.01$ pA/DAC calibration value an absolute gain in the order of 6.5 ADU/µA is obtained for each DCD.

2-bit DAC and ACMC

Once the DCDs are optimized, the next step is to enable the mechanisms at our disposal to homogenize the pedestal map, narrowing the pedestal distribution as much as possible.

First, an optimization of the 2-bit DAC is performed. The 2-bit DAC is a mechanism that allows to add current to individual pixel measurements. The *ipdac* parameter sets the baseline of the quantity to add, and 2-bit DAC *offset*

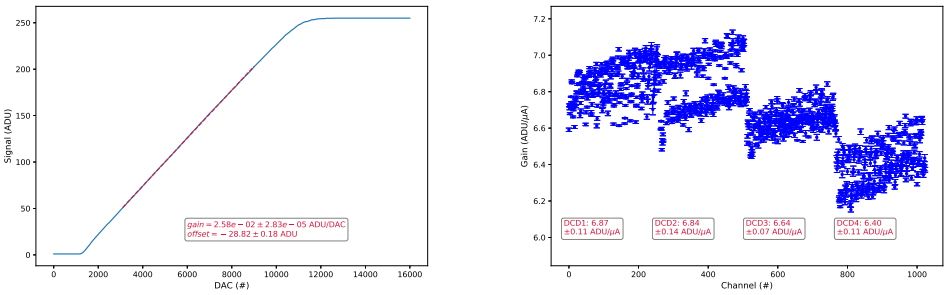

(a) ADC 19 transfer curve. **(b)** DCD gain calibration.

Fig. 5.6 DCD absolute gain calibration using the DHE as the current source.

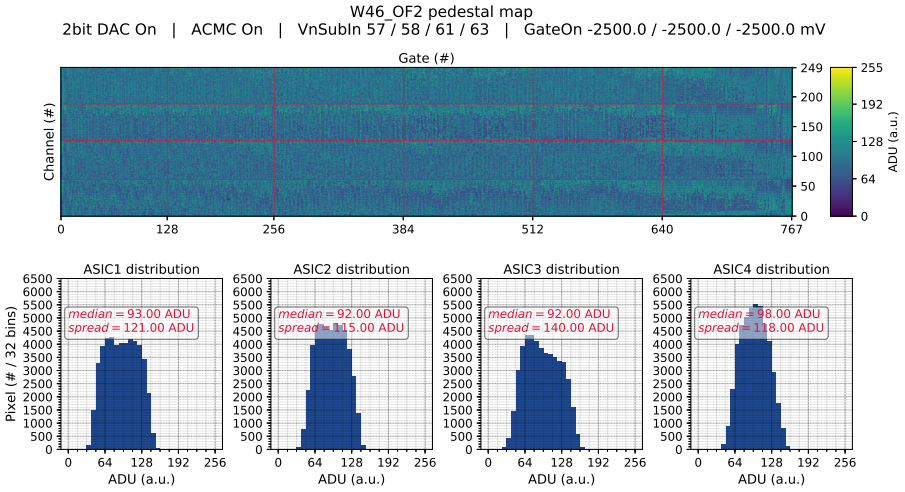

Fig. 5.7 Optimized pedestal map of the W46_OF2 module at $gate\text{-}on = -2.5$ V.

parameters for each pixel to add 0, 1, 2, or 3 times the *ipdac* value to the pixel current.

The measurement script takes pedestals applying the 4 possible 2-bit offsets for each pixel while sweeping over the *ipdac* parameter. Afterwards, the analysis script computes which settings yield the most homogeneous pedestals. By doing so, and enabling the *ACMC* to compensate the common mode noise, the pedestals shown in Figure 5.7 are obtained.

The resulting pedestals are distributed around 95 ADU with a spread of 120 ADUs. Leaving around 100 ADUs available to accommodate the collected charge. Signals that go over these values will exceed the dynamic range of the sensor, being indistinguishable from the maximum.

As seen in the Figure 5.7, using the 2bit DAC all the insensitive areas of the matrix could be recovered. Nevertheless, this recovery comes with a downside: the 2-bit DAC was designed to compress the pedestal distribution so that more dynamical range is available for the signal.

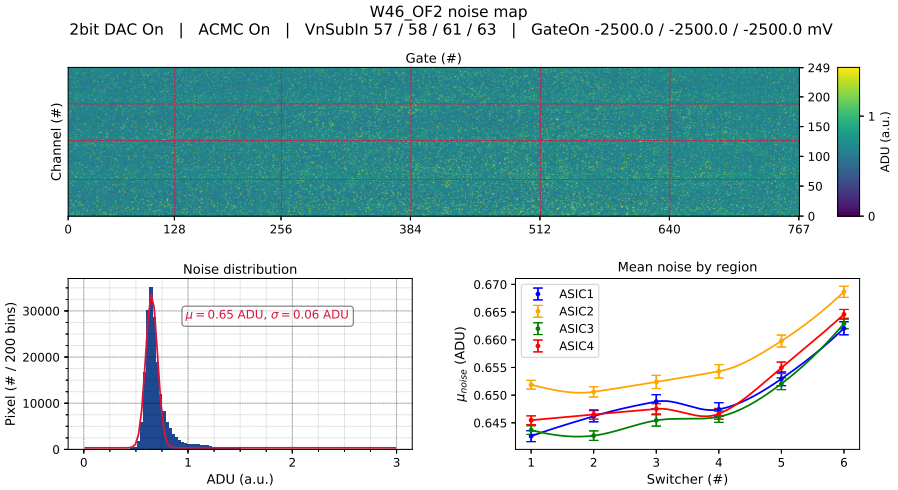

Fig. 5.8 Pedestal noise map of the W46_OF2 module at *gate-on* = −2.5 V. In the bottom left, a gaussian fit to the overall noise distribution is shown; in the bottom right, fitted gaussian μ of the noise distribution for the different ASIC regions.

Instead, most of the power of the 2-bit DAC is used to recover insensitive areas produced either by radiation damage or production inhomogeneities, resulting in a wider than designed pedestal distribution.

Another important quantity to consider is the pedestal noise. To measure it 1000 pedestal frames are recorded, and the noise is then computed as the standard deviation of the successive pedestal measured for each pixel. The corresponding noise map is shown in Figure 5.8. As seen in the figure, an overall 0.65 ADU noise is recorded, with values ranging from 0.64 to 0.67 depending strongly with the sensor region. Unsurprisingly, the closer the region is to the EOS, the higher is the noise in the pedestals.

5.1.3 DEPFET voltages

Once the ASICs are fully optimized, the last step consists on fine tuning the DEPFET voltages to achieve the highest signal to noise ratio (SNR) and homogeneity in the module response. To do so, a series of source measurements are

performed, placing radioactive sources above the module while recording zero suppressed data on the laboratory DAQ.

The PXD sends downstream the zero suppressed frames, containing information about the deposited charge in the sensor. The DAQ uses the data to reconstruct the hit, characterized by its position, and the deposited energy by the impinging particle. To do so, a clustering method is implemented [55].

First, the algorithm applies a seed cut to look for the pixels with the highest signal[7]. These are the pixels that acquired most of the charge deposited by the impinging particle.

Then, a second cut is applied to the pixels neighboring the seed, the neighbors that pass the cut are then considered part of the cluster. This cut is applied iteratively, including all the neighbors of the cluster that pass the cut. The cluster charge is then calculated as the sum of the charges of the seed and its neighbors.

Finally, the position of the cluster is calculated by a center of gravity method that considers that the charge is shared linearly between the pixels[8]. The position is then calculated as

$$\vec{x}_{cluster} = \frac{\sum Q_i \vec{x}_i}{\sum Q_i}, \tag{5.1}$$

where Q_i, $\vec{x}_i$ are the charge deposited in the i-th pixel, and the center of the pixel respectively, and $\vec{x}_{cluster}$ is the reconstructed position of the cluster.

As seen in Figure 5.9, depending on the DEPFET matrix voltages, some *rings* might appear on the cluster hitmaps when taking a source measurement, indicating loss of charge in the dimmed areas. Moreover, the recorded cluster charge distribution does not have the expected gaussian-like shape. Nevertheless, when using optimal sensor voltages, nice gaussian-like cluster charge distributions are recorded, and the *ring* structures are either minimized or erased as shown in

[7] In the event of finding two adjacent seeds, the smaller seed is considered part of the largest seed cluster.

[8] In fact, the charge is not shared linearly between the DEPFET pixels, in-depth studies of the charge sharing is required to implement a more robust method to reconstruct the hit position.

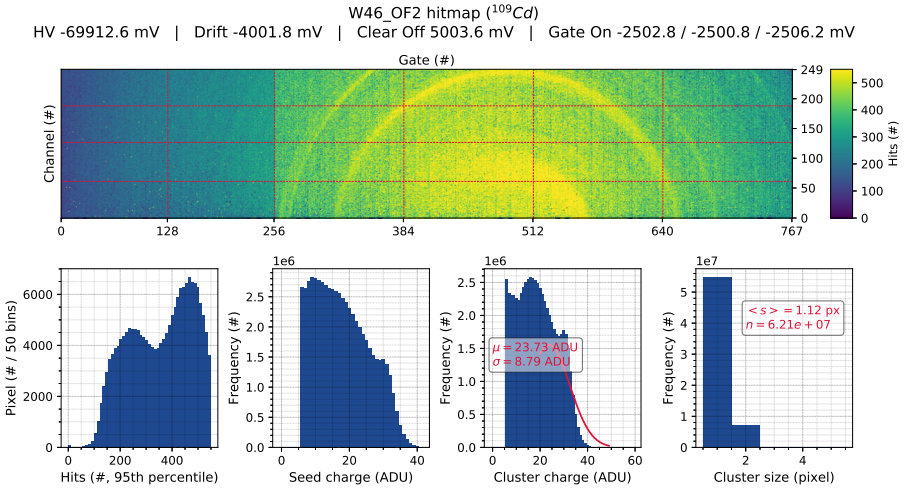

Fig. 5.9 ^{109}Cd hitmap in a non-optimal configuration (*high voltage* $= -70$ V, *drift* $= -4$ V, *clear-off* $= 5$ V). The hitmap represents the reconstructed clusters. In the bottom, histograms of the number of hits recorded per pixel, seed charge, cluster charge and cluster size. A fit to a gaussian is performed in the photopeak of the cluster charge. The number of clusters in the hitmap and its mean cluster size is also shown.

Figure 5.10). The contrast between Figures 5.9 and 5.10 illustrates the crucial importance of supplying the correct voltages to the DEPFET pixels.

Therefore, to obtain a great performance out of the sensor it is vital to find the DEPFET voltages that maximize the SNR and the hitmap homogeneity for minimum ionizing particles. To spot them, a series of ^{109}Cd source measurements[9] sweeping over *high voltage*, *drift* and *clear-off* are performed; while keeping *clear-on* $= 19$ V, *gate-on* $= -2.5$ V, *gate-off* $= 5$ V, *ccg* $= 0$ V and *source* $= 6$ V fixed.

A total of 132 source measurements are recorded, producing every possible iteration combining *drift* $= -4, -5, -6$ V, *clear-off* $= 2, 3, 4, 5$ V and *high voltage* $= -54, -56, -58, -60, -62, -64, -66, -68, -70, -72, -74$ V. As per

[9]The 22.1 KeV photons from the ^{109}Cd source deposit roughly the same energy that a minimum ionizing particle would leave in the 75 μm of silicon, which is around 21.6 KeV. Alternatively, a ^{90}Sr β-source could be used, as it emits quasi-relativistic electrons (with up to 2.28 MeV) leaving a *mip*-like signal.

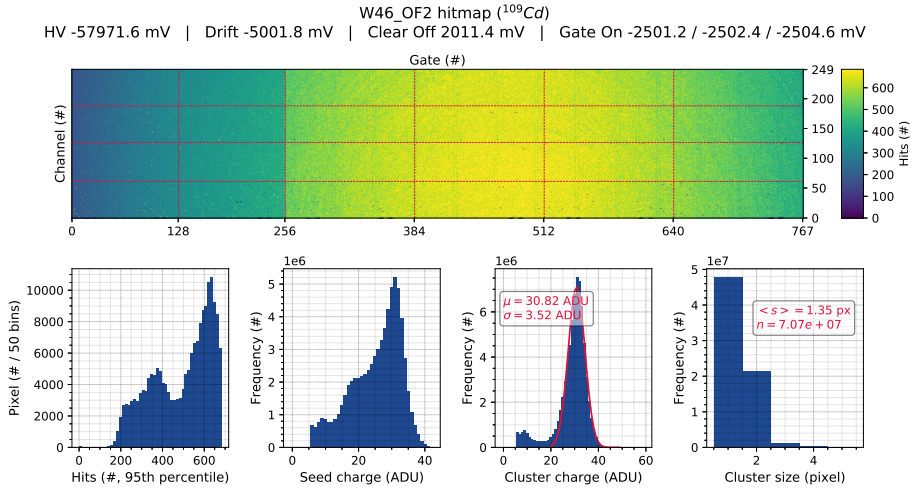

Fig. 5.10 ^{109}Cd hitmap in an optimal configuration (*high voltage* $= -58$ V, *drift* $= -5$ V, *clear-off* $= 2$ V).

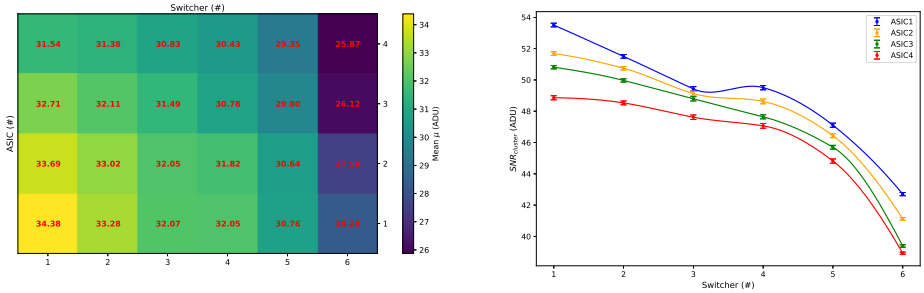

(a) Signal strength along the module. **(b)** Signal to noise ratio.

Fig. 5.11 Signal strength (in the left) and signal to noise ratio (in the right) for the different regions in the sensor. The signal strength is calculated as the fitted gaussian μ of the cluster distribution. The SNR is obtained by dividing the signal strength between the mean recorded signal in Figure 5.8.

the handbook guidelines, the hitmaps are evaluated by eye, choosing the configuration that minimizes the perceived *rings* while maximizing the collected charge. The chosen configuration, shown in Figure 5.10, was *high voltage* $= -58$ V, *drift* $= -5$ V, *clear-off* $= 2$ V.

As seen in Figure 5.11a, the reconstructed clusters from the 22.1 KeV photons yields a fitted gaussian *mu* between 25 and 35 ADUs, depending strongly with the sensor region. A trend is observed along the balcony: the farther away from the EOS, the higher the recorded signal.

Taking this results into account, and using the mean recorded noise from Figure 5.8 the signal to noise ratio of the detector can be calculated for the different sensor regions. Figure 5.11b shows the computed SNR for the different parts of the sensor. The trend observed in the signal is translated into the SNR. The values obtained range from 40 in the regions closest to the EOS to 54 in the farthest, resulting in great SNR values for such a thin silicon detector.

Overall, the sensor is evaluated as prime grade, having a great pixel yield, a high SNR, and enough dynamical range to accommodate up to three *mips* per pixel.

5.2 DEPFET voltages quantitative optimization

As the methodology to optimize the DEPFET voltages defined in the handbook is subjective and prone to bias, in this subsection an alternative approach is proposed and applied to data recorded in the sweep.

To quantify the quality of the recorded clusters three figures of merit are considered: the signal strength, estimated as the gaussian mean of the cluster charge distribution; the shared charge between the pixels, estimated as the mean cluster size (i.e. the mean number of pixels that make up the clusters); and the homogeneity of the cluster map, estimated as

$$h = \sum_{gates} \frac{< \text{cluster charge} >^2_{gate_i}}{Var(\text{cluster charge})_{gate_i}}. \tag{5.2}$$

When the rings are present in the hitmap, the variance of the cluster charge for an affected gate lane grows, thus reducing our homogeneity estimator h. The $< \text{cluster charge} >^2_{gate_i}$ term is included to make the quantity dimensionless.

These estimators are calculated for the cluster hitmaps recorded in the previous section, obtaining Figures 5.12, 5.13a and 5.13b. A high correlation between the signal strength and the homogeneity of the hitmaps is observed: optimizing for the maximum cluster charge distribution yields homogeneous *ring*-free hitmaps.

The voltage that seems to have a biggest impact on the quality of the hitmaps is the *high voltage*. A general trend is observed in Figures 5.12 and 5.13a, for low *HV* bias, growing the bias has a positive impact in the recorded hitmaps; but from a given point the trend reverses, and growing the bias yields worse results. The turnaround point depends on the *drift* and *clear-off* values, ranging from -58 V to -62 V. Taking a look at Figure 5.13b also reveals that a greater bias of the *HV* results in less charge sharing.

One could make an educated guess that before the turnaround point the DEPFET pixels are not yet fully depleted, so the detector performance improves with the bias increase. After reaching the fully depletion point (around 60 V), it seems that if the voltage is further increased the performance starts to deteriorate.

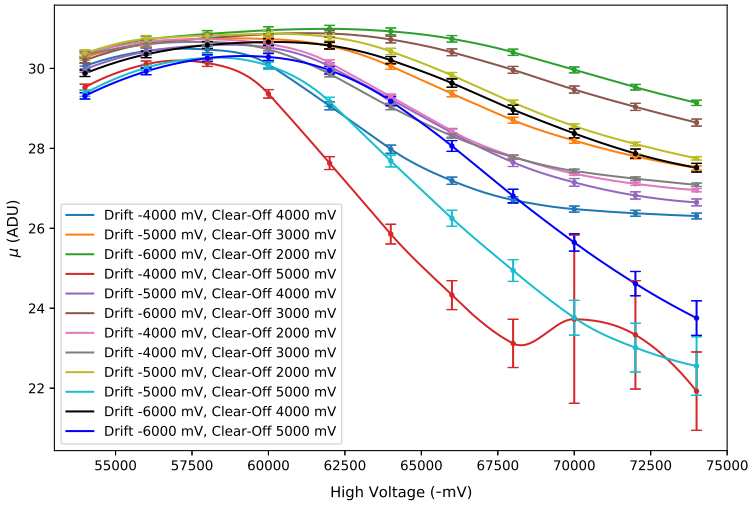

Fig. 5.12 Signal strength estimated as the fitted gaussian mean μ of the cluster charge distribution for the different ^{109}Cd source measurements in the DEPFET voltages characertization sweep.

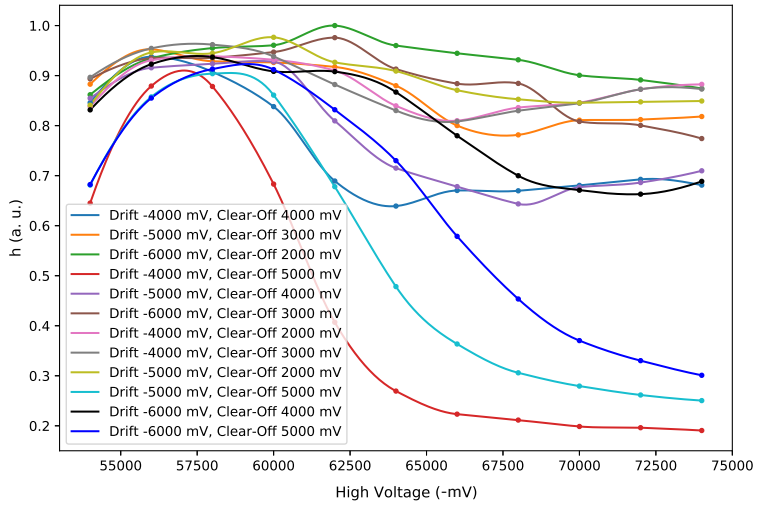

(a) Homogeneity estimated as the h parameter defined in Equation 5.2, normalized to the maximum value.

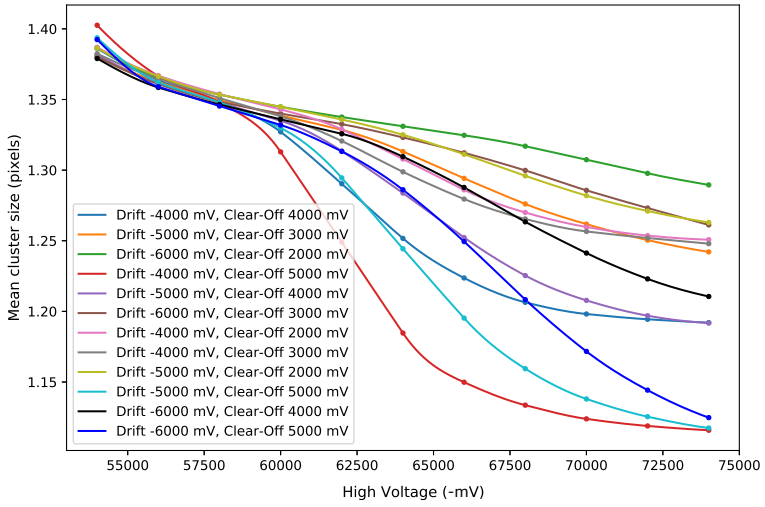

(b) Shared charge estimated as the mean cluster size, i.e. the mean numbers of pixels that make up the clusters.

Fig. 5.13 Homogeneity and shared charge for the different ^{109}Cd source measurements in the DEPFET voltages characertization sweep.

Then, the higher *HV* bias can interfere with the other electrical fields in the DEPFET pixel, deteriorating the signal collection or the clearing mechanism. Further investigations would be needed to obtain a definitive explanation of the observed behavior.

After carefully studying the results, it was observed that some *drift*, *clear-off* pairs produced better cluster hitmaps than others in absolute terms while also reducing the impact of the *HV* variation. These values yield more stable hitmaps, where small changes in the voltages do not translate in big differences in the recorded clusters. In particular, the $drift = -6$ V, $clear\text{-}off = 2$ V and $drift = -6$ V, $clear\text{-}off = 3$ V curves produce the better strength signal, hitmap homogeneity, and shared charge across the board. In these curves, the point of $drift = -6$ V, $clear\text{-}off = 2$ $V, high\ voltage = -62$ V would be chosen as the optimum, because of its maximal signal strength and homogeneity.

To crosscheck the results, these measurements were repeated using a ^{90}Sr source. The sweep produced pretty similar results, yielding identical conclusions to those obtained for the ^{109}Cd source measurements.

Unfortunately, at the moment in which the measurements were performed the quantitative analysis optimization was not yet proposed, and therefore the voltages supplied in the following measurements were the previous optimal configuration chosen subjectively. Still, the chosen point does not fall far from the objective optimum.

5.2.1 Signal homogeneity

As seen in the previous section, the *high voltage* parameter has the biggest impact on the sensor performance. To further investigate its impact, an extended sweep over *high voltage* was performed with a ^{90}Sr source, from -46 V to -80 V in steps of 2 V. The *drift* and *clear-off* voltages were set to -5 and 2 volts respectively.

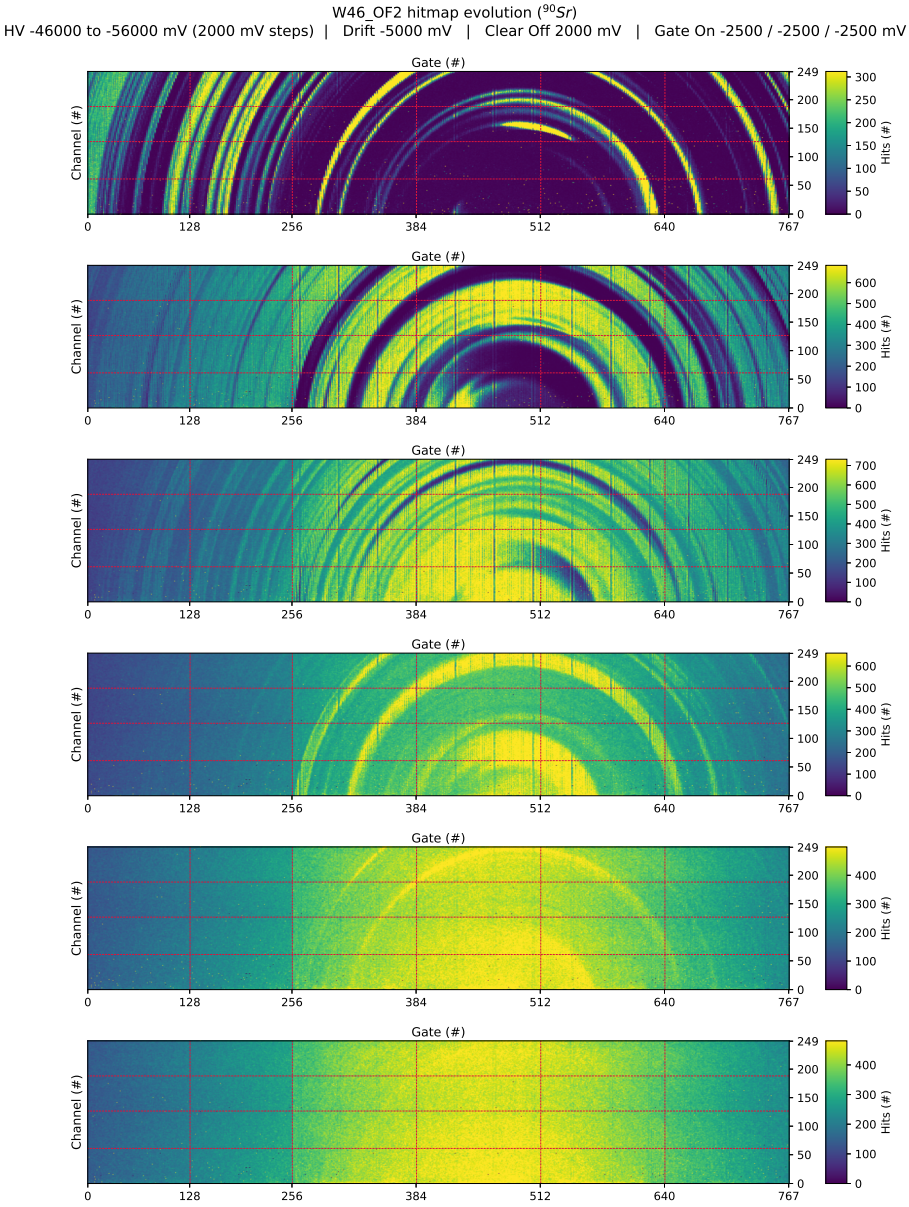

Fig. 5.14 Evolution of the cluster hitmap as a function of the *high voltage* for measurements taken with a ^{90}Sr source with *drift* $= -5$ V, *clear-off* $= 2$ V.

Figure 5.14 shows the evolution of the depletion for the different regions in the sensor as the *HV* bias grows. The pixels are depleted following the ring distribution, pointing to differences in the full depletion voltage as the origin of these. These differences might be explained by inhomogeneities in the resistivity of the silicon wafer used to manufacture the module.

If the *HV* is set too low, then the rings with a higher full depletion threshold will not be fully depleted. On the contrary, if *HV* is set too high, the rings with a lower full depletion threshold will be way overbiased, disrupting the electrical fields in the DEPFET pixels and reducing their performance.

Optimizing the *high voltage* consists on reaching the exact point in which the whole sensor is fully depleted, avoiding as much as possible the overbias of the rings with the lower depletion threshold.

This interpretation would explain the trends seen in Figures 5.15a and 5.15b, where the performance of the detector improves with greater *high voltage* biasing, peaking at around −58 V and starting to deteriorate afterwards.

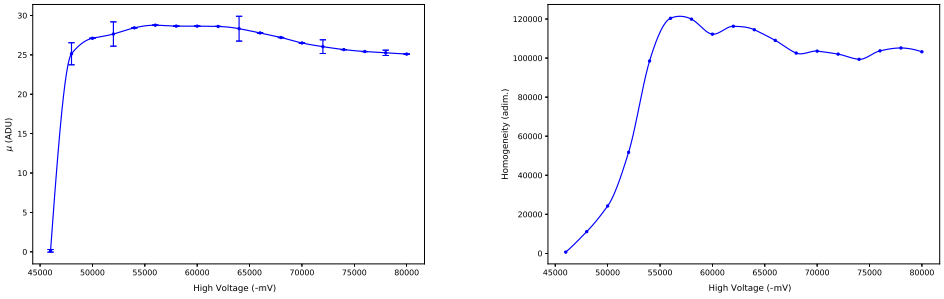

(a) Signal strength. **(b)** Hitmap homogeneity.

Fig. 5.15 Signal strength estimated as the fitted Landau's *mpv* of the cluster charge distribution (in the left) and hitmap homogeneity as the h parameter defined in Equation 5.2 (in the right), for the ^{90}Sr source measurements sweeping *high voltage*.

5.3 Zero suppressed data threshold study

The zero suppressed threshold is one of the most important settings relating the module's data acquisition. If the threshold is set too high the charge sharing for multi-pixel clusters decreases, affecting both the spatial and energy resolution; on the other hand, if the threshold is set too low, then the occupancy skyrockets, as more pixels have to be included in the zero suppressed frames. An optimal threshold value has to compromise a small amount of noise in exchange for more charge sharing between the DEPFET pixels, making sure that the 3% occupancy cutoff is never reached.

By default, the threshold is set to 5 ADU for the PXD modules. To evaluate the impact of the threshold on the noise, a series of zero suppressed data measurements without a source were taken using a threshold of 3, 5 and 7 ADUs.

In the case of the 3 ADU threshold, the maximum occupancy is reached for many individual pixels. To avoid exceeding the 3% occupancy, the control system masks these pixels, so that they do not submit any data. As a result, the noisy pixels are automatically masked, thus making impossible the comparison with higher hit thresholds. For this reason, the 3 ADU threshold is not included in the discussion below.

In Figures 5.16b and 5.16a measurements without radiation sources are shown for thresholds of 5 ADU and 7 ADU respectively. In these, the module is taking zero suppressed data with a frequency of 10 kHz over 1800 seconds. From the results obtained, the hits per frame are calculated in Table 5.1.

Table 5.1 Comparison of the hitmap noise for 5 ADU and 7 ADU thresholds.

Threshold	Hits	Hits per frame
5 ADU	1.26×10^6	0.07
7 ADU	3.48×10^4	0.002

To assess the impact on the charge sharing between the pixels ^{109}Cd source measurements are performed for 5 ADU and 7 ADU thresholds. The ratios of the

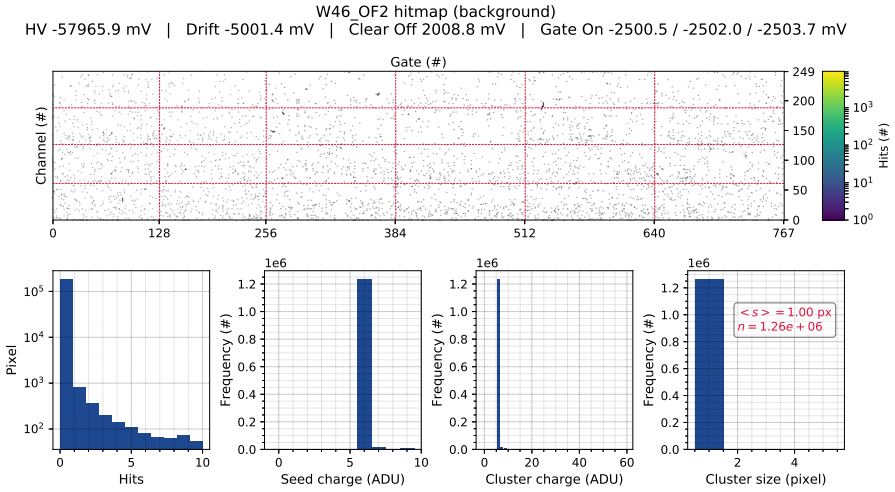

(a) Zero suppressed threshold of 5 ADU.

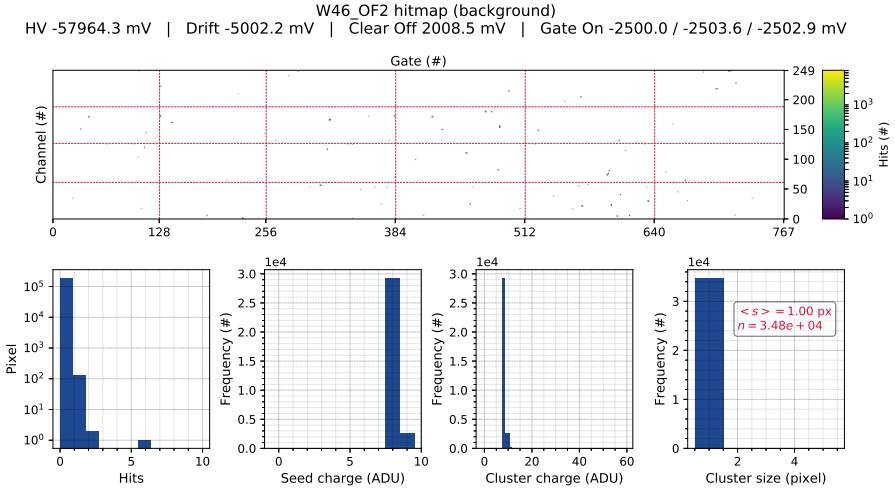

(b) Zero suppressed threshold of 7 ADU.

Fig. 5.16 Hitmap in the absence of a radioactive source for a ZS threshold of 5 ADU (in the top) and 7 ADU (in the bottom).

signal strength and the number of clusters of a given size are showed in Figures 5.17a and 5.17b, respectively.

The results show that mildly increasing the ZS threshold has a negligible impact (in the order of 1%) for the signal strength, and a huge impact on the cluster size. A 2 ADU increase of the threshold results in a conversion of 20% of the 2-pixel clusters and 80% of the >3-pixel clusters into single pixel clusters, greatly reducing the spatial resolution of the sensor.

On the other hand, the 2 ADU increase also reduces the noise by a factor 35, as seen in Table 5.1. Nevertheless, the absolute noise is already negligible for both configurations. A reduction does not yield any benefit in the clean background of the laboratory.

For low background environments, it is clear that the optimal choice is the 5 ADU threshold, providing better spatial resolution while still having excellent noise control. This assessment might not hold for higher background environments, such as in the accelerator.

5.4 DEPFET internal gain

As it was discussed in Chapter 3, the main characteriztic that defines the performance of a DEPFET pixel is its internal gain, g_q (see Equation 3.1). In order to calculate the internal gain, two main ingredients are needed: the calibration

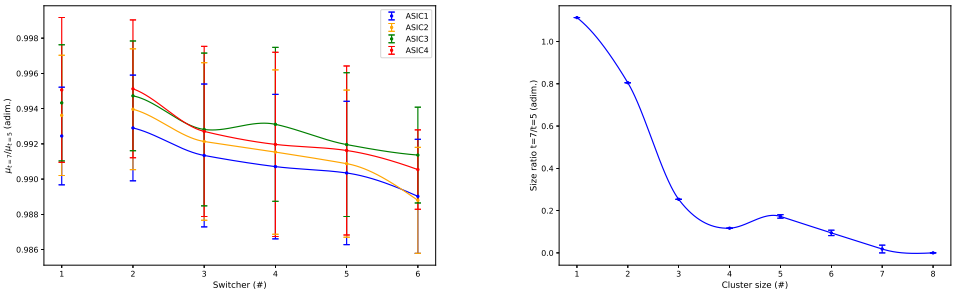

(a) Signal strength ratio. **(b)** Cluster size ratio.

Fig. 5.17 Signal strength (in the left) and cluster size (in the right) ratios for 7 ADU over 5 ADU threshold ^{109}Cd source measurements.

of the ADCs absolute gains, already performed in section 5.1.2: and, the energy calibration of the sensor.

The energy calibration consists in correlating the measured signal strength for different known energy depositions in the sensor. To perform the calibration, different γ radioactive sources with photopeaks within the sensor's dynamical range are measured. Then, the energy gain can be estimated as the slope of the linear fit of the measured signals against the deposited energies.

Table 5.2 Radioactive γ-sources used in the energy calibration of the module. Barium and terbium isotopes are not indicated, their emissions are fluorescent radiation caused by a ^{241}Am source.

Source	Energy (KeV)
^{55}Fe	5.9
^{109}Cd	22.1
Ba	32.06
Tb	44.23

By recording the cluster hitmaps of the γ-sources inTable 5.2, and performing the linear fit of the gaussian mean of the cluster distribution against the known deposited energy by the photon (as in Figure 5.18a), the energy gains are obtained

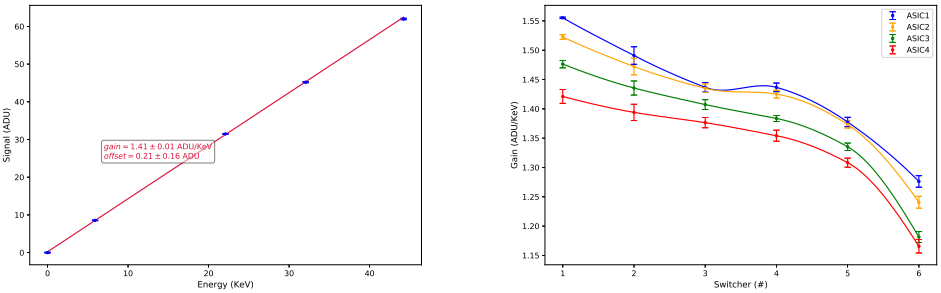

(a) Energy calibration of a region. **(b)** Energy gain across the sensor.

Fig. 5.18 Energy calibration of the Switcher 3, ASIC 3 region (in the left); and the energy gain of the different regions in the sensor (in the right), calculated as the slope of their respective energy calibrations.

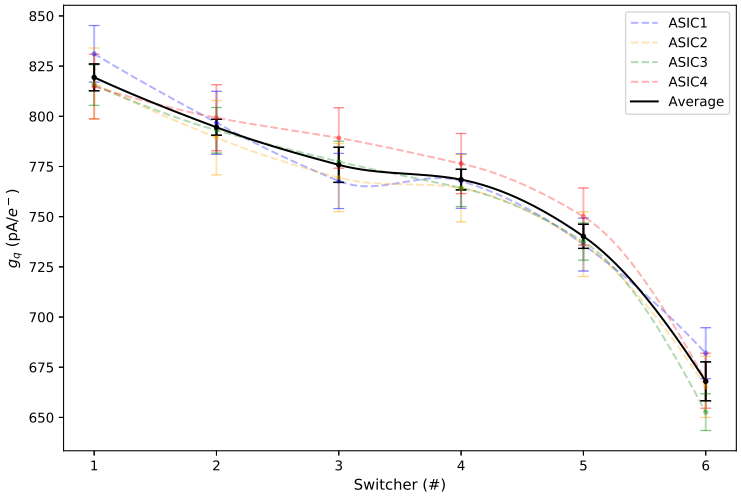

Fig. 5.19 Internal gain g_q for the different regions in the sensor at *gate-on* $= -2.5$ V. In black, the average for the four ASICs in a given Switcher region.

for each sensor region[10]. The results shown in Figure 5.18b reveal energy gains in the order of 1.2 to 1.5 ADU/KeV, depending strongly with the sensor region.

Multiplying the 3.67 eV that are needed to create an electron-hole pair in the depleted silicon by the energy gain in Figure 5.18b, and dividing by the absolute ADC gain obtained in Figure 5.6b, the internal gain g_q of the sensor is computed.

The resulting g_q, shown in Figure 5.19, is in the range of 675 to 820 pA/e^- from the regions closest to the EOS, to the regions farther from it. This trend, that has been observed across all the measurements might be explained by the sampling point chosen at the ADCs.

Timing of the ADC sampling is kept constant along the digitization of the different pixels during the rolling shutter. But, the distance that the signals have to travel from pixels to the ADCs is not constant. In fact, the pixels farther away

[10]In the case of the Switcher 1 region, only the cadmium and iron sources were used in the energy calibration. Due to the Ba and Tb sources low activity, the smaller pixel pitch, and the positioning of the source respect to the sensor, there was not enough statistics to include them in the fits in this region.

will have a higher capacitance due to the longer path. The sampling point in the ADCs have to be chosen so that the transient state after enabling the external gate in the DEPFETs is vanished, and only the steady state is measured. It could happen that the chosen sampling point is too aggressive, so that part of the transient state is being measured.

Considering that the transient state starts with an overshoot, followed by an undershoot, it could explain why for higher capacities (farther from the ADCs) the internal gain is noticeably greater than for lower capacities (closer to the ADCs). An extended sweep measurement over the ADCs sampling point recording the signal strength, such as in Figure 5.11a, would suffice to test the hypothesis.

5.4.1 Lower DEPFET gain

Additionally, to study the impact of the *gate-on* voltage in the DEPFET gain g_q the whole characterization was repeated for a lower DEPFET gain configuration. The chosen configuration was *gate-on* $= -2.0$ V with a DCD gain configuration of *En90*[11]. The details of the repeated characterization are summarized in Appendix C. Overall, the same behavior was observed in this configuration, and the conclusions obtained for the *En60* configuration remained valid. The g_q results are shown in Figure 5.20. In this configuration, the obtained g_q values ranged from 630 to 750 pA/e^-.

The reduction of the *gate-on* biasing from -2.5 to -2.0 V produced a decrease in the DEPFET gain in the order of the 10%, while the ADC gain increased around a 50%, yielding a total overall higher signal strength. Moreover, as shown in Appendix C, the recorded pedestal noise for the higher ADC gain is in the same order as for the baseline configuration (see Figure C.4); resulting in an even higher signal to noise ratio (see Figure C.7).

These results indicate that by changing the ADC receiver gain the system is able to preserve its performance after the reduction of the DEPFET gain.

[11] With the *En90* resistor activated, the relative gain of the ADC receiver yields $G = R_f/R_s = 19k\Omega/15k\Omega \approx 1.26$, approximately a 50% more than the $G \approx 0.86$ of the *En60* configuration.

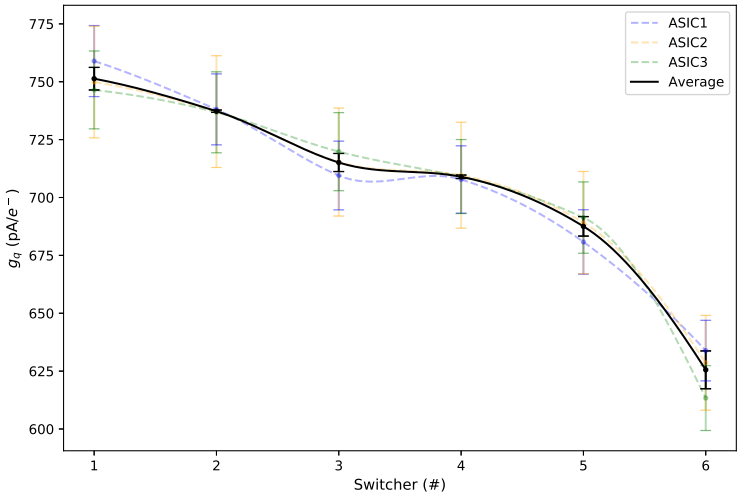

Fig. 5.20 Internal gain g_q for the different regions in the sensor at *gate-on* $= -2.0$ V. In black, the average for the four ASICs in a given Switcher region.

Therefore, by tracking the sensor performance and reconfiguring the module when necessary, the PXD operators will be able to mitigate the future radiation damage, retaining the original performance.

5.5 Conclusions

This Chapter discussed the detailed characterization of the W46_OF1 module. First, a by the book standard characterization was performed, checking the interchip communications, the healthiness of the sensor pedestals and the voltage and parameter optimization for data acquisition. Then, the impact of the zero suppressed data threshold was studied. And, last, the DEPFET internal gain g_q was measured.

As part of the standard characterization High Speed Link and DCD delays measurement scans were performed, finding wide areas in the parameter space where stable data transmission could be achieved. These wide working areas secure

the module performance against little changes in the environment conditions such as induced noise by surrounding electronics, or variabilities in the power supply. Moreover, the system was operated for three weeks, being continuously operated for more than four days without any connection drop or data corruption.

After ensuring the correct data transmission, the matrix pedestals were inspected. Unfortunately, the module was irradiated during assembly, producing radiation damage in some areas; it had some gate lanes affected by a manufacturing inefficiency that reduced the DEPFET current; and four individual pixels were dead. By activating the 2-bit DAC the affected gates and irradiated areas could be brought back to life, resulting in a remarkable pixel yield for the matrix, with just 4 out of 192000 pixels dead. Nevertheless, in order to recover these areas part of the power of the 2-bit DAC had to be sacrificed, resulting in wider than expected pedestal distributions.

The last step of the standard characterization consisted in the DEPFET voltages optimization, searching for the best-looking cluster hitmaps. During the data taking a high susceptibility of the system to the supplied voltages was observed. Deviation from the optimal voltages lead to quick performance deterioration, leading to inhomogeneous cluster hitmaps with a series of *rings* where charge seemed to be lost. An in-depth investigation of the observed behavior was performed, finding as the most probable cause the inhomogeneities in the silicon wafer resistivity.

Given the crucial importance of choosing the right value, an alternative method is proposed in this thesis. The method fixes three figures of merit (signal strength, hitmap homogeneity and shared charge between the pixels) and looks for the voltages that maximize their value. Fortunately, the correlation between them is high, so that a voltage configuration that maximizes them is in reach. The results from the proposed quantitative method yield standardized repeatable results with *ring*-free homogeneous hitmaps and great signal to noise ratios.

Next, the impact on the zero suppressed data threshold was studied. Increasing the threshold decreases the recorded noise by the sensor. But it comes with a

downside, increasing the threshold also reduces the recorded signal strength and the charge sharing between pixels, reducing the spatial resolution of the sensor. As the noise recorded by the sensor is already negligible, it was concluded that lower threshold do more good than harm in clean environments such as the laboratory. The conclusion might not hold for high background environments such as Belle II.

To finalize, once the module was fully optimized, an energy calibration was performed in order to obtain the internal gain g_q of the module. The results were in the range of 675 to 820 pA/e^- from the regions closest to the EOS, to the regions farther from it. The observed trend might be explained for differences in the rising times and transients of the DEPFET currents along the matrix. Studies varying the ADCs sampling point might be needed to corroborate the explanation.

Chapter 6

Top quark mass measurement through radiative events

The top quark plays an important role in the Standard Model (SM) and in many of its extensions. Assuming the validity of the SM, the only free parameters in the top sector that are not predicted by the model are the top mass and its associated entries in the CKM matrix. Due to its large mass, the lifetime of the top quark is really short ($\sim 10^{-25}$ s), decaying before hadronization can occur, thus behaving as a quasi-free quark. Thus, the top quark properties can be related with high precision to predictions in perturbation theory. That makes the top quark experiments ideal for precise tests of the SM.

As quarks can not be observed as physical particles due to color confinement[1], their masses cannot be directly measured. Their mass has to be determined through their influence on QCD processes, making them theory dependent. These measurements provide the parameters of the Lagrangian in a given renormalization scheme. Given the quantitative differences in the values of the mass for the different renormalization schemes, it is of crucial importance to keep in mind the scheme dependence when assessing quark mass values.

[1] The top quark does not actually hadronize, but due to its short lifetime, it cannot be observed directly either.

The direct top quark mass measurements at the Tevatron and the LHC experiments have reached approximately 500 MeV precision [61–63] (world average $m_t = 172.9 \pm 0.4\,\text{GeV}$ [15][2]). The experimental uncertainties are expected to improve to approximately 200 MeV at the HL-LHC [64], while work is ongoing to clarify how the measured top mass value is related to a well-defined top mass in a short-distance renormalization scheme. Pole mass extractions from (differential) cross-section measurements at the LHC have achieved GeV precision [65, 66] (world average $m_t^{\text{pole}} = 173.1 \pm 0.9\,\text{GeV}$ [15]). At electron-positron colliders, a very precise measurement of the top quark mass in a theoretically sound renormalization scheme, with a total uncertainty of around 50 MeV, is possible by scanning the center-of-mass energy through the $t\bar{t}$ production threshold [67–69].

This Chapter assesses the potential of linear electron-positron colliders to measure the top quark mass in associated production of a top quark pair with an energetic photon. A new method is presented, based on a robust experimental technique with a rigorous interpretation of the extracted top quark mass with respect to renormalization schemes. Such a measurement can be performed in continuum $t\bar{t}\gamma$ production at any center-of-mass energy above the $t\bar{t}$ production threshold and does not require a dedicated threshold scan.

The proposed method reconstructs the differential cross section as a function of the invariant mass of the $t\bar{t}$ system. The radiated hard photon reduces the phase available for $t\bar{t}$ production, and the spectrum develops a strong dependence on the top quark mass, as the events effectively return to the $t\bar{t}$ pair production threshold.

The potential for a top quark mass measurement is studied in two concrete scenarios, the CLIC [26, 70] initial-stage run colliding at a center-of-mass energy of 380 GeV and the ILC [23, 25] run at 500 GeV. The statistical uncertainties are estimated for the most up-to-date operating scenarios, which envisage an integrated luminosity of $1\,\text{ab}^{-1}$ for the CLIC initial stage [71] and $4\,\text{ab}^{-1}$ for the ILC run [72]. Realistic experimental acceptance, selection efficiency and resolution

[2]The χ^2 of 6.7 has led the author to scale the uncertainty by a factor 1.3.

are taken into account, based on detailed simulation studies in Refs. [67, 73]. The impact of the luminosity spectrum on this measurement is also assessed in detail.

6.1 Observable definition

Radiative $e^+e^- \to t\,\bar{t} + X + \gamma$ events are considered, such as those depicted in the rightmost diagram of Figure 6.1, where a top quark pair is produced in association with an energetic photon. The momentum carried away by the radiated photon reduces the phase space available for $t\,\bar{t}$ production.

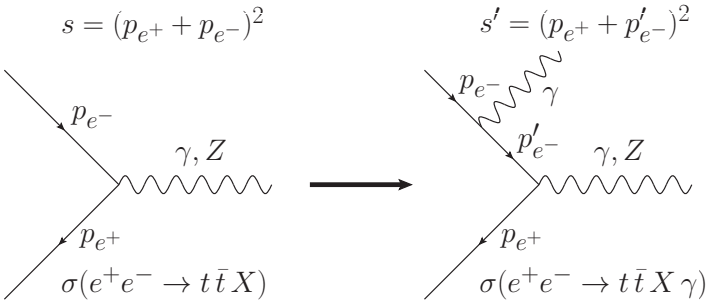

Fig. 6.1 Feynman diagrams representing the center-of-mass energy available for the $t\bar{t}$-pair production before (left) and after (right) the ISR photon emission.

The invariant mass of the $t\bar{t}$ system is labeled as $\sqrt{s'}$. After the photon emission, it is given by:

$$s' = s\left(1 - \frac{2E_\gamma}{\sqrt{s}}\right), \tag{6.1}$$

where $\sqrt{s}$ is the nominal center-of-mass energy of the e^+e^- collider and E_γ denotes the photon energy. The differential cross section as a function of $\sqrt{s'}$ is shown in Figure 6.2 for a center-of-mass energy of 380 GeV and two values of the top quark mass. The maximum sensitivity of the observable is reached at the $t\,\bar{t}$ production threshold (*radiative return* to the $t\,\bar{t}$ production threshold).

Importantly, s' depends only on the nominal center-of-mass energy $\sqrt{s}$ of the e^+e^- collision and on the photon energy E_γ. The center-of-mass energy is precisely

known and the photon energy can be measured accurately in the electromagnetic calorimeter system. Therefore, the reconstruction of s' only depends on these two quantities that are under excellent experimental control. The analysis only requires the identification of the $t\bar{t}+\gamma$ events, without the need of reconstructing the top quark candidates.

In this method, the top quark mass is extracted from a measurement of the differential $e^+e^- \to t\bar{t}\,\gamma_{\mathrm{ISR}}$ cross section versus $\sqrt{s'}$,

$$\frac{d\sigma_{t\bar{t}\gamma}}{d\sqrt{s'}}. \tag{6.2}$$

As seen in Figure 6.2, the sensitivity to the top quark mass is maximal in the region where the photon energy is $E_{\gamma,\mathrm{max}} \simeq \frac{s-4m_t^2}{2\sqrt{s}}$, and the dependence on s' shows the toponium state resonance enhancement.

In practice, photons collinear to the incoming electron and positron beams are not accessible experimentally. Therefore, the cross section differential in both the photon polar angle and the hadronic system invariant mass $\mathrm{d}\sigma_{t\bar{t}\gamma}/(\mathrm{d}\cos\theta\,\mathrm{d}\sqrt{s'})$ is used, where the angle is measured with respect to the beam pipe. The polar angle is integrated over a range limited by the experimental acceptance, typically down to a polar angle of 6 to 10^o.

6.2 Theoretical prediction

An accurate prediction of the $\sqrt{s'}$ distribution requires a *matched* calculation that includes the enhancement of the cross section at the $t\bar{t}$ production threshold due to bound-state effects and remains valid at center-of-mass energies well above threshold. The theoretical model used in this study is based on the NNLL resummed calculation [74] at threshold matched to an NNLO calculation for continuum production. The cross section for $e^+e^- \to t\bar{t}\,X\,\gamma_{\mathrm{ISR}}$ factorizes into the ISR photon emission from the incoming leptons and the $e^+e^- \to t\bar{t}\,X$ inclusive production [75]. The differential cross section of the $e^+e^- \to t\bar{t}+X+\gamma_{\mathrm{ISR}}$ process

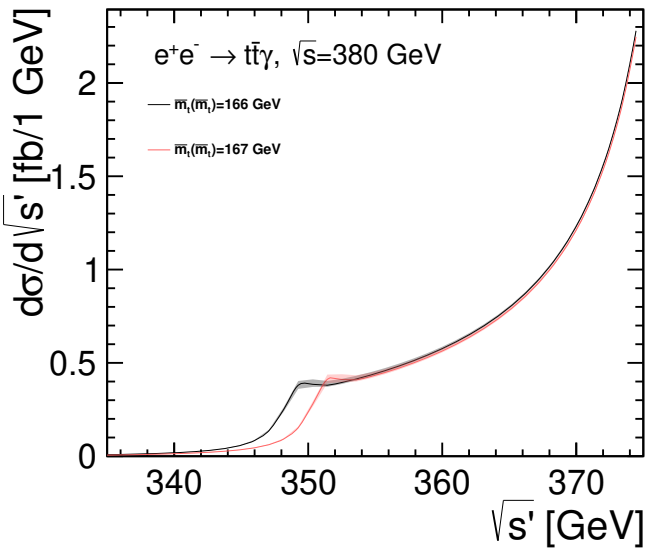

Fig. 6.2 Prediction of the differential cross section versus $\sqrt{s'}$ with the matched NNLL threshold and NNLO continuum calculation. The black and red curves correspond to two values of the top quark mass $\overline{m}_t = 166,\, 167\,\text{GeV}$, respectively. The gray and red shades represent the envelope of the theory uncertainty.

is given as a function of θ and E_γ (or, equivalently, s') for specific values of s and m_t.

The calculation keeps track of the dependence on the top quark mass. Internally, the 1S [76–78] and MSR [79, 80] renormalization schemes are used to compute the cross section. However, the input mass for the numerical evaluation of those is given in the $\overline{\text{MS}}$ scheme. From this point, all mass values and uncertainties will be presented in the $\overline{\text{MS}}$ scheme, as $\overline{m}_t(\overline{m}_t) \equiv \overline{m}_t$ [81].

Theoretical uncertainties on the prediction are estimated by varying the renormalization scales used in the calculation. The hard, soft and ultra-soft scales in the NRQCD calculation are parametrized as a function of two parameters h and f following [82]. The scales h, hf and hf^2 then correspond roughly to the top-quark mass, top-quark three-momentum, and the kinetic energy of the $t\bar{t}$ pair in the center-of-mass frame, respectively. The h and f parameters are varied in

the intervals shown in Table 6.1. In this procedure, the combinations of h and f are chosen such that the ultra-soft renormalization scale remains within a factor two of its nominal value.

Table 6.1 Variations of the parameters h and f that determine the hard, soft and ultra-soft scales of the matched calculation. The nominal calculation corresponds to $h = f = 1$ and the variations follow the procedure of Ref. [82]. The resulting $\sqrt{s'}$ distribution is fitted with the nominal calculation and the resulting shifts in the extracted value of $\overline{m}_t$ are given in the third and fourth rows.

h variations	1/2	1/2	1/2	1	1	1	2	2	2
f variations	1	3/2	2	$\sqrt{1/2}$	1	$\sqrt{2}$	1/2	3/4	1
$\Delta\overline{m}_t$ (MeV) at $\sqrt{s} = 380$ GeV	−43	−46	−44	8	0	−0.3	45	30	29
$\Delta\overline{m}_t$ (MeV) at $\sqrt{s} = 500$ GeV	−54	−58	−55	12	0	−1.5	51	34	32

The differential cross section predictions in terms of $\sqrt{s'}$ with varied scale settings are fitted with the nominal calculation ($h = f = 1$), where the top quark mass in the latter is floated as a free parameter. The difference of the fitted mass with respect to the nominal mass is listed in the third and fourth rows in Table 6.1 for center-of-mass energies of 380 GeV and 500 GeV. The perturbative uncertainty in the mass extraction due to missing higher-order contributions is estimated as the envelope of all top mass variations. This theory uncertainty[3] corresponds to ± 46 MeV at $\sqrt{s} = 380$ GeV and ± 55 MeV at $\sqrt{s} = 500$ GeV.

6.3 Experimental study

In this section the strategy to take into account experimental uncertainties is presented. As seen in Equation 6.1 and Equation 6.2, the measurement of the

[3]This estimate is performed before accounting for the luminisity spectrum of the collider, for collisions with the nominal center-of-mass energy. After accounting it, the impact of the scale variations may be significantly larger. For instance, when accounting for CLIC's luminosity spectrum, the uncertainty grows up to ± 100 MeV. In the following it is assumed that the data can be corrected before extracting the mass.

observable depends exclusively on: the correct identification of the $t\,\bar{t}\,\gamma_{ISR}$ events, the reconstruction of the hard ISR photon energy, and the knowledge of the interaction energy $\sqrt{s}$.

6.3.1 Event selection

The top quark pair production mechanism is the dominant six-fermion process in the relevant range of energies. With its striking signature it is readily identified, reducing the background due to other Standard Model processes to the few %-level. As seen in Figure 6.3, the $t\,\bar{t}$ pairs can decay in leptonic, semi-leptonic and hadronic modes. Each of the modes is reconstructed with a different experimental strategy.

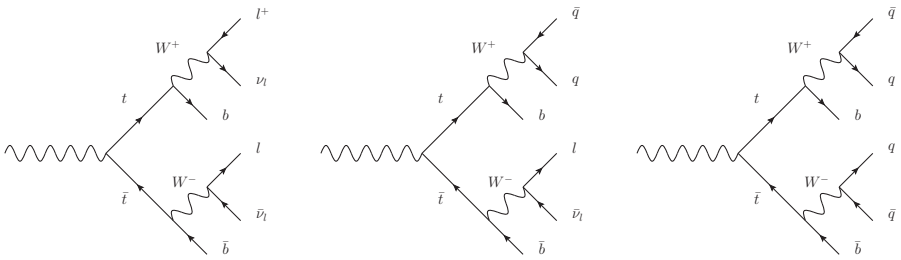

(a) Leptonic decay. **(b)** Semi-leptonic decay. **(c)** Hadronic decay.

Fig. 6.3 Decay channels for the $t\,\bar{t}$ pairs.

For the three decay channels, jets are reconstructed with the VLC algorithm, a sequential recombination algorithm for e^+e^- collisions with robust performance in the presence of background [83]. The two b-tagged jets are identified with the LCFI package [84], a crucial step in the selection. In the case of the semi-leptonic decays, the selection of the lepton+jets final state [67, 73] is furthermore based on the presence of an isolated charged lepton[4]. Also the fully hadronic final state can be efficiently selected [85]. No full-simulation studies are available for the leptonic final state.

Based on the studies in [67], a 90% classification efficiency for $t\bar{t}$ events while suppressing four fermion and quark-pair production backgrounds is achievable.

[4]Electron or muon. Events with hadronic τ-decays are not considered at this stage.

Furthermore, as discussed in the following section, the ISR photon can be identified with efficiencies of the 80% [55]. Nevertheless, to be on the safe side, a conservative overall selection efficiency of 50% is adopted.

6.3.2 Luminosity spectrum

The curves in Figure 6.2 assume that the distribution of the e^+e^- center-of-mass energy is a δ-function at the nominal center-of-mass energy. In practice, beam energy spread leads to a non-negligible width, while beamstrahlung causes a tail towards lower energies. In Figure 6.4 the expected luminosity spectra for the CLIC run at $\sqrt{s} = 380\,\text{GeV}$ and the ILC run at 500 GeV are shown, as generated with the GuineaPig program [86] for the nominal accelerator settings.

The luminosity spectrum has an important effect on the observed $\sqrt{s'}$ distribution. In Figure 6.5 the two dashed curves represent the distribution weighted by the luminosity spectrum expected at CLIC. Compared to the ideal luminosity spectrum, the threshold peak gets smeared out substantially. If left unaccounted, the deviation results in large uncertainties of up to 1 GeV in the top quark mass. Therefore, the correct determination of the luminosity spectrum is paramount for the measurement of the proposed observable.

In Ref. [87] a method was developed to reconstruct the luminosity spectrum in-situ. The Bhabha scattering process $e^+e^- \to e^+e^-$, with a large cross section, simple final state, and precisely predicted angular distribution, is an ideal calibration process. Following the same approach, the luminosity spectrum for CLIC at 380 GeV and ILC at 500 GeV is reconstructed by fitting a complex functional form to the Bhabha spectrum. A detailed account is found in Ref [88].

To realize the full potential of this method the effect of the luminosity spectrum must be included in the observable prediction. To do so, calculations at several center-of-mass energies are weighted by the luminosity spectrum, emulating the sum of many experiments at different center-of-mass energies. Mathematically, the weighting takes the following form

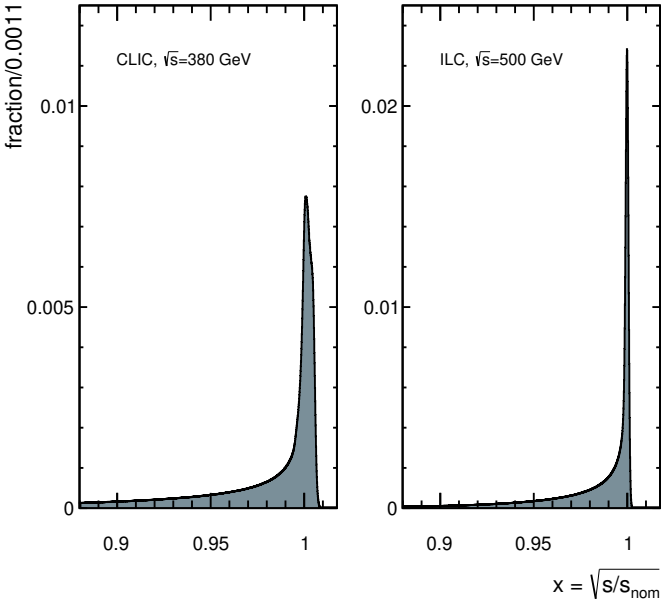

Fig. 6.4 The luminosity spectrum, expressed as the fraction of events per x bin, where x represents the center-of-mass energy of the collision relative to the nominal center-of-mass energy. The spectra correspond to CLIC at $\sqrt{s} = 380\,\text{GeV}$ (left panel) and the ILC at $\sqrt{s} = 500\,\text{GeV}$ (right panel). Note that the y-axis of the ILC spectrum is scaled by a factor two for better visibility.

$$\frac{d\tilde{\sigma}_{t\bar{t}\gamma}}{dE_\gamma} = \sum_{\tilde{s}} \frac{d\sigma_{t\bar{t}\gamma,\tilde{s}}}{dE_\gamma} \times l_{\tilde{s}}, \tag{6.3}$$

where $\frac{d\sigma_{t\bar{t}\gamma,\tilde{s}}}{dE_\gamma}$ is the computation of the observable for a center-of-mass energy of $\sqrt{\tilde{s}}$, and $l_{\tilde{s}}$ is the fraction of the luminosity at $\sqrt{\tilde{s}}$. By transforming E_γ to $\sqrt{s'}$ assuming that $\sqrt{s}$ is the actual collision value, the weighted observable can be defined as

$$\frac{d\tilde{\sigma}_{t\bar{t}\gamma}}{d\sqrt{s'}}. \tag{6.4}$$

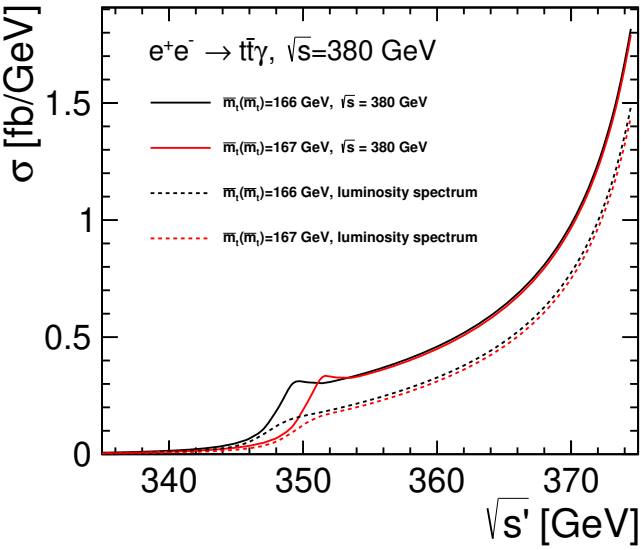

Fig. 6.5 Prediction of the differential cross section versus $\sqrt{s'}$ with the matched NNLL threshold and NNLO continuum calculation. The black and red curves correspond to two values of the top quark mass $\overline{m}_t = 166$, 167 GeV, respectively. The solid curves represent an ideal collider, where all collisions occur at exactly $\sqrt{s} = 380$ GeV, the dashed curves include the effect of the CLIC luminosity spectrum.

The redefinition of the observable makes it dependent on the accuracy of determining the luminosity spectrum. To propagate the uncertainty, a number of spectra are generated by varying the parameters p of the luminosity spectrum fit function within their uncertainty. For each one of these variations a weighted observable is computed, and fitted to Equation 6.4, with the top quark mass floating as a free parameter. The propagated uncertainty is then calculated as $\epsilon_p \, cov \, \epsilon_p^T$, where ϵ_p are the mass shifts for the different p, and cov is the covariance matrix of the parameters p.

6.3.3 Photon reconstruction

Energetic photons leave a characteristic electromagnetic shower in the silicon-tungsten EM calorimeter [89] of the ILD [90] and CLICdet [91] detector concepts envisaged for the ILC and CLIC. They are efficiently reconstructed by the Pandora Particle Flow package [92]. The expected energy resolution of the electromagnetic calorimeter [93] of the linear collider experiments is in the order of

$$\sigma/E = 0.166/\sqrt{E} \oplus 1.1\,\% \tag{6.5}$$

In the following the E_γ distribution will be binned according to this resolution and the result propagated to the $\sqrt{s'}$ distribution.

The most important limitation of the CLIC and ILC detectors for this analysis is the limited coverage in the forward and backward region. The tracking system and the main granular calorimeters extend out to a polar angle of approximately 8°. Therefore, the acceptance of the analysis is limited to the fiducial region $8° < \theta < 172°$. As the distribution of ISR photons is very forward-peaked, this restriction results in a strong penalty. An extension of the acceptance to include the forward calorimeter systems ($4° < \theta < 176°$ would double the available statistics. An extension to $2° < \theta < 178°$ would even quadruple it. As the forward calorimeters are less finely segmented, have relatively poor resolution and must deal with important background levels, this possibility requires a detailed study, that is left for future work.

Finally, as the used theoretical prediction applies to photons from initial-state radiation, the presence of photons from final-state radiation must be suppressed[5]. The studies at the stable-particle level of Ref. [55] establish that a combination of cuts on the photon energy and the isolation angle (minimum angle with respect to the nearest particle, $\Omega_{\gamma,i} > 8°$) is very effective to remove FSR photons, while retaining the sensitivity of the measurement.

[5] In principle, as the FSR is also sensitive to the top quark mass, its contribution could be added to the model.

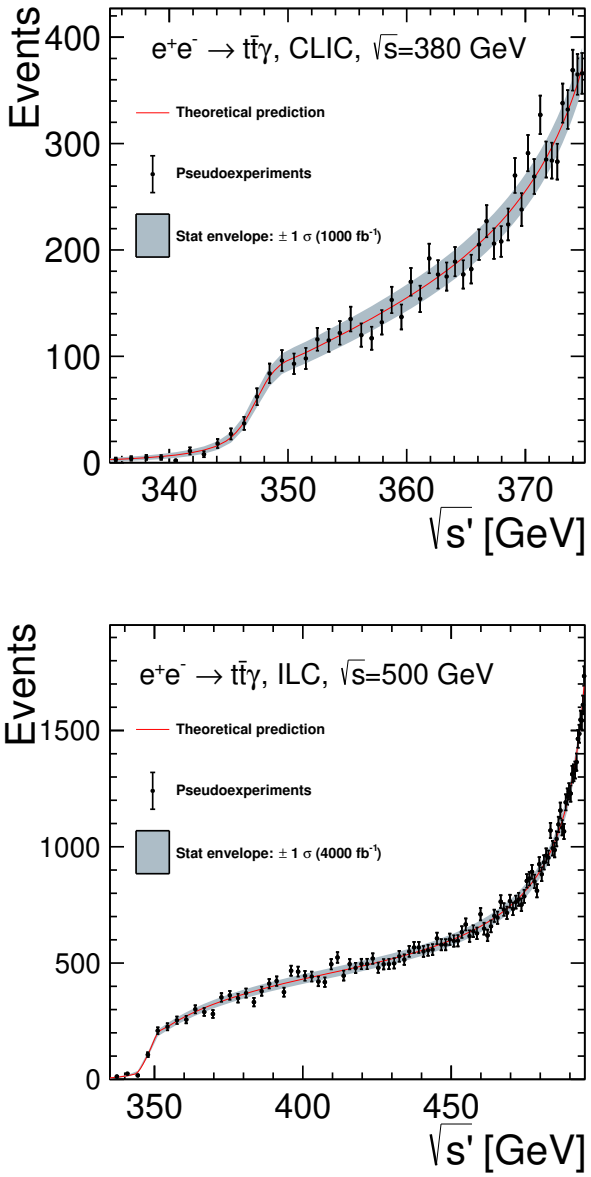

Fig. 6.6 Pseudoexperiments generated with the matched NNLL threshold and NNLO continuum calculation. The top panel shows the result for $\sqrt{s} = 380\,\text{GeV}$, accounting for the CLIC luminosity spectrum, the bottom panel the result for $\sqrt{s} = 500\,\text{GeV}$, accounting for the ILC luminosity spectrum.

The photon energy measurement is the key to the $\sqrt{s'}$ observable. The response of the electromagnetic calorimeter must be calibrated in-situ to achieve a precise control over the photon energy scale. The electron energy response can be calibrated using $Z \to e^+e^-$ decays with a statistical uncertainty smaller than 0.01% [94]. A direct handle on the photon response is found in radiative Z-boson decays (i.e. $Z \to \mu^+\mu^-\gamma$). ATLAS and CMS have applied both methods [95, 96]. Following their results, a conservative uncertainty of 0.1% is assumed.

To propagate this uncertainty, a weighted observable is computed with overestimated and underestimated photon energies, and it is fitted to Equation 6.4, with the top quark mass floated as a free parameter. The propagated uncertainty is directly estimated as the mass shifts.

6.4 Results

The prospects for the top quark mass determination at CLIC and the ILC are estimated producing pseudo-experiments datasets. The expected number of events in a given $\sqrt{s'}$ bin is calculated through Equation 6.4, assuming a mass of $\overline{m}_t = 166$ GeV. The bin width is given by the expected energy resolution of the electromagnetic calorimeter of Equation 6.5. For each scenario 1000 pseudo-experiments are generated by applying poissonian fluctuations around the expected central value.

The magnitude of the fluctuations reflects the expected statistical uncertainty, taking into account the production cross-section, the reshape of the observable by the luminosity spectrum, the integrated luminosity of the official run scenarios[6] and a selection and reconstruction efficiency of 50%. Examples of the pseudo-experiments are shown in Figure 6.6 for CLIC (top) and ILC (bottom). The error bars on the data points correspond to the $\pm 1\,\sigma$ statistical uncertainty. The solid

[6]The nominal polarizations are also accounted for. In the case of ILC the polarized beams suppose an increase of 24% in the statistics. For CLIC the polarization has no effect on the overall luminosity.

Table 6.2 The expected uncertainty on the top $\overline{\text{MS}}$ mass for the runs at $\sqrt{s} = 380\,\text{GeV}$ at CLIC, and at $\sqrt{s} = 500\,\text{GeV}$ at the ILC. For both machines, results are presented for an integrated luminosity of $500\,\text{fb}^{-1}$ and for the nominal operating scenario, from Ref. [26] for CLIC and Ref. [72] for the ILC.

Experiment	CLIC, $\sqrt{s} = 380\,\text{GeV}$		ILC, $\sqrt{s} = 500\,\text{GeV}$	
L_{int} (fb^{-1})	500	1000	500	4000
Statistical	138 MeV	93 MeV	348 MeV	109 MeV
Theory	46 MeV		55 MeV	
Luminosity spectrum[7]	7 MeV		7 MeV	
Photon energy scale[8]	16 MeV		85 MeV	
Total	147 MeV	105 MeV	363 MeV	149 MeV

curve is the nominal prediction and the gray shade represents the envelope of the $\pm 1\,\sigma$ statistical uncertainty.

The pseudo-datasets are fitted to the nominal theoretical prediction with the mass as a free parameter. The statistical uncertainty is estimated as the mean of the uncertainties provided by the TMinuit χ^2 minimization, which is in excellent agreement with the spread of the fitted masses distribution.

The results of the pseudo-experiments as well as the uncertainties assessed in the previous section are presented in Table 6.2.

6.5 Conclusions

A new method to measure the top-quark mass at electron-positron colliders operated at a center-of-mass energy that exceeds the top quark pair production threshold is proposed. In this method, the top quark mass is extracted from the differential distribution of $t\bar{t}\gamma$ events with respect to the invariant mass of the $t\bar{t}$ system, which is related to the photon energy. This method does not require a

[7] The luminosity spectrum uncertainty could not be assessed for ILC in time to be included in this thesis. As a first order approximation, the value for CLIC is assumed.

[8] The photon energy scale systematic affects the observable in a proportionally to $E_{\gamma,\text{max}}$. Given its higher center-of-mass energy, the ILC scenario results more affected.

dedicated threshold scan, while it can provide a mass measurement with a rigorous interpretation in terms of a field-theoretical mass scheme.

The predictions for the observable are based on the factorization of the photon emission and the inclusive $t\bar{t}$ production, which builds on a *matched* NNLL+NNLO calculation. This calculation provides an accurate description of the QCD enhancement of the cross section in the threshold region and remains valid for continuum $t\bar{t}$ production well above the threshold.

The uncertainties that are expected for the CLIC initial stage at $\sqrt{s} = 380\,\text{GeV}$ and the ILC run at $\sqrt{s} = 500\,\text{GeV}$ have been assessed. Statistical uncertainties are evaluated in the realistic conditions and for the nominal operating scenarios. The theory uncertainty is estimated by varying the normalization scales in the calculation. A realistic estimate of the acceptance, selection efficiency, photon energy resolution and luminosity spectrum are also taken into account. A detailed break-down of the uncertainties is presented in Table 6.2.

With relatively modest luminosity, this method can reach a precision of the order of a few 100 MeV, improving the top-quark mass measurement beyond the current precision at hadron colliders. For the nominal integrated luminosity ($1\,\text{ab}^{-1}$) a total uncertainty of 105 MeV is expected for the initial stage of CLIC at $\sqrt{s} = 380\,\text{GeV}$. The ILC run at $\sqrt{s} = 500\,\text{GeV}$ can achieve 149 MeV, making up (to some extent) for the smaller statistics in the threshold region with a very large integrated luminosity ($4\,\text{ab}^{-1}$).

The precision of this method is not quite competitive with that of a dedicated threshold scan [68], but can confirm that measurement with partially orthogonal systematic uncertainties. Further improvements of the method can be envisaged in several directions. The inclusion of photons detected in the forward calorimeters could extend the polar angle range of the analysis and thus reduce the statistical uncertainty. Even greater gain is possible by including associated production of a top quark pair with a (final-state-radiation) gluon in the analysis. Progress in the theory calculation is required to reduce the dominant systematic uncertainty.

This method can access the top quark mass at various energy scales, either by extracting the mass from different parts of the $\sqrt{s'}$ spectrum, or by repeating the measurement in runs at different center-of-mass energies, providing the means to test the running of the top quark mass.

Summary

The works in this thesis are framed within the efforts to build the new generation of particle colliders. The thesis is structured in two parts, and three studies. The first part treats the construction of the Belle II Pixel Detector (PXD), and the second assesses the potential of a new observable to measure the top quark mass in the continuum of the future linear collider.

The first work consisted in the implementation of a quality control test in the main production of the Belle II Pixel Detector. In total, 66 final modules (6 for Belle II phase 2, and 60 for Belle II phase 3) were tested, of which 58 passed the test and 8 were marked as defective. Giving an initial production yield of 87.9%. Thanks to early detection of failures, these modules could be successfully repaired at an intermediate production step, increasing the production yield to 95.5%. The mass production of the PXD modules was a clear success. Taking into account that it included a 50% contingency allowance, and given the 95+% yields, enough modules were produced to populate the PXD while keeping a healthy stock of spares.

After the PXD mass production was completed and the testing was finished, the detailed characterization of the W46_OF1 PXD module was carried out, constituting the second work. First, a standard characterization was performed, checking the overall fitness of the sensor and optimizing its response. From the characterization it was concluded that the module could be categorized as A grade, meaning that no serious problem was spotted and could be installed into the PXD. As part of the characterization, a new method to optimize the sensor

voltages is proposed, providing a quantitative approach that yield standardized and repeatable results that produce homogeneous hitmaps and great signal to noise ratios. To finalize, once the module was fully optimized, an energy calibration was performed in order to calculate the internal gain g_q of the DEPFET sensor. The results were in the order of ~ 750 pA/e^- for a *gate-on* voltage of -2.5 V.

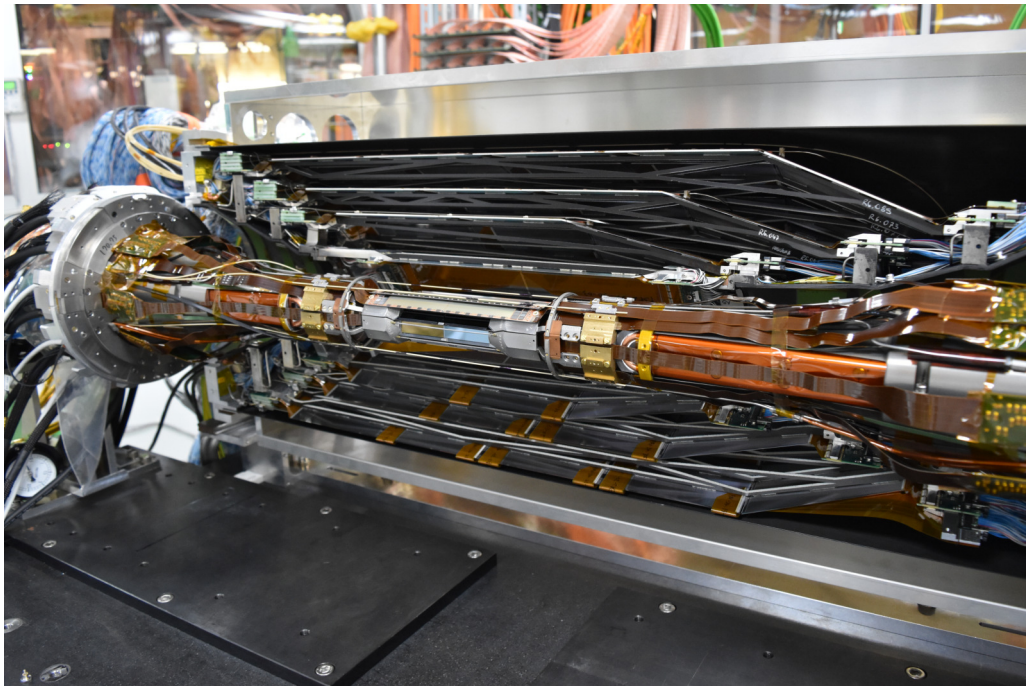

Fig. S.1 Photograph of the VXD installed in September 2018 for the Phase 3 of the Belle II experiment [54]. The PXD could not be completely produced in time, and a de-scoped PXD was installed. Only two ladders out of twelve of the outer layer (in the picture, the ladders facing the outside of the PXD) could be installed. The eight ladders of the inner layer (in the picture, the ladders facing the interior of the PXD) were installed.

In the summer of 2018 the PXD was comissioned and installed onto the beampipe of the Belle II experiment. Unfortunately, a hitch appeared during the glueing stage of the PXD production, dramatically reducing the production yield, and forcing us to stop the procedure before running out of modules. Apparently, small particles were present in the clean room where the modules where glued, and these particles were pressed against the passivation layer on top of the sensors

when they were manipulated in the glueing procedure. These particles pierced the passivation layer, generating different shorts between the DEPFET nets, producing different problems for each affected module.

Nevertheless, the problem was identified timely, and the production could be halted before running out of spares. As seen in Figure S.1, as a result of this hitch, only the first layer and two ladders of the second layer could be produced in time for the Belle II comissioning. As of today, the de-scoped PXD is functional and it participates actively in the data taking, contributing to the tracking system and allowing for precise vertex identification. As for the remaining modules, the production problem has already been solved, and it is expected that a fully populated PXD will be produced and installed in Belle II by late 2020 [97].

Finally, the third and last work, evaluated the potential of linear e^+e^- colliders to measure the top quark mass in radiative events. The uncertainty in the top mass determination was assessed in realistic operating scenarios for the Compact Linear Collider (CLIC) and the International Linear Collider (ILC), including the statistical uncertainty, the theory uncertainty, and dominant experimental systematic uncertainties. With this observable, the top quark mass $\overline{m}_t$ can be determined in a well-defined theoretical scheme with a precision of 105 MeV in the initial stage of CLIC, with $1\,\mathrm{ab}^{-1}$ at $\sqrt{s} = 380\,\mathrm{GeV}$, and with a precision of approximately 149 MeV at the ILC, with $L = 4\,\mathrm{ab}^{-1}$ at $\sqrt{s} = 500\,\mathrm{GeV}$, improving the top-quark mass measurement beyond the precisions at reach in the LHC.

Resumen

La física de partículas es la disciplina que trata la descripción de los componentes elementales de la materia y sus interacciones. Dichas partículas elementales (ver Figura R.1) se dividen entre fermiones (de espín 1/2), que, a su vez, se subdividen en quarks (con carga de color y carga eléctrica), leptones cargados (con carga eléctrica) y leptones neutros (neutrinos); y bosones (de espín 0 o 1).

En el sector fermiónico, seis sabores (i.e. variedades) de partículas elementales llamadas quarks (u, d, c, s, t y b) poseen carga de color y eléctrica. No pueden ser observados directamente debido al *confinamiento del color*, que incentiva la

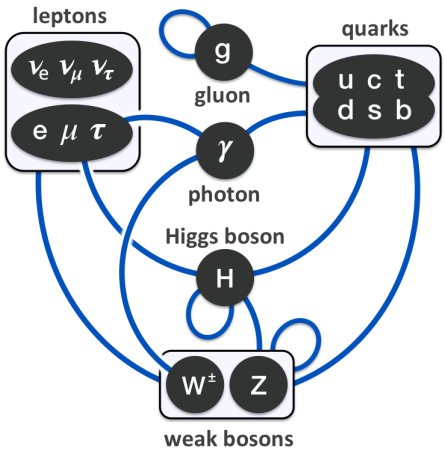

Fig. R.1 Partículas elementales del modelo estándar y sus posibles interacciones [7].

neutralización de la carga de color, formando *hadrones*. Los hadrones pueden ser subdivididos en dos especies: los mesones, formados por un quark y un antiquark de colores opuestos (e.g. rojo y antirojo); y los bariones, formados por tres quarks con los tres colores posibles (rojo, verde y azul). Los mesones (como por ejemplo los piones) son inestables y se desintegran a partículas más estables. Algunos bariones por otra parte son estables y forman los nucleos atómicos de la materia que nos rodea. Por ejemplo, el protón ($u\ u\ d$) y el neutrón ($u\ d\ d$) son bariones.

Por otro lado, hay tres sabores de leptones (e^-, μ^- y τ^-) que poseen carga eléctrica y otros tres sabores (ν_e, ν_μ, ν_τ) que son neutros. A diferencia de los quarks, los leptones sí pueden ser observados directamente. El electrón e^- es el más representativo de los leptones, formando estados ligados tales como los átomos o las moléculas. Para cada uno de los 12 fermiones fundamentales, existe una copia con la misma masa y cargas y números cuánticos opuestos, llamada antipartícula. Resultando en un total de 24 fermiones fundamentales. Sin embargo, la mayor parte de la materia que nos rodea, está formada por tan solo tres de estos fermiones: los quarks u y d que componen los nucleos atómicos, y el electrón e^- que neutraliza la carga eléctrica de los núcleos dando lugar a los átomos.

En el sector bosónico, los cuatro bosones fundamentales de espín 1 (γ, g, Z y $W^\pm$) actúan como mediadores de las interacciones fundamentales, mientras que el bosón de Higgs (de espín 0) proporciona el mecanismo de Higgs que dota al resto de partículas de masa. En concreto, el fotón γ es el propagador de la fuerza electromagnética que actúa sobre la carga eléctrica. El gluón g propaga la fuerza fuerte, que actúa sobre la carga de color. Y los bosones Z y W propagan la fuerza débil, que actúa sobre el isospín débil.

El modelo estándar (SM) es un marco teórico autocontenido que describe las interacciones débiles, fuertes y electromagnéticas entre las particulas elementales. Fue formulada a mitad de los años 70, prediciendo una serie de partículas que no habían sido observadas en aquél momento. En la Tabla R.1 se recopilan aquellas partículas predichas por el SM que fueron posteriormente descubiertas por distintos experimentos. En la actualidad, todas las partículas del SM han sido confirmadas experimentalmente.

Tabla R.1 Partículas elementales predichas por el modelo estándar y observadas a posteriori en los distintos experimentos. [15].

Año	Partícula	Institución	Colisionador (experimento)	Haces
1977	b	Fermilab	Proton Area (E288)	p
1979	g	DESY	PETRA (TASSO)	e^+e^-
1983	W y Z	CERN	Sp$\bar{p}$S (UA1 y UA2)	$p\bar{p}$
1995	t	Fermilab	Tevatron (CDF y DØ)	$p\bar{p}$
2000	ν_τ	Fermilab	Tevatron (DONUT)	p
2012	h	CERN	LHC (CMS y ATLAS)	pp

Su formulación se basa en la Teoría Cuántica de Campos (QFT), donde cada partícula (y antipartícula) es descrita como la excitación de su campo cuántico afín, que permea completamente el espacio-tiempo. Las partículas y sus interacciones están descritas en su Lagrangiano $\mathcal{L}_{SM}$, que es construido como el más general que es renormalizable e incluye las siguientes simetrías: el grupo de simetrías globales de Poincaré, que da lugar a la invarianza de cambios de referencia inerciales, a las rotaciones en el espacio y a las traslaciones en el espacio-tiempo; y, a las simetrías gauge locales $\mathrm{SU}(3)_C \otimes \mathrm{SU}(2)_L \otimes \mathrm{U}(1)_Y$, que describen las interacciones fuertes y electrodébiles.

Pese al gran éxito que supuso la formulación del SM, la teoría no es perfecta. En concreto, el modelo no es capaz de explicar la masa de los neutrinos y sus oscilaciones, la interacción gravitatoria, la ausencia de observaciones de la violación de CP en el sector fuerte y la composición del universo (i.e. no explica la materia oscura, la energía oscura ni la asimetría entre materia y antimateria en el universo).

Es por ello que para avanzar en nuestro conocimiento del campo necesitamos de experimentos que aporten nueva física, ayudándonos a elaborar nuevos modelos que solventen las deficiencias del SM. En este sentido, tal y como se muestra en la Tabla R.2 la construcción de nuevos colisionadores leptónicos nos permite acceder a distintos programas de física para las distintas escalas energéticas. En concreto, dichos colisionadores nos permiten por un lado realizar medidas de gran precisión

Tabla R.2 Principales procesos físicos del modelo estándar (y más allá del modelo estándar) accesibles en colisionadores leptónicos a diferentes escalas energéticas [16].

Energía	Proceso	Programa de física
10.6 GeV	$e^+e^- \to \Upsilon(4s) \to B^0\bar{B}^0$	física del sabor
91 GeV	$e^+e^- \to Z$	parámetros electrodébiles
160 GeV	$e^+e^- \to WW$	masa del W
250 GeV	$e^+e^- \to Zh$	acoplamientos del Higgs
350 - 400 GeV	$e^+e^- \to t\bar{t}$	masa y acoplamientos del top
	$e^+e^- \to WW$	acoplamientos del W
	$e^+e^- \to \nu\bar{\nu}h$	acoplamientos del Higgs
500 GeV	$e^+e^- \to f\bar{f}$	búsqueda del Z'
	$e^+e^- \to t\bar{t}h$	acoplamiento del Higgs-top
	$e^+e^- \to Zhh$	autoacoplamiento del Higgs
	$e^+e^- \to \tilde{\chi}\tilde{\chi}$	búsqueda de supersimetría
	$e^+e^- \to AH, H^+H^-$	búsqueda de Higgs adicionales
700 - 1000 GeV	$e^+e^- \to \nu\bar{\nu}hh$	autoacoplamiento del Higgs
	$e^+e^- \to \nu\bar{\nu}VV$	búsqueda del Higgs compuesto
	$e^+e^- \to \nu\bar{\nu}t\bar{t}$	búsqueda del top compuesto
	$e^+e^- \to \tilde{t}\tilde{t}^*$	búsqueda de supersimetría

que nos ayuden a encontrar discrepancias en el SM, y por otro lado explorar la frontera energética, buscando nuevos sucesos y partículas.

Los trabajos en esta tesis aportan un granito de arena al desarrollo y construcción de los colisionadores e^+e^- de última generación. La tesis puede ser dividida en dos partes: por un lado, el desarrollo y construcción del Detector de Píxeles del experimento Belle II de la factoría de mesones B SuperKEKB; y por otro lado, la propuesta de un nuevo observable para medir la masa del quark top en el continuo de los futuros colisionadores lineales propuestos: el International Linear Collider (ILC) y el Compact Linear Collider (CLIC).

Detector de Píxeles del experimento Belle II

El Detector de Píxeles (PXD) del experimento Belle II consiste en las dos capas más internas de silicio activo del detector. Dichas capas se situan a 14 y 22 mm del punto de interacción, estando la primera capa a tan solo 4 mm del tubo del haz. Dada la cercanía del detector al punto de interacción, el PXD debe ser granular, rápido, ligero y capaz de soportar grandes dosis de radiación. Es por ello se decide construir el PXD utilizando la tecnología de píxeles DEPFET.

El Transistor de Campo Eléctrico Desertizado (DEPFET) es una tecnología avanzada de detectores de semiconducción que permite la detección de partículas y amplificación de la señal en el mismo dispositivo. Como puede verse en la Figura R.2, el píxel diseñado para el PXD consiste en un MOSFET de canal P integrado en un sustrato de silicio de tipo N de alta resistividad completamente desertizado. Un mínimo de potencial llamado *puerta interna* es creado bajo la puerta del MOSFET, atrayendo los electrones excitados en su alrededor.

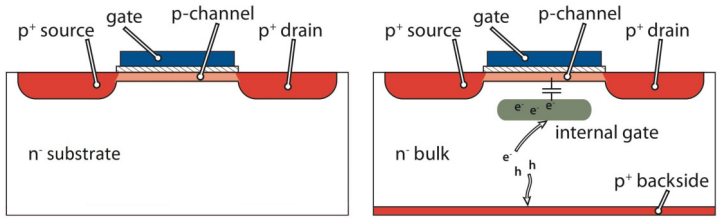

(a) MOSFET de canal P. **(b)** Píxel DEPFET.

Fig. R.2 Representación esquemática de un MOSFET de canal P (a la izquierda), y de un píxel DEPFET (a la derecha) [34].

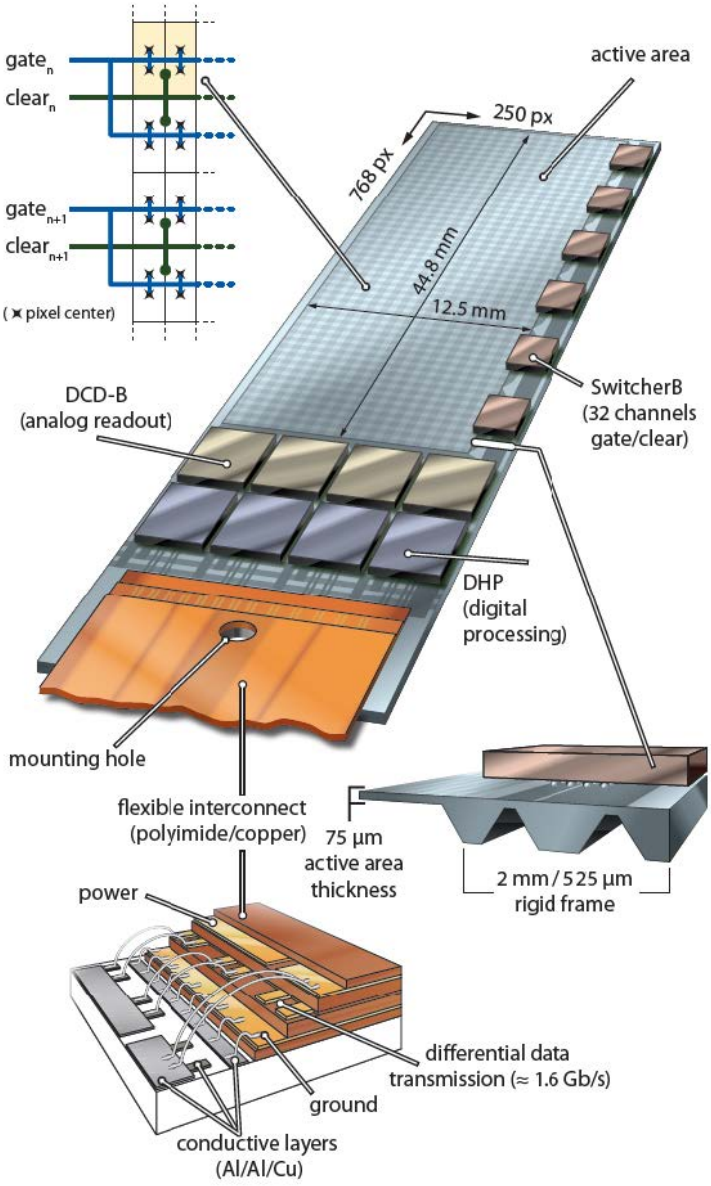

Fig. R.3 Representación de un módulo de la capa interna del PXD, con detalles de la matriz de píxeles DEPFET, los tres ASICs necesarios para operar el sensor y el cable de Kapton usado para conectar el módulo con la fuente de alimentación, la electrónica de control y el sistema de adquisición de datos [34].

La carga atrapada bajo la puerta interna se acopla capacitivamente a la puerta del MOSFET, modulando así la corriente que fluye desde la fuente hacia el sumidero del transistor, proporcionando una medida amplificada de la carga depositada en la puerta interna. A través de implantes adicionales las cargas son guiadas hacia la puerta interna de una forma efectiva, y tras la medida, la puerta interna puede ser vaciada de cargas con el mecanismo de limpieza.

Los sensores DEPFET diseñados para el PXD están compuestos por una matrizde píxeles de 250 columnas $\times$ 768 filas, que son leídos mediante obturación iterativa de cuatro filas. Es decir, primero se leen las cuatro primeras filas del sensor, después las cuatro siguientes, y así sucesivamente. El Switcher se encarga de coordinar la alimentación de los píxeles con la electrónica de lectura para realizar correctamente la obturación iterativa.

La estructura mínima funcional del PXD son los módulos. Tal y como se puede ver en la Figura R.3, el módulo consta de un sensor DEPFET, los Switchers, los DCDs que digitalizan la corriente proveniente de los píxeles, los DHPs que controlan el resto de elementos del sensor y manipulan y transmiten los datos, y el cable de Kapton usado para conectar el módulo con el mundo exterior.

Pegando dos módulos de forma enfrentada (final con final) se forma una lámina del PXD. Para construir la primera capa, 8 láminas se posicionan se posicionan alrededor del tubo del haz formando un octógono ligeramente solapado de 14 mm de radio. Asimismo, la segunda capa se forma con 12 láminas formando un dodecágono ligeramente solapado a 22 mm de radio. En total, 40 módulos de cuatro geometrías distintas[1] son necesarios para la construcción del PXD.

Control de calidad en la producción del PXD

La producción de módulos para el PXD es un proceso complejo que requiere multitud de pasos. El proceso comienza con dos obleas de silicio, una oblea

[1] Los módulos de la primera capa son más cortos que los de la segunda. Y los módulos de la sección “hacia delante” son un reflejo especular de la sección “hacia atrás”.

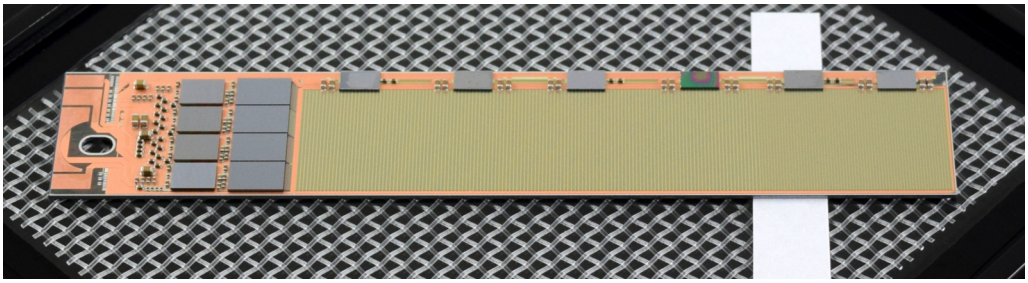

Fig. R.4 Fotografía de un módulo de la capa exterior hacia delante del PXD después del soldado de los ASICs y los SMDs.

de alta calidad donde las estructuras DEPFET y las capas de metalización son implementadas a través de una serie de procesos litográficos e implantaciones de dopantes; y otra oblea que es adherida bajo la oblea del detector dotando de rigidez mecánica al conjunto. Tras la fusión de ambas obleas, la oblea inferior es adelgazada a través de un proceso de rascado anisotrópico profundo, que deja completamente expuesta la zona sensora (con un grosor de 75 µm) mientras que preserva un marco rígido a su alrededor (de 525 µm).

Posteriormente, la oblea de silicio es cortada obteniendo los diferentes módulos. Y sobre éstos, se sueldan los ASICs y los SMDs que convierten el módulo (Figura R.4) en una unidad funcional. Tras finalizar el módulo, el cable de Kapton es soldado sobre éste, aportando rigidez mecánica al conjunto y la conexión eléctrica para las redes eléctricas de mayor corriente. Finalmente, una serie de hilos son soldados entre la superficie del módulo y la superficie del cable de Kapton, proporcionando el resto de conexiones eléctricas necesarias para operar el módulo.

Una vez el cable de Kapton ha sido ensamblado, el módulo es caracterizado y optimizado en el laboratorio. Si la calidad de éste es suficiente, el módulo se pega a otro módulo formando una lámina del PXD. La construcción del PXD concluye con la instalación de estas láminas formando un octógono y dodecágono, para la primera y la segunda capa respectivamente, alrededor del tubo del haz.

Dada la complejidad en la producción de los módulos del PXD, hay un alto número de puntos de fallos posibles durante el ensamblado. Dichos fallos serían

detectados tras el soldado del cable Kapton, durante la caracterización del módulo. Sin embargo, el ensamblado del Kapton supone una seria limitación para la posible reparación del módulo defectuoso. La solución pasa por operar los módulos tras el soldado de los componentes electrónicos, justo antes del soldado del Kapton. Para ello, una tarjeta de agujas a medida fue diseñada, actuando de interfaz entre los sistemas de control y adquisición de datos y el módulo.

Para realizar el testado de los módulos, una estación de pruebas con la tarjeta de puntas (Figura R.5b) fue instalada en la sala blanca del MPG HLL (Figura R.5a). Como parte del compromiso del IFIC con la colaboración DEPFET del PXD de Belle II, y de los trabajos realizados en esta tesis, un protocolo de calidad de control y testado de los módulos fue desarrollado, puesto en servicio con módulos de preproducción, y realizado sobre la producción masiva de módulos finales del PXD.

El protocolo consiste en la realización del aterrizaje de las agujas de la tarjeta sobre el módulo, encendiéndolo y comprobando el consumo energético de las distintas redes de alimentación. Si la alimentación es correcta, el protocolo prosigue probando la correcta interpretación de los comandos de control enviados al módulo y la integridad en la transmisión de datos al DAQ. En caso de que la

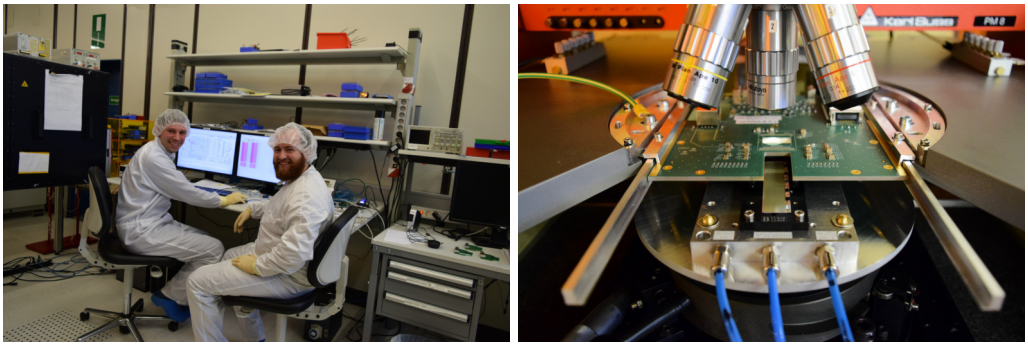

(a) Sala blanca del HLL. **(b)** Estación de pruebas.

Fig. R.5 En la fotografía de la izquierda, Christian Koffmane y yo en la sala blanca del HLL depurando un módulo del PXD. En la de la derecha, módulo en la estación de pruebas de la sala blanca bajo la tarjeta de agujas listo para ser testado.

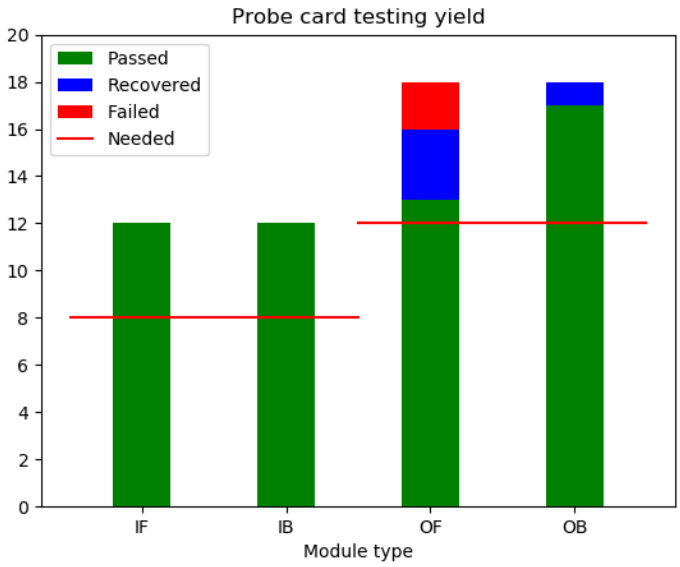

Fig. R.6 Resultados de la producción masiva de módulos del PXD (solo los módulos para la fase 3 de Belle II) en el testado realizado con la tarjeta de agujas. De los 60 módulos producidos, 54 pasaron el test y 6 resultaron defectuosos. De esos 6, 4 pudieron ser reparados.

comunicación entre el mundo exterior y el módulo funcione adecuadamente, el sensor es encendido y el módulo es operado completamente, excitando los píxeles y comprobando la respuesta obtenida.

En total, 60 módulos finales fueron testados durante la campaña de producción masiva del PXD, participando como un eslabón más de la cadena de producción de módulos. De los 60 módulos, inicialmente 54 pasaron las pruebas, y 6 fueron marcados como defectuosos. Éstos últimos fueron depurados, identificando los fallos que los afectaban y estudiando la posibilidad de su reparación. Gracias a la detección temprana de estos fallos, 4 de los 6 módulos defectuosos pudieron ser reparados, elevando el rendimiento de la producción del 90% al 96.7%.

Pese a que la producción fue un éxito rotundo, un fallo en el pegado de los módulos redujo el rendimiento de la producción en el último paso, resultando

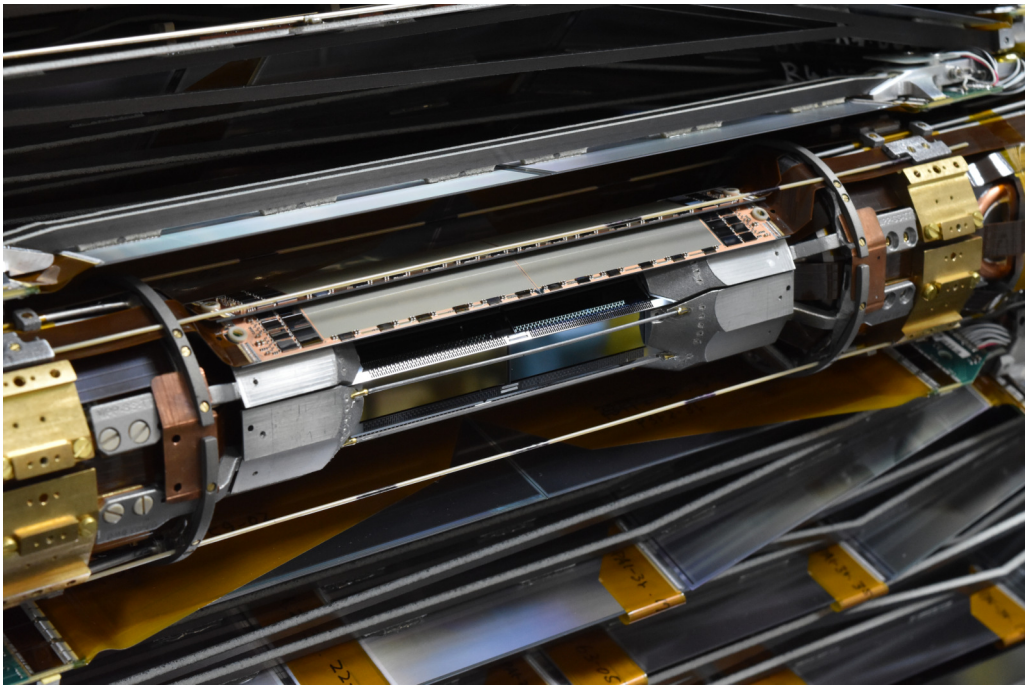

Fig. R.7 Fotografía del Detector de Píxeles instalado en el experimento Belle II en septiembre del año 2018. Por problemas en la producción de las láminas (durante el pegado de los módulos) la segunda capa del detector no pudo ser completamente producida a tiempo, y solo dos láminas de la segunda capa fueron instaladas. La primera capa pudo ser instalada completa.

imposible la entrega del PXD completo a tiempo para su instalación en Belle II durante el verano del año 2018. Para la puesta a punto del detector se llegó a entregar la primera capa completa del PXD y 2 láminas de la segunda capa.

Esta versión reducida del PXD pasó la puesta a punto del experimento y participa activamente a día de hoy en la toma de datos de Belle II. Una versión completa está siendo producida en la actualidad, con vistas a ser instalada en el parón técnico del año 2020.

Caracterización de módulos del PXD

Como se comentaba en la sección anterior, durante la producción masiva del PXD los módulos son caracterizados y optimizados previo paso al pegado de las láminas. Tras la finalización del testado de calidad de producción, hice una pequeña estancia en el Laboratorio de Silicio del Instituto de Física de la Universidad de Bonn, donde colaboré en la caracterización final de los módulos tras el ensamblado de los cables de Kapton. Por otra parte, aprovechando la disponibilidad del módulo, también realicé estudios en profundidad de la respuesta del sensor ante cambios en los voltajes suministrados, de la variación del umbral en la transmisión de datos con supresión de ceros[2], y de la ganancia interna $g_q = \frac{dI}{dq}$ del sensor DEPFET.

Dada la importancia de la uniformidad de respuesta en los módulos del PXD, el primer paso consiste en realizar una caracterización estándar del módulo. Dicha caracterización se realiza siguiendo el documento técnico "The PXD Mass Testing Handbook", que detalla el protocolo a seguir. En concreto, la caracterización consta de

- Una serie de comprobaciones de seguridad, tales como la comprobación del consumo eléctrico de las diferentes redes, la correcta interpretación de los comandos de control o la integridad en la transmisión de datos al DAQ.
- La correcta elección del punto de muestreo en la comunicación de datos entre los distintos ASICs.
- Configuración y calibración de las curvas de transferencia de los ADCs.
- Optimización de los pedestales del sensor y activación de sus mecanismos de compresión y corrección.
- Evaluación de los voltajes óptimos de operación de los píxeles DEPFET.

[2]Esta técnica consiste en comunicar solo los valores que superan cierto umbral en lugar de todo el fotograma obtenido por el sensor. De esta manera se reduce la cantidad de datos a transmitir, relajando así los requerimientos técnicos en la tranferencia y almacenaje de datos.

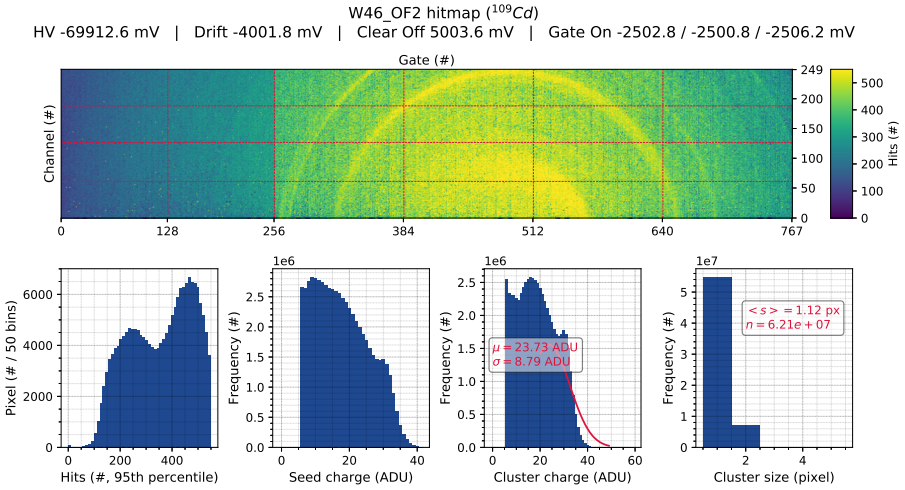

Fig. R.8 Mapa de impactos registrados por el módulo usando la fuente ^{109}Cd, en una configuración ineficiente (*high voltage* = −70 V, *drift* = −4 V, *clear-off* = 5 V). El mapa de impactos representa los clústeres reconstruidos. Bajo el mapa, los histogramas representan la distribución del número de impactos registrados en cada píxel, de la carga en la semilla del clúster, de la carga del clúster y del tamaño del clúster. El fotopico en la carga del clúster es ajustado a una distribución gausiana. El número de clústeres en el mapa de impactos y el tamaño medio del clúster también se indica.

En general, los resultados de la caracterización fueron altamente satisfactorios, y el módulo fue calificado como de alta calidad. Sin embargo, durante el último paso, la evaluación de los voltajes óptimos de operación, se observó una dependencia dramática del rendimiento del módulo con los voltajes suministrados. Como se puede ver en la Figura R.8, para ciertos voltajes, el mapa de impactos muestra una serie de *anillos* que indican una eficiencia de detección inhomogénea. Asimismo, en estos casos la carga reconstruida no tiene la forma gausiana esperada del fotopico del espectro de la fuente radiactiva empleada (^{109}Cd).

Sin embargo, en otras configuraciones, el rendimiento del módulo es más acorde a lo esperado. Como puede comprobarse en la Figura R.9, con una mejor elección de los voltajes suministrados el módulo es capaz de proporcionar fotogramas homogéneos y distribuciones de carga con un perfil claramente gausiano.

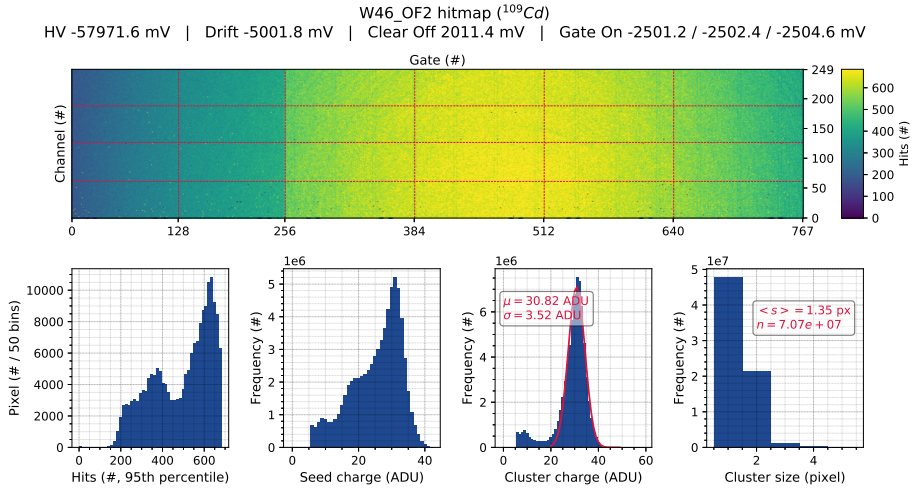

Fig. R.9 Mapa de impactos registrados por el módulo usando la fuente ^{109}Cd, en una configuración funcional (*high voltage* $= -58$ V, *drift* $= -5$ V, *clear-off* $= 2$ V).

Vista la importancia en la elección de los voltajes suministrados, un nuevo método más robusto de optimización es propuesto. Dicho método consiste en la determinación cuantitativa de tres figuras de mérito con las cuales evaluar objetivamente la calidad de los fotogramas obtenidos en las distintas configuraciones. Concretamente se evaluan

- La amplitud de la señal, estimada como el parámetro μ del ajuste a una gausiana de la distribución de carga de los clústeres.
- La homogeneidad del mapa de impactos, estimada como el parámetro $h = \sum_{puertas} \frac{<\text{carga del clúster}>^2_{puerta_i}}{Var(\text{carga del clúster})_{puerta_i}}$.
- La compartición de carga entre píxeles, estimada como el tamaño medio de los clústeres reconstruidos.

Como puede verse en las Figuras R.10a y R.10b, un comportamiento muy similar se observa en la amplitud de la señal y en la homogeneidad del mapa de impactos: en general, el aumento de HV empieza teniendo un impacto positivo

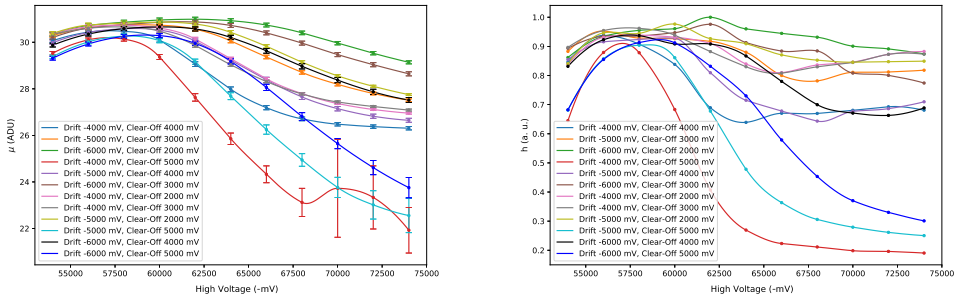

(a) Amplitud de la señal. **(b)** Homogeneidad del mapa de impactos.

Fig. R.10 Amplitud de la señal estimada como el parámetro μ obtenido del ajuste gausiano al fotopico de la distribución de la carga del clúster; y homogeneidad del mapa de impactos estimada según el parámetro h definido en Equation 5.2 para las medidas de la fuente radioactiva ^{109}Cd variando los voltajes suministrados al sensor DEPFET.

en los mapas obtenidos, pero llegado cierto punto la tendencia cambia, y el crecimiento de HV empieza a deteriorar los resultados obtenidos. Dicho punto de inflexión depende de los valores de *drift* y *clear-off*, habiendo ciertos valores para los cuales la dependencia con HV es más suave. Aparentemente, mientras que el silicio no está completamente desertizado, el aumento de HV es beneficioso para la respuesta del sensor, pero una vez alcanzada la completa desertización, el incremento de HV perturba los campos eléctricos vecinos (como *drift* y *clear-off*), empeorando el rendimiento del sensor.

Respecto a los anillos, su aparición puede explicarse por pequeñas inhomogeneidades en la resistividad de las obleas de silicio empleadas en la manufactura de los módulos. Estas diferencias en la resistividad se traducen en diferentes voltajes para la completa desertización del píxel en distintas regiones, y manifestándose como anillos en el mapa de impactos. De esta forma, la correcta optimización de los voltajes consiste en elegir los pares de *drift* y *clear-off* que son menos susceptibles a las variaciones en HV, y el valor de HV que maximiza las figuras de mérito mencionadas anteriormente.

Una vez optimizado, se realizó el estudio de la variación del umbral en la transmisión de datos con supresión de ceros. Para ello se tomaron datos con

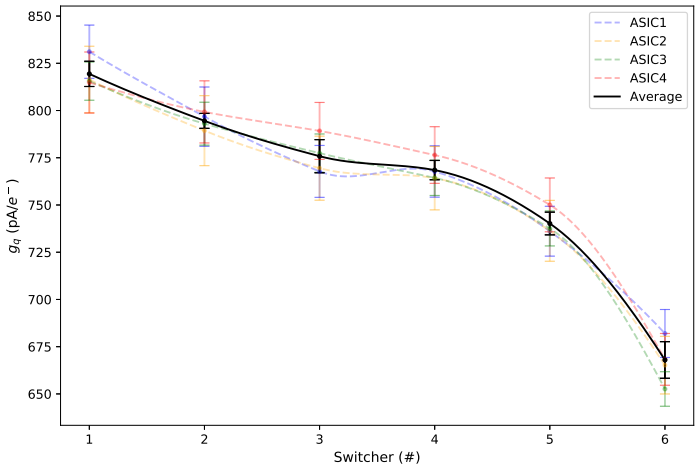

Fig. R.11 Ganancia interna g_q de los píxeles DEPFET para las distintas regiones del sensor, con *gate-on* $= -2.5$ V. En negro, la media para los cuatro ASICs en función de la región de los Switchers.

y sin fuentes radiactivas a diferentes umbrales. Se observó que el aumento del umbral en dos unidades suponía una reducción importante del ruido en el mapa de impactos (por un factor 35), aunque por otro lado, también supone un descenso importante en el tamaño medio de los clústeres. Al aumentar el umbral una parte importante de la carga compartida no es registrada, perdiendo información valiosa para aumentar la resolución espacial del sensor. Dado que el ruido registrado es insignificante ya en el umbral nominal, el aumento del umbral solo proporciona inconvenientes[3].

Por último, la ganancia interna g_q del módulo fue medida. Para ello, primero se realizó una calibración energética del módulo con cuatro fuentes de radiación γ. Sabiendo la cantidad de pares electrón-hueco creados en el silicio[4], la relación entre la carga depositada y la corriente digitalizada, y la calibración ADU/nA de los ADC se obtienen los resultados mostrados en la Figura R.11.

[3] Al menos en el entorno limpio de fondo radiactivo del laboratorio, las conclusiones podrían cambiar en ambientes de gran fondo radiactivo.

[4] Crear un par electrón-hueco en el silicio desertizado requiere 3.67 eV de energía.

Los resultados van desde los 675 a los 820 pA/e^- desde las regiones más alejadas de la electrónica a las más cercanas. Esta diferencia en la ganancia podría ser explicada debido a la diferencia en los tiempos transitorios de subida y bajada de la señal de los píxeles. La corriente de los píxeles más lejanos experimentaría una mayor capacitancia en su camino a la electrónica, traduciéndose en transitorios más largos. Dado que el punto de muestro de los ADCs es fijo, la diferencia en los transitorios podría manifestarse en la medida de g_q, explicando el comportamiento observado.

Medida de la masa del quark top a través de sucesos radiativos

El quark top juega un rol importante en el modelo estándar. Siendo el quark más pesado, el valor de su masa tiene un papel fundamental en el cálculo de multitud de predicciones teóricas en el modelo estándar. Sin embargo, la medida de su masa resulta especialmente compleja. Dado que los quarks hadronizan instantáneamente, no pueden ser observados en libertad, y por tanto su masa no puede ser medida directamente. Sus masas deben ser determinadas a través de su influencia en los procesos de QCD, haciendo dichas medidas dependientes de la teoría. En concreto, las masas medidas se corresponden con el parámetro de la masa en un esquema de renormalización dado.

En la actualidad, las medidas más precisas de la masa del quark top se han producido en el Tevatron y el LHC, dando lugar a un resultado combinado de $m_t = 172.9 \pm 0.4\,\text{GeV}$, en un esquema de renormalización indeterminado. Dicha indeterminación en la definición de la masa medida añade una incertidumbre extra del orden del GeV. La medida actual más precisa en un esquema de renormalización fijado ha sido obtenida en el LHC, obteniendo una medida de la masa polo de $m_t^{\text{pole}} = 173.1 \pm 0.9\,\text{GeV}$. En el entorno limpio de los colisionadores leptónicos, medidas de la masa del quark top con precisiones del orden de 50 MeV son alcanzables en un esquema de renormalización conocido a través del barrido del umbral de producción del par $t\bar{t}$.

Como parte de esta tesis, se evalua el potencial de un nuevo método para medir la masa del quark top en un esquema de renormalización concreto en el continuo[5] de un futuro colisionador leptónico. Dicho método supone una medida alternativa que no compite en la precisión alcanzable con el barrido del umbral, sino que proporciona una medida adicional con errores sistemáticos parcialmente ortogonales a la medida dedicada.

La propuesta consiste en la medida de sucesos radiativos en los que el par $t\bar{t}$ se produce en asociación con un fotón duro ISR proveniente del electrón o del positrón del estado inicial. Como se puede ver en la Figura R.12, el fotón radiado reduce el espacio fásico disponible para la producción del par $t\bar{t}$, y su espectro energético tiene una gran dependencia con la masa del quark top, dependencia mayor conforme los sucesos retornan a nivel efectivo al umbral de producción[6] del par $t\bar{t}$.

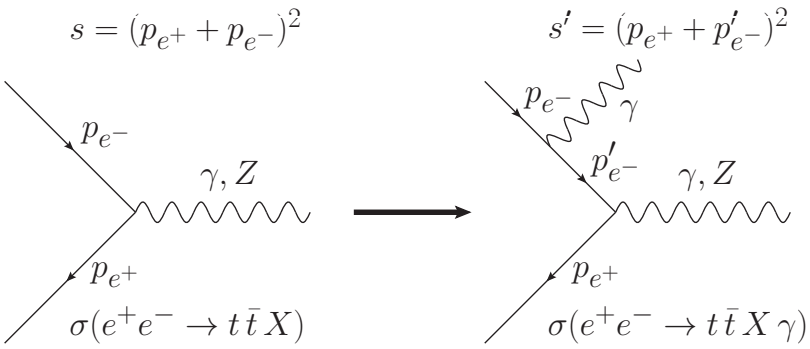

Fig. R.12 Diagramas de Feynman representando la energía en el centro de masas disponible para la producción de un par $t\bar{t}$ antes (a la izquierda) y después (a la derecha) de la emisión de un fotón ISR.

[5]El observable puede ser medido en cualquier colisionador leptónico cuya energía de centro de masas sea superior al umbral de producción de pares $t\bar{t}$. Sin embargo, cuanto más alejada sea la energía de colisión de dicho umbral, peor será la resolución del observable respecto de la masa del quark top.

[6]La sensibilidad del método es máxima en la región en la que el fotón radiado produce el retorno al umbral de producción, es decir, cuando la energía del fotón es del orden de $E_{\gamma,\max} \simeq \frac{s-4m_t^2}{2\sqrt{s}}$.

La energía en el centro de masas $\sqrt{s'}$ del sistema $t\bar{t}$ se ve reducida por la emisión del fotón, tomando el valor

$$s' = s\left(1 - \frac{2E_\gamma}{\sqrt{s}}\right), \tag{R.1}$$

donde $\sqrt{s}$ es la energía nominal del colisionador e^+e^- y E_γ es la energía del fotón ISR. El observable es por tanto definido como la sección eficaz diferencial del proceso $e^+e^- \to t\bar{t}\gamma_{ISR}$ en función de $\sqrt{s'}$,

$$\frac{d\sigma_{t\,\bar{t}\,\gamma}}{d\sqrt{s'}}, \tag{R.2}$$

que depende fuertemente del valor de la masa del quark top, tal y como puede verse en la Figura R.13. A nivel experimental, la medida del observable requiere únicamente de la identificación de sucesos $t\bar{t}\gamma$ y la reconstrucción de la energía del fotón en el calorímetro electromagnético.

A nivel teórico, el observable está descrito por la factorización de la sección eficaz por un lado de la emisión de fotones ISR por parte del electrón o positrón inicial, y por otro lado del cálculo de la sección eficaz inclusiva de producción de pares $t\bar{t}X$. Éste último consiste en un cálculo de última generación a orden 3 en α_s combinando la descripción del umbral en un cálculo resumado NNLL, que incluye el aumento de la sección eficaz debido a los efectos de estado ligado del par $t\bar{t}$; con la descripción del continuo a orden NNLO, que modela el comportamiento más allá del umbral de producción.

El modelo utiliza como parámetro la masa del quark top $\overline{m}_t(\overline{m}_t) \equiv \overline{m}_t$ en el esquema de renormalización de substracción mínima, $\overline{\text{MS}}$. Aunque internamente las masas en los esquemas 1S y MSR son utilizadas en los cálculos NNLL y NNLO, respectivamente.

El error teórico del modelo debido a los órdenes no calculados es estimado variando las escalas de renormalización del cálculo asociadas a: la masa y momento de los quark top, y la energía cinemática del par $t\bar{t}$ en el sistema de referencia de centro de masas. El impacto de la variación de escalas es evaluado para dos

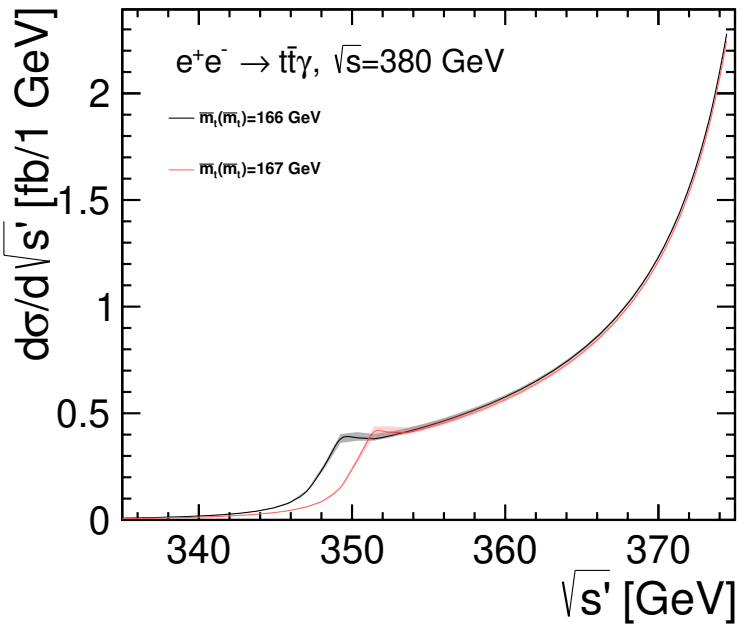

Fig. R.13 Predicción de la sección eficaz diferencial en función de $\sqrt{s'}$ con el cálculo combinado NNLL en el umbral y NNLO en el continuo. Las curvas negras y rojas corresponden a dos valores para la masa del quark top, $\overline{m}_t(\overline{m}_t) = 166, 167\,\text{GeV}$, respectivamente. Las sombras grises y rojas representan la banda de incertidumbre teórica.

escenarios: CLIC a 380 GeV e ILC a 500 GeV. Los resultados obtenidos son de una incertidumbre en la masa medida de 46 MeV para CLIC y 55 MeV para ILC.

Por otro lado, el estudio también evalua las fuentes más importantes de errores sistemáticos a nivel experimental. Dado que el observable depende únicamente de la identificación de sucesos $t\bar{t}\gamma$ y de la reconstrucción de s', tres variables experimentales pueden afectar al observable: la selección de sucesos, la indeterminación de la energía de colisión, y, la precisión en la reconstrucción de los fotones.

Respecto a la selección de sucesos, confiamos en los estudios de simulación completa del detector realizados por la comunidad para estimar la selección de eventos $t\bar{t}$, y en el estudio a nivel partículas de Marçà Boronat para estimar la eficiencia de selección de fotones ISR en eventos $t\bar{t}\gamma$. Por un lado, la identificación

de eventos $t\bar{t}$ se puede realizar con una eficiencia del orden del 90%, y por el otro lado, el fotón ISR puede ser aislado con una eficiencia de en torno al 80%. Adoptamos una estimación conservadora de una eficiencia global del 50% para el estudio.

El espectro de luminosidad tanto de CLIC como de ILC nos muestra que la energía de colisión no es una función δ en el valor nominal, si no que tiene una distribución que proviene de la anchura del espectro energético de los haces y el efecto de *beamstrahlung*. Para tener en cuenta este efecto, el observable es redefinido como la suma de los cálculos teóricos a distintas energías de centro

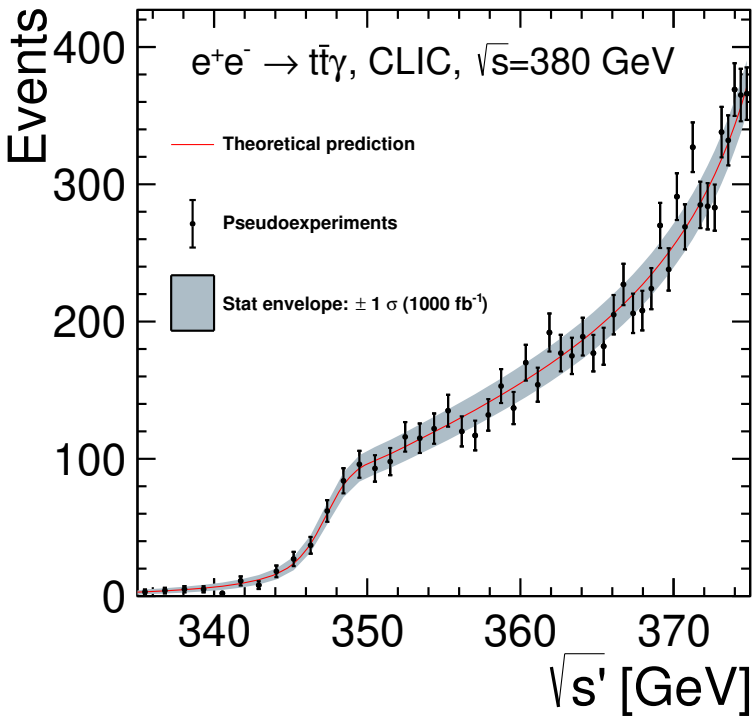

Fig. R.14 Pseudoexperimento generado como fluctuaciones poissonianas del cálculo combinado NNLL en el umbral y NNLO a $\sqrt{s} = 380\,\text{GeV}$y $\overline{m}_t = 166\,\text{GeV}$, teniendo en cuenta el espectro de luminosidad de CLIC.

Tabla R.3 Incertidumbres esperadas en la masa $\overline{m}_t(\overline{m}_t)$ del quark top para las etapas a $\sqrt{s} = 380\,\text{GeV}$ en CLIC, y a $\sqrt{s} = 500\,\text{GeV}$ en ILC. Para ambos colisionadores, los resultados se presentan para una luminosidad integrada de $500\,\text{fb}^{-1}$ y para sus luminosidades integradas nominales de $1000\,\text{fb}^{-1}$ en CLIC [26] y $4000\,\text{fb}^{-1}$en ILC [72].

Experimento	CLIC, $\sqrt{s} = 380\,\text{GeV}$		ILC, $\sqrt{s} = 500\,\text{GeV}$	
L_{int} (fb^{-1})	500	1000	500	4000
Estadístico	138 MeV	93 MeV	348 MeV	109 MeV
Teoría	46 MeV		55 MeV	
Espectro de luminosidad[7]	7 MeV		7 MeV	
Escala de energía del fotón	16 MeV		85 MeV	
Total	147 MeV	105 MeV	363 MeV	149 MeV

de masas $\sqrt{s}$, pesados por la fracción de colisiones a dicha energía. El error proveniente de la precisión con la cual puede ser determinado el espectro de luminosidad es propagado al observable, encontrando una incertidumbre del orden de 7 MeV en la masa del top para el caso de CLIC.

Por último, el error en la reconstrucción de la energía del fotón puede provenir de dos fuentes: la resolución energética, y el error de calibración de la escala energética del calorímetro. Para mitigar el primero, se adopta la resolución del calorímetro para el binado de E_γ, y el binado es propagado a la distribución de $\sqrt{s'}$. Y respecto al segundo, se estudia el efecto de una sobreestimación y subestimación en la medida de la energía del fotón del 0.1% sobre el observable, obteniendo desviaciones del orden de 16 MeV para el caso de CLIC, y 85 MeV para el caso de ILC. No es sorprendente esta diferencia entre ambos colisionadores, dado que los fotones más sensibles a la masa del quark top ($E_{\gamma,\text{max}} \simeq \frac{s-4m_t^2}{2\sqrt{s}}$) en el ILC son mucho más energéticos que los de CLIC, afectando el sesgo en la medida de la energía del fotón al primero en mayor medida.

Para evaluar la precisión estadística, se generan pseudoexperimentos a través de métodos de Monte Carlo (ver Figura R.14), y se ajustan al modelo teórico con la masa como parámetro libre, obteniendo una masa ajustada y una estimación del

[7]La incertidumbre del espectro de luminosidad de ILC no pudo ser estimada a tiempo para ser incluida en la tesis. Como aproximación, asumimos el valor obtenido para CLIC.

error a través del paquete de minimización TMinuit. Dichos pseudoexperimentos se realizan teniendo en cuenta una reducción del 50% de la estadística debido a la efiencia de selección, y con el observable pesado por el espectro de luminosidad. El error estadístico es estimado como la media de los errores estimados por TMinuit para 1000 sucesos.

Los resultados en la Tabla R.3 muestran que precisiones del orden de 100 MeVy 150 MeVson alcanzables para las luminosidades integrales nominales de CLIC a 380 GeV e ILC a 500 GeV, mejorando sustancialmente la precisión alcanzable en los colisionadores hadrónicos.

Appendix A

Probe card test report

Probe card test report of the W05_IF module, tested on the 28th of July of 2017. The report uploaded to the database is reproduced below as-is.

```
The W05_IF module is the seventh IF module of the final production
(phase 3, batch 2). It has the latest chips available for all the ASICS
(DHPT 1.2b/DCDB 4.2/ SW 2.1).

Using the A2 probe card:
  1. 50 um: boundary scan toggling between passed/failed.
    +10 um: no JTAG init.
    +10 um: sw-dvdd 0 mA.
  2. 50 um: dhp-io and dhp-core 0 mA.
    +10 um: same.
    +10 um: same.
    +10 um: dhp-core 200 mA, consistently passed boundary scan.
  3. 60 um: everything went fine.

Measurements:
  * Current consumption of ASICS looked fine.
  * I could configure all the ASICS, reading and writing JTAG worked
      fine.
  * Switcher sequence uploaded and read back fine.
```

```
* The boundary scan passed OK.
* All HSL were achieved. The testpattern could be retrieved.
* DCD analog had a normal current consumption.
* Matrix power consumption looked fine.
* Pedestals were taken. Also illuminating with a laser.
```

Apart from the text, the report includes six figures attached: a picture of the pad damage from the touchdowns, the DCD test pattern, the boundary scan result, the power consumption of the module, the pedestals, and the laser pointer illuminating the sensor. These are shown below.

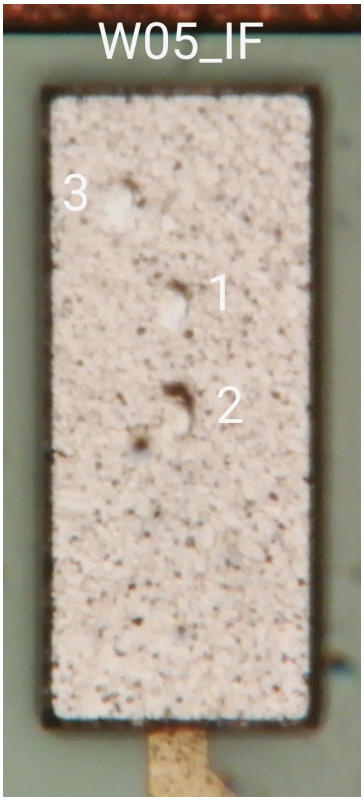

Fig. A.1 Marks in the pads from the touchdowns.

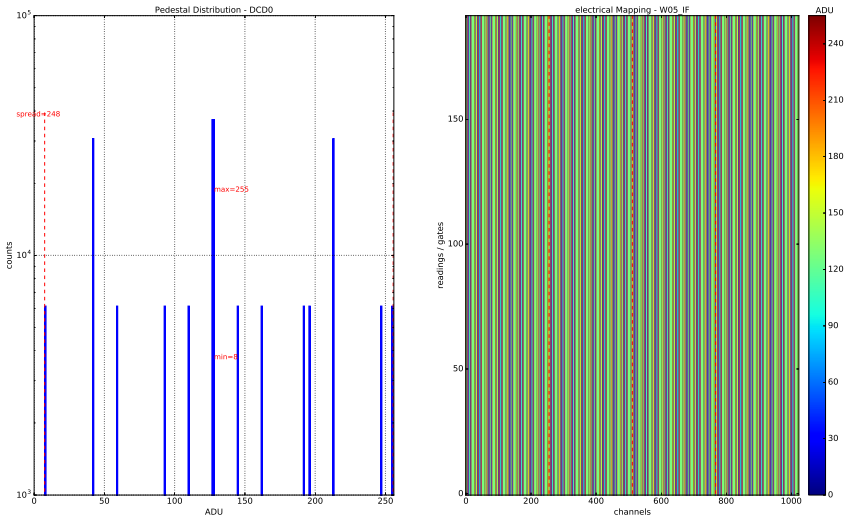

Fig. A.2 Retrieved test pattern.

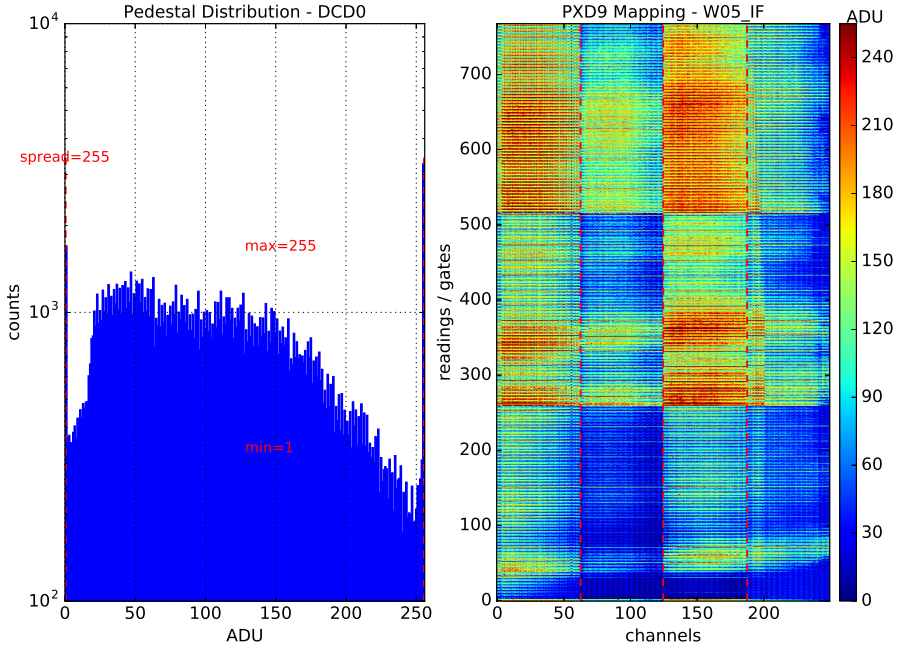

Fig. A.3 Sensor pedestals.

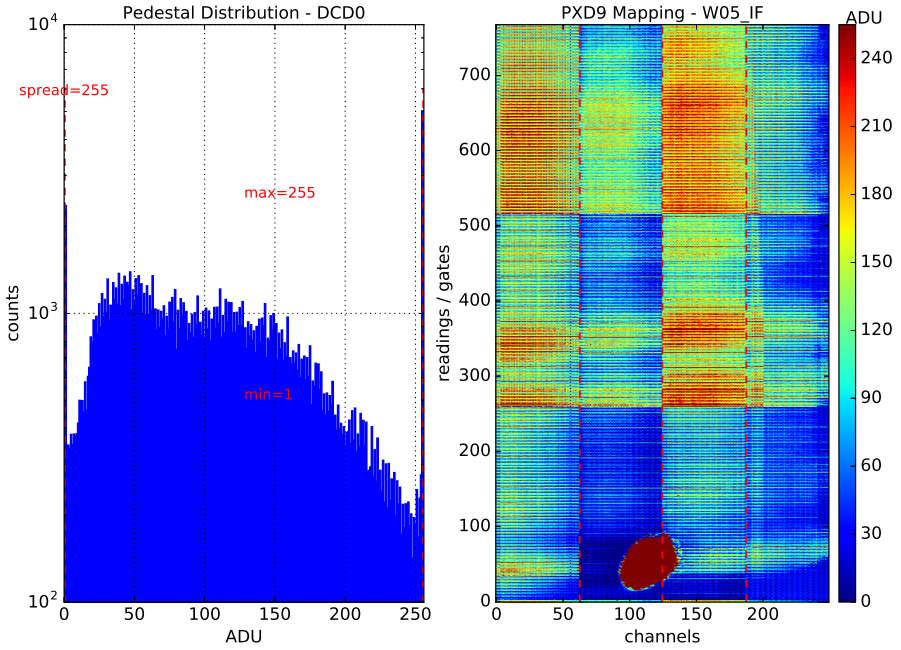

Fig. A.4 Sensor pedestals, illuminating with a laser pointer.

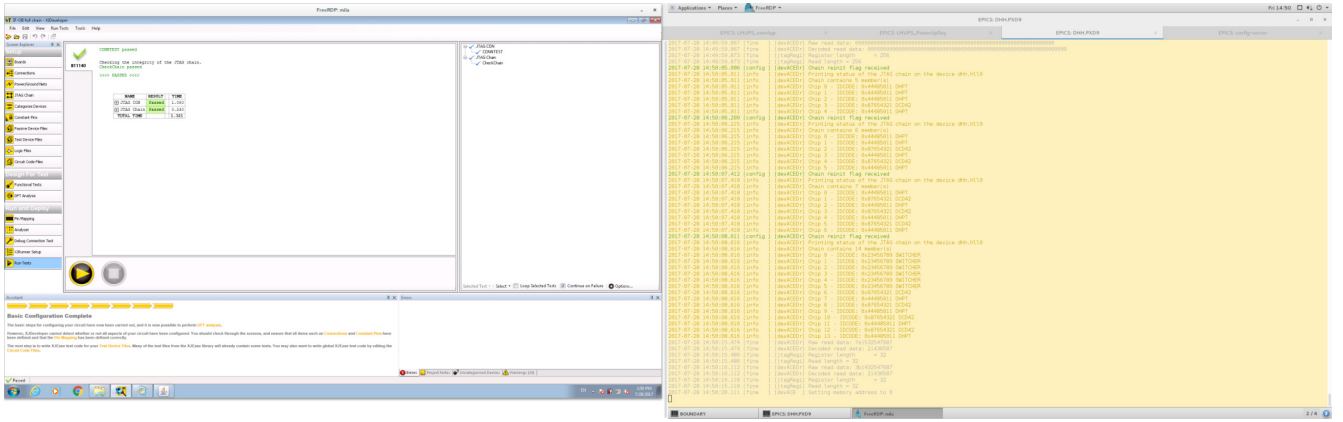

(a) Boundary scan, passed.

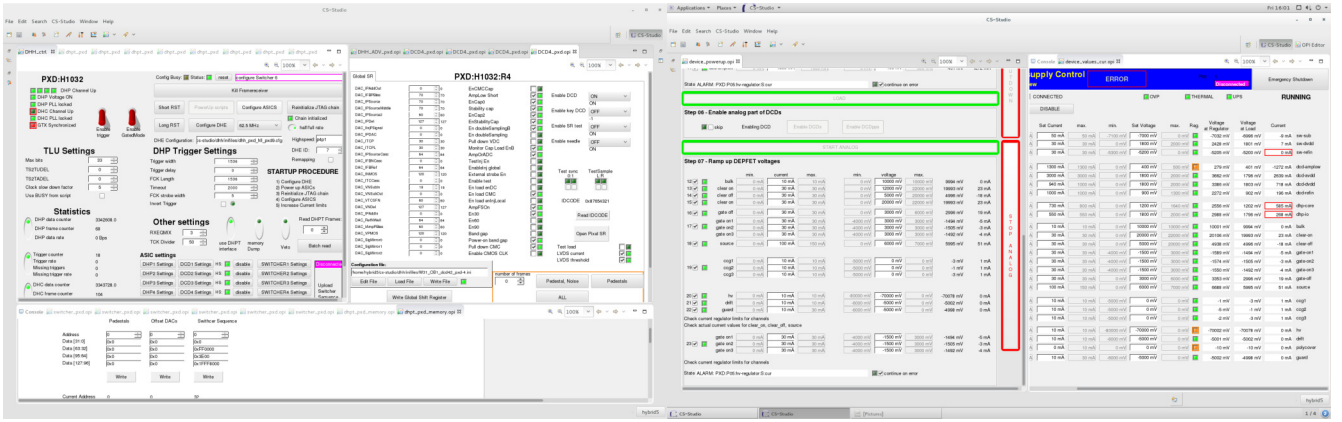

(b) Power consumption

Fig. A.5 Screenshots of the boundary scan test (top picture), and the power control panel (bottom picture).

Appendix B

ADC optimization

The ADC performance depends mainly on four parameters (commonly shared within a DCD) and two power voltages (common for all the channels in the module). The first two parameters *dacipsource* and *dacipsource_middle* relate to the current comparators used in the pipeline ADCs, while *dacipsource2* and *dacifbpbias* are related to the transconductors in the memory cells. The power nets *dcd_refin* and *dcd_amplow* supply the required voltage to the analog block of the DCDs.

The ADCs are characterized by their transfer curves, as shown in Figure 5.6a. These relate the incoming current with the digital ADU output. A series of quality criteria are established to evaluate their performance:

Dynamic range The digital output of the ADC can range from 0 to 255 ADU. Ideally, the transfer curve should fill the entire range, starting at 0 ADU for low currents up to saturation at 255 ADU.

Differential non-linearity The differential non-linearity measures the difference between the real step width from the ideal one. In a perfect ADC, each ADU value would correspond to

$$1 \text{ LSB} = \frac{\text{dyn. range}}{\text{ADU steps}} \simeq \frac{35\ \mu\text{A}}{255} \sim 140 \text{ nA}.$$

Deviations of the ADU step width from the LSB value increase the differential non-linearity. When a given code[1] exceeds the LSB it is called a *wide code*, likewise, if the code falls behind the LSB, it is called a *narrow code*.

Noise The ADC noise is measured by performing multiple measurements of the same input current and checking the digitized output. An optimal ADC would always yield the same output.

Communication error Such as *missing codes*. These manifest when a given code is unreachable, i.e. when an infinitesimal increase of the current yields an increment of two codes instead of one code. For example, if currents ranging from 150 to 300 nA are digitized as 2 ADU, and 300 to 500 nA as 4 ADU, then, the 3th code is missing.

Integrated non-linearity The integrated non-linearity measures the residuals of the linear fit respect to the centers of the codes. A low INL value implies a great linearity in the transfer curve.

A *pass* or *fail* result is assigned to each criteria, depending on a series of predefined tolerances. Finally, the product of the results for all the criteria is calculated to evaluate if the transfer curve falls within specification or not.

A series of sweeps over the DCD parameters and voltages are performed, recording the transfer curves of all the ADC channels to later analyze their quality. Then, the parameters that maximize the number of channels within specification are chosen as the optimal point for the DCD.

To obtain it, a sweep over the *dacipsource* and *dacipsource2* parameters (see Figure B.1) is performed for each DCD, keeping the rest of the parameters at their default values. Out of the sweep the optimal *dacipsource* and *dacipsource2* values are extracted.

[1] Each of the ADU values is referred to as *code*.

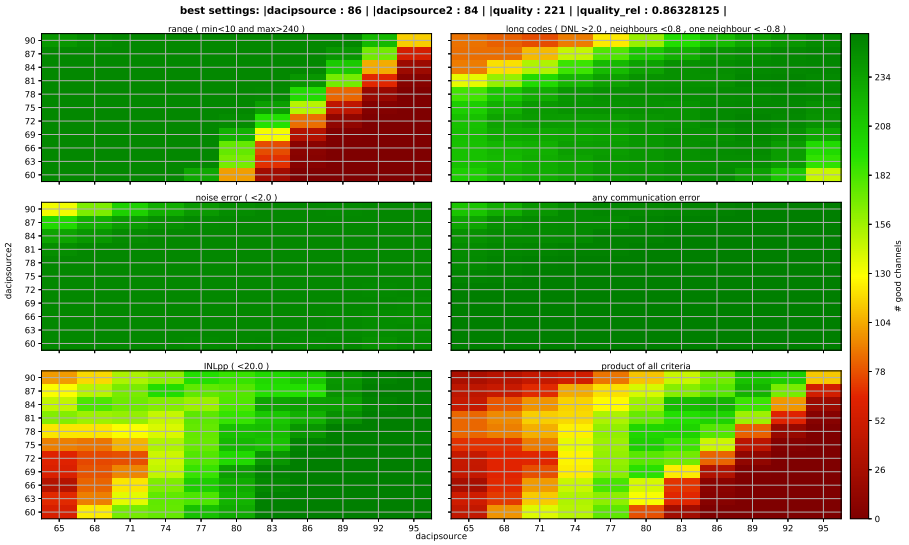

Fig. B.1 Sweep over the *dacipsource* and *dacipsource2* parameters in the channels of the fourth DCD.

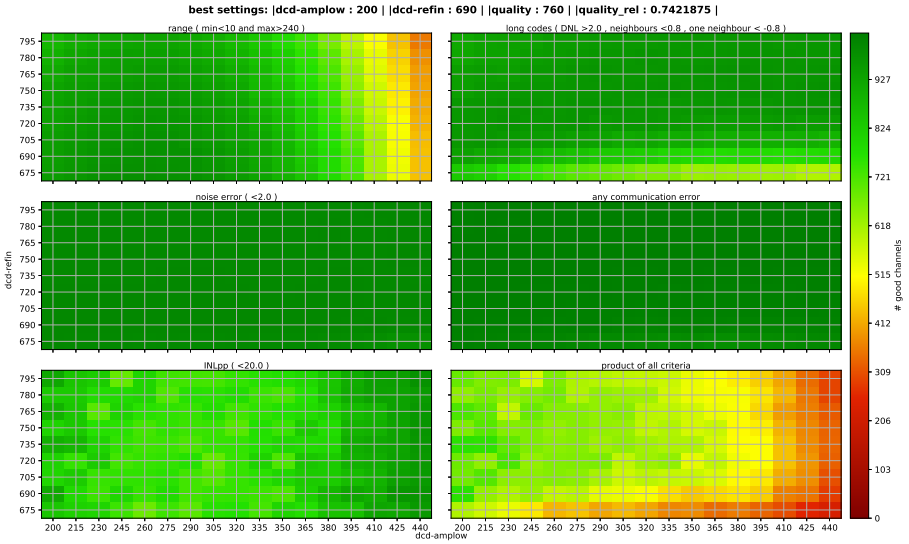

Fig. B.2 Sweep over the *dcd_amplow* and *dcd_refin* voltages in all the channels simultaneusly.

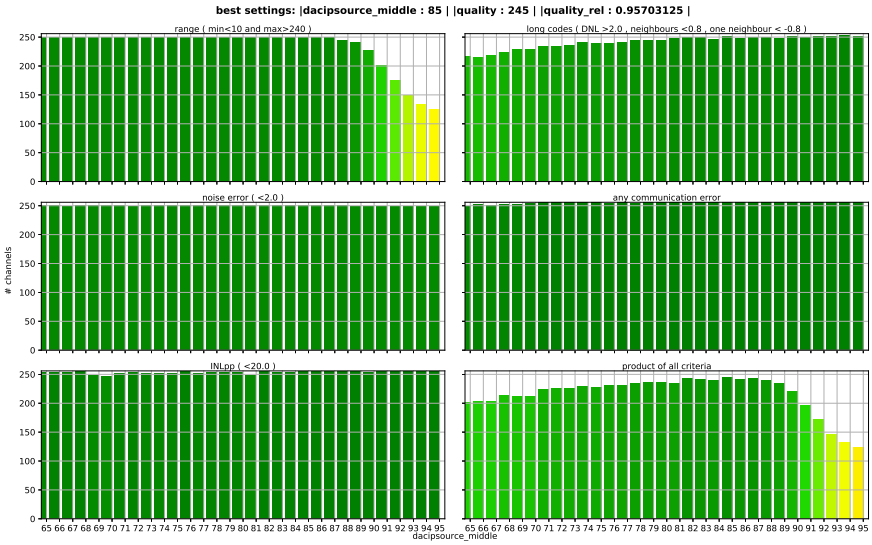

Fig. B.3 Sweep over the *dacipsource_middle* parameter in the channels of the fourth DCD.

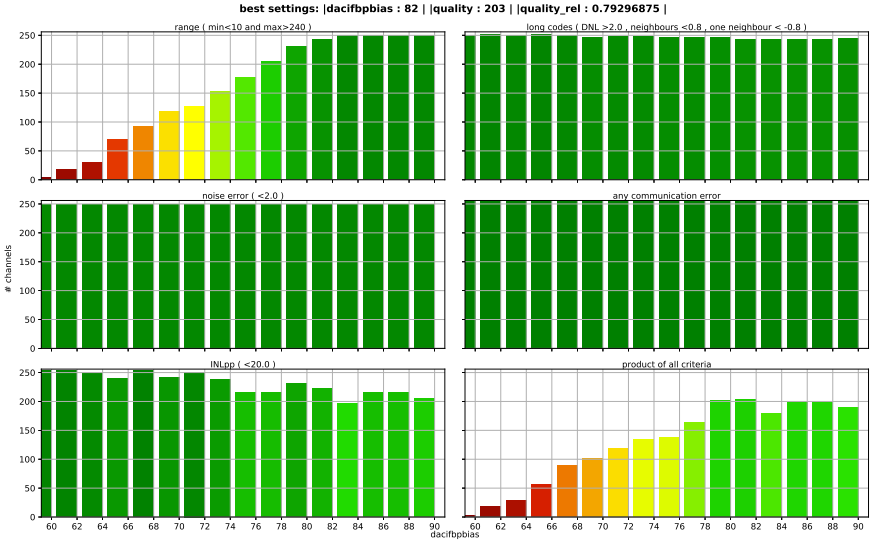

Fig. B.4 Sweep over the *dacifbpbias* parameter in the channels of the fourth DCD.

Once these are fixed, a common sweep over all the DCDs is performed over the *dcd_amplow* and *dcd_refin* voltages (see Figure B.2), fixing the common voltages for the four DCDs.

Then, a third sweep over the *dacipsource_middle* parameter (see Figure B.3) is done, finding its optimal value and fixing its value. A fourth sweep over *dacifbpbias* parameter (see Figure B.4) is performed, fixing its optimal value. These two sweeps are performed independently for each DCD.

Finally, the *dacipsource* versus *dacipsource2* and the *dacipsource_middle* sweeps are repeated after fixing the *dacifbpbias*, *dcd_amplow* and *dcd_refin* values, obtaining the final values for all the parameters.

Appendix C

Module characterization at lower DEPFET gain

To study the internal gain g_q of the DEPFET pixels at a different *gate-on* voltage the full module characterization has to be repeated. In this appendix the most relevant results of the characterization are shown.

C.1 Sensor pedestals

As the **Interchip Communication** parameters do not depend in the DEPFET gain, the characterization starts directly by the pedestal optimization.

As the *gate-on* voltage had been set to -2.0 V, in order to maintain the sensor performance, the ADC gain had to be raised from *En60* to *En90*. So, the first step consisted in repeating the **ADC scan** to find the new optimal operating point. The results of the scan are shown in Figure C.1.

After the **ADC scan**, the **ADC calibration** was repeated to find the new absolute DCD gains. Unfortunately, the measurement failed for the fourth DCD without resulting in any warning, and only the first three DCDs could be analyzed, as seen in Figure C.2.

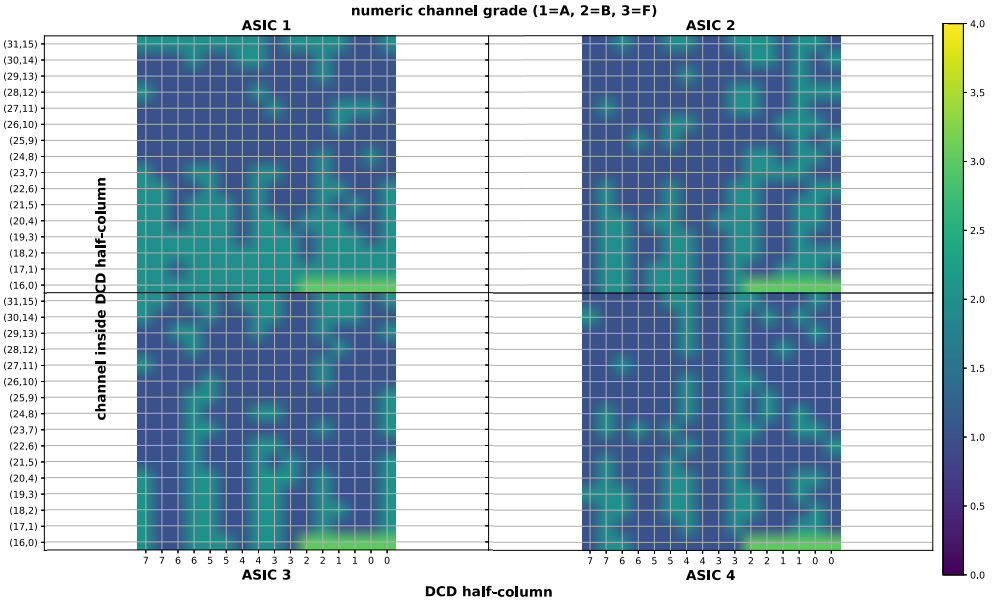

Fig. C.1 Quality grades of the ADCs in their optimal configuration. The grading system is defined as: 1 - perfectly working ADC, 2 - minor issues in the ADC, 3 - major issues or disconnected ADC. The last 6 channels of each DCD are disconnected from the sensor.

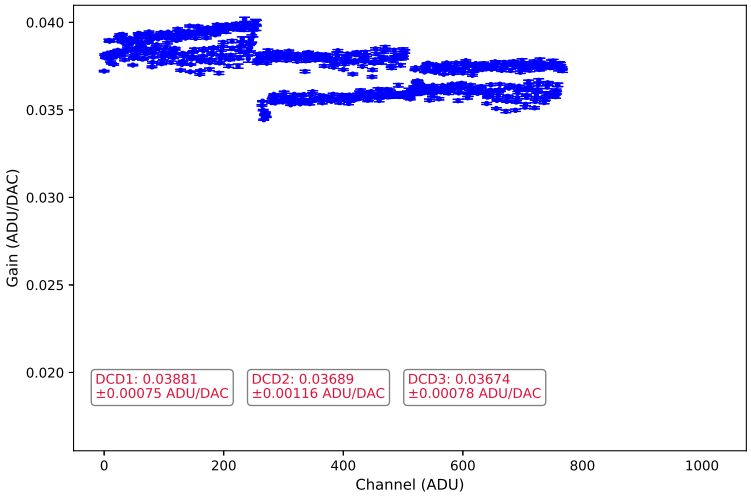

Fig. C.2 DCD absolute gain calibration using the DHE as the current source.

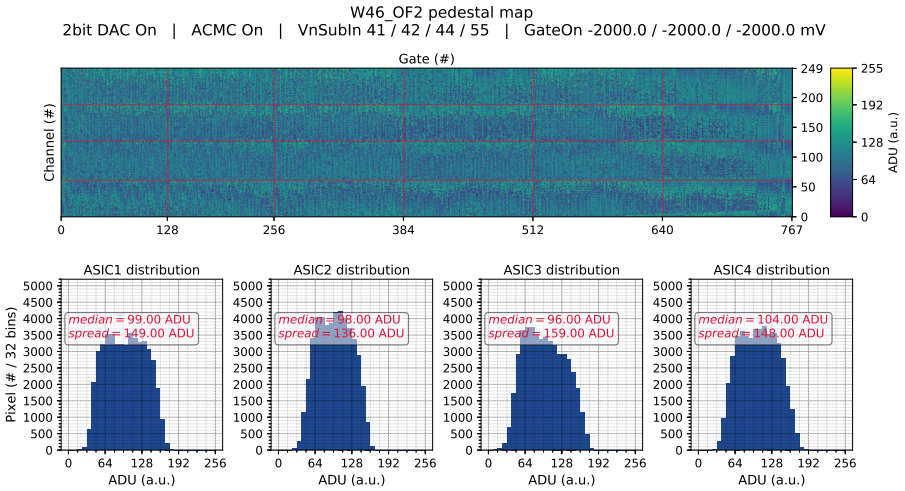

Fig. C.3 Optimized pedestal map of the W46_OF2 module at $gate\text{-}on = -2.0\ V$.

Once the ADCs were fully optimized, the next step consisted in activating the **ACMC** and repeating the **2-bit DAC** optimization. The resulting pedestals and its recorded noise are available at Figures C.3 and C.4, respectively.

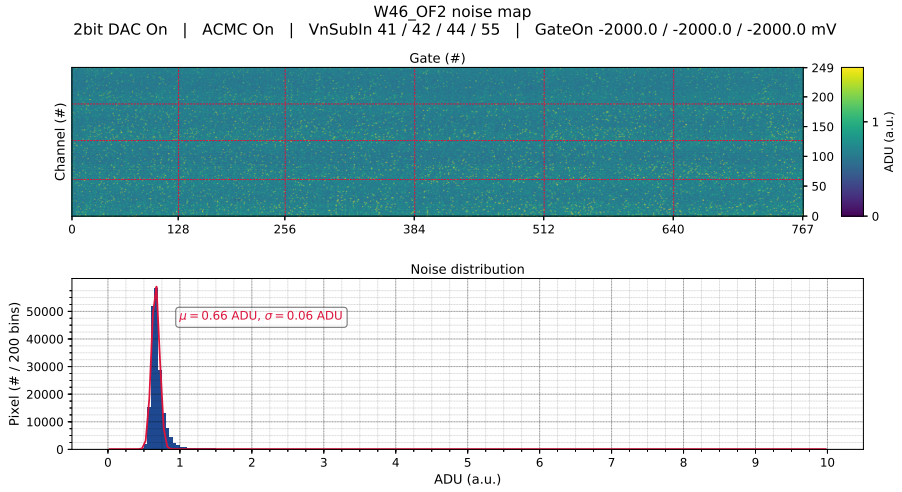

Fig. C.4 Pedestal noise map of the W46_OF2 module at *gate-on* $= -2.0$ *V*. In the bottom, a gaussian fit to the overall noise distribution is shown.

C.2 DEPFET voltages

The next step consists on repeating the measurements in the **DEPFET voltages** optimization with the proposed quantitative procedure. The results shown in Figure C.5 follow the same trends found in Figure 5.12, and the same optimal value of *drift* $= -6$ V, *clear-off* $= 2$ *V*, *high voltage* $= 62$ V is found. Nevertheless, as the measurements were taken before performing the analysis, the subjective optimal of *high voltage* $= -58$ V, *drift* $= -5$ V, *clear-off* $= 2$ V is used from here on.

At the chosen optimal point the signal strength and SNR for the ^{109}Cd source are measured. The results are shown in Figures C.6 and C.7, respectively.

Given that the overall gain for this configuration is much higher than for the *En60* case, and that the pedestal noise does not seem to scale with the DCD gain[1], the SNR obtained for this settings is much higher than what was found in

[1]For the *En60* setting, the mean noise was 0.65 ADU. For *En90*, it is 0.66 ADU.

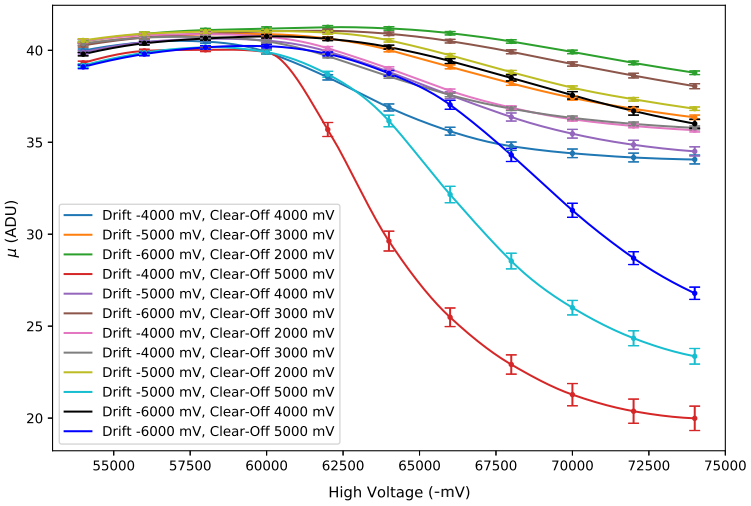

Fig. C.5 Signal strength estimated as the fitted gaussian mean μ of the cluster charge distribution for the different ^{109}Cd source measurements in the DEPFET voltages characertization sweep.

Chapter 5. It ranges between 52 and 70, from the EOS to the end of the module, respectively.

C.3 DEPFET internal gain

Last, the measurements of the sources in Table 5.2 are repeated to perform the energy calibrations. Using the energy calibrations, the energy gain is computed for each sensor region, as seen in Figure C.8.

Finally, with the data from the energy gain in Figure C.8 and the ADCs absolute gain in Figure 5.6, the internal gain g_q is calculated for each region in the sensor, as seen in Figure 5.20.

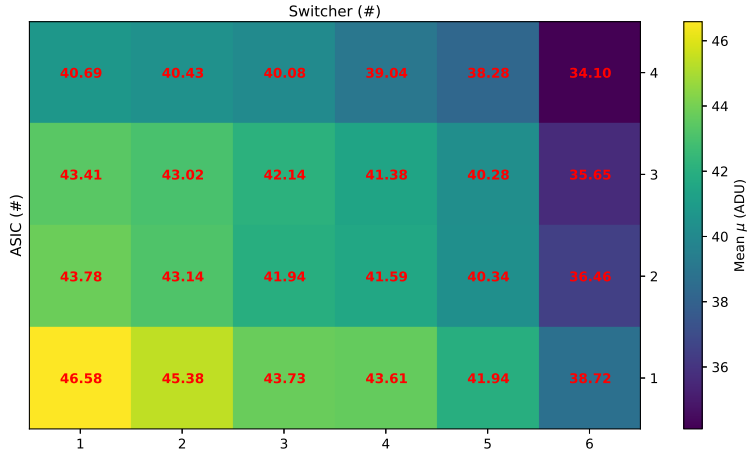

Fig. C.6 Signal strength for the different regions in the sensor. The signal strength is calculated as the fitted gaussian μ of the cluster distribution.

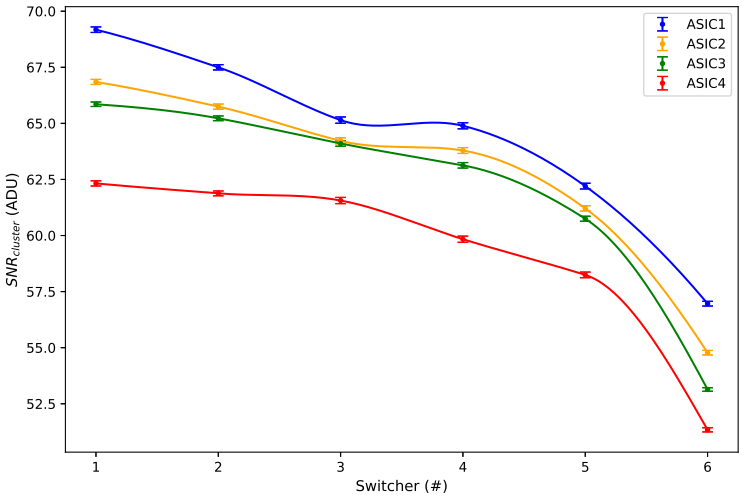

Fig. C.7 Signal to noise ratio for the different regions in the sensor. The SNR is obtained by dividing the signal strength in Figure C.6 between the mean recorded signal in Figure C.4.

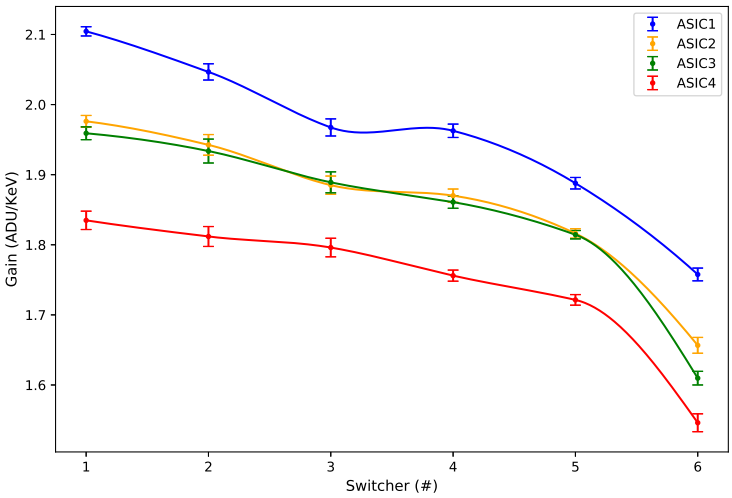

Fig. C.8 Energy gain of the different regions in the sensor, calculated as the slope of their respective energy calibrations.

References

[1] S. W. Hawking and M. Jackson, *A brief history of time*. Bantam, 2008. Cited on page 1.

[2] D. Griffiths, *Introduction to elementary particles*. Wiley Online Library, 1987. Cited on page 1.

[3] M. E. Peskin and D. V. Schroeder, *An Introduction to quantum field theory*. Addison-Wesley, Reading, USA, 1995. Cited on page 2.

[4] M. D. Schwartz, *Quantum Field Theory and the Standard Model*. Cambridge University Press, 2013. Cited on page 2.

[5] CERN, "The standard model and beyond." http://united-states.cern/physics/standard-model-and-beyond, 2019. Cited on page 3.

[6] M. Kobayashi and T. Maskawa, *CP Violation in the Renormalizable Theory of Weak Interaction*, *Prog. Theor. Phys.* **49** (1973) 652–657. Cited on page 6.

[7] Wikimedia, "Elementary particle interactions in the standard model." https://commons.wikimedia.org/wiki/File:Elementary_particle_interactions_in_the_Standard_Model.png, 2019. Cited on pages 9 and 153.

[8] A. Djouadi, *The Anatomy of electro-weak symmetry breaking. I: The Higgs boson in the standard model*, *Phys. Rept.* **457** (2008) 1–216, [hep-ph/0503172]. Cited on page 10.

[9] J. E. Kim and H. P. Nilles, *The mu Problem and the Strong CP Problem*, *Phys. Lett.* **138B** (1984) 150–154. Cited on page 12.

[10] Planck collaboration, N. Aghanim et al., *Planck 2018 results. VI. Cosmological parameters*, 1807.06209. Cited on page 12.

[11] P. Langacker, *Grand Unified Theories and Proton Decay*, *Phys. Rept.* **72** (1981) 185. Cited on page 13.

[12] H. E. Haber and G. L. Kane, *The Search for Supersymmetry: Probing Physics Beyond the Standard Model*, *Phys. Rept.* **117** (1985) 75–263. Cited on page 13.

[13] M. Tegmark, *Is the theory of everything merely the ultimate ensemble theory?*, *Annals Phys.* **270** (1998) 1–51, [gr-qc/9704009]. Cited on page 13.

[14] J. L. Hewett et al., *Fundamental Physics at the Intensity Frontier*, 1205.2671. Cited on pages 15 and 16.

[15] Particle Data Group collaboration, M. Tanabashi et al., *Review of Particle Physics*, *Phys. Rev.* **D98** (2018) 030001, numbers correspond to the 2019 update. Cited on pages 16, 134, and 155.

[16] T. Behnke, J. E. Brau, B. Foster, J. Fuster, M. Harrison, J. M. Paterson et al., *The International Linear Collider Technical Design Report - Volume 1: Executive Summary*, 1306.6327. Cited on pages 18, 26, 29, 31, and 156.

[17] SuperKEKB collaboration, K. Akai, K. Furukawa and H. Koiso, *SuperKEKB Collider*, *Nucl. Instrum. Meth.* **A907** (2018) 188–199, [1809.01958]. Cited on pages 18 and 20.

[18] S. Kurokawa and E. Kikutani, *Overview of the KEKB accelerators*, *Nucl. Instrum. Meth.* **A499** (2003) 1–7. Cited on page 18.

[19] SuperKEKB collaboration, "Projected luminosity." http://www-superkekb.kek.jp/img/ProjectedLuminosity_v20190128.png, 2019. Cited on page 19.

[20] A. D. Sakharov, *Violation of CP Invariance, C asymmetry, and baryon asymmetry of the universe*, *Pisma Zh. Eksp. Teor. Fiz.* **5** (1967) 32–35. Cited on page 19.

[21] Belle-II collaboration, T. Abe et al., *Belle II Technical Design Report*, 1011.0352. Cited on pages 22, 43, 45, 61, and 63.

[22] Belle-II collaboration, W. Altmannshofer et al., *The Belle II Physics Book*, 1808.10567. Cited on pages 23, 24, 25, and 43.

[23] P. Bambade et al., *The International Linear Collider: A Global Project*, 1903.01629. Cited on pages 25, 26, 27, 28, 30, 33, and 134.

[24] A. M al and R. Romaniuk, *XFEL, The European X-Ray Free-Electron Laser (TDR)*. 01, 2006. Cited on page 27.

[25] H. Abramowicz et al., *The International Linear Collider Technical Design Report - Volume 4: Detectors*, 1306.6329. Cited on pages 34 and 134.

[26] CLICdp, CLIC collaboration, T. K. Charles et al., *The Compact Linear Collider (CLIC) - 2018 Summary Report*, *CERN Yellow Rep. Monogr.* **1802** (2018) 1–98, [1812.06018]. Cited on pages 34, 35, 36, 37, 134, 146, and 174.

[27] L. Linssen, A. Miyamoto, M. Stanitzki and H. Weerts, *Physics and Detectors at CLIC: CLIC Conceptual Design Report*, *arXiv e-prints* (Feb, 2012) arXiv:1202.5940, [1202.5940]. Cited on page 35.

[28] A. C. Abusleme Hoffman et al., *Detector Technologies for CLIC*, 1905.02520. Cited on pages 39 and 40.

[29] Belle-II DEPFET, PXD, SVD collaboration, P. Kodyš et al., *The Belle II vertex detector integration*, *Nucl. Instrum. Meth.* **A936** (2019) 616–620. Cited on page 44.

[30] M. Friedl et al., *The Belle II Silicon Vertex Detector*, *Nucl. Instrum. Meth.* **A732** (2013) 83–86. Cited on page 44.

[31] C. Marinas and M. Vos, *The Belle-II DEPFET pixel detector: A step forward in vertexing in the SuperKEKB flavour factory*, *Nucl. Instrum. Meth.* **A650** (2011) 59–63. Cited on page 44.

[32] J. Kemmer and G. Lutz, *New detector concepts*, *Nuclear Instruments and Methods in Physics Research Section A: Accelerators, Spectrometers, Detectors and Associated Equipment* **253** (1987) 365 – 377. Cited on page 45.

[33] J. Kemmer, G. Lutz, U. Prechtel, K. Schuster, M. Sterzik, L. Strüder et al., *Experimental confirmation of a new semiconductor detector principle*, *Nuclear Instruments and Methods in Physics Research Section A: Accelerators, Spectrometers, Detectors and Associated Equipment* **288** (1990) 92 – 98. Cited on page 45.

[34] M. Koch, *Development of a test environment for the characterization of the current difitizer chip DCD2 and the DEPFET pixel system for the Belle II experiment at SuperKEKB*, *PhD thesis* **U. Bonn** (2011) . Cited on pages 46, 50, 52, 157, and 158.

[35] Belle-II DEPFET, PXD collaboration, C. Kiesling, H.-G. Moser et al., *The PXD Whitebook*. 2017. Cited on pages 47, 49, 53, 67, 72, 73, and 76.

[36] E. Prinker, *Testing of the Gated Mode for the Belle II Pixel Detector*, *MSc thesis* **LMU München** (2015) . Cited on page 51.

[37] Belle-II DEPFET, PXD collaboration, Z. Drasal and K. Prothmann, *Optimization of the Belle II Vertex Detector*, *The XIth International Conference on Heavy Quarks and Leptons (HQL 2012)* **Volume 166** (2012) . Cited on page 53.

[38] Belle-II DEPFET, PXD collaboration, P. Fischer, I. Peric and C. Kreidl, *SwitcherB Reference Manual*, *Internal documentation* **U. Heidelberg** (2012) . Cited on page 53.

[39] Belle-II DEPFET, PXD collaboration, *Flip-chip and SMD assembly of Belle II PXD pixel sensors*, *Internal documentation* **MPG Halbleiterlabor** (2015) . Cited on pages 53, 54, and 58.

[40] Belle-II DEPFET, PXD collaboration, I. Peric, *Production ASICs: DCDB4.2 Reference Manual*, *Internal documentation* **KIT Karlsruhe** (2016) . Cited on pages 54, 55, and 56.

[41] Belle-II DEPFET, PXD collaboration, M. Lemarenko, L. Germic and T. Hemperek, *Data Handling Processor Manual*, *Internal documentation* **U. Bonn** (2016) . Cited on pages 58, 59, and 60.

[42] L. Germic, *Data Handling Processor and Signal Transmission in the Belle II DEPFET Pixel Detector*, *PhD thesis* **U. Bonn** (2018) . Cited on pages 60, 61, and 106.

[43] Belle-II DEPFET, PXD collaboration, C. Wessel, *DEPFET Pixel Detector Situated on the Belle II Experiment*, *Pisa Meeting 2018* . Cited on page 62.

[44] T. Konno, R. Itoh, M. Nakao, S. Y. Suzuki and S. Yamada, *The slow control and data quality monitoring systems for the Belle II experiment*, *IEEE Trans. Nucl. Sci.* **62** (2015) 897–902. Cited on page 62.

[45] L. R. Dalesio, J. O. Hill, M. Kraimer, S. Lewis, D. Murray, S. Hunt et al., *The Experimental Physics and Industrial Control System architecture: Past, present, and future*, *Nucl. Instrum. Meth.* **A352** (1994) 179–184. Cited on page 63.

[46] Belle-II DEPFET, PXD collaboration, "Powering Scheme - LMU PS." https://confluence.desy.de/download/attachments/43903271/Schematic_Voltages.pdf?version=1&modificationDate=1514973826327&api=v2, 2019. Cited on page 64.

[47] D. Levit, I. Konorov and S. Paul, *FPGA based data read-out system of the Belle II pixel detector*, in *2014 19th IEEE-NPSS Real Time Conference*, pp. 1–2, May, 2014. DOI. Cited on page 65.

[48] Belle-II DEPFET, PXD collaboration, "DHH Scheme." https://confluence.desy.de/download/attachments/43903275/scheme.pdf?version=2&modificationDate=1520864177508&api=v2, 2019. Cited on pages 65 and 66.

[49] R. Itoh, T. Higuchi, M. Nakao, S. Y. Suzuki and S. Lee, *Data flow and high level trigger of Belle II DAQ system*, *IEEE Trans. Nucl. Sci.* **60** (2013) 3720–3724. Cited on page 65.

[50] T. Geßler, W. Kühn, J. S. Lange, Z. Liu, D. Münchow, B. Spruck et al., *The ONSEN Data Reduction System for the Belle II Pixel Detector*, *IEEE Trans. Nucl. Sci.* **62** (2015) 1149–1154, [1406.4028]. Cited on page 66.

[51] Belle-II DEPFET, PXD collaboration, "Support and cooling block." https://confluence.desy.de/pages/viewpage.action?pageId=102015538&preview=/102015538/102015545/image2018-8-27_9-41-45.png, 2019. Cited on page 67.

[52] A. Moll, *Comprehensive study of the background for the Pixel Vertex Detector at Belle II*, *PhD thesis* **LMU München** (2015) . Cited on page 67.

[53] DEPFET collaboration, P. Ruiz-Valls and C. Marinas, *The ultra low mass cooling system of the Belle II DEPFET detector*, *Nucl. Instrum. Meth.* **A731** (2013) 280–282. Cited on page 68.

[54] Belle II collaboration, *Official photograph album of the Phase 3 commissioning*, 2018. Cited on pages 68 and 150.

[55] M. Boronat, J. A. Fuster and C. Lacasta, *Development of the quality test protocol for the DEPFET pixel detectors and top-quark mass measurement at high energy e^+e^- colliders*, *PhD thesis* **U. Valencia** (2017) . Cited on pages 71, 77, 82, 114, 140, and 143.

[56] M. Hensel, *PXD9 production wafer*, *Internal communication* **MPG Halbleiterlabor** (2017) . Cited on page 74.

[57] P. Leitl, *JTAG Boundary-Scan of the Belle II Pixel Vertex Detector*, *MSc thesis* **LMU München** (2015) . Cited on pages 77 and 86.

[58] Belle-II DEPFET, PXD collaboration, L. Andricek, *PXD Status Report*, *BPAC* **MPG Halbleiterlabor** (February 2017) . Cited on page 91.

[59] Belle-II collaboration, M. Nayak, *SuperKEKB, Beast and Belle II prospects*, *PoS* **BEAUTY2016** (2016) 059. Cited on page 93.

[60] B. Paschen, *DHE DAC calibration*, *Private communication* **U. Bonn** (2018) . Cited on page 111.

[61] ATLAS collaboration, *Measurement of the top quark mass in the $t\bar{t} \to$ lepton+jets channel from $\sqrt{s} = 8$ TeV ATLAS data and combination with previous results*, *Eur. Phys. J.* **C79** (2019) 290, [1810.01772]. Cited on page 134.

[62] CMS collaboration, V. Khachatryan et al., *Measurement of the top quark mass using proton-proton data at $\sqrt{s} = 7$ and 8 TeV*, *Phys. Rev.* **D93** (2016) 072004, [1509.04044]. Not cited.

[63] ATLAS, CDF, CMS, D0 collaboration, *First combination of Tevatron and LHC measurements of the top-quark mass*, 1403.4427. Cited on page 134.

[64] HL-LHC, HE-LHC Working Group collaboration, P. Azzi et al., *Standard Model Physics at the HL-LHC and HE-LHC*, 1902.04070. Cited on page 134.

[65] ATLAS collaboration, *Measurement of the top-quark mass in $t\bar{t} + 1$-jet events collected with the ATLAS detector in pp collisions at $\sqrt{s} = 8$ TeV*, 1905.02302. Cited on page 134.

[66] CMS collaboration, *Measurement of $\mathrm{t\bar{t}}$ normalised multi-differential cross sections in pp collisions at $\sqrt{s} = 13$ TeV, and simultaneous determination of the strong coupling strength, top quark pole mass, and parton distribution functions*, *Submitted to: Eur. Phys. J.* (2019) , [1904.05237]. Cited on page 134.

[67] CLICdp collaboration, H. Abramowicz et al., *Top-Quark Physics at the CLIC Electron-Positron Linear Collider*, 1807.02441. Cited on pages 134, 135, and 139.

[68] M. Vos et al., *Top physics at high-energy lepton colliders*, 1604.08122. Cited on page 147.

[69] S. Gusken, J. H. Kuhn and P. M. Zerwas, *Threshold Behavior of Top Production in e^+e^- Annihilation*, *Phys. Lett.* **B155** (1985) 185. Cited on page 134.

[70] L. Linssen, A. Miyamoto, M. Stanitzki and H. Weerts, *Physics and Detectors at CLIC: CLIC Conceptual Design Report*, 1202.5940. Cited on page 134.

[71] CLIC, CLICdp collaboration, M. J. Boland et al., *Updated baseline for a staged Compact Linear Collider*, 1608.07537. Cited on page 134.

[72] T. Barklow, J. Brau, K. Fujii, J. Gao, J. List, N. Walker et al., *ILC Operating Scenarios*, 1506.07830. Cited on pages 134, 146, and 174.

[73] M. S. Amjad et al., *A precise characterisation of the top quark electro-weak vertices at the ILC*, *Eur. Phys. J.* **C75** (2015) 512, [1505.06020]. Cited on pages 135 and 139.

[74] A. H. Hoang, A. V. Manohar, I. W. Stewart and T. Teubner, *The Threshold t anti-t cross-section at NNLL order*, *Phys. Rev.* **D65** (2002) 014014, [hep-ph/0107144]. Cited on page 136.

[75] M. Boronat, E. Fullana, J. Fuster, P. Gomis, A. H. Hoang, V. Mateu et al., *Top quark mass measurement in radiative events at electron-positron colliders*, . Cited on page 136.

[76] A. H. Hoang, Z. Ligeti and A. V. Manohar, *B decay and the Upsilon mass*, *Phys. Rev. Lett.* **82** (1999) 277–280, [hep-ph/9809423]. Cited on page 137.

[77] A. H. Hoang, Z. Ligeti and A. V. Manohar, *B decays in the Upsilon expansion*, *Phys. Rev.* **D59** (1999) 074017, [hep-ph/9811239]. Not cited.

[78] A. H. Hoang, *1S and* $\overline{\rm MS}$ *bottom quark masses from Upsilon sum rules*, *Phys. Rev.* **D61** (2000) 034005, [hep-ph/9905550]. Cited on page 137.

[79] A. H. Hoang, A. Jain, I. Scimemi and I. W. Stewart, *Infrared Renormalization Group Flow for Heavy Quark Masses*, *Phys. Rev. Lett.* **101** (2008) 151602, [0803.4214]. Cited on page 137.

[80] A. H. Hoang, A. Jain, C. Lepenik, V. Mateu, M. Preisser, I. Scimemi et al., *The MSR Mass and the* $\mathcal{O}(\Lambda_{\rm QCD})$ *Renormalon Sum Rule*, 1704.01580. Cited on page 137.

[81] A. Widl, "$t\bar{t}$-threshold continuum matching results at NNLL/NNLO - $\mathcal{O}(\alpha_s^3)$." https://agenda.linearcollider.org/event/7645/contributions/40095/attachments/32392/49208/matching.pdf, 2017. Cited on page 137.

[82] A. Hoang, P. Ruiz-Femenia and M. Stahlhofen, *Renormalization Group Improved Bottom Mass from Upsilon Sum Rules at NNLL Order*, *JHEP* **10** (2012) 188, [1209.0450]. Cited on pages 137 and 138.

[83] M. Boronat, J. Fuster, I. Garcia, P. Roloff, R. Simoniello and M. Vos, *Jet reconstruction at high-energy lepton colliders*, 1607.05039. Cited on page 139.

[84] T. Suehara and T. Tanabe, *LCFIPlus: A Framework for Jet Analysis in Linear Collider Studies*, *Nucl. Instrum. Meth.* **A808** (2016) 109–116, [1506.08371]. Cited on page 139.

[85] M. Sohail Amjad, *Forward-Backward asymmetry in top pair production at the ILC*. PhD thesis, Orsay, LAL, 2014. Cited on page 139.

[86] D. Schulte, *Beam-beam simulations with GUINEA-PIG*, . Cited on page 140.

[87] S. Poss and A. Sailer, *Luminosity spectrum reconstruction at linear colliders*, *The European Physical Journal C* **74** (Apr, 2014) 2833. Cited on page 140.

[88] D. Arominski, E. Fullana and P. Gomis, *Reconstruction of the luminosity spectrum*, *CLIC-PUB* **2019** (2019) . Cited on page 140.

[89] K. Kawagoe et al., *Beam test performance of the highly granular SiW-ECAL technological prototype for the ILC*, 1902.00110. Cited on page 143.

[90] Linear Collider ILD Concept Group - collaboration, T. Abe et al., *The International Large Detector: Letter of Intent*, 1006.3396. Cited on page 143.

[91] N. Alipour Tehrani et al., *CLICdet: The post-CDR CLIC detector model*, . Cited on page 143.

[92] J. S. Marshall and M. A. Thomson, *Pandora Particle Flow Algorithm*, in *Proceedings, International Conference on Calorimetry for the High Energy Frontier (CHEF 2013): Paris, France, April 22-25, 2013*, pp. 305–315, 2013. 1308.4537. Cited on page 143.

[93] CALICE collaboration, C. Adloff et al., *Response of the CALICE Si-W electromagnetic calorimeter physics prototype to electrons*, *Nucl. Instrum. Meth.* **A608** (2009) 372–383, [0811.2354]. Cited on page 143.

[94] CLIC collaboration, J. J. Blaising, D. Dannheim and A. Sailer, *In-situ detector calibration at CLIC*, CLICdp-Note-2019-003. Cited on page 145.

[95] ATLAS collaboration, *Electron and photon energy calibration with the ATLAS detector using 2015–2016 LHC proton-proton collision data*, *JINST* **14** (2019) P03017, [1812.03848]. Cited on page 145.

[96] CMS collaboration, V. Khachatryan et al., *Performance of Photon Reconstruction and Identification with the CMS Detector in Proton-Proton Collisions at* $\sqrt{s} = 8$ *TeV*, *JINST* **10** (2015) P08010, [1502.02702]. Cited on page 145.

[97] Belle Programme Advisory Panel, *B-factory Programme Advisory Committee Full report for the 14th Focused Meeting Review on Readiness toward Phase 3*, . Cited on page 151.